博士論文

論文題目　Numerical Simulations on Combustion Characteristics in a Pre-Cooled Turbo Jet Afterburner

（予冷ターボジェットエンジンアフターバーナーの燃焼特性に関する数値計算）

氏　名　　ヤヌシ　ジョージ

Numerical Simulations on Combustion Characteristics in a Pre-Cooled Turbo Jet Afterburner

A Dissertation by

IANUS GEORGE 37-107396

in Partial Fulfillment of

the Requirements for the Degree

Doctor of Philosophy

Advisor: Professor Tsue Mitsuhiro

Department of Aeronautics and Astronautics

Graduate School of Engineering

THE UNIVERSITY OF TOKYO

October 2013

Numerical Simulations on Combustion Characteristics in a

Pre-Cooled Turbo Jet Afterburner

Abstract

A study to investigate the combustion characteristics on hydrogen angled injection has been performed in a model afterburner of the Pre-Cooled Turbo Jet engine (PCTJ). Fuel-lean and fuel-rich simulations have been performed at different injection configurations to evaluate the chemical heat release, total heat loss, combustion efficiency and NOx production. The study is useful to provide good understanding on the flow behavior and combustion characteristics that will later be used in the experimental evaluation of the PCTJ combustor. Computational Fluid Dynamics (CFD) simulations are run in a steady state manner solving the Reynolds Averaged Navier-Stokes (RANS) conservation equations augmented by a two-layer k-ε turbulence model using the SIMPLEST algorithm, over a three dimensional domain (3D). The domain boundary conditions isothermal upper and lower side of the axial flow and periodic on the left and right sides of the axial flow. The chemical interactions taking place in the combustion process were calculated using the CHEMKIN sub-routine. The chemical reaction mechanism used in this simulation involved 188 elementary reactions and 28 chemical compounds. The detailed NO chemical reaction system has been selected to provide a detail understanding of the NOx emission in the combustion process. The angle configurations used throughout the calculations for all equivalence ratios range from 10° to 120°. Data for different configurations is plotted at a constant equivalence ratio (0.26 – lean and 2.0 – rich) when one pair of angles is kept constant and the other varied, with the process repeated for the other case respectively. The combustion efficiency is evaluated using two approaches, (A) uses an enthalpy difference between the outlet and inlet enthalpies in relation to hydrogen theoretical heat release. This first approach is used to have a comparison basis between experiments and numerical simulations. The (B) second

approach evaluates the combustion efficiency as the ratio between the chemical heat release and the theoretical heat release. The heat loss at the walls is investigated in the entire chamber. The combustion efficiency is investigated near the nozzle area for comparison with experiments, and throughout the combustor to determine the flow influence induced by the angles injection. The EINOx is investigated at the exit of the combustor for different injection configurations. Experiments have shown a large temperature difference between the injection region, around the injector, and the nozzle region. As the equivalence ratio increased, the temperature difference decreased. This phenomenon has been investigated numerically, and the cause was determined to be due to the flow behavior induced by various angles of injection and heat loss incurred during the combustion process. Experiments were performed using a high enthalpy wind tunnel on model combustor with one injector. Using a system of thermocouples and static pressure sensors, relevant data was recorded for a fixed fuel-lean and fuel-rich equivalence ratio.

Simulations at fuel-lean conditions have found a that constant angled injection on one pair (upstream or downstream) coupled with increasing angles on the other pair, lead to higher combustion efficiency, when it is evaluated as an enthalpy difference. Higher angles on the downstream increase the mixing in the area and as a result, the temperature in the area. With increasing mixing, and a higher temperature, the NOx emission increase. However, as a result of higher angles, the heat loss at the walls also increased. This lead to the evaluation of the combustion efficiency using the chemical heat release approach, near the injector. The second approach is fairly independent of the flame temperature and heat loss in the combustor. Following this approach, we find that combustion efficiency is higher for increasing angles and lower when angles inject fuel perpendicular and up-flow.

For fuel-rich combustion the performance is substantially influenced by upstream angles due to the vortices that form in front of the injector at high angles lowering the maximum temperature of the flame. Another factor is the presence of the recirculation zones in the wake of the injector, which is found to lower the combustion efficiency. As the mixture becomes richer the combustion zone moves closer to the injector producing a smaller amount of NOx in the exhaust gas. Simulations at fuel-rich conditions show the heat loss is influenced by the mixture's prolonged contact with the walls, and by vortices forming between the two pairs of injection holes. The chemical heat release was influenced by the size of the vortices in the wake of the injector which affected the velocity flow field. The large vortices that form in the wake of the injector break down into smaller formations, when large angles inject fuel closer to the walls and are reflected, increasing turbulence and combustion efficiency, and heat loss at the walls. It has been found that NO is created in the post-flame region and increases downstream in the combustor. The concentration of NO2 decreased significantly in the wake of the injector, in the post-flame region, and was coincident with a corresponding formation of NO.

A sensitivity study has also been performed to determine the important reactions that create NOx in the current combustor. NO is produced in the center of the high temperature values of the flame through the Zel'dovich mechanism, NO2 recombination and to a smaller degree, by the N2O destruction. The NO2 production is more pronounced in large vortices that form as a result of angled injection. The NNH route is found to have a small influence on the creation of NO through re-dissociation into NO precursors.

Dedication

This thesis is dedicated to my father who has passed away during the course of this study. All his love and encouragement has stayed with me.

Secondly, this work is dedicated to my girlfriend to whom I mean to propose through this thesis.

Lastly but not in the least, it is dedicated to my family, my mother and my sister; without their support and encouragement, it couldn’t have been done.

Thank you.

Mulțumesc pentru tot sprijinul oferit, fără voi nu ar fi putut fi posibil.

Table of Contents

List of Tables

List of Figures

Nomenclature

Roman characters

B = flux limiter function [adimensional]

C_μ, C_d = turbulence model constants [adimensional]

$C_{\varepsilon 1,2,3,4}$ = turbulence model constants [adimensional]

$C_{p,k}$ = specific heat at constant pressure for species k [J kg^{-1} K^{-1}]

$Cv_{trans,rot,vib}$ = molar heat capacity from translation, rotation and vibration [J kg^{-1} K^{-1}]

d = diameter of hydrogen inlet [m]

D_k = diffusion coefficient for species k [m^2 s^{-1}]

F_i = the flux of the cell i [[quantity]/(time · area)]

$f_{k,i}$ = volume forces acting on species k in the ith direction [kg m^{-2} s^{-2}]

$f_{trans,rot,vib}$ = conductivity contribution form translation, rotation and vibration

G_b = the volumetric production of k by gravitational forces interacting with density gradients

$\Delta h_{f,k}^0$ = formation enthalpy for species k [J kg^{-1}]

Δh = distance between cell nodes [m]

$H(T)$ = enthalpy at standard state for k species [J kg^{-1}]

H_{ex} = exhaust enthalpy [J s^{-1}]

H_{in} = inlet enthalpy [J s^{-1}]

K_a = equilibrium constant of reaction (a) [adimensional]

k = turbulent kinetic energy [m^2 s^{-2}]

k_B = Boltzmann constant [1.3806488 × 10^{-23} m^2 kg s^{-2} K^{-1}]

L_s = turbulent length scale [m]

m = total mass of fluid in the control volume [kg]

m_k = molar mass of species k [mole]

$\dot{m}_{burn}$ = hydrogen mass flow rate [kg s^{-1}]

$\dot{m}_k$ = mass flow rate for *k* species (H2O, H2ex, O2ex, N2) [kg s^{-1}]

M_k = the molecular weight of species k [g mol^{-1}]

p = pressure [N m^{-2}]

P_k = volumetric production of k by shear forces

Pr_L = Prandtl number for laminar flow [adimensional]

Pr_T = Prandtl number for turbulent flow [adimensional]

$\dot{Q}$ = chemical reaction heat [J s^{-1}]

Q_{tot} = total heat loss in the chamber [J s^{-1}]

Q_{loss} = heat loss at the walls [J s^{-1}]

Q_{th} = theoretical heat release [J s^{-1}]

q_{H2} = hydrogen LHV energy value [J kg^{-1}]

Q_{ac} = actual enthalpy [J s^{-1}]

r_i = the position of the cell i [m]

Re = Reynolds number [adimensional]

S = area of the control volume [m^3]

S_c = Schmidt number [adimensional]

S_ε = source term in the energy dissipation equation

$S_u, S_u{}'$ = momentum equation sources

S_T = energy equation sources

t = time [s]

T = temperature [K]

T_{near_wall} = temperature of the closest cell node near the wall [K]

T_{wall} = temperature at the wall [K]

T_{CFD_nozzle} = numerical temperature near the nozzle [K]

T_{exp_nozzle} = experimental temperature near the nozzle [K]

$u_{i,j}$ = velocity component on the ith and jth direction [m s^{-1}]

V = velocity at cell face [m s^{-1}]

ΔV = cell volume [m^3]

$V_{k,i}$ = ith component of the diffusion velocity of species k [m s^{-1}]

$x_{i,j}$ = Cartesian coordinates

ΔX_{ij} = area on the X axis [m^2]

ΔY_{ij} = area on the Y axis [m^2]

Y_k = mass fraction of species k [adimensional]

Greek characters

α = thermal diffusivity [m^2 s^{-1}]

β = upstream injection angle [°]

ε = dissipation rate of turbulent kinetic energy [m^2 s^{-3}]

ι = local equivalence ratio

η_A = numerical combustion efficiency (A) approach [adimensional]

η_B = numerical combustion efficiency (B) approach [adimensional]

$\eta_{CFD_{nozzle}}$ = numerical combustion efficiency at the nozzle [adimensional]

$\eta_{exp_{nozzle}}$ = experimental combustion efficiency at the nozzle [adimensional]

θ = downstream injection angle [°]

λ = thermal conductivity [W m^{-1} K^{-1}]

μ = dynamic viscosity [kg m^{-1} s^{-1}]

μ_T = turbulent viscosity [kg m^{-1} s^{-1}]

υ_T = kinematic viscosity [m^{2} s^{-1}]

π = the mathematical constant

ρ = density [kg m^{-3}]

σ = normalized scalar value of the residual [adimensional]

$\sigma_{K,1,2}$ = molecule diameter for species k [Å]

$\sigma_\varepsilon, \sigma_k$ = turbulence constants [adimensional]

τ_{ij} = viscous tensor

$\dot{\omega}_k$ = reaction rate of species k [mole m^{-1} s^{-1}]

$\dot{\omega}_T$ = total heat release rate [W]

Φ = equivalence ratio of the mixture [adimensional]

ϕ_ω = variable at cell face

$\phi_{W,P,S,E}$ = variable at cell node W,P,S,E

$\Omega^{(2,2)}$ = Lennard-Jones potential reduced collision integral

$\Omega^{(1,1)}$ = Lennard-Jones potential reduced collision integral

1. Introduction

The process of combustion has been at the core of energy producing industries for many years. Most of our energy (~80%) comes from the combustion of various substances, solids, liquids and gases[1]. This has dominated our industrial revolution and evolution. It is also predicted, based on the amount of resources available, that combustion will remain the main source of energy for the next centuries. This process has remained in the focus of researchers, because many combustion-related questions have yet to be answered. Since the study of combustion is a “polyscience” study, a background of the different sciences associated is necessary. To answer some of these questions, a theoretical and an experimental approach is recommended. The theoretical approach includes analytical models, numerical predictions and predictive algorithms. Any theoretical approach has to be compared, validated and checked empirically after which another step can be put on the foundation of what is the combustion process.

Combustion has applications in many fields and industries from power generation, material production, heating, safety, pollutant emission and control being just a few. In the power generation field, two divisions are distinguished. One is the electricity generating stations using coal or natural gas. The other is the ground, water and air transport industry using liquid and gaseous fuels.

Propulsion challenges are closely related to the problems affecting the aerodynamics of the aircraft. Basically what can work for a flight speed corridor, will not work or be efficient in others. Thus a combination of propulsion system is suggested to enable engine operation over various regimes. One such example is a turbojet based combined cycle (TBCC) engine which is a combination of a compressor - turbine and ramjet/scramjet propulsion system.

According to Barber et al. [2], challenges that need to be addressed in resolving propulsion system for TBCC include variable geometry designs, thermal management, materials and engine components, fuels, environmentally friendly exhaust products, injector type and flow paths.

The current study is focused on helping to tackle the propulsion challenges which are related to the power generation combustion process in aircrafts. The combustion chamber's purpose, whether it is a main combustor or an afterburner, is to burn large quantities of fuel, with suitable volumes of air, and to direct and release the heat resulted from the combustion, with minimum heat loss and maximum heat release, in the limited space available [3-Ch. 4]. Combustion must be stable, efficient and with low pollutant emissions [3]. Stable combustion means the ability of the flame to remain alight for the entire flight regime and aircraft envelope. A strict control of the efficiency is necessary to achieve the most thrust with minimum losses out of a propulsion system. Due to severe environmental damage, unwanted pollutants, created within the combustion chamber, must be strictly controlled.

While the main combustor's purpose is to generate the necessary thrust needed for the aircraft to function, afterburning (or reheat) is a method of augmenting the basic thrust of the engine to improve the aircraft take-off, climb and (for military aircraft) combat performance. The increased power could be obtained by the use of a larger engine, but as this would increase the weight, afterburning provides the best method of thrust augmentation for short periods. Exhaust gases coming from the engine turbine are mixed and burned with unburned oxygen and fuel before the jet chamber propelling nozzle. The resulting combustion increases the temperature of the exhaust gas giving increased velocity of the exhaust gases and therefore increasing the engine thrust.

Trying to satisfy all of the above conditions requires a compromise which would give a noticeable reduction of pollution with the least sacrifice in engine thrust, fuel consumption, and addition of weight. However with the possibility of supersonic and hypersonic flight around the corner, a continuous research effort is put forth on ramjet and scramjet combustors [4]. They offer a simple geometry with a high specific impulse, and can be used at high speed flight regimes [5]. Although ramjet engines are fuel-efficient for supersonic regimes [6], they are inefficient at subsonic speeds since they depend on the high speed of the aircraft to compress the intake air, needed for the combustion of fuel. To allow operation of the ramjet engine at subsonic regimes, a combined cycle engine is used to cover the entire flight regime. One major challenge of the combined cycle engine is to have an optimized flow path through the engine. This implies the use of variable geometry engine parts.

A design that incorporates the advantages of the ramjet with the capabilities of the turbojet, the Pre-Cooled Turbo Jet engine (PCTJ) [7,8], is an air turboramjet engine equipped with a heat exchanger, that is expected to power the next generation of hypersonic transport in Japan [9]. Following its predecessor, the ATREX engine [10,11], the PCTJ employs a variable intake, a pre-cooler or heat exchanger, a turbojet core and a ram combustor (afterburner) fitted with a plug variable nozzle. The intake, equipped with variable ramps to produce the appropriate shock pattern for the free stream flight regime. A rectangular shape for the variable nozzle is selected because it is simpler in design and has a larger throat area. It is fitted with three ramps, two of which are variable to produce the suitable shock patterns according to the flight regime [12]. The pre-cooler, placed in front of the turbojet core, is used to cool the incoming air, as well as the afterburner walls. Because the airflow temperature entering the compressor stage is reduced by the pre-cooler, and the density of the fluid is increased, larger airflow rates are achieved with lower compressor loads. This allows the turbojet engine, with its metal structure, to operate at regimes up to Mach 6. The turbojet engine comprises of a six stage axial compressor, an annular-type combustor and a two stage turbine. A reverse annular-type combustor was chosen to reduce the total engine length for the s-engine experiments [13]. The afterburner is equipped with injectors to provide after-burning and is fitted with a single-ramp rectangular variable exhaust nozzle. Using this set-up, the PCTJ can operate from 0 to a flight Mach number of 6[7].

Combustion in the afterburner depends on the mixing of reactants, ignition, flame holding and completion of combustion [14]. The mixing process in the combustor is influenced by the fuel and the injector. To achieve efficient mixing in an afterburner, a high energy, fast reacting fuel is needed. For supersonic regimes, hydrocarbon fuels are the better alternative because they offer advantages in volumetric storage and operation costs. However, while liquid hydrocarbon fuels are useful for supersonic to hypersonic regimes, they are limited by the rate of energy consumption at high temperatures [15], a fact that cannot be compensated by injecting additional fuel to raise the exhaust speed, as in the case of simple di-atomic gases like hydrogen. For high Mach ($M > 4$) number regimes, hydrogen fuel is the desirable alternative. Hydrogen is well-known for its low greenhouse emissions and high efficiency [16], as well as high-calorific value content per unit mass, and fast reaction [17]. There is a participation to the greenhouse gases via water vapors that influence cloud formation and affect precipitation[18], especially in the lower atmosphere (<5km)[19]. However, water vapors are just a natural feedback effect to the changing weather. “The point is that water vapor responds to climate – and therefore influences climate as a feedback. The concern is that humans adding CO2 to the atmosphere will cause a change to the climate and water vapor will have a feedback effect”[20]. The PCTJ uses liquid hydrogen for the pre-cooler and gaseous hydrogen for the turbo machinery core and afterburner. After the liquid hydrogen absorbs the heat of air in the pre-cooler, it later becomes gas and is supplied to the core engine and afterburner. By controlling the equivalence ratio, a high specific impulse, high thrust and weight ratio can be theoretically achieved. Fuel-lean combustion is used in the core turbojet, to obtain a high specific impulse and fuel-rich combustion is used for the afterburner to facilitate the air cooling ability in hypersonic flight, a fact that makes hydrogen even more desirable as the fuel [21]. As a result, the decrease of the specific impulse incurred when a fuel-rich composition is used, is small.

Studies on the combustion in ramjets and scramjets [22] have shown that increasing vorticity on the streamwise direction enhances mixture by the formation of pressure and density gradients. This is achieved by different types of injector designs like swirl injectors[23], strut injectors[24], wall injectors [25] which include transverse injectors [26] and swept ramp injectors when ramps are mounted on the walls [27], the latter mainly used in scramjet engines. Swirl injectors are predominantly used in liquid rockets with staged combustion, gas turbines, and diesel engines for their high mixing and atomization efficiency. Strut and wall injectors are preferred for ram combustors with subsonic or supersonic airflow. If wall injectors are used, mixing is enhanced, but significant flow blockages are caused due to shock waves and thrust losses. If strut injectors are used, fuel can be injected continuously in the combustor, without the production of shocks. Through parallel fuel injection, strut injectors can also increase the engine thrust by adding additional momentum. However they have limited mixing capabilities. This can be increased through the use of shock waves or the creation of streamwise vorticity [28,29].

The PCTJ afterburner is equipped with struts to provide flame holding that also act as injectors. To increase vorticity in the streamwise direction, suitable geometry of the struts is necessary. Studies done by Araki [30] have focused on the mixing enhancements by Karman vortex breakdown, equipping the injector with various trailing edge struts, when the injection angle of the fuel, was unchanged. This study is based on the effects of injection angles on the combustion process in the PCTJ afterburner. The purpose is finding a configuration that can help improve the combustion efficiency with minimum NOx emissions.

Reducing air pollution and its effects on the immediate environment became a common global goal in the last years due to the various degradations encountered in the environment we live in. The net of restrictions spread further and tighter on the known pollutant producers as research became more advanced. The major products resulting from a combustion process include carbon dioxide and water. With the increase in stringent environmental rules [31], an increase control and examination is necessary. Less obvious products of the combustion include nitric oxides (NOx) [32]. NOx refers to chemical mixtures of nitric oxide and nitric dioxide (NO and NO_2), substances that can be dangerous to humans and to environmental health [33]. These NOx have an impact on the radiatively active trace gases found in the Earth’s atmosphere like ozone, methane and water vapors found in the stratosphere. NOx resulting from the combustion of aviation fuels, alongside carbon dioxide (CO_2), sulfur dioxide (SO_2) and other combustion exhaust gases impact the ozone layer (O3) [34]. In the atmosphere, through different transport and mixing phenomena and depending on the altitude, ozone-destroying chemical processes take place. If we add extra amounts of NOx to these chemical processes, the NOx cycle enhances catalytic ozone destruction [35].

The complex chemistry that leads to pollutant emissions in combustion can be estimated using numerical calculated fields of temperature and chemical radical concentrations. The NO formation rates in an aircraft based propulsion system as a function of gas composition and temperature are usually formed through several mechanisms: thermal-NO, prompt-NO, nitrous-oxide-NO and nitrogen dioxide-NO, NO from fuel bound nitrogen like coal and derivates, and the NNH mechanism introduced by Bozzelli and Dean [36].

In this study, since we deal with a hydrogen-air non-premixed flame, the effects of injection angles on the NOx emissions are considered and a reaction study regarding the various NOx formation mechanisms is investigated for the configuration that yields the higher combustion efficiency and lowest NOx concentration. In order to perform the reaction study, a sensitivity analysis has been performed where separate simulations have been run for only one configuration at fuel-rich conditions. The next step was to analyze and explain the various reactions that have sensitivity in our mechanisms and special conditions and validate them through other literature studies. Using this study we can have a better understanding of the main mechanisms that generate NOx, that later can help devise appropriate measures to control pollution emission.

2. Numerical

2.1. Problem formulation

With the increase in hardware power and software development in the recent years, Computational Fluid Dynamics (CFD) codes have become popular and more complex compared to yesterday’s codes. Hydrogen combustion in the afterburner was simulated using PHOENICS v.2011 64 bit from CHAM ltd.

The objective of the analysis is to determine the effect of the angled injection on the combustion and flame. This can help determine configurations that provide high combustion efficiency, low heat loss and low NOx emissions. Although experiments are being performed at the Kashiwa wind tunnel of the University of Tokyo by Nishida et al.[37,38], achieving this objective is proving to be a long process. Given the fact that the experimental process involves high costs, CFD simulations are the alternative in augmenting, evaluating and elucidating the experimental results. Experiments are carried for a 1:10 scale combustor with one injector, so simulations need to follow the same model. However, because 3D simulations involve a high computation time, a 3D simulation with periodic boundary conditions was carried out for only one pair of injection holes. In this way, the same experimental conditions could be used in the simulations.

The scope of the study is focused on the combustion efficiency thus a steady simulation is more than sufficient. The mean Reynolds number value estimated from experiments and used in the computational domain in higher than 5×10^4 and as a result the flow can be considered turbulent. To account for the turbulence in the flow, a $k-\varepsilon$ turbulence model has been used.

The code is based on three main elements – pre-processor, processor and post-processor. The pre-processor stage consists of *creation of geometry*, *mesh generation*, *material properties* and *boundary conditions*. The processor treats the *transport equations* (mass, momentum, energy, other transport variables, equation of state and supporting physical models) while taking into account the *physical models* (turbulence, combustion, radiation of other processes) and the solver settings which might be the *initial conditions, solution control, monitoring solution and convergence criteria*. The post-processor details the measuring parameters and analytical modeling used. Before we have a look at the main elements the equations base of the code will be detailed.

2.2. Governing equations

The governing equations solved in the present study are

$$\frac{\partial \rho}{\partial t} + \frac{\partial (\rho u_i)}{\partial x_i} = 0 \qquad (1)$$

The chemical species are characterized by their mass fractions Y_k for $k = 1$ to N is defined as

$$Y_k = \frac{m_k}{m} \qquad (2)$$

The conservation of species is given by:

$$\frac{\partial \rho Y_k}{\partial t} + \frac{\partial}{\partial x_i}\left[\rho\left(u_i + V_{k,i}\right)Y_k\right] = \dot{\omega}_k \qquad (3)$$

The momentum equation

$$\frac{\partial \rho u_j}{\partial t} + \frac{\partial (\rho u_i u_j)}{\partial x_i} = \frac{\partial \tau_{ij}}{\partial x_i} + \rho \sum\nolimits_{k=1}^{N} Y_k f_{k,j} + \left(S_u = -\frac{\partial p}{\partial x_j} + S_u'\right) \qquad (4)$$

The energy equation

$$\rho C_p \frac{DT}{Dt} + \rho \frac{\partial T}{\partial x_i}\left(\sum_{k=1}^{N} C_{p,k} Y_k V_{k,i}\right) = \frac{\partial}{\partial x_i}\left(\lambda \frac{\partial T}{\partial x_i}\right) + \dot{\omega}_T + S_T \qquad (5)$$

2.3. Geometry and flow domain

The first step in the pre-processor stage is the modeling of the geometry of the computational flow domain. To evaluate the combustion efficiency of the afterburner of the PCTJ, a ~ 1/10 scale combustor was fitted with one injector. To evaluate the different angles of injection, different injectors (in experiments) with the same shape but different angles were used. In Figure 1, the test section is shown, measuring 68 mm x 5 mm on the cross section, with 10 mm walls on the inside. The test chamber was fitted with a ramp shaped nozzle at the exhaust area and the total length measured 390 mm.

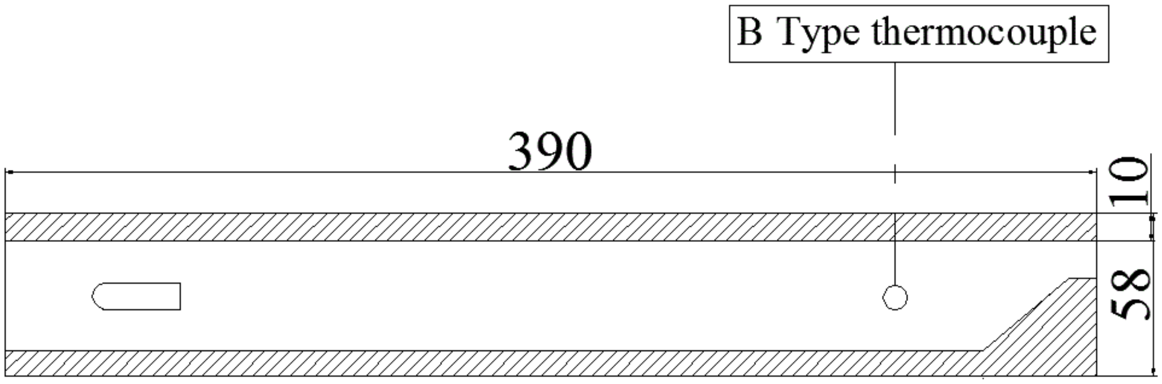

Figure 1 Schematic of combustor

The strut injector, as shown in Figure 2, was of a rectangular shape with a rounded face on the upstream side, measuring 27.25 mm x 9.5 mm with a height of 56.5 mm. Two different diameter holes were used to simulate the fuel-lean and fuel-rich compositions. Four $\phi = 1$ mm in diameter injection holes were used for fuel-lean, and four $\phi = 2.5$ mm in diameter were used for fuel-rich configurations. The inlets were arranged in two rows on the upper side and underside of the injector and the effect of different angles of injecting fuel for each line was investigated.

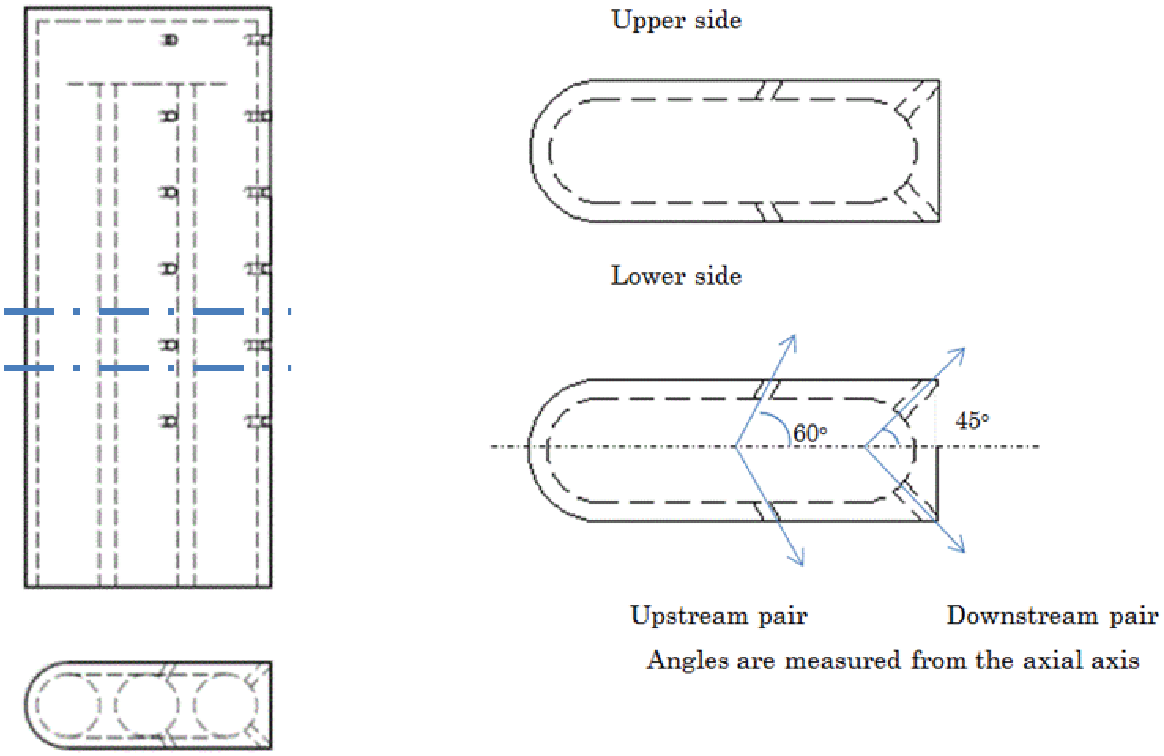

Figure 2 Schematic of injector

The injection holes were treated in pairs, the closest pair to the air inlet is named upstream injection pair (holes) and the closest to the exhaust nozzle downstream injection pair (holes) shown in Figure 2 right side. Upstream injection is fuel injection with at the angle made by the upstream injection pair with the axisymmetric axis of the injector (Figure 2 right side). Downstream injection is fuel injection at the angle made by the downstream injection pair with the axisymmetric axis of the injector.

The concept of the afterburner chamber, employed in our experiments, introduces 6 injectors placed head down with the injection holes on the right and left side of the chamber and not up and down as in our simulations and experiments. The experimental version of the afterburner chamber is based on a sub-scale engine introduced here[39,40]. A schematic, introduced by Sato et al.[41], is presented in Figure 3. Since experiments and numerical simulations have been performed with a rotated chamber (Figure 4), a set of numerical simulations have been performed for the same scenario with the original chamber and the configuration is found to have very little influence on the combustion phenomena involved. Thus all other simulations and experiments are performed with a rotated chamber.

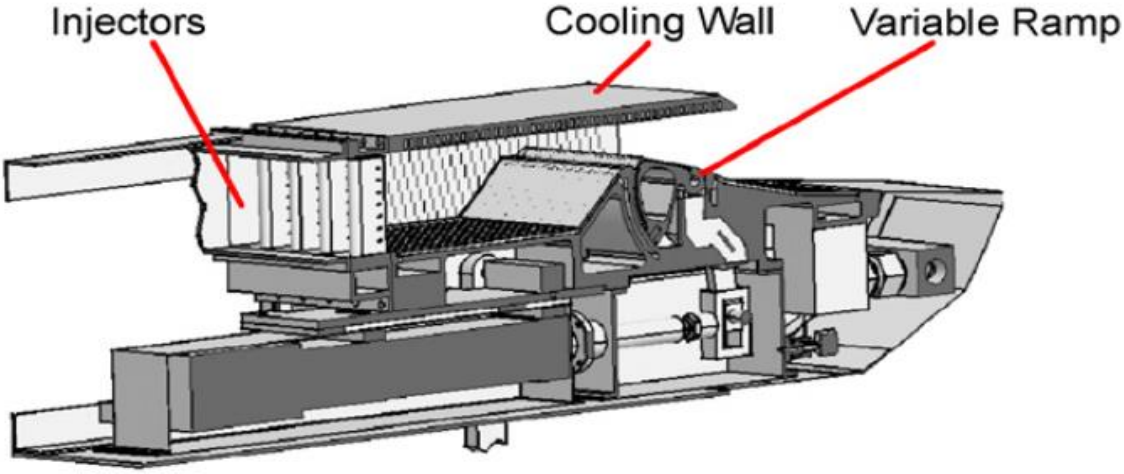

Figure 3 Afterburner chamber of the PCTJ introduced by Sato et al.[41]

2.4. Initial and boundary conditions

The combustion of Hydrogen in air in a turbulent non-premixed diffusion flame has important implications in which the boundary conditions must be prescribed. The second step in the pre-processor stage is dealing with the specification of permissible conditions that must be imposed on the flow and test combustor. In the case of inflow and outflow in the combustor, air inlet and fuel inlets have been created to accommodate flow inflow and an outlet to designate the outflow area. As can be seen in the Figure 4 below, the air inlet was created at the left side and the flow outflow was created on the right side.

In Figure 4-a, the red boundary represents the “slice” that is simulated. It measures 5 mm in width and 390 mm in length with 52 mm in height. Figure 4-b shows the fuel inlet layout used in fuel-rich simulations. The diameter of the inlet circle is 2.5 mm. Figure 4-c shows the ramp shaped nozzle and outlet used. Figure 4-d shows the fuel inlet layout used in fuel-lean simulations. The diameter of the inlet circle is 1.0 mm. The air inlet covers 80% of the area of inflow (max X and max Z) and has zero thickness on the Y axis. The air inlet boundary conditions are set through a manual defined patch to integrate the CHEMKIN interface fuel injection. The initial temperature of air flow is set with a value between 800 K and 1050 K depending on the simulated case. The pressure is set as a fixed flux, the air composition is set through mass ratios for O2 and N2 depending on the simulated equivalence ratio i.e. air mass flow varied from 1.1097 - 1.3658 kg/s; the pressure of injection is set through the density value of 1.067 kg/m^3 which is 0.3 MPa. The velocity of injection is set to 80 m/s.

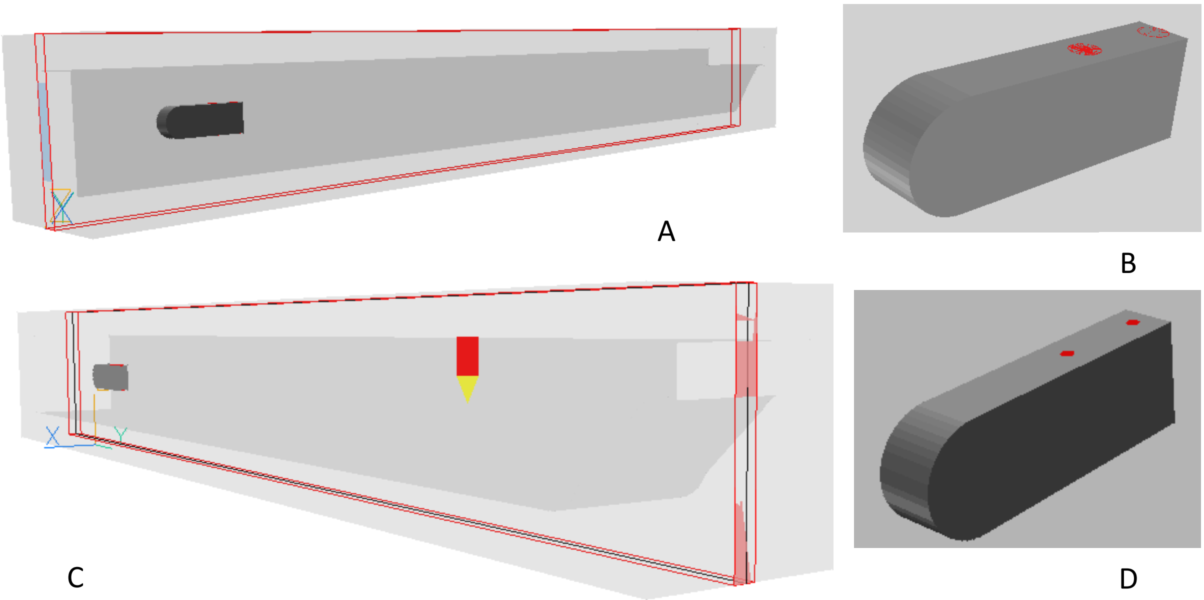

Figure 4 Isometric schematic of chamber in 3D

A summary of the boundary and initial conditions used is presented in table 1. Airflow is considered to circulate in the chamber with a velocity of 80 m/s, and a standard composition.

Table 1 Boundary conditions

Parameter	Fuel inlets	Air inlet
Temperature [K]	300	980
Density [kg/m^3]	0.2406	1.067
Velocity [m/s]	800	80
Composition	0.1511 - 0.9447 [kg/s]	1.1097 - 1.3658 [kg/s]
Reynolds number	~8.3 x 10^4	~3.5 x 10^4

The outlet boundary condition replicates the incoming fluid characteristics. The reference temperature on the outside is 300 K, standard pressure is considered, velocity calculated is in-cell, deduced on the inside, turbulence is in-cell deduced, and exit area is considered maximum.

In order to correctly approximate the 3D experiments, performed using the injector in Figure 2, only one pair of injection holes was simulated using periodic boundary conditions on the ordinate axis. The sliced projection of the injector is presented in Figure 2 in between the blue lines. Since a 3D injector is equipped with 24 injection holes, adapting the similar equivalence ratio into the boundary conditions projection, the area of the fuel inlet is variable for fuel-lean and fuel-rich cases. As a result, the hydrogen or fuel inlets are created as circles of zero thickness on the Z axis (vertical) and placed on top of the would-be injection holes of the injector. They measure $d = 1$ mm in diameter for fuel-lean cases and

$d = 2.5$ for fuel-rich cases. They are placed, on the upper side and lower side both on the downstream and upstream of the injector. Fuel is injected with an angled velocity of 800 m/s. The angles are obtained by injection on the vertical and horizontal axis and applying a trigonometric function (sinus or cosinus) to obtain the inclined angle. A table of all the angle velocities is shown below in table 2. The temperature of injection is set to 300 K, the pressure of injection is set through the density of 0.2406 to 0.3 MPa, and the mass ratio composition of the fuel is set through H2 injection depending on the equivalence ratio simulated i.e. fuel mass flow varied between 0.1511 - 0.9447 kg/s.

The upper and lower side walls of the chamber, as well as the nozzle ramp and the injector itself are considered solids, made of steel at 25°C. Isothermal conditions were applied at the walls with a constant temperature of 980 K. The flow side walls follow periodic boundary conditions for all slabs. The walls are fitted with no-slip conditions, with standard roughness and equilibrium logarithmic wall functions.

Table 2 Velocity values for angled injection

Angle	$\boldsymbol{V} = \boldsymbol{V_y}$ [m/s]	$\boldsymbol{W} = \boldsymbol{V_z}$ [m/s]
10°	787.84	138.91
15°	772.74	207.05
20°	751.75	273.61
25°	725.04	338.09
30°	692.82	400
35°	655.32	458.86
40°	612.83	514.23
45°	565.68	565.68
50°	514.23	612.83
55°	458.86	655.32
60°	400	692.82
65°	338.09	725.04
70°	273.61	751.75
75°	207.05	772.74
80°	138.91	787.84
85°	69.72	796.95
90°	0	800
95°	-69.72	796.95
100°	-138.91	787.84
105°	-207.05	772.74
110°	-273.61	751.75
115°	-338.09	725.04
120°	-400	692.82

2.5. Mesh details

The mesh in our study is made up of 6-sided staggered, hexahedral volume control cells. The scalars are stored at the center points of six-sided cells with values supposed to be typical for the whole cells, and the vectors are stores at the center points of the six cell faces. The geometry was discretized into 1.28 x 10^6 finite volume cells in a structured manner (Figure 5). The cells on the Y axis (axial flow axis) are 800. The cells on the Z axis (vertical axis in Figure 5) are 80. The cells on the X axis number 20. The cells were finer near the walls, the injector and towards the center of the combustor. Elsewhere, the cells were coarser.

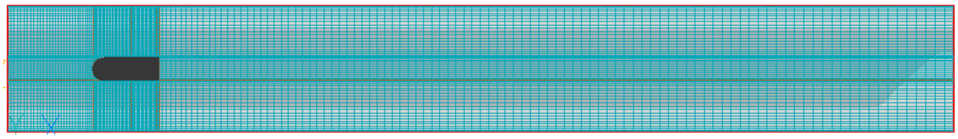

Figure 5 Schematic of reduced grid arrangement

2.6. The turbulence model

Many combustion flow problems revolve around chemical kinetics, turbulence modeling and heat conduction, making it a very complex flow process. During our research study both unsteady and steady simulations have been performed. The chemical interactions taking place in the combustion of hydrogen in air were calculated using the CHEMKIN II sub-routine supplied by Sandia National Laboratories [42,43]. The chemical reaction mechanism used in this simulation involved 188 elementary reactions and 28 chemical compounds introduced by Konnov et al.[44]. The mechanism is presented in Appendix 1. The hydrogen-air chemical kinetics can be described rather easily and the reaction paths and rate coefficients are well understood to allow the use of the mechanism without much difficulty in a wide range of cases [45, 46]. The detailed NO chemical reaction system has been selected to provide a detail understanding of the NOx emission in the combustion process. The insertion of the reaction mechanism had to be done manually (manual programming through Phoenics Input Language (PIL)) by which we mean definition of each species in the code separate from the reaction mechanism in CHEMIN format, setting the numbering of each variable, and finally providing appropriate transport and reaction coefficients. Afterwards, using the built-in CHEMKIN interpreter, the variables are assigned their own numbers and memory allocation.

Three primary tools of using CFD simulations are available for fluid flows to account for turbulence: direct numerical simulations (DNS), large-eddy simulations (LES) and Reynolds- or Favre-Averaged Navier-Stokes (RANS) simulations. Each technique has its specific uses as well as assumptions and thus posing different advantages and disadvantages [47,48,49]. DNS has prohibitive costs in terms of hardware and time requirements and so is limited to simplified combustor models. Even with the present day computing power we are still far off in the requirements to perform a DNS of the time dependent Navier Stokes equations of fully turbulent flows at high Reynolds numbers. As an example for a typical 2D domain of 0.1 m x 0.1 m with a high Reynolds number flow, might contain vortices down to 10 to 100 μm in size [50]. As a result, in order to describe this flow properly a mesh comprised of up to 10^{12} grid nodes would be required and this only for a Steady state flow. If we mean to factor in the unsteady derivatives, and considering that some of the fastest events can happen around 10 kHz, the time step would need to be in the order of 100 μs.

LES is the alternative to offer computational time savings however sub-routines or filters to correctly approximate the non-premixed or premixed chemical reacting flows are scarce or not available [47,49,51]. LES involves solution of the 3D time-dependent N-S equations by doing direct simulation of the large-scale motion and by using a sub-grid-scale (SGS) model for turbulence of scales smaller that the computational grid spacing. The advantage of LES is its ability to correctly approximate large vortices which are hard to model in a universal way, by simulating them directly. However the application of LES to practical flows has been limited because of prohibitive expense in both computational time and power at high Reynolds numbers, by the difficulties in specifying correct initial and boundary conditions and by the need to perform 3D time-dependent simulations, even if the flow is 2D and statistically stationary. Another disadvantage is that LES is largely used in non-reactive flows and its application to combustion modeling especially complex chemical reacting flows is still in its incipient stage [48].

As most experiments have proved [47] that the majority of the engineering flows is within Prandtl numbers of unity ($Pr < 1$ available for liquid metals where the thermal boundary layer far exceeds the velocity boundary layer and $Pr > 1$ available for water and oils where the velocity boundary layer far exceeds the thermal boundary layer) it is possible to apply the similar transport equations to accommodate k, the turbulent energy and ε, the dissipation of turbulent energy.

The $k - \varepsilon$ turbulence model is one of the most widely used and validated turbulence models around. However despite the many advantages it provides it also has a series of moderate disagreements when predicting unconfined flows or weak-shear layers with or without mixing –layers separated flows. The difficulties can be overcome by making adjustments to the model constants and thus customizing its robustness for each particular simulated case.

To represent the turbulence equations for the $k-\varepsilon$ model:

$$\rho\frac{\partial k}{\partial t}+\rho\frac{\partial}{\partial x_i}\left[u_i k-\frac{\upsilon_T}{\mathrm{Pr}(k)}\frac{\partial k}{\partial x_i}\right]=\rho\,[(P=P_k+G_b)-\varepsilon] \tag{6}$$

$$\rho\frac{\partial \varepsilon}{\partial t}+\frac{\partial}{\partial x_i}\left[u_i \varepsilon-\frac{\upsilon_T}{\mathrm{Pr}(\varepsilon)}\frac{\partial \varepsilon}{\partial x_i}\right]=\rho\frac{\varepsilon}{k}(C_{\varepsilon 1}P_k+C_{\varepsilon 3}G_b-C_{\varepsilon 2}\varepsilon) \tag{7}$$

Since in the present simulation the gravity forces effect is not considered,

$$G_b=0 \tag{8}$$

It is possible, in principle like mentioned above to simulate any turbulent flow by solving the above equations and that is categorized as a Direct Numerical Simulation (DNS), but in practice it is rarely done[49]. But since we are not concerned so far with all the details of the turbulent mention but rather with its effects on the gross properties of the flow, there is no need to solve the *instantaneous* variables if *averaged* variables are all that is required.

The over dissipative nature of the $k-\varepsilon$ model is somewhat corrected in the Chen and Kim's turbulence model. This variant of the standard two layer model uses slightly different constants and introduces an additional source term into the ε equation defined as

$$S_\varepsilon=\frac{-\rho C_{\varepsilon 4}\cdot P_k^2}{k} \tag{9}$$

The final form of the $k-\varepsilon$ Chen and Kim's turbulence model designated KECHNEN is:

$$\rho\frac{\partial k}{\partial t}+\rho\frac{\partial}{\partial x_i}\left[u_i k-\frac{\upsilon_T}{\mathrm{Pr}(k)}\frac{\partial k}{\partial x_i}\right]=\rho\,(P_k-\varepsilon) \tag{10}$$

$$\rho\frac{\partial \varepsilon}{\partial t}+\frac{\partial}{\partial x_i}\left[u_i \varepsilon-\frac{\upsilon_T}{\mathrm{Pr}(\varepsilon)}\frac{\partial \varepsilon}{\partial x_i}\right]=\rho\frac{\varepsilon}{k}\left(C_{\varepsilon 1}P_k-C_{\varepsilon 2}\varepsilon-\frac{C_{\varepsilon 4}\cdot P_k^2}{\varepsilon}\right) \tag{11}$$

With the kinematic viscosity and the length scale L_s defined as:

$$\upsilon_T = C_\mu C_d \frac{k^2}{\varepsilon}, \quad L_s = C_d \frac{k^{3/2}}{\varepsilon} \tag{12}$$

This variant of the standard $k - \varepsilon$ model uses different slightly different constants:

$$C_\mu = 0.5478, \qquad C_d = 0.1643, \qquad \Pr(k) = 0.75, \qquad \Pr(\varepsilon) = 1.15 \tag{13}$$

$$C_{\varepsilon 1} = 1.15, \qquad C_{\varepsilon 2} = 1.90, \qquad C_{\varepsilon 3} = 1.0, \qquad C_{\varepsilon 4} = 0.25 \tag{14}$$

The advantages of this version of the model are further detailed here [52,53] but suffice to say it has a good prediction of separation and reattachments points as well as for vortices and on top of that it preserves good behavior for jets and plumes compared with the standard model.

2.7. The Chemkin interface

The CHEMKIN interface is built into the PHOENICS code, which includes the implementation of the TRANLIB and TRANS databases. Though a *.ckm file, (Chemkin format) the chemical reaction system is interpreted and integrated into the code solver[54]. The viscosity, diffusion coefficients and heat conduction of gases are defined as:

$$\mu_k = \frac{5}{16} \frac{\sqrt{\pi m_k k_B T}}{\pi \sigma_k^2 \Omega^{(2,2)}} \tag{15}$$

$$D_{12} = \frac{3}{16} \frac{\sqrt{2\pi k_B^3 T\,(m_1 + m_2)/m_1\,/m_2}}{p\pi\big(0.5(\sigma_1 + \sigma_2)\big)^2 \Omega^{(2,2)}} \tag{16}$$

$$\lambda_k = \frac{\mu_k}{M_k}(f_{trans} Cv_{trans} + f_{rot} Cv_{rot} + f_{vib} Cv_{vib}) \tag{17}$$

2.8. Solver algorithm

PHOENICS adopts the finite volume method as the standard solution technique. This means that the code solves sets of algebraic equations which represent the consequences of integrating the differential equations over the finite volume of a computational cell and (for transient problems) over a finite time; and approximating the resulting volume, area and time averages by way of interpolation assumptions.

All the simulations performed with the PHOENICS have been made using the HYBRID version of the UPWIND side of the cell. The HYBRID discretization scheme is a combination of UDS (Upwind Discretization Scheme) and CDS (Central-Differencing Scheme). Figure 6 presents a cell diagram for an UPWIND discretization scheme.

$$\phi_\omega = \phi_W \rightarrow when\ flow\ moves\ from\ W \rightarrow P \qquad (18)$$

$$\phi_\omega = \phi_P \rightarrow when\ flow\ moves\ from\ P \rightarrow W \qquad (19)$$

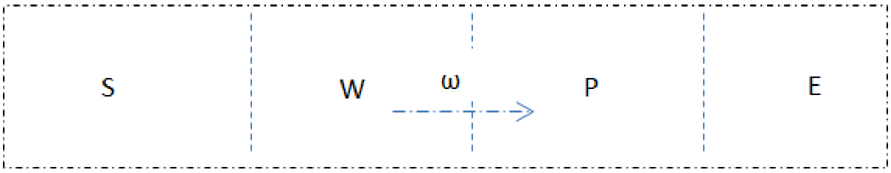

Figure 6 Cell diagram for discretization schemes

When the Peclet number (the normal to the face velocity X and the inter-node distance divided by diffusivity) is below 2.0, the simple first order UDS is used, where the Pe number is defined as:

$$Pe = Re \cdot Pr = \frac{\Delta h \cdot V}{\alpha}\ for\ thermal\ diffusion \qquad (20)$$

$$Pe = Re \cdot Sc = \frac{\Delta h \cdot V}{D_m} \; for\; mass\; diffusion \tag{21}$$

The general form of the discretization result [55] is given by:

$$\phi_\omega = \phi_W + {}^1\!/_2 \cdot B \cdot (\phi_W - \phi_S) \tag{22}$$

Where B is the flux limiter and has the form:

$$B = f(r) = \frac{(\phi_P - \phi_W)}{(\phi_W - \phi_S)} \tag{23}$$

Thus the HYBRID scheme can be written as:

$$When\; Pe < 2, \rightarrow B = 0, then\; \phi_\omega = \phi_W \tag{24}$$

$$When\; Pe > 2, \rightarrow B = \frac{(\phi_P - \phi_W)}{(\phi_W - \phi_S)}, then\; \phi_\omega = \phi_W + \frac{(\phi_P - \phi_W)}{2} \tag{25}$$

The disadvantages presented by this scheme are related to the flow direction. In a typical 2D flow, when the flow is diagonal to the grid, cell P receives fluid from both the West and the South cells, and so takes up an intermediate value. This intermediate value is then passed on to cell N and so on.

The result is that physically-present discontinuities become “smeared” by the numerical procedure. Many remedies have been proposed for reducing the magnitude of this effect, which for obvious reasons is called “numerical diffusion” or “false diffusion”. Some, such as Raithby’s “skew-upwind scheme”[56], address directly the influence of the diagonality of the flow. Other authors have sought to find formulae for cell-face values in simpler ways, involving only the resulting value of the variable (ϕ) on either side of the face, or one still farther upstream. More details on other schemes can be found here [55,57]. Unless otherwise specified the simulations have been performed using the HYBRID discretization scheme.

Its use implies that:

1. In time dependent terms, all fluid properties are presumed to be independent of position within a cell, so that the integral over the cell volume of $d(r_i \cdot \rho_i \cdot F_i)/dt$ is replaced by:
$$\frac{(r_i \cdot \rho_i \cdot F_i \cdot \Delta V), new - (r_i \cdot \rho_i \cdot F_i \cdot \Delta V), old}{t, new - t, old} \tag{26}$$
2. In convection terms, all fluid properties are uniform over cell faces; further the “new” (end of time interval) values are supposed to prevail throughout the time interval; and, except in respect of the velocities for which the face-center values are stored, the values prevailing at the cell face are those at the nearest grid node on the “upwind” side of the face.
3. In terms representing diffusion (and heat conduction and viscous action), the property gradients and the transport properties which they multiply are uniform over cell faces; further the “new-time” values in a time-dependent calculation are supposed to prevail throughout the time interval.
4. In terms representing sources, the nodal values are supposed to prevail over the whole of the cell volume, and the “new-time” values (the late-time ones) are supposed to prevail over the whole of the time interval.

The diffusion fluxes are taken to be the product of the cell-to-cell difference in the flux values and the cell-face area, divided by the resistance to diffusion represented by the integral over the distance between the cell centers of $(distance\ increment)$ /

$(exchange\ coefficient)$. Thus for the simplest case of brick-shaped cells, and single-phase flow, the diffusion flux of variable ϕ from cell P to cell E is computed.

This discretization scheme is built toward guaranteeing correct linkage between the pressure and velocity, which predominantly account for the mass conservation within the flow domain.

For a simulation the solutions to the conservation equations governing the fluid flow are complicated by the lack of an independent equation for pressure. For a simple case of 3D flow and in an adiabatic domain, four variables need to be solved using the RANS equations: $u, v, w\ and\ p$. For such a case the continuity equation is kinematically linked to the velocity field rather than to a given equation. In order to link the pressure with the velocity for an incompressible flow, one possible way introduced by Patankar and Spalding (1972) is to construct a pressure field to ensure the conservation of the continuity equation.

This algorithm named Semi-Implicit Method for Pressure-Linkage Equations or SIMPLE is one of the most popular pressure-velocity linking scheme for incompressible flow. In its simple form the SIMPLE algorithm is a guess-and-correct method for calculation of pressure throughout the pressure correction equation. When the governing equations are coupled with the energy conservation and other turbulent quantities conservation the calculation will be performed sequentially since it is an iterative method.

The current solution algorithm is the steady version of *SIMPLEST* [58]. SIMPLE ShorTened is the SIMPLE algorithm with a few modifications. The momentum and continuity equations are linked in so far as the transport equations share the pressure and the velocity, via the density in compressible flows. There steps followed by the algorithm are presented here [59].

The SIMPLEST algorithm follows the same 7 steps; however it modifies the way in which the momentum is defined by way of the $du\ /\ dp$ ratio. The modifications are related on how the convective and diffusive influences are treated.

The influences of the velocity at the main node P i.e. u_P, are presented as

$$a_P \cdot u_P = a_N \cdot u_N + a_S \cdot u_S + a_E \cdot u_E + a_W \cdot u_W + etc. \tag{27}$$

where the $a_N, a_S, a_E, a_W, etc.$ are the coefficients representing both the convection and diffusion in the flow. However due to the major differences between the phenomena, wherein the diffusive influences are reciprocal while the other are just “one-way”, the SIMPLEST algorithm splits the coefficients into two parts:

$$a_k = c_k + d_k \tag{28}$$

where c_k is the convection coefficient of node k and $d_k$is the diffusion coefficient of node k.

This separation allow the terms in the finite-volume equation to be represented as

$$a_P \cdot u_P = c_N \cdot u_N + d_N \cdot u_N + c_S \cdot u_S + d_S \cdot u_S + etc. \tag{29}$$

Once the terms are separated, the next step is to separate the convective terms from the diffusion terms in the momentum balance where they are treated as known constants.

$$a_P \cdot u_P = d_N \cdot u_N + d_S \cdot u_S + etc. + \{c_N \cdot u_N + c_S \cdot u_S + etc. + sources\} \tag{30}$$

These artificial modifications produce convergence much smoothly than the SIMPLE algorithm with less under-relaxation factors[59].

Each time, through the SIMPLEST loop, a_P^u and b^u are updated with the newest information about the $u, v\ and\ p$ fields.

Before solving

$$a_P^u \cdot u_P = b^u \tag{31}$$

A residual is computed with the following formula:

$$r^u = b^u - a_P^u \cdot u_P \tag{32}$$

If r^u is small, then the old u is a good approximation to the system of equations defined by the newly updated coefficients in a_P^u and b^u. Similarly, for all other dimensions r^{u_k} are residual vectors. To check convergence, we need to look at a scalar value. Let σ be a normalized scalar value of the residual.

$$\sigma = \frac{\|r_u\|}{\|r_{u,ref}\|} \tag{33}$$

The values of $r_{u,ref}$ are chosen so that $\sigma \sim 1$ on the first iteration.

Convergence was considered when the source balance had values smaller than 1%, the reference residual was lower than 10^{-6} and the solution error for each parameter was satisfied to 10^{-3}.

2.9. Chemical heat release

To evaluate the combustion efficiency of each configuration we used two approaches. In determining the efficiency we evaluated several parameters: the chemical heat release [54], is investigated near the injection zone. The heat loss at the walls [60] was evaluated for the entire chamber. In order to compare the numerical results and experimental data, values from the nozzle were used, described in Nishida et al.'s [38] work.

The chemical reaction heat is given by

$$\dot{Q} = \sum_{k=1}^{N} (\dot{\omega}_k \cdot M_k \cdot \Delta h_{f,k}^0) \tag{34}$$

2.10. Heat loss

Heat loss at the wall is given by

$$Q_{loss/cell} = \lambda \cdot A \frac{\left(T_{near_{wall}} - T_{wall}\right)}{\Delta h/2} \tag{35}$$

The thermal conductivity is given by Hedberg et al. [54]

The total heat loss in the chamber is given by

$$Q_{tot} = \sum_{ij} Q_{\frac{loss}{cell}_{ij}} \cdot \Delta X_{ij} \cdot \Delta Y_{ij} \tag{36}$$

2.11. Combustion efficiency

In order to compare the numerical results and experimental data, the numerical combustion efficiency is evaluated using two approaches and evaluated a configuration by

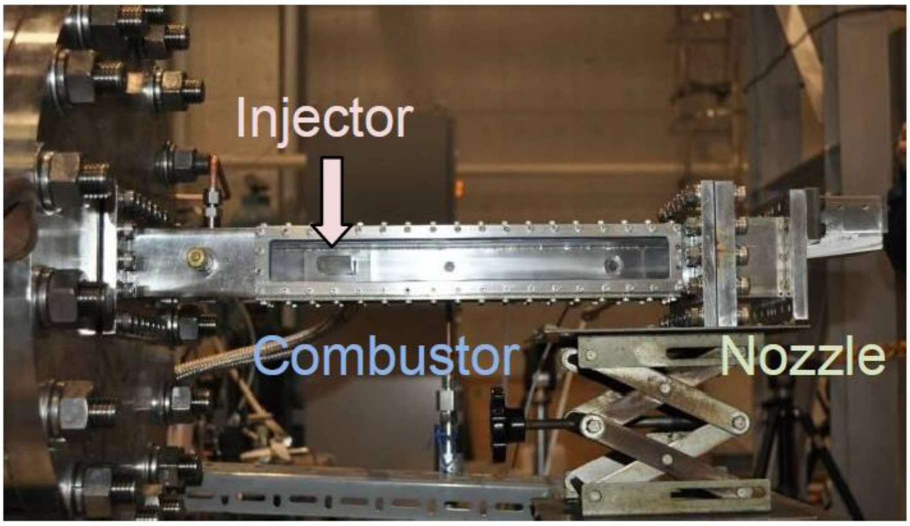

Figure 7 Experimental model afterburner combustor introduced by Nishida et al.[38]

using the values of the combustion efficiency near the nozzle, in the same way as Nishida et al. [38,61]. In experiments the exhaust temperature, used in the calculation of the combustion efficiency, is considered the spot value recorded by the thermocouple near the nozzle, seen in Figure 7.

The thermocouple is placed at 300 mm from the air inlet. To have a similar value, in the numerical results, the temperature values used were the averaged value obtained from the plane of the temperature field at the same spatial coordinate from the nozzle as the thermocouple is, as shown in Figure 7.

The combustion efficiency using the first approach is expressed as:

$$\eta_A = \frac{Q_{ac}}{Q_{th}} \tag{37}$$

where $Q_{ac} = H_{ex} - H_{in}$ is the difference between the exit enthalpy of the combustor, and entrance enthalpy. The enthalpy at the exit depends on the temperature through the enthalpy of the burned gases, while the entrance enthalpy is depended on the inlet temperature. The numerical combustion efficiency at the nozzle used for comparison purposes introduced by Nishida et al.[38] is defined as

$$\eta_{nozzle} = \frac{Q_{ac\_nozzle}}{Q_{th}} \tag{38}$$

The entrance enthalpy and exit enthalpy are calculated as

$$H_{in} = Y_{O2}H_{O2}(T_{air}) + Y_{N2}H_{N2}(T_{air}) + \mathrm{Y}_{H2in}H_{H2}(T_{H2}) \tag{39}$$

$$H_{ex} = \sum_{k=1}^{NC} Y_k H_k(T_{ex}) \tag{40}$$

The comparison nozzle combustion efficiency uses different estimations of the inlet and exit enthalpies. The forms are:

$$H_{nozzle\_in} = \dot{m}_{air} H_{air}(T_{air}) + \dot{m}_{H2} H_{H2}(T_{H2}) \tag{41}$$

$$\begin{aligned} H_{nozzle\_ex} = {} & \dot{m}_{N2} H_{N2}(T_{ex}) + \dot{m}_{H2O} H_{H2O}(T_{ex}) + \dot{m}_{H2ex} H_{H2}(T_{ex}) + \dot{m}_{O2ex} H_{O2}(T_{ex}) \\ & + \dot{m}_{Ar} H_{Ar}(T_{ex}) + \dot{m}_{CO2} H_{CO2}(T_{ex}) \end{aligned} \tag{42}$$

The respective enthalpies were calculated using the CHEMKIN thermodynamic data in the form used in the NASA chemical equilibrium code[62,63]. The enthalpy is expressed as a 6-coefficient - power series in T (in Kelvin) detailed in the CHEMKIN manual [42], as

$$\frac{H_k(T)}{RT_k} = a_{1k} + a_{2k}\frac{T}{2} + a_{3k}\frac{T^2}{3} + a_{4k}\frac{T^3}{4} + a_{5k}\frac{T^4}{5} + \frac{a_{6k}}{T} \tag{43}$$

The mass flow rates used in the nozzle combustion efficiency formula are given by

$$\dot{m}_{N2} = 0.769 \cdot \dot{m}_{air} \tag{44}$$

$$\dot{m}_{H2O} = \frac{18}{32} \cdot 0.231 \cdot \dot{m}_{air} \tag{45}$$

$$\dot{m}_{H2ex} = \dot{m}_{H2} - \frac{0.231}{8} \dot{m}_{air} \tag{46}$$

$$\dot{m}_{O2ex} = 0.23142 \cdot \dot{m}_{air} - 8 \cdot \dot{m}_{burn} \tag{47}$$

$$\dot{m}_{Ar} = 1.29 \cdot \dot{m}_{air} \tag{48}$$

The theoretical heat release is given by:

$$Q_{th} = \dot{m}_{burn} \cdot q_{H2} \tag{49}$$

The energy density of hydrogen is very high (1kg of hydrogen contains 132.5 MJ, which is 2.5x more than that in 1kg of natural gas), being one of the reasons why hydrogen is the preferred fuel [64]. The energy content of hydrogen is given by the gravimetric LHV which is 120.0 MJ/kg [65].

$$\dot{m}_{burn} = \begin{vmatrix} \dot{m}_{H2} & for\ fuel - lean\ combustion \\ \frac{0.231}{8} \cdot \dot{m}_{air} & for\ fuel - rich\ combustion \end{vmatrix} \tag{50}$$

The second approach used to determine the combustion efficiency is using the ratio between the chemical heat release and the theoretical heat release of hydrogen.

The (B) approach of the combustion efficiency is given by:

$$\eta_B = \frac{\dot{Q}}{Q_{th}} \tag{51}$$

Another measuring parameter that is used throughout the discussion part is the local equivalence ratio that is introduced as the ratio between the amounts of fuel present in the area in relation to the oxidant in the area. The local equivalence ratio is defined as:

$$\iota = \frac{Y_{H2}}{(Y_{O2} + Y_{N2})} \tag{52}$$

2.12. NOx study

NOx emissions from combustion are primarily in the form of NO and NO2. Due to the fact that NO is largely anthropogenic (i.e. generated by human activity)[66], stricter control is necessary to diminish the effects on the environment. NO produces a blocking effect on the human body to absorb oxygen, similar to CO radicals, however because NO is slightly soluble in water, it poses more dangers to the environment than to humans (excepting infants or very sensitive individuals)[33]. NO in the atmosphere can react to deplete or enhance ozone concentrations. NO2 reacts in the atmosphere to form ozone (O3), through ionizing energy coming from the sun, and acid rain. While the stratospheric ozone layer, found in the upper atmosphere that we cannot breathe, is what protects us and the troposphere from the dangerous levels of ionizing radiation coming from the sun, tropospheric ozone, the ozone in the ambient air that we breathe, is a significant part of air pollution through smog. As a result, NOx are considered ozone depleting substances which react with O2 in both the troposphere (i.e. below 3 km above sea level) and in the stratosphere (i.e. 15 to 45 km). NOx resulting from the combustion of aviation fuels have a greater impact on our ozone layer (O3) than on the greenhouse gas (CO2)[34]. If we add extra amounts of NOx to this chemical process, the NOx cycle enhances the catalytic ozone destruction[67].

In order to control the NOx formation, a thorough understanding of the chemical reactions and subsequent reaction mechanisms is necessary. Before a reaction study of the NO is undertaken, a simple analysis of the resulting NOx in the exhaust gas has to be performed. To achieve this, we measured the NOx emission index at the exit of the combustor. The emission index for NO, NO2 and NOx is calculated at the nozzle of the combustor. The formula used is:

$$EINO_x = \frac{\sum \rho_{NO_x} \cdot A \cdot u_k \cdot Y_{NO_{xk}}}{\dot{m}_{H2}} \qquad \left[\frac{g_{NO}}{kg_{fuel}}\right] \tag{53}$$

After the trend of the NOx, plotted for different angle configurations, is investigated a study of the formation routes is performed. The widely validated formation mechanisms include (1) Thermal NO introduced by Zel'dovich [68], (2) prompt NO or Fenimore NO, which account for the NO produced at the flame front [69]; (3) the N2O mechanism, when additional

NO is generated via the nitric dioxide compound [70]; (4) NO produced from fuel-bound-nitrogen[35]; and (5) the NO2 route. Another mechanism has come into attention as of late, and according to Bozzelli et al. [71] and Miller et al.[72], significant amounts of NO2 can be produced due to conversion of NO in low-temperature mixing regions of non-premixed systems. The formation of NO via the (6) NNH path, has recently been under investigation[73,74] and has been found that NO production is favored by this mechanism in different cases like flame fronts where relatively high concentrations of O2 and H2 can be found.

A formation mechanism is usually given as a set of reversible reactions where the reaction rates are represented by the forward reaction rates, while thermodynamic data are used to calculate the reaction rate coefficients for the reverse reaction. The current reaction mechanism accounts for the hydrogen-oxygen reactions and detailed H-N-O reactions. The hydrogen-oxygen reactions shall not be discussed here in detail, since there are comprehensive reviews found in literature, on the elementary reactions and rate coefficients of this system. [46,75,76]. The reaction mechanism used in our simulations accounts for 188 reactions, with 28 chemical species. The H_2 /O_2 mechanism comprises of 23 reversible reactions while the rest account for the various formation mechanism of NO introduced by Konnov et al. [44].

The widely validated mechanisms are detailed in the following section.

(1) In the combustion of clean fuel (non-nitrogen based) with air as the oxidizer, NO is formed using the Zel’dovich mechanism. According to the Zel’dovich equations, NO is formed at temperatures above 1500 K. At lower temperatures, NO is generated through other mechanisms, the Zel’dovich mechanism participating only slightly or not at all. NO produced through this mechanism is generated as a function of the

equivalence ratio and is more pronounced on the fuel-lean side of the stoichiometric mixture [77]. This mechanism is comprised of 3 main reactions: R25, R26 and R100.

$$N2 + O = NO + N \qquad (R25)$$

$$N + O2 = NO + O \qquad (R26)$$

$$N + OH = NO + H \qquad (R100)$$

The Zel'dovich mechanism is known as the thermal mechanism due to the large activation energy given by R25, which make it sufficiently fast only at high temperatures. Due to the low rate constant of R25, it is also considered a rate-determining step.

(2) Prompt NO or Fenimore NO are the NO formed in hydrocarbon flames by a rapid reaction of hydrocarbon radicals with molecular nitrogen which lead to the formation of amines and hydrocyanic acid (HCN) which later reacts to form NO. These NO are formed much earlier than thermal NO, thus the name prompt NO.

According to Miller and Bowman [78], at low temperatures when T < 2000 K, depending on the fuel, NO formation is dominated by the prompt NO formation channel but as the temperature increases, the thermal NO channel becomes the dominant channel. Taking into account that the fuel used in our simulations has been hydrogen and the reaction mechanism does not account the C element, the prompt-NO formation mechanism, is not investigated here.

(3) The N2O mechanism form when oxygen atoms attack N2 atoms. It is mainly formed at fuel-lean conditions when the CH radical forming the base of prompt-NO is suppressed, and due to low temperatures, so is the thermal-NO mechanism. This leaves the NOx formation to come from the N2O channel. N2O is also a precursor in flames.

The cannel is formed by the three-molecule reaction

$$N_2 + O + M = N_2O + M \qquad (R29)$$

Due to the nature of reaction 29, it is assumed[44] that reaction 29 is a rate-limiting step in the nitrous-oxide channel and the bulk of the NO is given by the fast reaction if N2O consumption as well as the reactions in which oxygen and hydrogen effectively convert it into NO

$$N2O + O = N2 + O2 \qquad (R30)$$

$$N2O + O = NO + NO \qquad (R31)$$

$$N2O + H = NO + NH \qquad (R101)$$

$$NH + NO = N2O + H \qquad (R102)$$

The main source of N2O is given by reaction 102 especially for rich mixtures[1-chapter 2.16.5]. The N2O from this reaction quickly reacts with hydrogen in R102. At the same time the removal of N2O is enabled by R102 in fuel-lean flames.

(4) NO from fuel bound nitrogen is one of the main products from coal and coal-derived fuels. It is mainly the oxidation of HCN and NH3. Since the fuel at scope is not coal-derived, or C-based, this mechanism is not presented.

(5) The NO formed via the NO2 route, is found near flame zones. The reactions involved in this formation are

$$NO + HO2 = NO2 + OH \qquad (R111)$$

$$NO2 + H = NO + OH \qquad (R110)$$

$$NO2 + O = NO + O2 \qquad (R35)$$

The main source of NO coming from the NO2 route is given by R111 when significant HO2 molecules are found to react with NO in high-temperature region and later transported by diffusion to low-temperature regions. The HO2 molecule is very sensitive to the addition and removal introduced by R8

$$H + O2 + M = HO2 + M \qquad (R8)$$

Through molecular diffusion, H atoms resulting from R8, are transported to high-temperature regions of the flame and later converted into HO2 – N2O – NO (R8 - R111 – R110)[1 ch.2.16.4].

(6) The NNH NO formation mechanism is controlled by NNH, a highly transient and unstable molecule formed in R68

$$NNH = N2 + H \qquad (R68)$$

Studies performed by Bozzelli et al. [71] and Miller et al.[72] point later to an oxidizing step that leads to NO in R165

$$O + NNH = NH + NO \qquad (R165)$$

To determine the effect of reactions on the current combustion process, the reaction rate of each reaction has been multiplied by a factor of 10 and the resulting NO, NO2 and NOx have been determined. The obtained NOx values have then been normalized by the NOx obtained with the standard reaction mechanism at the same conditions. The resulting sensitivity index represents the effect of each reaction on the combustion process.

3. Experimental

Following experiments initiated by Taguchi et al.[8] and then followed by Nishida et al.[37,61] , in the course of 2008-2012, flame ignition, temperature and flame shape have been identified. Based on theoretical studies done by Taguchi et al.[8], the in-flight equivalence ratio of the mixtures, in the combustors of the engine i.e. turbojet combustor and afterburner chamber, varied from fuel-lean (0.6) to a fuel-rich regime (2.0), depending on different flight scenarios. The PCTJ was formally designed to maximize the payload of a TSTO craft[7] and as a result experiments were carried out to investigate the fundamental behavior of combustion and pollutant emission in the afterburner chamber of the PCTJ. Thereby the effect of different angles of injection was investigated for equivalence ratios from lean (0.13) to rich (4.0) mixtures. These results are briefly presented in the next chapter. Consequently, from these results we have learned that the flame shape is very different for fuel-lean combustion cases and fuel-rich combustion. The difference in shape has been assumed as a result of the experiments as a consequence of a temperature difference in the flame distribution between the injector area of and the area of the nozzle exit. To validate this theory, a second series of experiments have been carried to measure the temperature near the injector and close to the nozzle.

3.1. Apparatus

To evaluate the temperature gap, a 1:10 scale combustor of the original design, was fitted with one injector. The combustor was placed in the hypersonic and high enthalpy wind tunnel of the University of Tokyo in Kashiwa campus, Kashiwa, Japan. Figure 8 presents the experimental apparatus used. One gas cylinder provided gas hydrogen and the wind tunnel provided the air. A gas cylinder of N_2 was used to purge remaining combustion products from the chamber. Flame temperature was recorded through two thermocouples placed in the combustor shown in Figure 9.

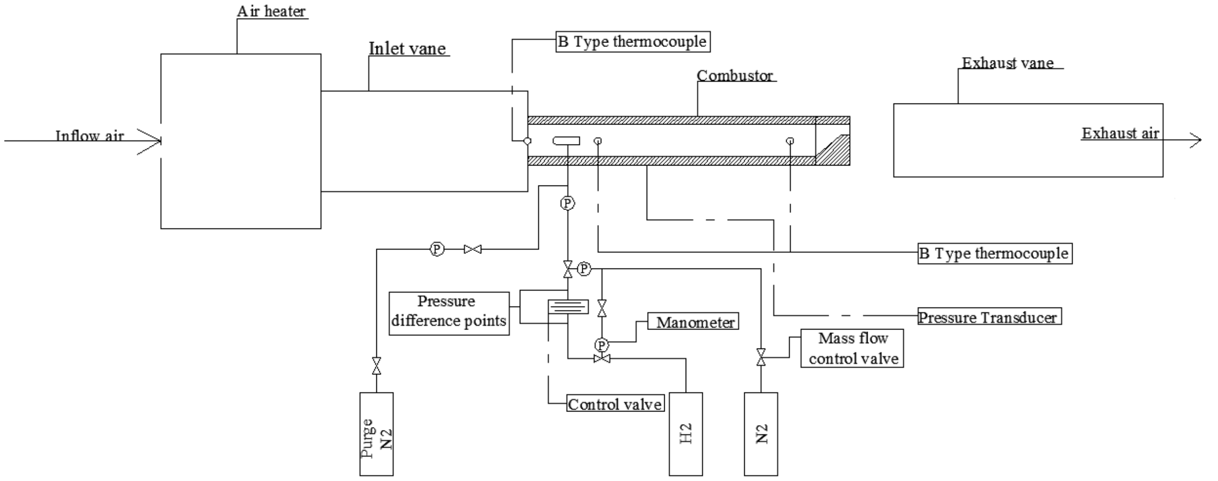

Figure 8 Schematic of the experimental apparatus

In Figure 9, the test section is shown, measuring 68 mm x 52 mm on the cross section, with 10 mm walls on the inside. The test chamber was fitted with a ramp shaped nozzle at the exhaust area and the total length measured 390 mm. The walls were made of stainless steel (SUS304) on the outside, with heat-resistant cement (AGC Co. Ltd. - LC-17U) on the inside. They were fitted with an injector made of stainless steel (SUS304), three B type thermocouples (THERMOTEX Co. Ltd., 4 mm in diameter) at the entrance, at 130 mm from the inlet and near the nozzle (at 300 mm from the inlet) shown in Figure 9, and static pressure transducers (TEAC, TP-AR series). The exhaust nozzle was made of carbon/carbon (C/C) composite to support the high temperatures expected.

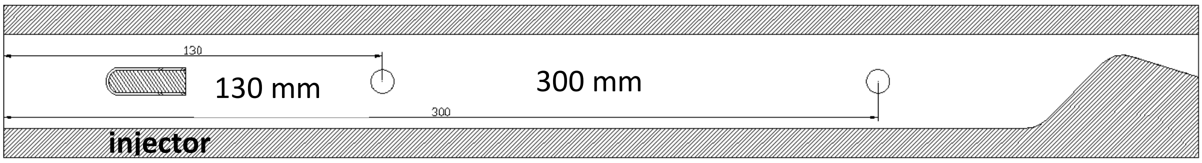

Figure 9 Schematic of the combustor using two thermocouples

The strut injector, as shown in Figure 2, was of a rectangular shape with a rounded face on the upstream side, measuring 27.25 mm x 9.5 mm with a height of 56.5 mm. Twenty-four, $d = 1$ mm in diameter injection holes were arranged in two parallel lines and the effect of different angles of injecting fuel for each line was investigated.

In previous experiments performed with a sub-scale engine by Taguchi et al. [8], liquid hydrogen supplied to the pre-cooler and afterburner walls was burned in the afterburner. As the nozzle and the afterburner are exposed to combustion gases at temperatures above 2000 K, liquid hydrogen was supplied to the afterburner walls. After the fuel absorbed the heat of both the pre-cooler and afterburner walls, its temperature stabilized around 350 K. At this temperature gaseous hydrogen was then supplied to the afterburner injector. In our experiments, the gaseous hydrogen injection temperature was fixed at 300 K.

The thermodynamic conditions of the air flow entering the test section were set as the calculated conditions coming from the turbine stage under a Mach 5 flight condition in an actual PCTJ engine [8,79] : air at an atmospheric pressure of 0.3 MPa with a temperature of 980 K. The air velocity coming from the turbine stage is assumed to be around 80 m/s so the same value was kept. The hydrogen was injected with a pressure of 0.3 MPa at a temperature of 300 K with a velocity of 800 m/s. Air composition is considered 21% O2 and 79% N2. The mass flow values of air varied between 0.083 and 0.23 kg/s and the fuel mass flow varied between 0.71 to 5.19 g/s.

3.2. Method and Measurement

To determine the combustion temperature, the injector was inserted into the test section and while airflow was circulated in the chamber, fuel was injected in the chamber through the injection holes and the temperature and pressure of the combustion were recorded. Hot air provided by a heater with heated pebbles was circulated in the tunnel through the test section and, after the flow rate was stabilized, around 30 seconds, gas hydrogen was injected in the hot air and burnt for 6 seconds. The heater produced high-temperature gas through the heat exchange between the air and pre-heated pebbles. The high temperature (980 K) coupled with the high velocity of gas hydrogen injection (800 m/s) combusted the mixture without the need of an external igniter. Hydrogen fuel supply was controlled by a set of two independent pneumatic valves. After the measurements were ended, the remaining hydrogen in the test section was purged by nitrogen gas. The parameter in the different experiment sessions was the fuel-to-air equivalence ratio varying the fuel mass flow and air mass flow rate, and the initial temperature of the airflow. Hydrogen flow rate was measured by the flow meter of the control valve and the pressure difference between the two sensors upstream and downstream of the control valve. Pressure in the test section was measured using pressure transducers and temperature using three B-type thermocouples (THERMOTEX Co. Ltd., 4 mm in diameter) inside the combustor and at the entrance of the combustor for the airflow as seen in Figure 8 and Figure 9. All measurements were recorded in a computer system via amplifiers (KYOWA – Instrumentation amplifiers) and converters (KYOWA - DC converters). A full list of sensors and amplifiers is presented in table 3.

Table 3 Amplifiers and sensors used in the experiments

Measurement items	Sensor	Amplifier
Combustion pressure	TEAC 500kPa	KYOWA - Instrumentation Amplifier DPM 305A
Hydrogen mass flow, upstream control valve pressure	TEAC 2MPa	KYOWA - Instrumentation Amplifier DPM 305A
Hydrogen injection pressure	TEAC 2MPa	KYOWA - Instrumentation Amplifier DPM 911B
Hydrogen mass flow, differential pressure	1MPa pressure gauge	KYOWA - Instrumentation Amplifier DPM 911B
Combustion temperature	Thermotex Co. Ltd B type thermocouple	KYOWA - DC Amplifier DA 710A

4. Results and discussion

4.1. Flame comparison

Following previous experiments performed on the afterburner chamber of the PCTJ, simulations have been performed to help investigate the combustion process.

The experimental data is available for different airflow and fuel flow rates, at different inlet temperatures. Given the fact that experiments have been performed with a fully sized injector with 24 injection holes, performing a similar CFD simulation would have taken a lot of computation time. For the purpose of similarity, in our numerical simulations, the injector simulated is only a “slice” of the actual injector with a total of 4 injection holes and periodic boundary conditions on the left and right side of the injector. The slice is presented in Figure 10. Using periodic boundary conditions we have been able to simulate the effect of only one pair of injection holes on the combustion process. With this simplification, the equivalence ratio of the numerical simulations had a different form. The equivalence ratio introduced in experiments is presented in the following formulas

$$\Phi = \frac{\left(\frac{\dot{m_{air}}}{\dot{m}_f}\right)_{st}}{\left(\frac{\dot{m_{air}}}{\dot{m}_f}\right)_{ac}} \tag{54}$$

Given that the $\left(\dot{m_{air}}/\dot{m}_f\right)_{st}$does not change, the actual equivalence ratio presented in eq. 58 as the denominator is $\left(\dot{m_{air}}/\dot{m}_f\right)_{ac}$ where the mass flow rate is given by:

$$\dot{m} = \rho \cdot u \cdot A \tag{55}$$

In experiments and simulations we have kept the same density and injection velocity for both air and fuel, values presented in table 1. However since the experimental injector has 24 injection holes with a diameter of 1 mm, the area used for injection of fuel is given by:

$$A_{ex_{fuel}} = 24 \cdot \pi \cdot R^2 = 18.8495\, mm^2 \tag{56}$$

With the area used for air inlet as:

$$A_{ex_{air}} = 32 \cdot 48 = 1536\, mm^2 \tag{57}$$

The area used in our periodic-condition simulations, using the same fuel injection-hole diameter i.e. $d = 1\, mm$, is evaluated as:

$$A_{CFD_{fuel}} = 4 \cdot \pi \cdot R^2 = 3.1415\, mm^2 \tag{58}$$

With the air injection area given by the small slice width of $L = 5\, mm$ as:

$$A_{CFD_{air}} = 32 \cdot 5 = 160\, mm^2 \tag{59}$$

Thus an equivalence ratio of 2.0 in experiments is equivalent with a numerical equivalence ratio of 3.2079, at the same densities and injection velocities. As a result we see an equivalence factor of 1.60 between experiments and numerical simulations.

To compare experimental results with simulations in term of equivalence ratios, we had a variation of only hydrogen mass flow rate for each of the configurations used in the experiments. The air mass flow rate remained unchanged for the same airflow inlet temperature. For our discussion in the first part we re-created all the experimental conditions at the equivalence factor and for the angle effects performance, we chose a fixed equivalence ratio and varied only the angles of injection.

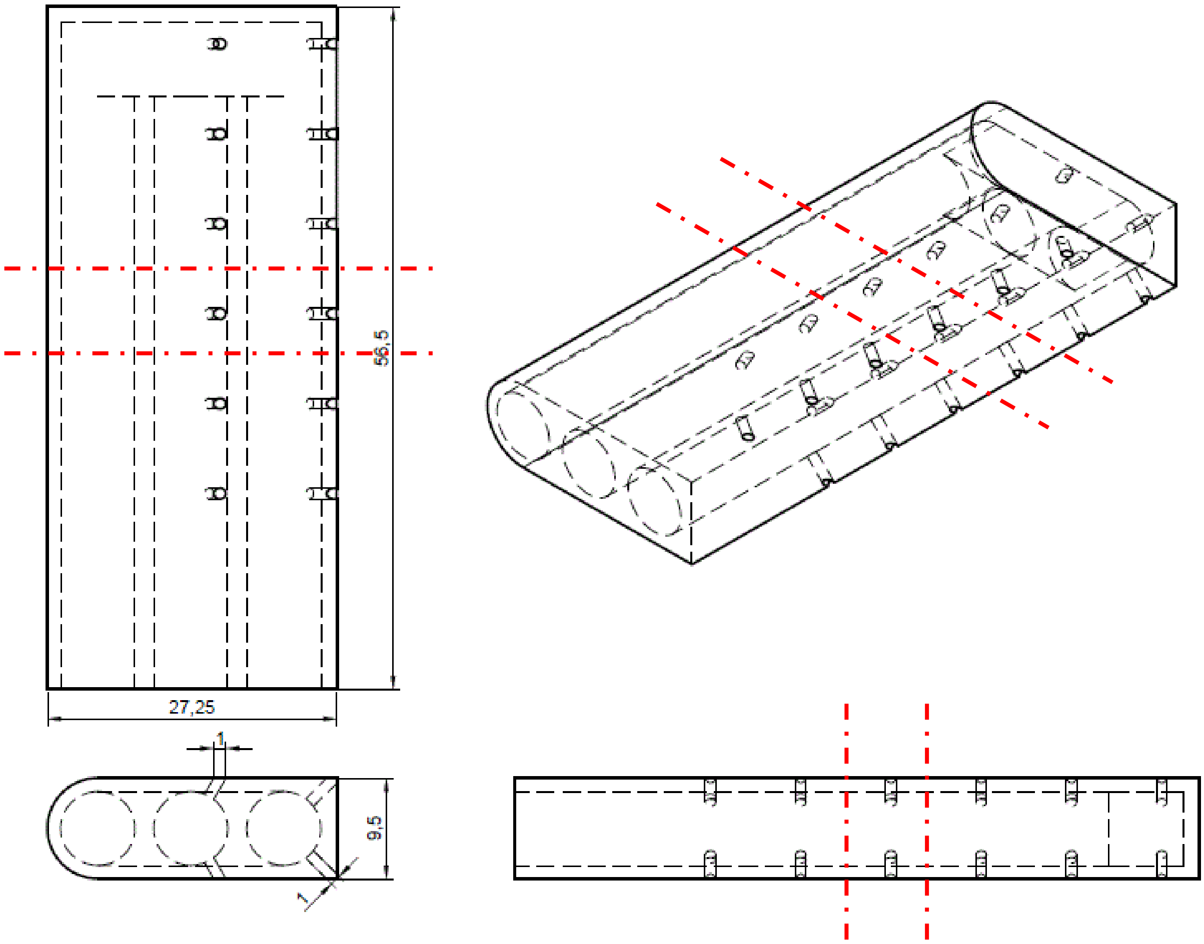

Figure 10 Schematic of Injector "slice" used in numerical simulations

Figure 11 shows a fuel-lean combustion case. The configuration shown is 60°x45° at an experimental equivalence ratio of 0.57, air inlet temperature 806 K. The upper part of Figure 11 represents emissions from the combustion gas approximately 1.5 seconds after ignition when the flame has stabilized; the lower part represents a distribution field of temperature for a steady state simulation. The numerical equivalence ratio, having kept the same conditions as in the experiments is 0.35. Two separate flame fronts are observed. This is easily understandable since the amount of fuel injected is scarce and is quickly consumed near the injector and around its sides. The fuel flow injected through the upper side and the lower sides do not meet and the overall temperature is highest around the injector and lower near the nozzle. Our numerical results are found in good quantitative agreement with the experimental results.

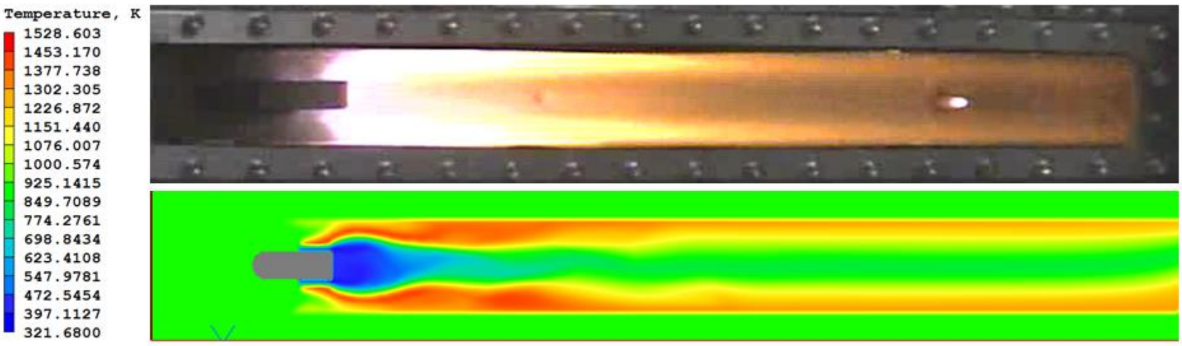

Figure 11 Fuel-lean ($\phi_{ex} = 0.57$) combustion for 60°x45°, air inlet temperature 806 K; upper side emission from combustion gas motion picture at 1.5 seconds and lower side temperature distribution field at steady state conditions at $\phi_{CFD} = 0.35$

Figure 12 shows a 45°x60° configuration in fuel-rich combustion. The experimental equivalence ratio was 3.28, air inlet temperature 850 K, and the numerical equivalence ratio was 2.05. The upper part of Figure 12 represents emissions from the combustion gas approximately 1.0 second after ignition. The lower part of Figure 12 represents the distribution field of temperature, for a steady state calculation, at the similar conditions. The flame was made up of one fully developed structure. When combustion took place, the flame encompassed the full injector, creating boundary layers around it. Having excess

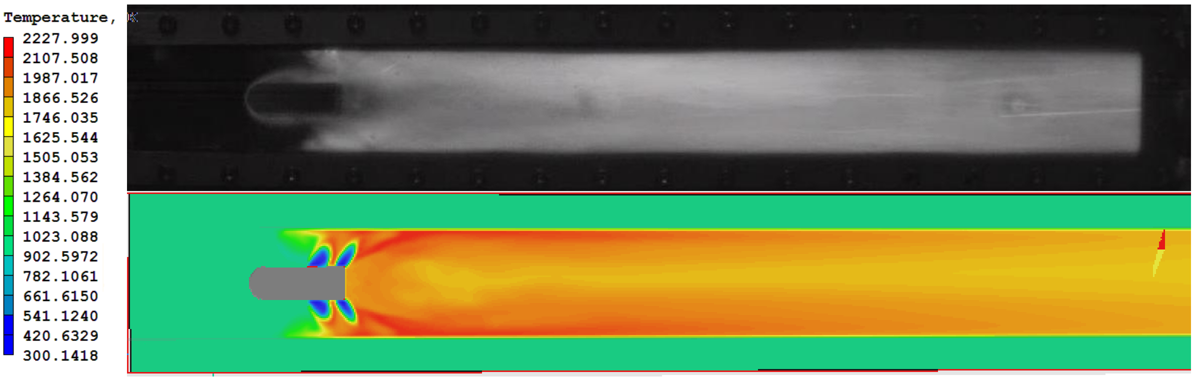

Figure 12 Fuel-rich ($\phi = 3.28$) combustion for 45°x60°, air inlet temperature 850 K; upper side emission from combustion gas motion picture at 1.0 seconds and lower side temperature distribution field at $\phi = 2.05$ and steady state conditions

hydrogen, the mixture is diffused quickly around the injector and downstream towards the nozzle.

4.2. Simulation results compared with experimental data

Table 4 presents a wide range of experimental results and the simulations performed at similar conditions. For a fuel-rich configuration (for equivalence ratios of 2.0 to 3.2) there is a lot of experimental data available for different initial parameters like different air mass flows, fuel mass flows and initial temperatures[38]. The air inlet temperature varied between 800 K and 1050 K. Air mass flow varied between 0.04 and 0.12 kg/s. Fuel mass flow varied between 4.0 and 8.0 g/s. As a result it proved quite difficult to ascertain specific properties of a single configuration or plot the values.

Table 4 Experimental and numerical data for different equivalence ratios and angle configurations

ϕ	β [°]	θ [°]	T_{air} [K]	$\dot{m}_f$ [g/s]	$\dot{m}_{air}$ [kg/s]	T_{exp_nozzle} [K]	T_{CFD_nozzle} [K]	$\eta_{exp_{nozzle}}$	$\eta_{CFD_{nozzle}}$
2.19	120	60	915	7.6	0.12	1860	1853.44	0.8102	0.8053
2.22	60	60	890	7.69	0.12	1765	1814.39	0.7541	0.7908
2.25	120	60	950	7.8	0.12	1850	1771.65	0.8029	0.7440
2.25	60	45	905	7.8	0.12	1805	1792.31	0.7850	0.7755
2.31	60	45	960	8.00	0.12	1810	1825.03	0.7816	0.7931
2.35	30	60	800	6.73	0.099	1700	1714.09	0.7640	0.7746
2.42	45	45	930	8.4	0.12	1730	1795.24	0.7548	0.8051
2.45	45	60	830	6.96	0.098	1650	1706.00	0.7358	0.7787
2.46	45	60	830	6.82	0.096	1670	1695.65	0.7512	0.7709
2.51	45	60	820	7.05	0.097	1620	1706.09	0.7270	0.7935
2.52	30	60	820	7.05	0.097	1760	1703.12	0.8357	0.7912
2.64	30	60	860	7.57	0.099	1630	1613.60	0.7448	0.7319
3.28	45	60	850	4.17	0.044	1600	1515.00	0.8390	0.7648

4.3. Temperature gap

From Figure 11 and Figure 12, we have seen a difference in flame shape. The different flame shape is the result of the equivalence ratio of the mixture, heat loss at the walls and injection configuration. For both configurations, the temperature near the injector is highest and, by a decreasing color, we assume the temperature is lower downstream. As a result there is a difference in flame temperature between the injection area i.e. near the injector, and the nozzle area. This temperature gap is assumed to be an effect of the heat loss in the chamber. To do a proper investigation of this difference another set of experiments has been carried out.

Two sets of experiments have been performed for a fuel-lean configuration ($\phi = 0.174$) and a fuel-rich configuration ($\phi = 3.18$) respectively. Combustion in the chamber was sustained for 5 seconds and the temperature was recorded using the thermocouples installed. The position of the thermocouples in the chamber is presented in Figure 9.

Figure 13 presents the experimental combustion temperature recorded by the thermocouples during the combustion. The black dots are the values of the temperature measured by the upstream thermocouple, while the red dots represent the temperature recorded by the downstream thermocouple. The right side of Figure 13, (Figure 13-a), represent the flame temperature for fuel-lean combustion while the right side – Figure 13-b, represents the flame temperature for fuel-rich. The conditions of the experiments are presented in table 5. The temperature rose as the fuel was injected, achieving combustion, and started to decrease dramatically when the fuel supply was cut off. What was observed is that for a fuel-lean case, the temperature near the injection area rose to a maximum of 1850 K, while the temperature near the nozzle reached a maximum value around 1330 K. The flame was mostly sustained near the injector, and then was substantially “cooled” towards the nozzle. This means a temperature gap of about 500 K. Given the fact that the complete combustion of 1 kg of H2 requires 8 kg of Air, and from table 5 we can see that the hydrogen mass flow in the fuel-lean experiment was 0.520 g/s, it means that the air required to completely burn this quantity, would be 0.00416 kg/s of air. And taking into account that in the experiment the quantity was 25 times that amount, the hydrogen was quickly consumed near the injection source, thus the flame was only sustained there. However, hydrogen is a very diffusive fuel, and with the help of the walls of the chamber, the flame spread along the upper and lower side walls as can be observed in Figure 11.

Table 5 Dual thermocouple experimental conditions

Parameter/Equivalence ratio	Lean	Rich
Fuel mass flow[g/sec]	0.520	6.08
Air mass flow [kg/sec]	0.104	0.0721
Equivalence ratio	0.174	3.18
Injection pressure [MPa]	0.301	0.321
Upstream thermocouple temperature [K]	1850	1870
$T_{EXP_{nozzle}}$ **[K]**	1330	1600
Temperature gap [K]	520	270

For fuel-rich combustion, the right side of Figure 13 shows the maximum temperature recorded by the upstream thermocouple to reach a maximum value of 1870 K, while the downstream value was around 1600 K. The flame was fully developed in the combustor covering the entire chamber. As in the previous experiment, temperature rose quickly as hydrogen combusted with the hot air and declined as fast, when the supply of fuel was stopped. If for a fuel-lean combustion case, the temperature gap is assumed to be the effect of the equivalence ratio, and due to heat loss, in the rich case, most of the difference in temperature is assumed to be an effect of the heat loss at the walls.

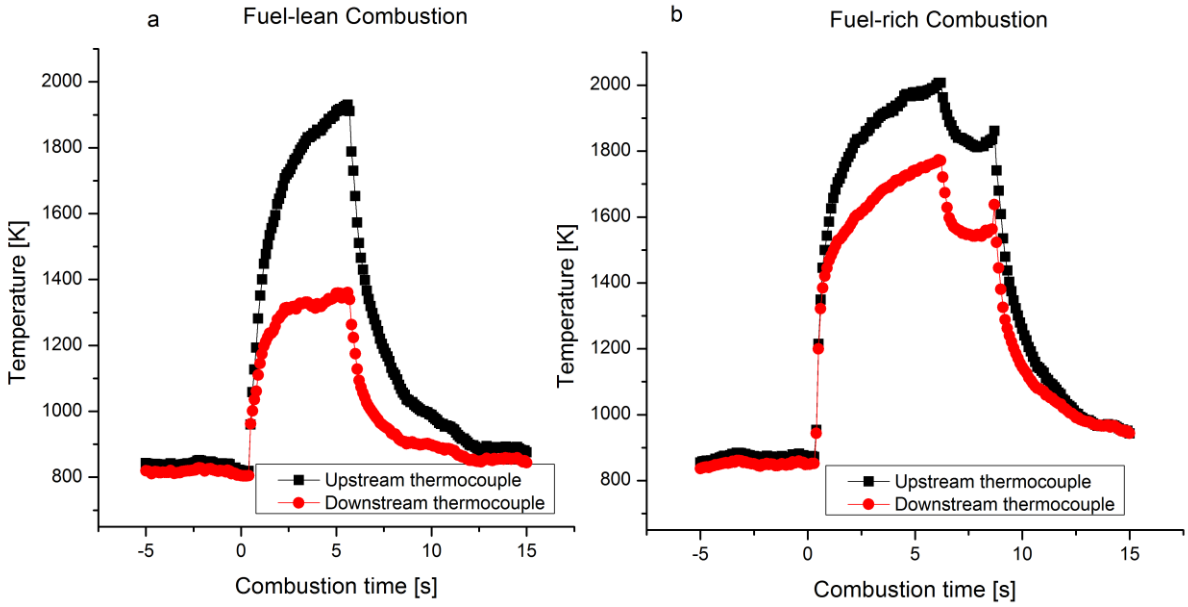

Figure 13 Combustion temperature measured with two thermocouples; a-fuel-lean combustion, b-fuel-rich combustion

The temperature gap measured in the experiments shows a difference of 500 – 600 K for fuel-lean combustion, and 100 – 200 K for fuel-rich combustion.

To further investigate the effect of heat loss in the chamber, numerical simulations have been performed for two equivalence ratios (numerical) of $\phi = 0.3$ for fuel-lean and $\phi = 2.0$ for a fuel-rich combustion. Table 6 presents the numerical conditions used in the simulations and the results at steady state for temperature and temperature gap. The values for the temperature were recorded as an average value of the plane at the same spatial coordinate as the position of the thermocouple in the experiments i.e. 130 mm and 300 mm. Figure 14 presents the temperature distribution field in the combustor for a fuel-lean case and a fuel-rich case, on the upper and bottom side, respectively. From the figure we observe a separated flame for the fuel-lean side and a fully developed flame for the fuel-rich case. This is in agreement with experiments. The area near the injector, in a fuel-lean case, has a higher temperature near the injector and a much lower value for the area near the nozzle. The red probes in the figures represent the position of the thermocouples in the experiments. As a result of the equivalence ratio, in a fuel-lean case, two flame fronts form along the walls, and as the hydrogen is consumed in the chamber, the flame “cools”, i.e. the temperature decreases in the chamber. As the fuel is consumed near the injector, the combustion process is no longer sustained, and as a result, the temperature drops, which explains the big temperature difference in the chamber.

Table 6 Dual thermocouple numerical simulation results

Parameter/Equivalence ratio	**Lean**	**Rich**
Configuration	45°x90°	45°x90°
Air temperature [K]	980	980
Equivalence ratio	0.3	2.00
Upstream thermocouple temperature [K]	1818.165	1930.85
Downstream thermocouple temperature [K]	1561.038	1825.38
Temperature gap [K]	257.127	105.4769

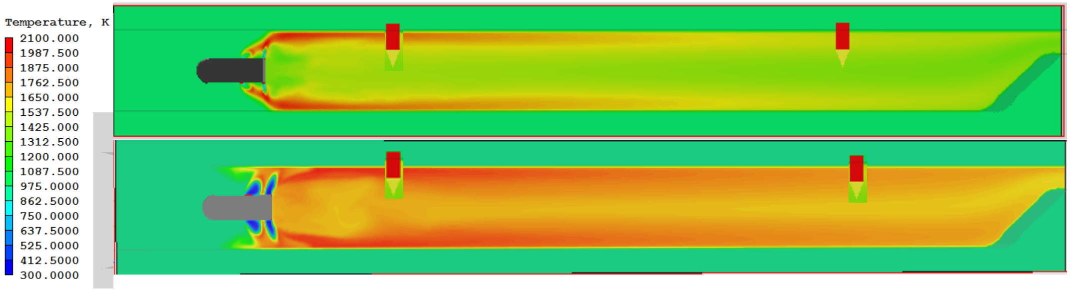

Figure 14 Temperature field distribution in the combustor; upper side represents fuel-lean at $\phi = 0.3$, and bottom side represents fuel-rich at $\phi = 2.0$

Keeping the same initial and boundary conditions similar for the fuel-lean case, we have increased the mass flow of hydrogen to achieve a numerical equivalence ratio of $\phi = 2.0$. For a fuel-rich case shown in Figure 14, bottom side, the flame expands in the whole chamber. Having a rich flame allows the fuel to spread into the chamber and be consumed more uniformly. As a consequence, the flame temperature decreases only slightly as the flame expands downstream. The temperature gap measured in our simulations was found to be less than that recorded in experiments. This is due to the fact that (1) the thermocouples record spot values throughout the combustion duration, which tend to be higher than averaged values, and (2) the configuration of the injector itself – although we have tried to recreate a similar 3D example, our simulations focus on only one pair of injection holes with periodic boundary conditions, while in an experiment for a full sized injector, the flame is expected to achieve a slightly higher temperature due to the augmentation of the flame, on a spot location, by the other injection holes. Nonetheless we observe higher temperature gaps for fuel-lean combustion than for fuel-rich combustion. This investigation will be presented in more detail in the next section.

4.4. Injector performance

The PCTJ engine planned by JAXA[8] is set to use fuel-lean combustion in the core turbojet, to obtain a high specific impulse and fuel-rich combustion for the afterburner to enhance the air cooling ability in hypersonic flight. A sub-scaled engine was designed for full engine experiments and the equivalence ratio of the mixture used in the afterburner was in the range of $\phi = 2 \sim 2.3$ [41,39,80,81]. However, in dedicated afterburner experiments, due to the high temperature of the flame, that could reach up to 2100 K, and the upper working limit of B-type thermocouples used, i.e. up to $\sim$2050 K, higher equivalence ratios have been used in experiments i.e. $\phi = 3{\sim}5$ where the maximum temperature of the flame reached values of up to 1900 K [61]. More experimental data is presented in Nishida et al.'s work[61].

In the simulations that have been performed to determine the effect of the injection configuration, a fuel-lean mixture has been selected to provide a fundamental study of the combustion process at these conditions. The fuel-lean equivalence ratio was 0.264. For numerical fuel-rich mixtures, not suffering by the physical limits imposed by the experimental apparatus, the fuel-rich equivalence ratio was fixed at 2.033. To investigate the effects, in the first phase we kept constant the upstream angles and varied the downstream angles from 10° to 120° for 6 different values - 10°, 30°, 45°, 60°, 90° and 120°. In the second phase, we repeated the simulations for 3 pairs of constant angles on the upstream: 30°, 45° and 60° respectively. Third and fourth phase have constant the downstream angles while the upstream angles are varied for the 3 pairs of constant angles on the downstream: 30°, 45° and 60° respectively.

4.4.1. Lean combustion

Using a constant equivalence ratio and varying the injection angles, sufficient data is obtained to help elucidate the effect of the hydrogen angled injection in the afterburner chamber of the PCTJ.

Experimental data for fuel-lean combustion is performed to determine the effects of combustion instabilities and CO_2 addition; as a consequence it cannot be compared with the study at hand. The data can be found here [61]. However, to understand the effect of the heat loss on the combustor, fuel-lean simulations have been performed and all the parameters introduced in the numerical chapter are presented in this section.

To understand the effect of the injection angle on the combustion process, flame distribution, velocity vector distribution, chemical heat release and total heat loss as well as combustion temperature and combustion efficiency will be presented. Due to the influence of each pair of angle on the flow, each set of pairs is treated separately.

4.4.1.1. Constant upstream combustion

Figure 15 presents the temperature, on the upper part, and velocity distribution field, on the lower part, for constant upstream angles of 30°. Figure 17 presents an enlargement of the injector region for the temperature field, on the right side, and velocity vector distribution, on the left side, for the same configurations. In Figure 15 and Figure 17, from a, to e, the downstream angles increase from 10° (a) to 120° (e).

As observed previously, fuel-lean combustion is characterized by a two flame fronts alongside the walls of the combustor. These two flame fronts do not connect but they become slightly longer, as the angles increase on the downstream side.

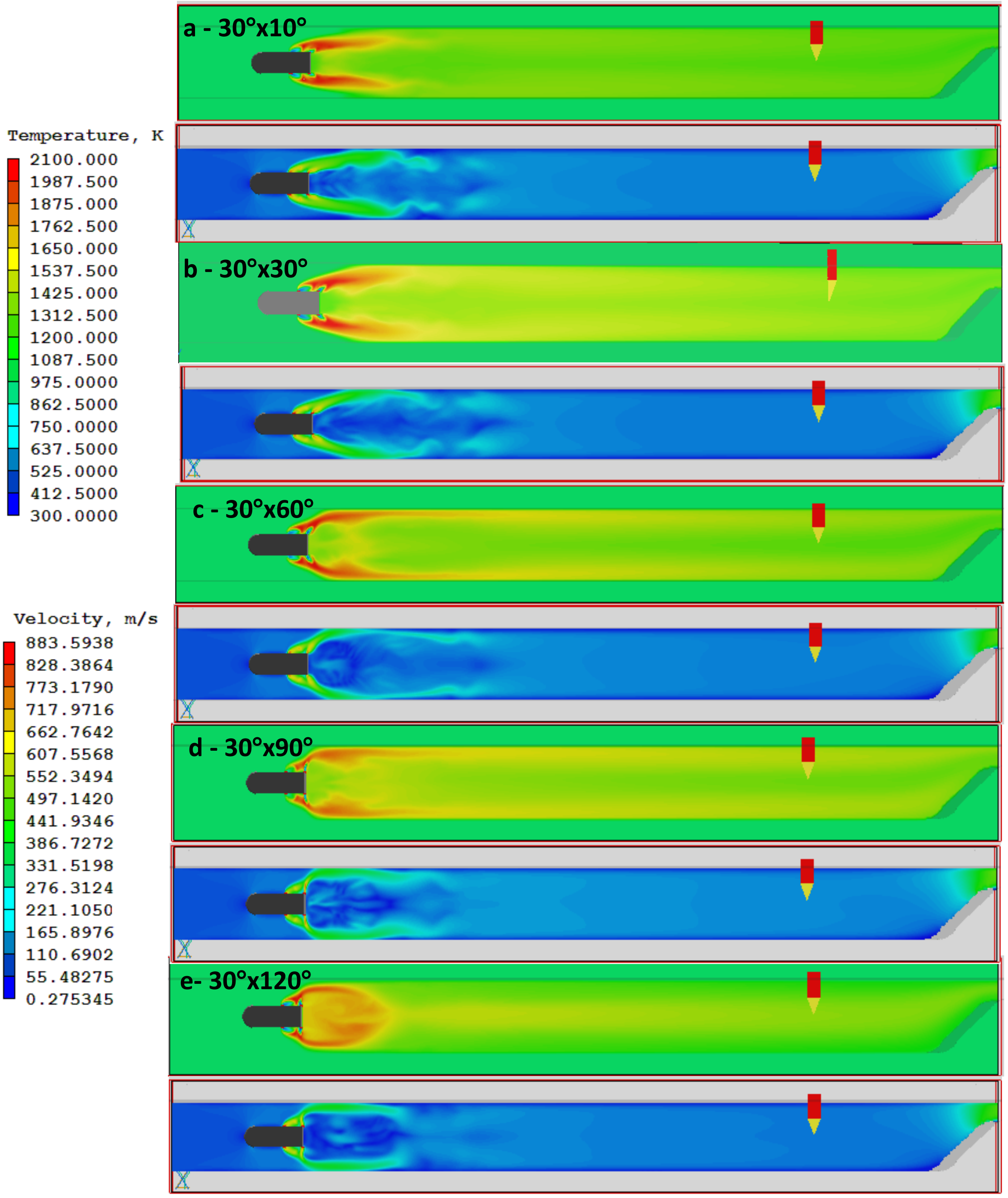

Figure 15 Temperature and velocity distribution field for constant upstream angle of 30° at fuel-lean conditions

For a 30°x10° configuration, seen in Figure 15 and Figure 17-a, the flame is concentrated near the injector. When the temperature is plotted for the length of the combustor on the left side of the figure, and the heat loss in the chamber on the right side (both shown in [black] squares), observed in Figure 16, we see that as the mixture combusts near the injector the heat loss is relatively small, compared with the rest of the chamber. Due to the equivalence ratio and small angles on the downstream side, a large amount of fuel is carried in the axial direction, downstream, thus having little contact with the walls of the chamber. As a result the heat loss increases at the walls when most of the fuel is consumed, with resulting heat released expanding in the chamber, decreasing as it is carried farther away from the injector. The highest value of the heat lost is seen at about 130 mm from the inlet and 70 mm from the injector.

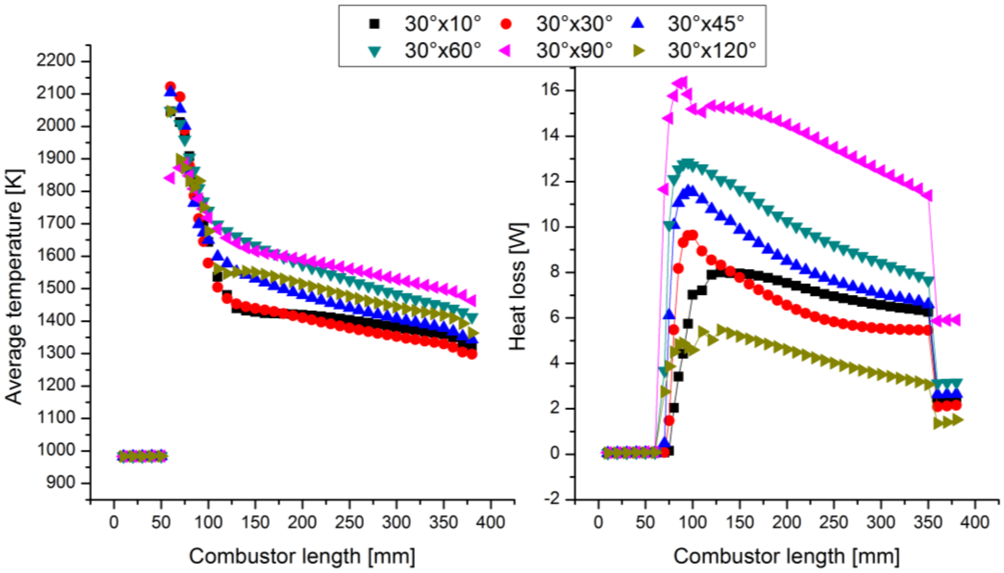

Figure 16 Average temperature (left side) and heat loss (right side) in the combustor for constant upstream 30° and variable downstream angles at fuel-lean conditions

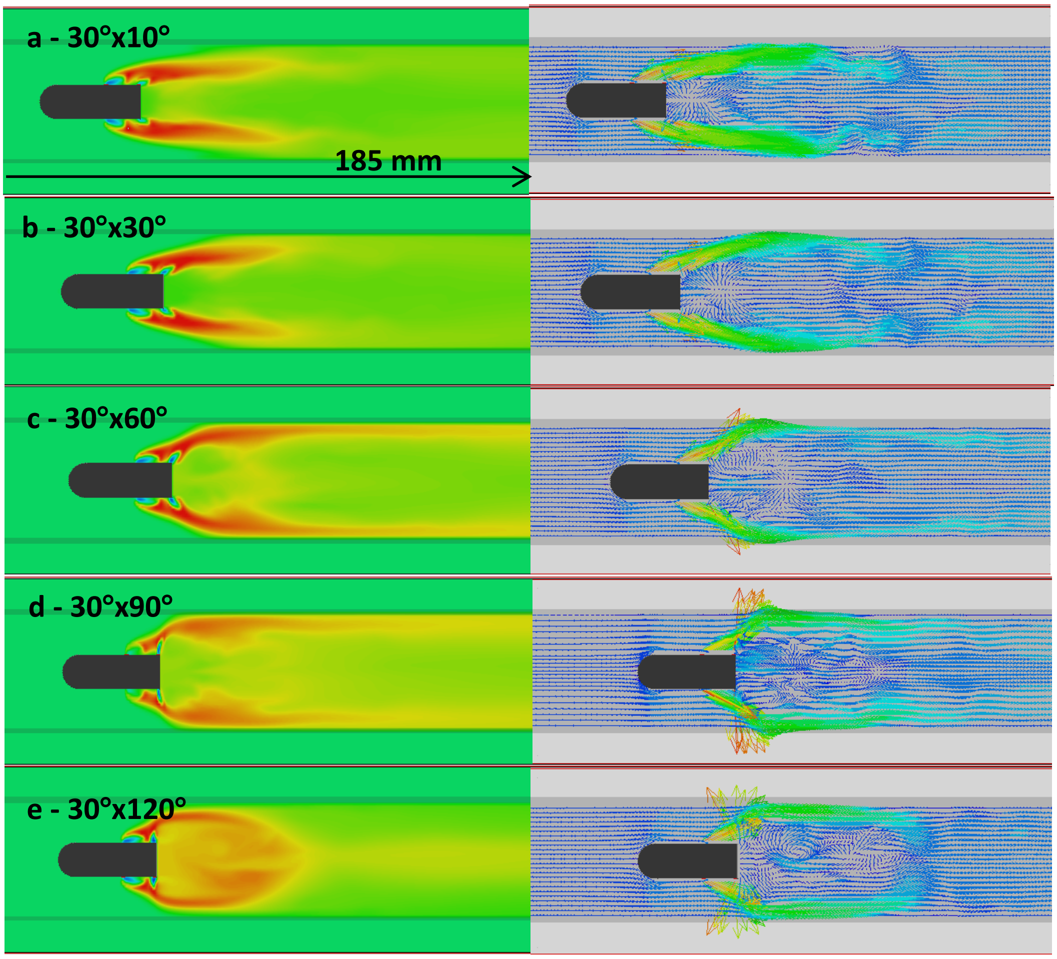

Figure 17 Enlarged temperature field distribution and velocity vector distribution near the injector for constant upstream angles 30°

As the angles increase, seen in Figure 15 and Figure 17-b, the injected fuel from the downstream pair, is carried closer to the walls of the combustor. This flow increases the contact of the mixture with the walls, increasing the heat loss. This trend is observed in Figure 16 denoted with the [red] circles. In this case, due to the increase in angled injection on the downstream side, the maximum heat lost moves closer to the injector to about 110 mm from the inlet and 50 mm from the injector.

For a configuration of 30°x45°, similar trend to the previous configuration is observed. The increasing angles inject fuel closer to the walls and as a result the highest value of heat lost is closer to the injector, this time situated around 35 mm, observed in Figure 16.

With larger angles on the downstream, for a 30°x60° configuration, fuel is injected towards the walls, enhancing the heat loss in the area. The peak of maximum heat loss for this configuration is similar to the previous case shown by inverted [cyan] triangles in Figure 16.

When the downstream angles are increased to 90°, larger heat loss is associated with larger angles, as more fuel is injected directly at the walls. However due to the fast injection, the jet is reflected by the walls, which create a short area of smaller heat loss. This is observed in Figure 16 by [pink] left side triangles. Another effect of higher angles on the downstream is that the recirculation zone in the wake of the injector breaks down in many smaller vortices, due to the large angles on the downstream side. Given the low equivalence ratio of the mixture, these smaller vortices do not increase mixture associated with increased turbulence, but actually lower the overall temperature downstream of the combustor.

When the downstream angle is increased to 120°, seen in Figure 15-e and Figure 17-e, a large recirculation formed in the wake of the injector. Due to these two velocity fronts, mixing in the wake of the injector is expected to enhance, and as a result most of the fuel combusts in the wake of the injector, forming what looks like a concentrate shaped, stable flame. It has an almost “teardrop” shaped. An overlay of the velocity field and temperature is presented in Figure 18.

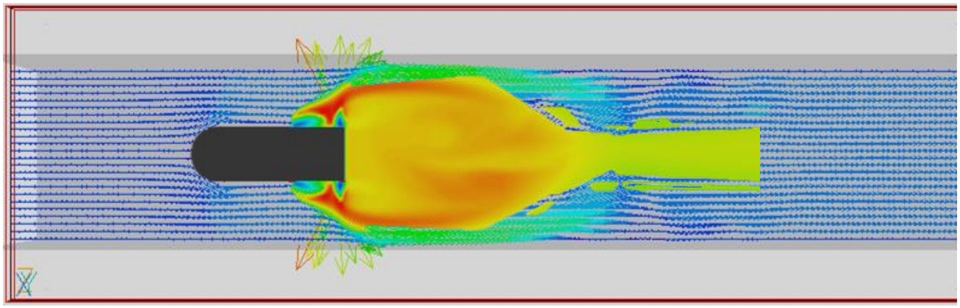

Figure 18 Overlay of the velocity field and temperature distribution field for a 30°x120° configuration at fuel-lean conditions

The average temperature and heat loss in the combustor for 30°x120° configuration is presented in Figure 16, alongside the other configurations denoted by the [light green] right side triangles.

From Figure 17-b, we can observe a recirculation zone in the wake of the injector that is induced by the angled injection on the downstream side. This recirculation zone is just a large eddy that entraps unburned air and fuel, and due to its position, lowers the temperature of the flame in the wake of the injector. When the fuel is injected at 60° downstream as observed in Figure 15 and Figure 17-c, the recirculation zone, having reached a maximum sustainable size, when the axial velocity is higher than the azimuthal velocity, the vortex breaks down into smaller vortices. In this case, two symmetrical vortices form on the axial direction of the combustor.

Another effect of the vortices breaking apart in the wake of the injector is the formation of a “bridge” between the upper and bottom flame fronts. Due to lower azimuthal velocities at the edge of the eddy formations, on one hand, and higher temperatures associated with this lower velocity on the other hand, fuel is carried from the upper side of the combustor and interacts/mixes with fuel from the lower side of the combustor.

From the temperature distribution fields in Figure 15 and Figure 17, plotted for length of the combustor in Figure 16 on the left side, we can observe that the temperature rises quickly in the wake of the injector, and later decreases substantially in the chamber, creating a temperature difference between the nozzle and injector area of almost 300 K.

Figure 19 presents the chemical heat release ($\dot{Q}$) plotted for constant upstream angles of 30°. When the upstream angles were kept constant, the trend was an increase in heat release as the downstream angles became larger. It can be seen that most of the combustion took place near or around the injector and not towards the nozzle area. This increase however, only rises until two flame fronts are connected as a result of the "bridge" forming in the wake of the injector. As that happens, the local equivalence ratio decreases which decreases the chemical heat release.

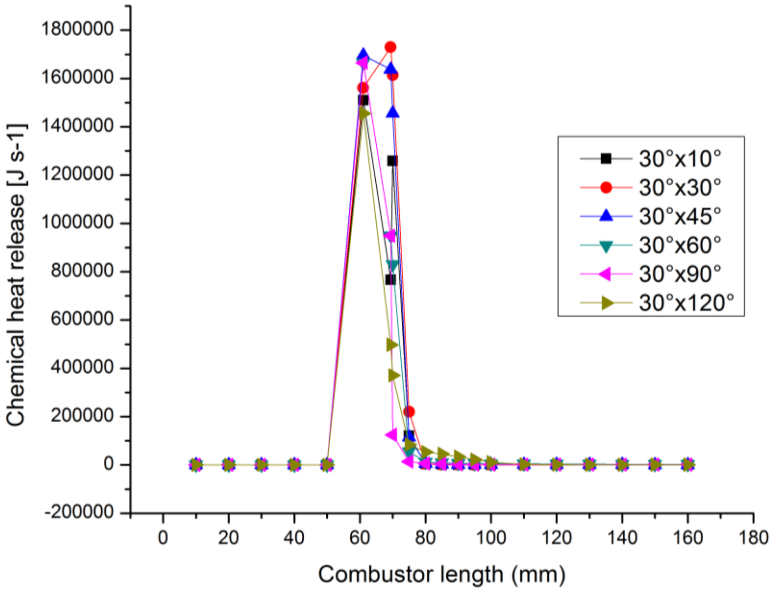

Figure 19 Chemical heat release for constant 30° upstream angles at fuel-lean conditions

As the angles increase on the downstream we have observed that the heat release maximum value moves closer to the injector, which is in agreement since the maximum heat loss peak follows the same trend. The amount of fuel is mostly consumed around the injector and in its immediate wake area.

Figure 20 presets the local equivalence ratio for constant upstream angles of 30°, and following the previous defined trend by the chemical heat release, as the angles increased on the downstream side, the local equivalence ratio rose. What is important however, from this figure is that a higher local equivalence ratio does not necessarily mean higher chemical release. What we observed as important was the area into which the fuel "expanded", the area in which the fuel was allowed to mix, shown in Figure 20 by the area under the curve.

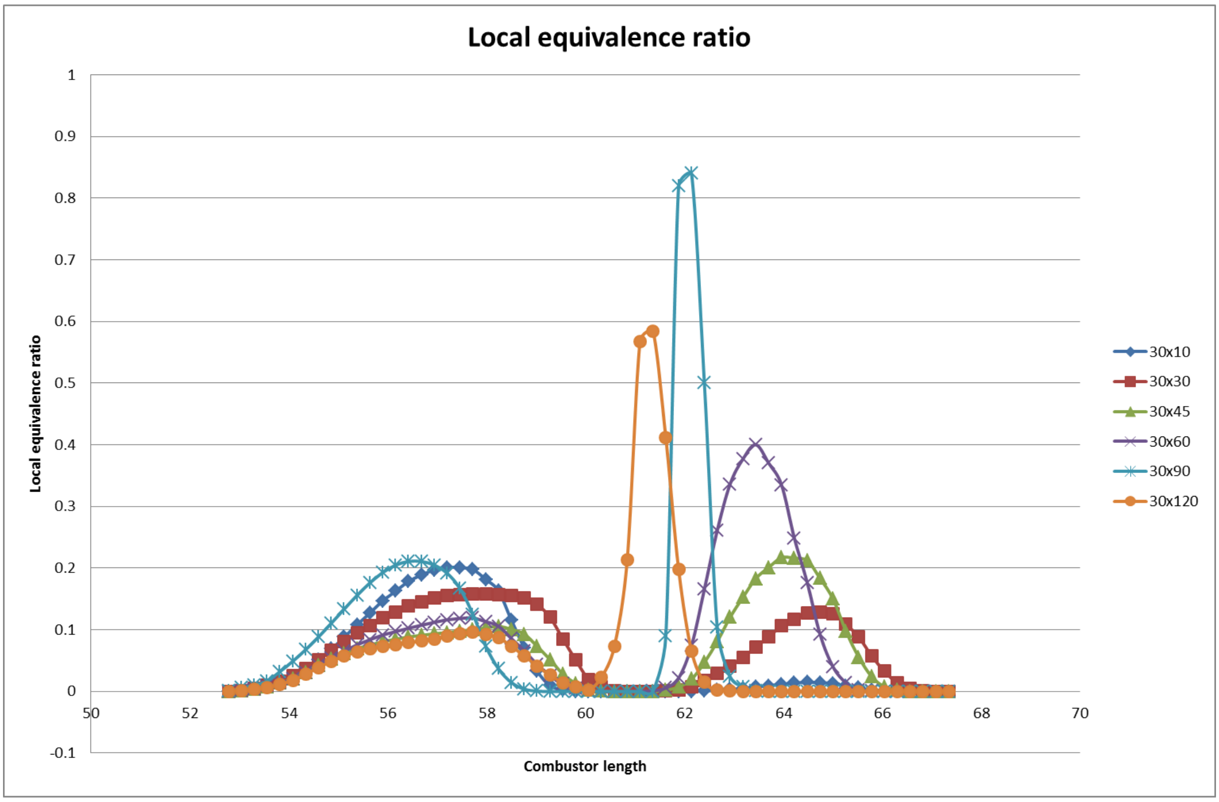

Figure 20 Local equivalence ratio of unburned products for a constant upstream angle of 30° and variable downstream angles at fuel-lean conditions

Figure 21 presents the total heat loss plotted this time for the variable downstream angles. The total heat loss is seen to increases as the angles increase on the downstream side. For constant upstream of 30°, the increasing angles on the downstream side push more fuel towards the walls increasing the heat loss.

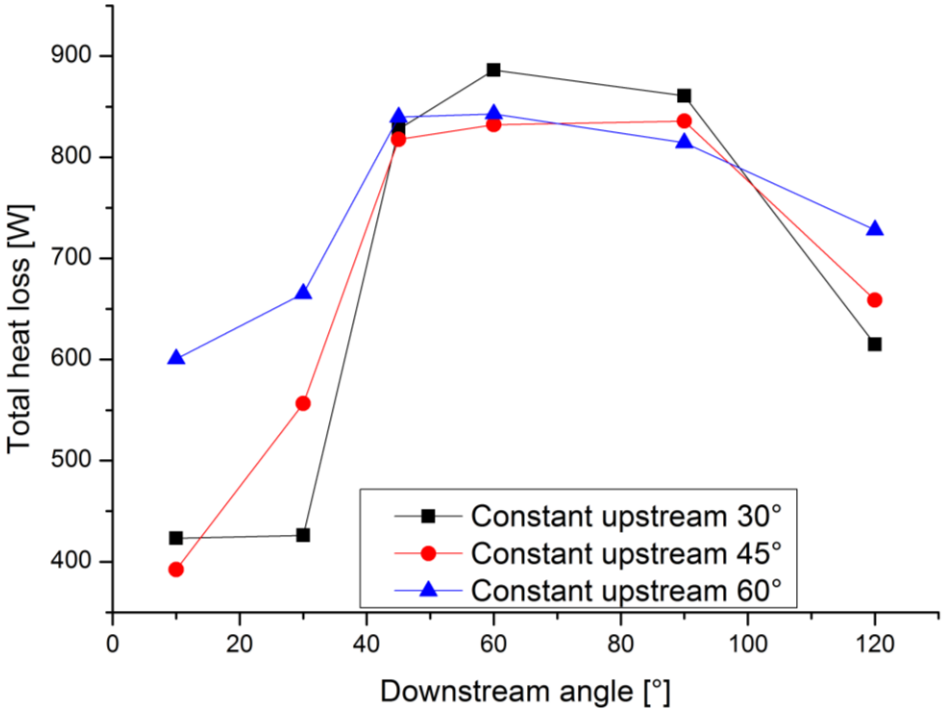

Figure 21 Total heat loss for constant upstream angles and variable downstream angles at fuel-lean conditions; [black] squares – upstream 30°,[red] circles – upstream 30°,[blue] triangles – upstream 30°

The total heat loss is calculated for every configuration and as presented in Figure 21, alongside other configuration for comparison; it is seen to increase as fuel is being injected towards the walls with increasing angles (45°, and 60°). However, when the two flame fronts start connecting through the "bridge", this lowers the maximum reaction heat. This lower value leads to lower heat loss values. The final configuration (30°x120°), due to the formation of the concentrated flame, the contact of the hot mixture with the walls of the injector is decreased and as a result the total heat loss decreases.

Figure 22 presents the combustion efficiency for constant upstream angles of 30° and combustor length on the right side using the enthalpy approach (-a), the left side presents the chemical heat release approach (–b). The combustion efficiency is close to zero near the air inlet and increased to its maximum value immediately after the injector. This increase near the injector is due to fresh fuel mixing with the incoming air and its following combustion. After, most of the fuel was consumed, the combustion efficiency decreased towards the nozzle area. Using a cumulative graph, the combustion efficiency is seen to maximize around the injection area, and remain constant throughout the combustor.

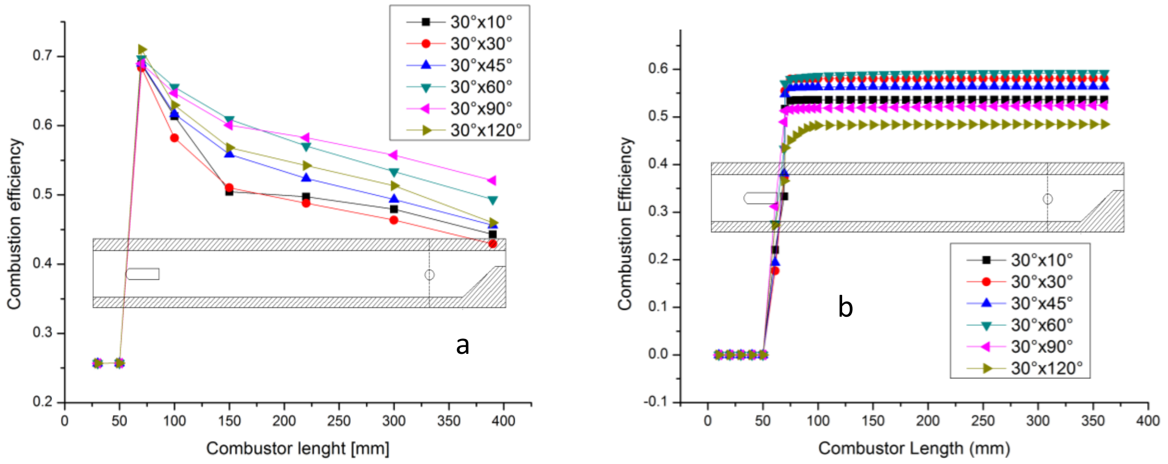

Figure 22 Combustion efficiency for constant upstream 30° angles at fuel-lean conditions; a- enthalpy difference approach, b- heat release approach

Experimental results of the combustion efficiency use the values near the nozzle to represent an injection configuration. The nozzle area as presented in Figure 9 is at 300 mm from the inlet area. When the values of the combustion efficiency, using the two approaches are plotted at the same spatial coordinate, a direct representation of the injection configuration is observed in Figure 23.

The combustion efficiency, using the enthalpy approach, observed in Figure 23 (black points), follows a similar trend with that of the total heat loss. The fuel is influenced by the increasing downstream angles as they generate higher chemical heat and subsequent heat loss at the walls. This influences the combustion efficiency and we observe a maximum value for a 30°x90°, when mixing is enhanced, throughout the chamber, yielding a higher temperature overall.

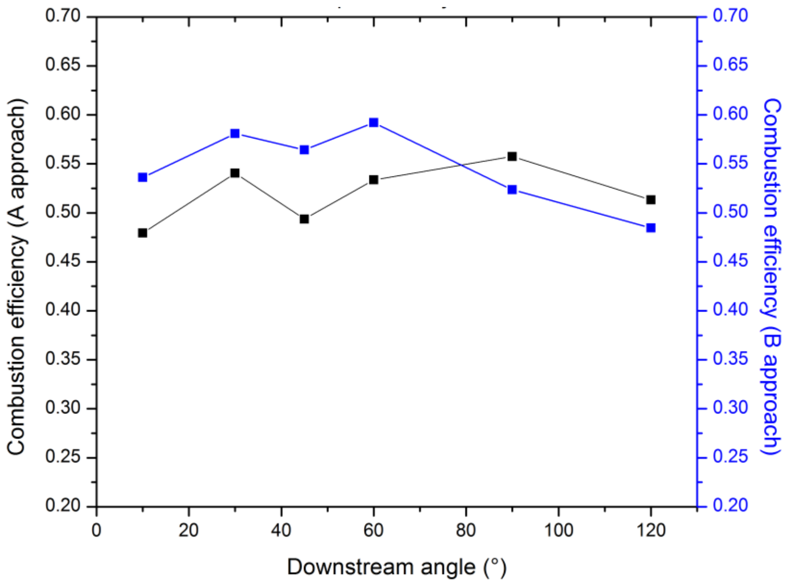

Figure 23 Overall combustion efficiency using the two approaches, enthalpy difference (black line) and chemical heat release (blue line) for constant upstream angles of 30°

The chemical release approach however, shows a peak around the 60° angles, when the mixing influenced by the velocity flow, is largest. Once the heat loss increased, due to larger values on the injection angles, i.e. past 90°, the combustion efficiency decreased.

Figure 24 presents the NO and NO2 distribution in the combustor for fuel-lean configuration. From the field distribution we can see that most of the NO and NO2 is formed in the wake of the injector when the flame temperature is highest then it slowly decreases downstream of the chamber. The values change significantly near the nozzle, due to the presence of the ramp, where pockets of burned mixture are trapped and create more NOx. The two configurations are shown here to provide an understanding of a small flame, and a fully developed flame. The bulk of NO, seen in Figure 24 –a, and -c, was created in the center of the flame fronts (although the picture shows a 2D representation, the simulations were done in 3D), in the post-flame region. The NOx formed more quickly in the recirculation zone behind the injector than in the post flame zone. NO studies in the flame have been well documented [68,82,83]. The NO in the postflame region, for this equivalence ratio, is mostly explained by the Zel'dovich mechanism presented in the chapter 4.5. NO first appears in the near postflame region; it appeared closer to the visible flame zone as the amount of oxygen in the area was sufficient to generate NO via the thermal NO mechanism. The NO2 on the other hand, can be seen forming earlier than the NO, starting to form early in the flame reactions, continuing to increase in concentration farther downstream, in the visible flame zone. The NO2, observed in Figure 24-b and –d, is formed closer to the edges of the flame as the oxygen concentration is higher. The concentration of NO2 decreased significantly in the wake of the injector, in the postflame region, and was coincident with a corresponding formation of NO.

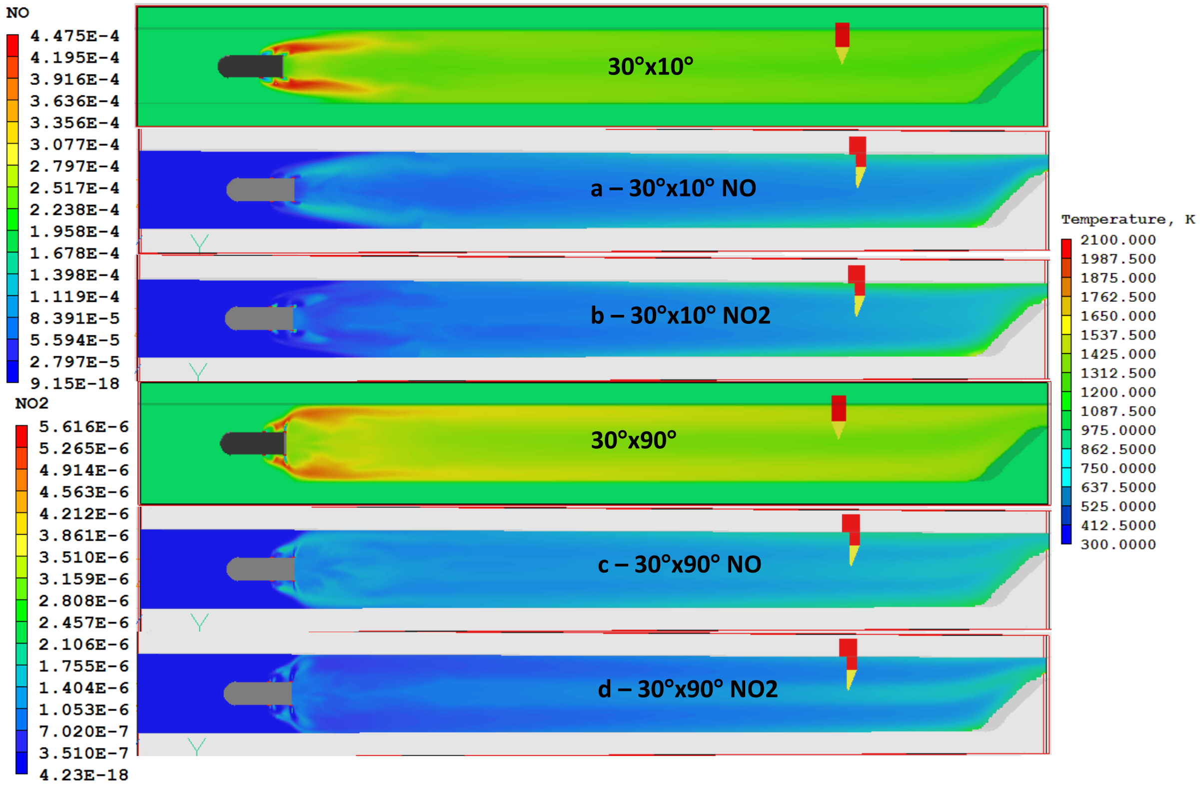

Figure 24 NO and NO2 mass fraction distribution fields in the combustor for a 30°x10° (a and b) and 30°x90° (c and d) configurations at fuel-lean conditions

Figure 25 presents the NO and NO2 mass fraction plotted in the length of the combustor for variable downstream angles at constant upstream angles of 30°. As we can see the NOx that forms in the combustor are results of increasing values of NO and NO2 being generated by the subsequent reaction. A details presentation and explanation of NOx formation and reaction is presented in section 4.5. NO is seen to be created near the hot region of the flames. As the amount of oxygen, as well as the temperature of the flame, decreases farther downstream, the NO production slowly decreases. The NO2, on the other hand, as seen from Figure 24, is produced earlier in the combustor. However, with the decrease in temperature, it decreases downstream. The results support previous conclusions, NO is active in high-temperature regions and, that NO2 is not present in the main reaction zones at high temperatures, and later NO2 is converted in NO. Also that it appears at the base of the flame and along the flame fronts, where temperatures are lower. As the concentration of NOx evens out downstream, the concentration of NO and NO2 seem to decrease are they are reduced by dilution.

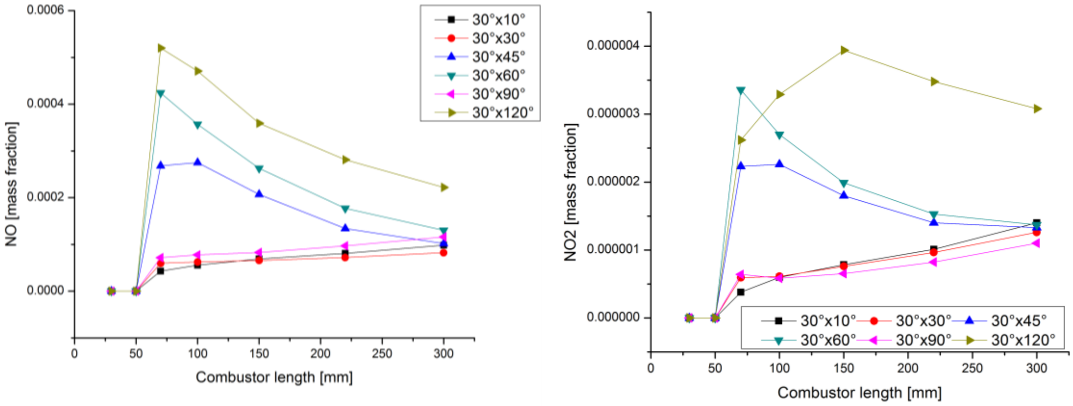

Figure 25 NO and NO2 mass fraction distribution in the combustor

When the EINOx is plotted, for variable downstream angles, in Figure 26, the EINOx is seen to be directly proportional to the evolution of the combustion efficiency presented in Figure 23. As the combustion efficiency increases, raised by the temperature near the nozzle, the NOx index increases with increasing temperature. While temperature alone is not the only cause of the NOx increase, various reactions taking place in the consumption and creation of NOx are of importance. A detail explanation of all reaction mechanism will be presented in section 4.5.

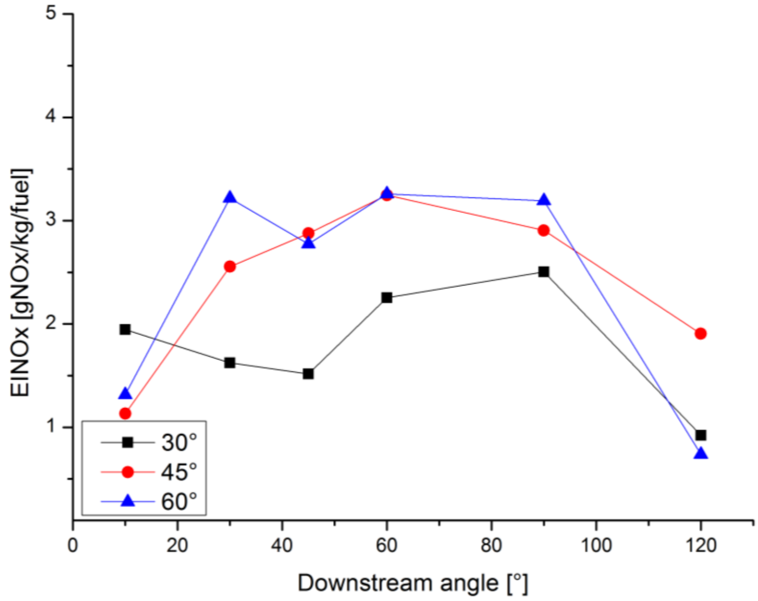

Figure 26 EINOx for constant upstream angles and variable downstream angles at fuel-lean conditions; [black] squares – upstream 30°,[red] circles – upstream 30°,[blue] triangles – upstream 30°

One observation made so far is that where we measure the combustion efficiency can affect the efficiency we consider to represent a configuration.

When the upstream angle is increased to 45° shown in Figure 27 and Figure 29, the larger angle on the upstream side allows for “thicker” flame fronts to form around the injector. Having a larger angle also allows for the fuel injected from the upstream pair to be carried slightly farther downstream before mixing with the fuel coming from the downstream pair. This slight difference, allows for better mixing in the wake of the injector, brought about by an increase in the local equivalence ratio.

For a 45°x10° configuration, seen in Figure 27 and Figure 29-a, the flame fronts extend close to the walls and farther downstream. Due to the low angles on the downstream side, the area in which the fuel and air mix, is larger, thus we observe “thicker” flame fronts. As mixture proceeds into the combustor, it is consumed towards the nozzle. While the hot region is still concentrated near the injector, in this configuration due to larger area for mixing, the hot zone proceeds farther downstream compared with the previous configuration (30°x10°).

When the temperature is plotted for the length of the combustor vs. the heat loss in the chamber, observed in Figure 29, we see that as the mixture combusts near the injector the heat loss is relatively small, compared with the rest of the chamber. Due to small angles on the downstream side, a large amount of fuel is carried downstream, thus having contact with the walls of the chamber. As a result the heat loss increases at the walls when the fuel is consumed, with resulting heat released expanding in the chamber, decreasing the heat loss farther away from the injector. The highest value of the heat lost is seen at about 90 mm from the inlet and 30 mm from the injector.

When the angles increase on the downstream side, seen in Figure 27 and Figure 29-b, the larger angles on the downstream side, allow for a larger recirculation zone in the wake of the injector. This eddy formation not only traps colder air and unburned mixture, it also forces the combusting mixture to flow along the wall of the combustor. This is seen to increase the mixture’s contact with the walls thus, increasing the heat loss in the chamber. This effect is seen plotted in Figure 28, alongside the average temperature in the chamber. Although the temperature is higher for this configuration, when fuel injected from the downstream pair mixes with fuel coming from the upstream pair, the main part of combustion still takes place near the injector, which is why the heat loss, decreases faster as it gets farther from the injector.

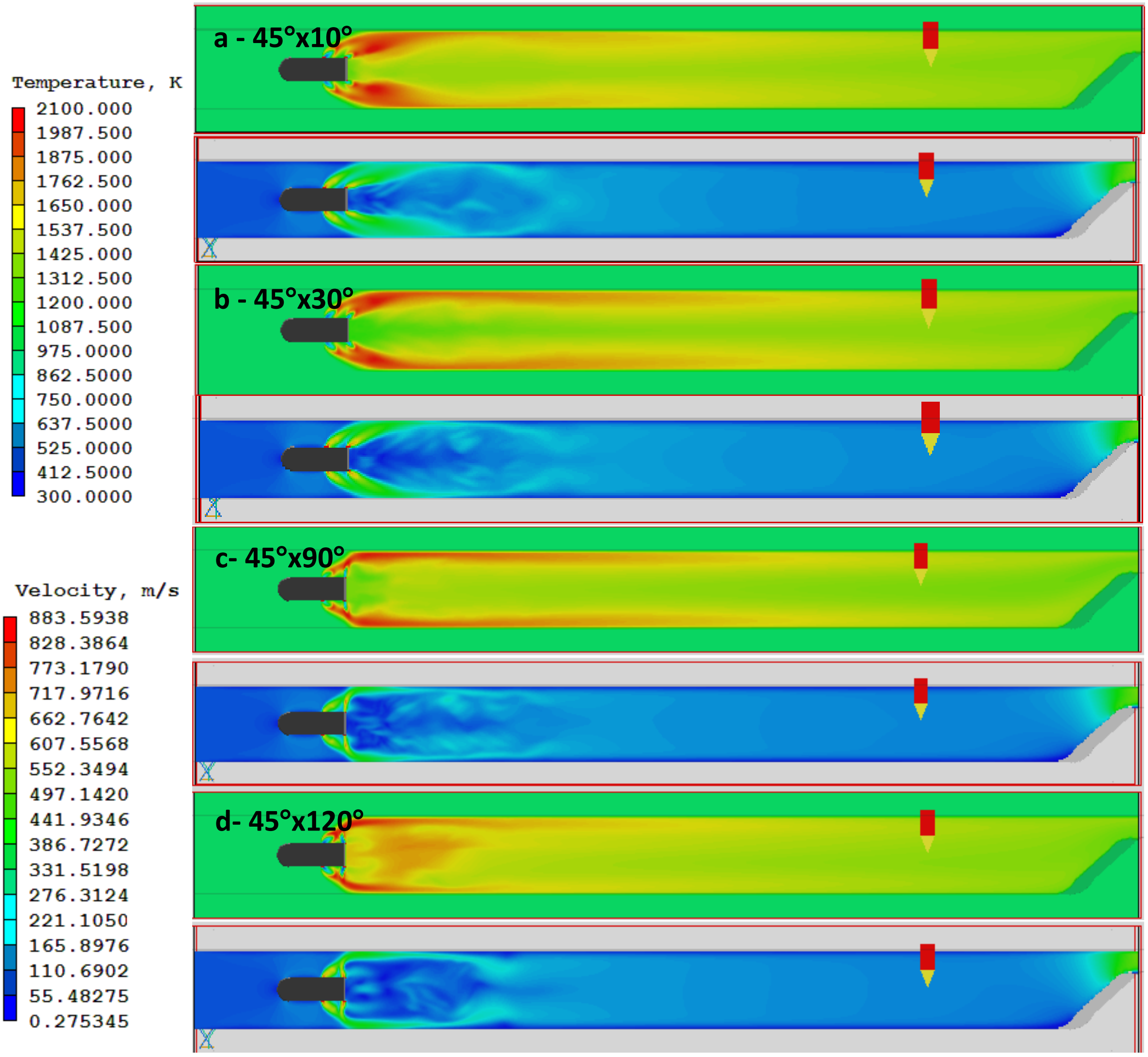

Figure 27 Temperature and velocity distribution field for constant upstream angle of 45° at fuel-lean conditions

For a configuration of 45°x45°, a similar trend to the previous configuration is observed so it is not shown. The increasing angles inject fuel closer to the walls and as a result the highest value of heat lost is closer to the injector, this time situated around 25 mm. However, due to a larger recirculation zone forming in the wake of the injector, shown in Figure 27 and Figure 29, for 45°x30° and 45°x45°, the strong vortices that form in the wake of the injector, fuel is carried along the upper and lower side walls. As the vortices become weaker farther downstream, the temperature is seen to increase, according to the Figure 29. In this second reaction area, while still close to the walls, the higher temperature is actually closer to the middle of the injector, directed by the increase in velocity after the vortices break apart, which explains the decreasing heat loss farther downstream in the chamber.

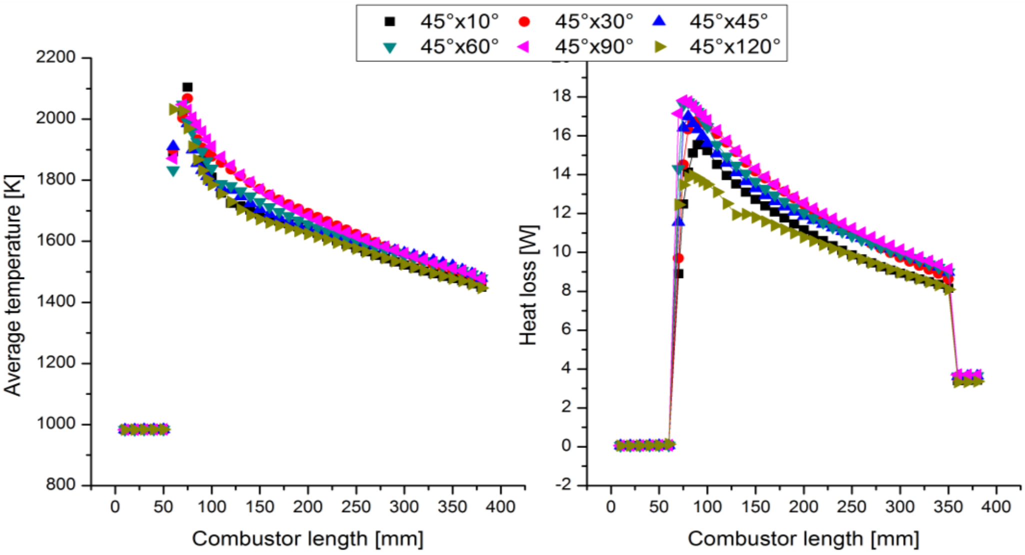

Figure 28 Average temperature (left side) and heat loss (right side) in the combustor for constant upstream 45° and variable downstream angles at fuel-lean conditions

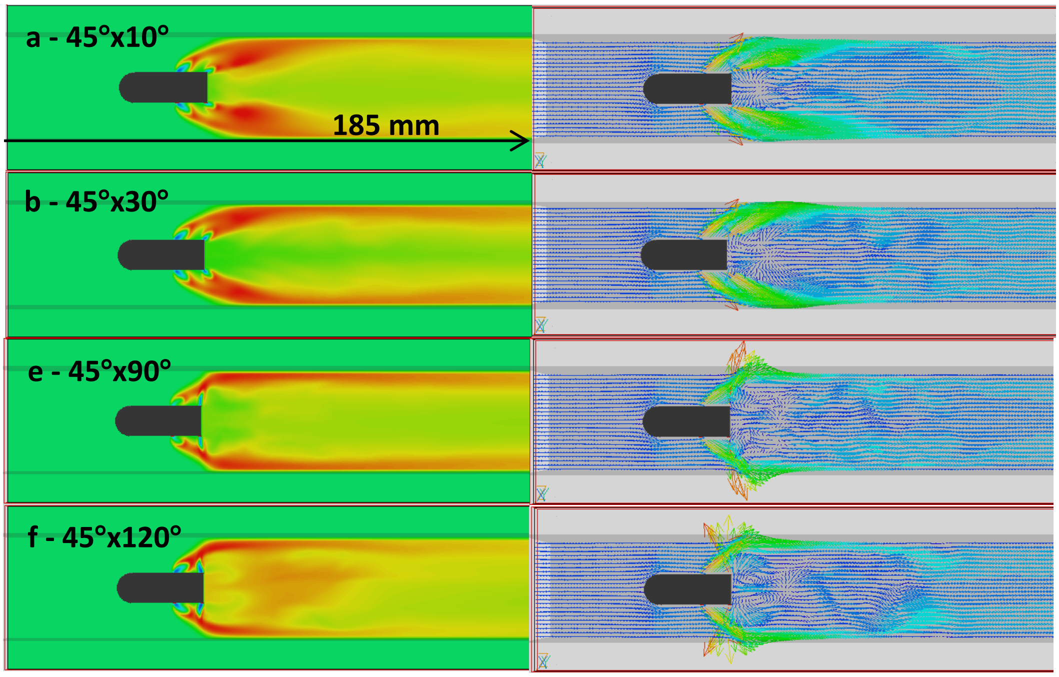

Figure 29 Enlarged temperature field distribution and velocity vector distribution near the injector for constant upstream angles 45°

For a 45°x60° configuration is similar to that of the lower angles i.e. 45°x30°, so it is not shown. What changes, however, is the size of the recirculation zone. As the angles increase, the eddy forming in the wake of the injector is larger but its epicenter is located closer to the injector, which leads to the second reaction area to “move” closer to the injector i.e. for 45°x45° it was located around 50 mm from the injector, for 45°x60° it is located at 40 mm from the injector.

When the downstream angles are increased to 90°, a direct effect of this is larger heat loss associated, as more fuel is injected directly at the walls observed in Figure 29. Another effect is that the recirculation zone in the wake of the injector breaks down in two symmetrical, smaller vortices, due to the large angles on the downstream side. These small symmetrical vortices, break down fast due their relative small size, which allow for the two flame fronts to connect, which as is expected creates a more uniform flame farther in the combustor.

When the downstream angle is increased to 120°, seen in Figure 27-d and Figure 29-d, the two smaller vortices that formed when the recirculation zone reached its maximum sustained size, have become even smaller for this configuration. This can be seen in Figure 30. As a result, the flame is fully developed in the wake of the injector. A slight effect of the asymmetry of chamber, induced by the presence of the ramp, is seen on the flame, when velocity is slightly increased on the lower side of the combustor. As a result of the fully development of the flame the heat loss at the walls decreased, shown in Figure 29.

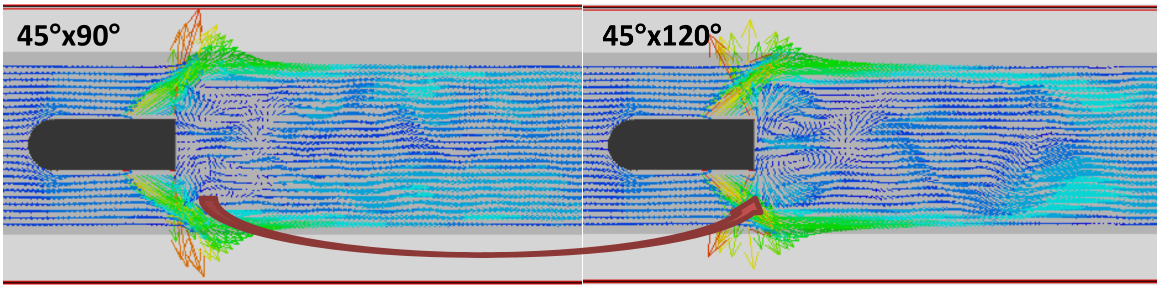

Figure 30 Eddy formations for 45°x90° and 45°x120° configurations at fuel-lean conditions

From the temperature distribution fields in Figure 29 plotted for length of the combustor, we can observe a similar trend with the previous upstream 30° configurations. The temperature gap measured for these configurations reaches a maximum of 250 K. In comparison with the previous configuration, an increase in upstream angles creates a more uniform flame, shown here by a more uniform average temperature in the combustor. Of course there are configurations i.e. 90° or 120° on the downstream, that modify the flame shape and temperature, but overall the temperature is seen around 1600 K with a maximum value around 1900 K.

Figure 31 presents the chemical heat release ($\dot{Q}$) plotted for constant upstream angles of 45°. When the upstream angles were kept constant at 45°, the heat release in the chamber is almost constant for angles up to 90°; however, as they increase past this value, the peak moves closer to the injector, when the chemical heat release is higher.

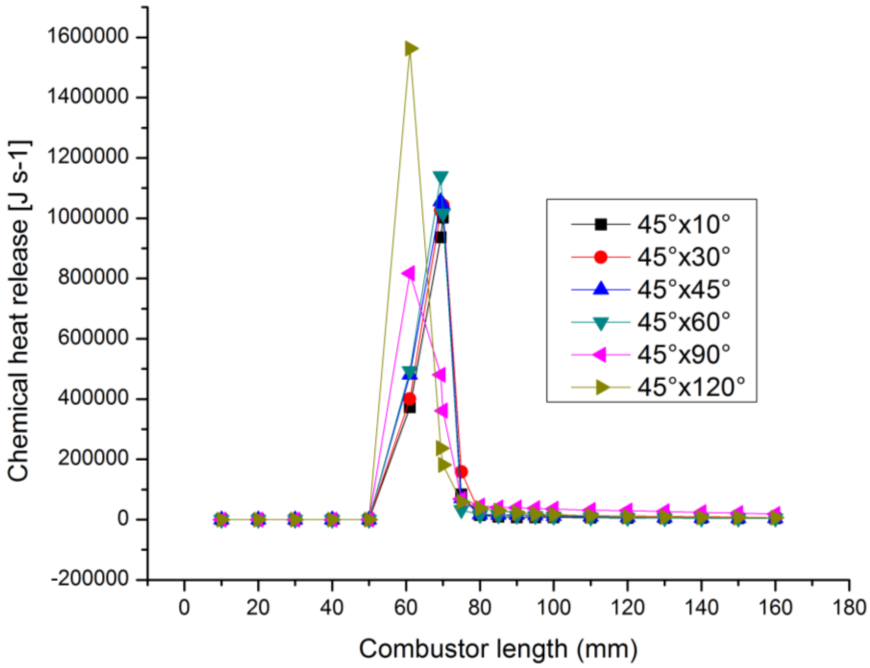

Figure 31 Chemical heat release for constant 45° upstream angles at fuel-lean conditions

The combustion takes place along the walls of the combustor, however, when angles on the downstream side are larger than 60°, due to the vortex breakdown in the recirculation zone, the local equivalence ratio is assumed to decrease and lower the heat release.

In Figure 21, the total heat loss in the combustor is plotted for variable downstream angles with a fixed upstream angle of 45° is presented by the [red] circles in comparison with the previous configurations. As the angles increased on the downstream we have observed that due to the vortex breakdown suffered by the large angles, the mixing is inhibited. This inhibited mixing lowers the heat loss suffered at the walls for large angles downstream i.e. 120°.The total heat loss is seen to increases as the angles increase on the downstream side. For constant upstream of 45°, the increasing angles on the downstream side push more fuel towards the walls increasing the heat loss, and later due to vortex breakdown, the heat loss evens out, decreasing once the mixture expands in the chamber, in the wake of the injector.

Figure 32 presents the combustion efficiency for constant upstream angles of 45° and combustor length on the right side using the enthalpy approach (-a), the left side presents the chemical heat release approach (–b). The combustion efficiency follows the same trend as in the previous configuration. The fuel is influenced by the increasing downstream angles as they generate higher chemical heat and subsequent heat loss at the walls.

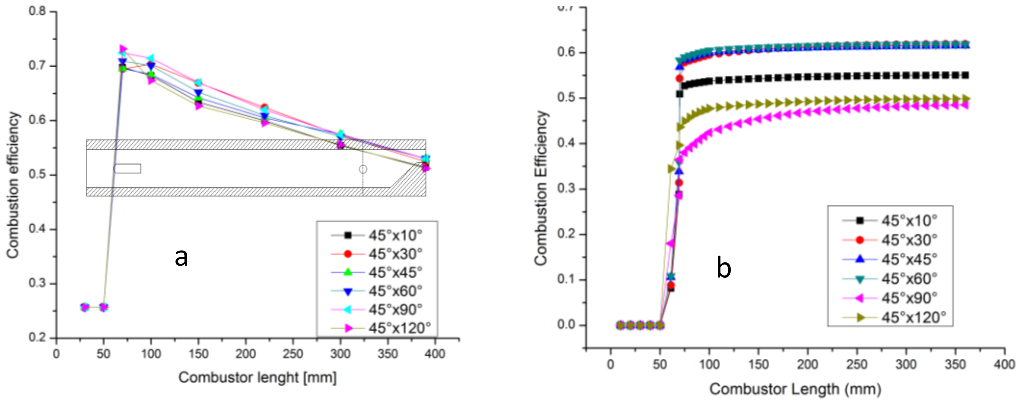

Figure 32 Combustion efficiency for constant upstream 45° angles at fuel-lean conditions; a- enthalpy difference approach, b- heat release approach

In comparison with the previous configuration, we observed, that larger angles downstream create more uniform combustion efficiency in the chamber, and the slope at which it decreases, is not as steep. As a result, the combustion efficiency recorded near the nozzle area is very little affected by the angle configuration. The combustion efficiency is increasing with larger angles downstream as mixing is enhanced, and the chemical heat release increased. However, due to these larger angles, a large vortex forms in the wake of the injector, which pushes fuel towards the walls and farther downstream. When this vortex breaks down, there is a small decrease in the combustion efficiency.

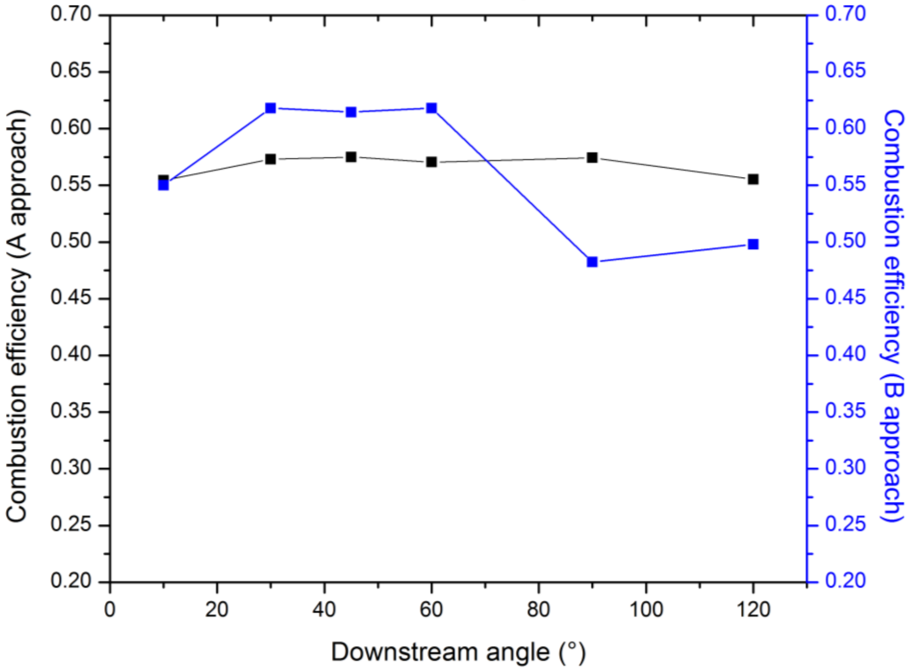

Figure 33 Overall combustion efficiency using the two approaches, enthalpy difference (black line) and chemical heat release (blue line) for constant upstream angles of 45°

Figure 33 present the combustion efficiency evaluated at the combustor nozzle using both approaches. The enthalpy difference is seen to show little difference near the nozzle, however using the chemical heat release shows a larger variation in the combustion efficiency of about 10%.

The chemical heat approach follows the same trend as seen in Figure 32. The combustion efficiency is highest when the flame fronts extend on a larger area, as the local equivalence ratio among the angled configurations, is highest. Beyond this configuration, the higher angled injection decreases the combustion efficiency.

Figure 34 presents the NO and NO2 mass fraction plotted in the length of the combustor for variable downstream angles at a fixed upstream angles of 45°. When the angles increase downstream up to 60°, generate an even value of NO and NO2, when the downstream angles are increased past this value to 90° and 120°, due to vortex breakdowns that occurs in the wake of the injector, smaller vortices generate turbulence which in turn contributes to the creation of NO and NO2. Not only that, we observed that the creation of NO was continuous for a 45°x90° configuration, brought about by the long flame fronts that form along the walls of the injector. The presence of the ramp shaped nozzle at the exit side of the combustor is seen to have a very large effect on the creation of NOx. Through small vortices forming at the base of the ramp, pockets of unburned oxygen is trapped that later on forms NOx through various reactions. Figure 35 presents the NO distribution field at the base of the ramp for a 45°x60°. The top part of the figure represents the NO field distribution with ramp present, and the bottom side represents the field distribution of the NO without ramp.

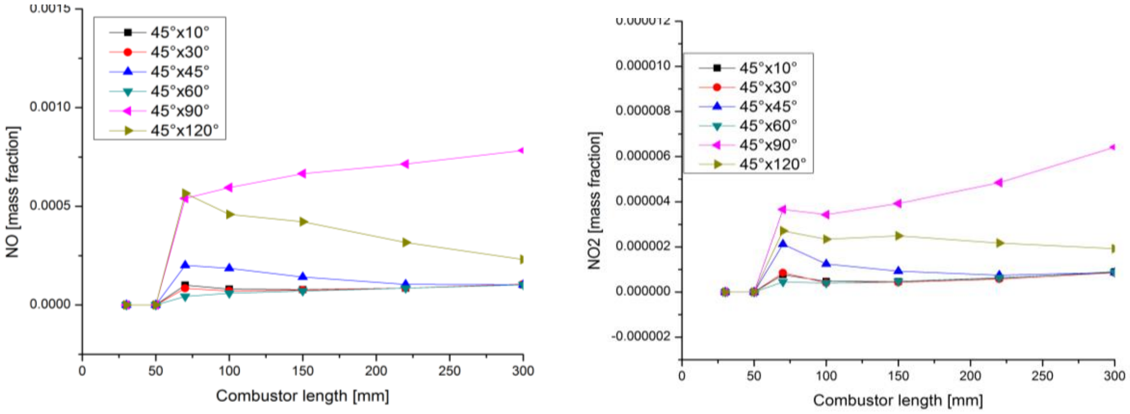

Figure 34 NO and NO2 mass fraction distribution in the combustor

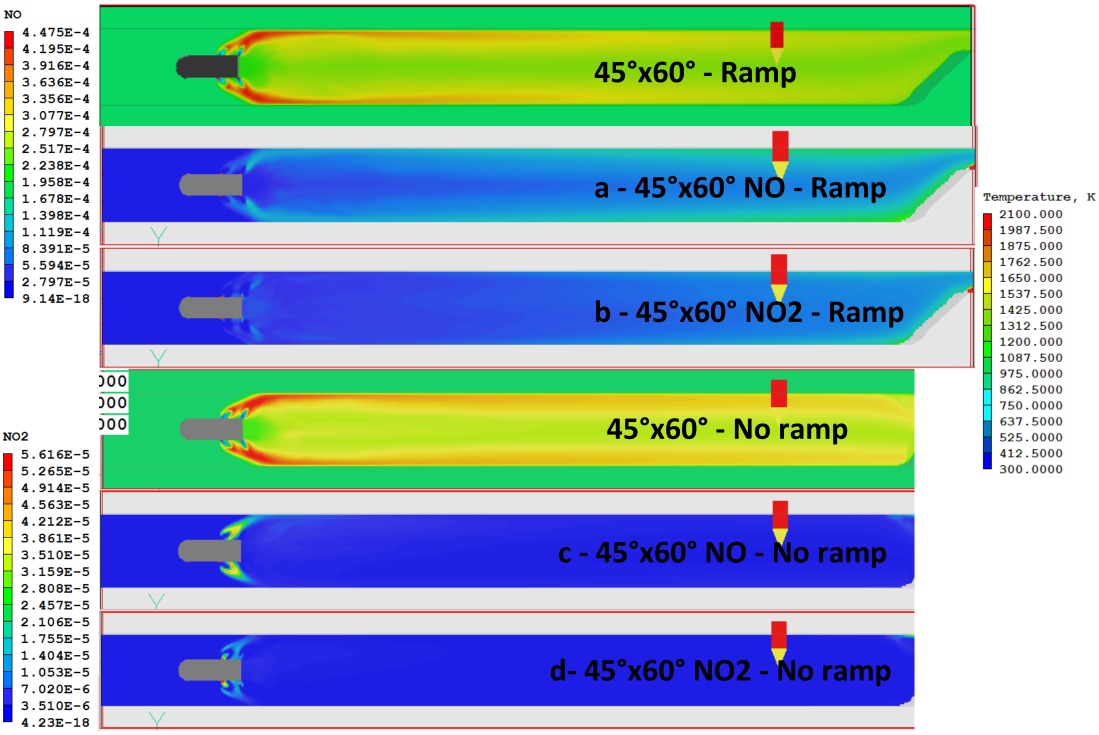

Figure 35 NO field and vector distribution around the ramp base for a 45°x60° fuel-lean configuration

The outlet of the configuration was moved from 390 mm (nozzle) to 350 mm, which stops just before the nozzle. From the figure, we can observe that not only does the presence of the ramp-shaped nozzle have a dampening effect on the flame, where the overall temperature in the combustor is smaller than for the same conditions without a ramp. As a result, the NO and NO2 production is in smaller concentrations for a configuration with a ramp, than without a ramp.

When the EINOx is plotted, for variable downstream angles in Figure 26, denoted by the [red] circles, the EINOx increased with increasing downstream angles. The ramp effect seems to be proportional to the amount of heat released in the chamber. This seems to corroborate the decrease of the EINOx with the "move" of the peak of maximum heat released. An important observation at this time is that the chemical heat release and position of the maximum combustion influences the amount of NO that gets trapped and is produced near the ramp-shaped nozzle. Given that large downstream angles cause the main reaction to occur closer to the injector, this translates as configurations with larger angles downstream tend to generate more NOx.

When the angles on the upstream side are fixed to 60°, presented through the temperature field on the top and velocity vector distribution on the bottom, in Figure 36 and enlarged in Figure 37 where temperature is presented on the left side, and the velocity vector distribution on the right side, larger angles on the upstream induce a larger recirculation zone in the wake of the injector. From a first look we observed that higher upstream angles, cause a hotter flame, a higher temperature of the flame in the combustor and is expected a higher heat loss at the walls.

In Figure 36 and Figure 37-a, when upstream angles are set to 60° coupled with smaller angles on the downstream side, due to the incoming airflow and fast injection velocity of fuel at these small angles, two overlapping flame fronts are observed. As a result, wider flame fronts prevent the formation of a strong recirculation zone in the wake of the injector, inducing it, rather, farther downstream seen in Figure 37-a through the vector distribution field. This means that, due to the presence of these two flame fronts, a region with high temperature is found in the immediate wake of the injector, and due to the fuel being deflected by the upper and lower side walls, a short drop in temperature takes place farther downstream. This can be observed in Figure 38, where the average temperature and heat loss are plotted alongside the combustor length, for variable downstream angles and a fixed upstream angle of 60°.The right side of the Figure 38 shows the heat loss in the combustor. We observe a small peak followed by a slight decrease, which when compared with the black points in the same figure, represent the small drop in temperature as the mixture is reflected by the walls and reacts towards the middle of the chamber.

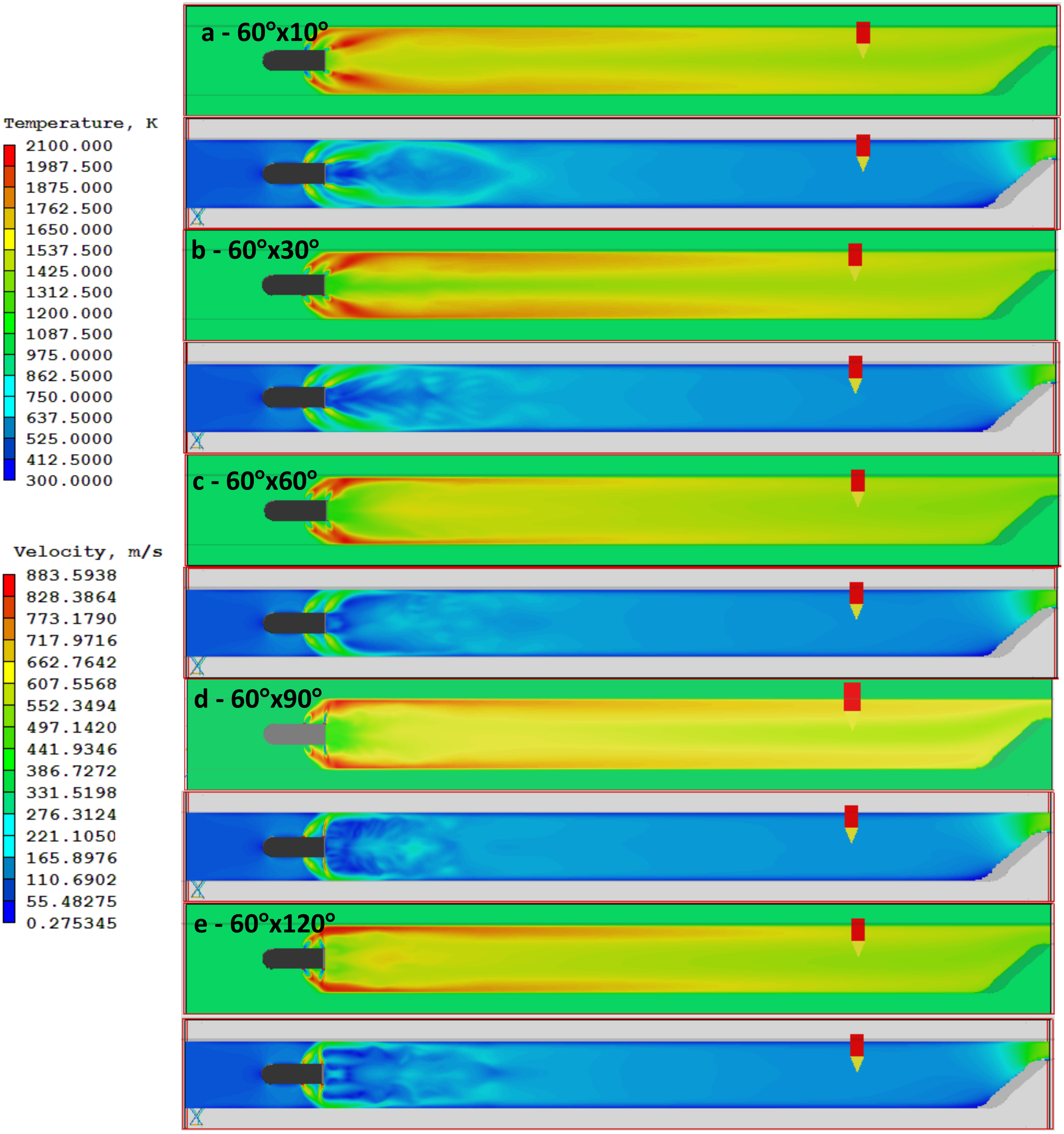

Figure 36 Temperature and velocity distribution field for constant upstream angle of 60° at fuel-lean conditions

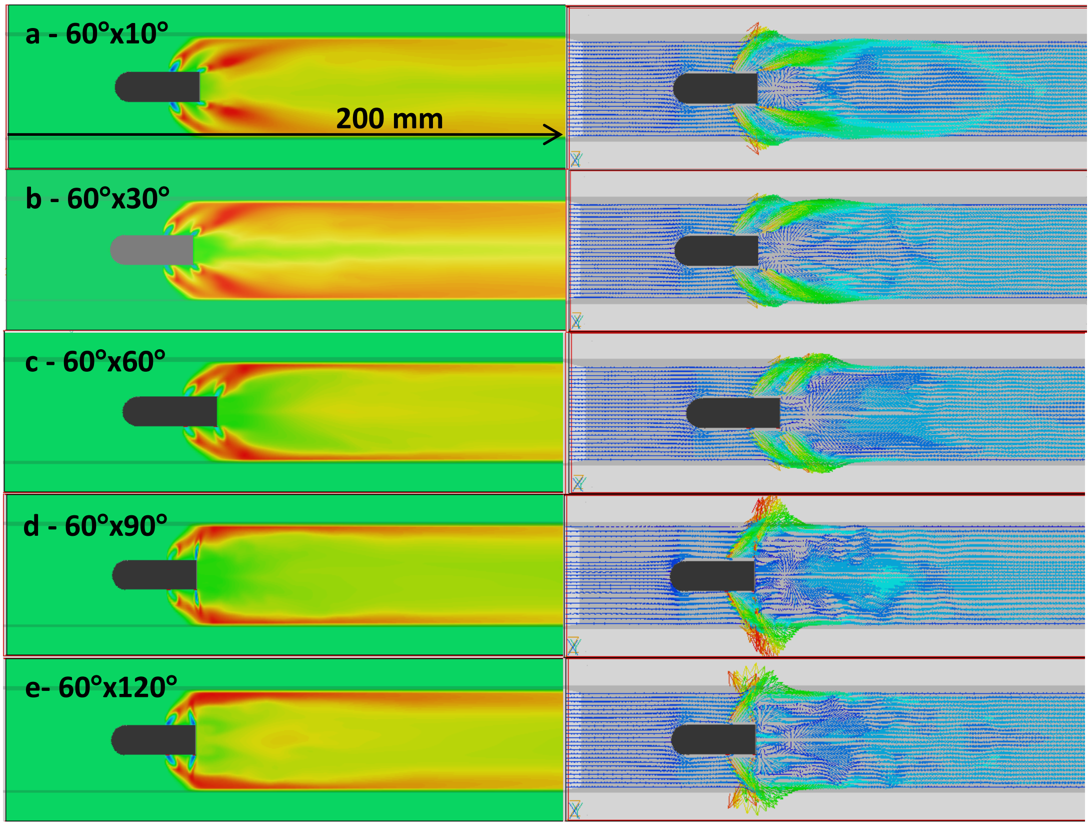

Figure 37 Enlarged temperature field distribution and velocity vector distribution near the injector for constant upstream angles 60°

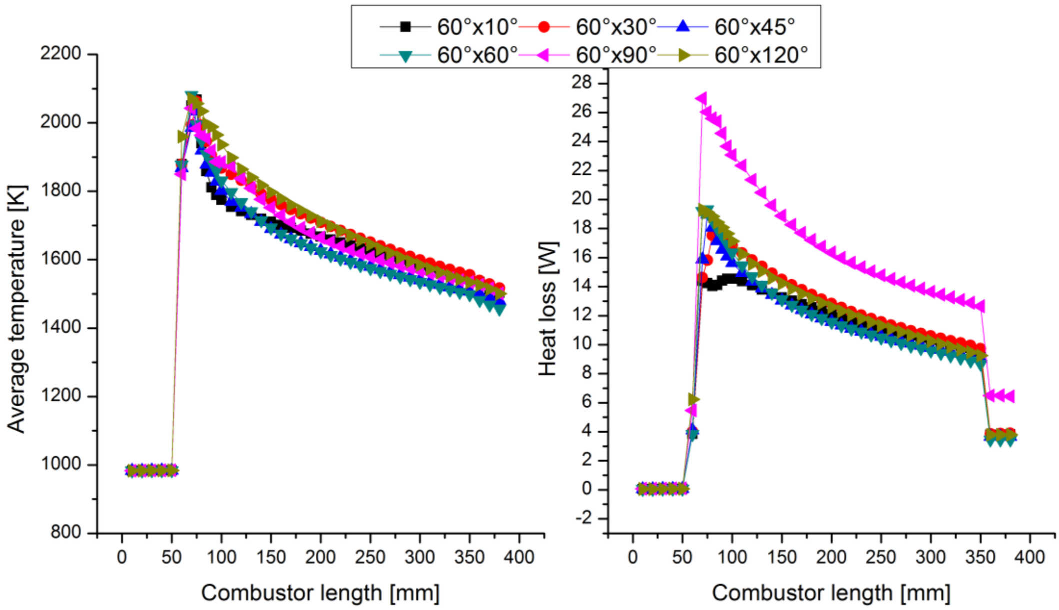

Figure 38 Average temperature (left side) and heat loss (right side) in the combustor for constant upstream 60° and variable downstream angles at fuel-lean conditions

After the small temperature drop, there is a slight increase, as the two fronts unite, easily observed in Figure 37-a, in the velocity vector distribution. There are two peaks for high heat loss, one when fuel injected from the two pair interact around 15 mm from the injector and the other at the top most tangent point of the recirculation zone forming in the wake around 35 mm from the injector. If we consider the temperature gap between the two areas, for this configuration a maximum of 480 K can be observed.

When the angles increase on the downstream side, seen in Figure 36 and Figure 37-b, the larger angles on the downstream side, allow for fuel to be reflected in the combustor faster, in a shorter distance which creates an almost full expanded flame. The average temperature for this configuration, plotted in Figure 38, is slightly smaller, due to a dilution of the mixture induced by the expansion of the flame fronts on the upper side and lower side. However, this front expansion occurred toward the center of the combustor, which allowed for a shorter contact with the walls. As a result, the heat loss decreased downstream of the injector. The maximum heat loss peak is found at 25 mm from the injector, which means that as the angles increased on the downstream, the two peaks observed in the previous configuration, united. The temperature gap found for this configuration is 450 K, a decrease explained by the dilution of the mixture. The local equivalence ratio of the unburned products for a constant upstream angles of 60° and variable downstream angles is presented in Figure 39, where the mixing enhancement can be observed, with increasing downstream angles, by the area under the curve.

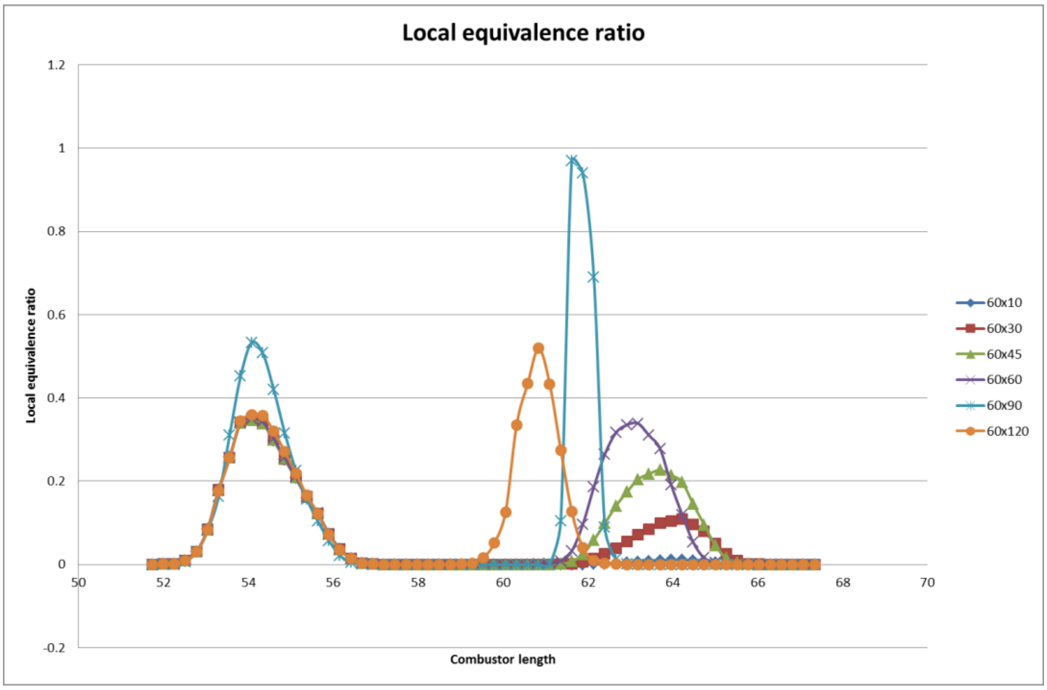

Figure 39 Local equivalence ratio of unburned products for a constant upstream angle of 60° and variable downstream angles at fuel-lean conditions

For a 60°x45° configuration, a similar trend to the previous configuration is observed. The small temperature gap suffered when fuel deflected by the wall flows back into the chamber, diluting the mixture. However, a second reaction zone is observed, when, due to the breaking of the recirculation zone in the wake of the injector, velocity increases and as a result mixing is enhanced. In this second reaction area, while still close to the walls, the higher temperature is actually closer to the middle of the injector, directed by the increase in velocity after the vortices break down, which explains the decreasing heat loss farther downstream in the chamber. Given that a large amount of fuel is pushed towards the walls, and most of the reaction takes place there, seen in Figure 36 and Figure 37 by the strong red flame fronts along the walls, heat loss is increased, the resulting flame being characterized by the burned gases. The peak of maximum heat loss peak, for this configuration is similar to the previous case seen in Figure 38.

For a 60°x60° configuration seen in Figure 36 and Figure 37-c, similar flow behavior is observed as in the previous configuration. What changes, however, are, the size of the recirculation zone, and the connection of the flame fronts. As the angles increase, the eddy forming in the wake of the injector is larger but its epicenter is located closer to the injector, which leads to the second reaction area to "move" closer to the as in the previous configuration when angles were fixed at 45° on the upstream. In Figure 38, the average temperature follows the same trend as the previous configuration however, at a smaller temperature. Since the mixture expands in the combustor, the heat loss is seen to decrease downstream observed on the right side of Figure 38. The temperature gap measured for this configuration increased to almost 580 K.

When the downstream angles are increased to 90°, a direct effect of this is larger heat loss associated, as more fuel is injected directly at the walls observed in Figure 38 on the right side. Another effect is that the recirculation zone in the wake of the injector breaks down into many smaller vortices, observed in Figure 36 and Figure 37-d, due to the large angles on the upstream and downstream side. After these smaller vortices, the two flame fronts connect and consume the amount of unburned fuel that remained. The maximum heat loss peak is found where the maximum temperature is recorded, due to the perpendicular injection and the temperature gap measured is found to be around 500 K, observed in Figure 38.

When the downstream angle is increased to 120°, seen in Figure 36-e and Figure 37-e, the smaller vortices, which formed in the recirculation zone, due to large angles on the upstream side, the flow velocity decreased. As a result, vortices arrange into symmetrical shapes alongside the axial direction. This can be seen in Figure 40. As a result, the flame is fully developed in the wake of the injector. A slight effect of the asymmetry of chamber, induced by the presence of the ramp, is seen on the flame, when velocity is slightly increased on the lower side of the combustor.

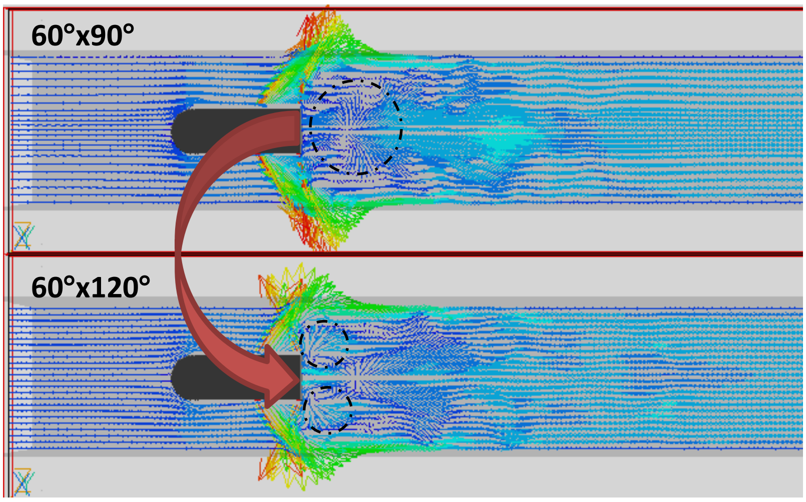

Figure 40 Eddy formations for 60°x90° and 60°x120° configurations at fuel-lean conditions

From the temperature distribution fields in Figure 38 plotted for length of the combustor, we can observe a similar trend with the previous upstream configurations. The temperature gap measured for these configurations reaches a maximum of varied between 500 and 580 K. In comparison with the previous configuration, an increase in upstream angles creates hotter flame fronts on the sides, which through velocity and wall effects, connects in the middle and the mixture is diluted.

Figure 41 presents the chemical heat release plotted for constant upstream angles of 60° and variable downstream angles. When the upstream angles were kept constant at 60°, the heat release in the chamber is constant for angles up to 60°, when, due to the wall effect, the mixture expands in the chamber, and is diluted, as it encounters unburned oxygen. However, as the angles increase past this value, an increase in heat release is seen due to perpendicular injection.

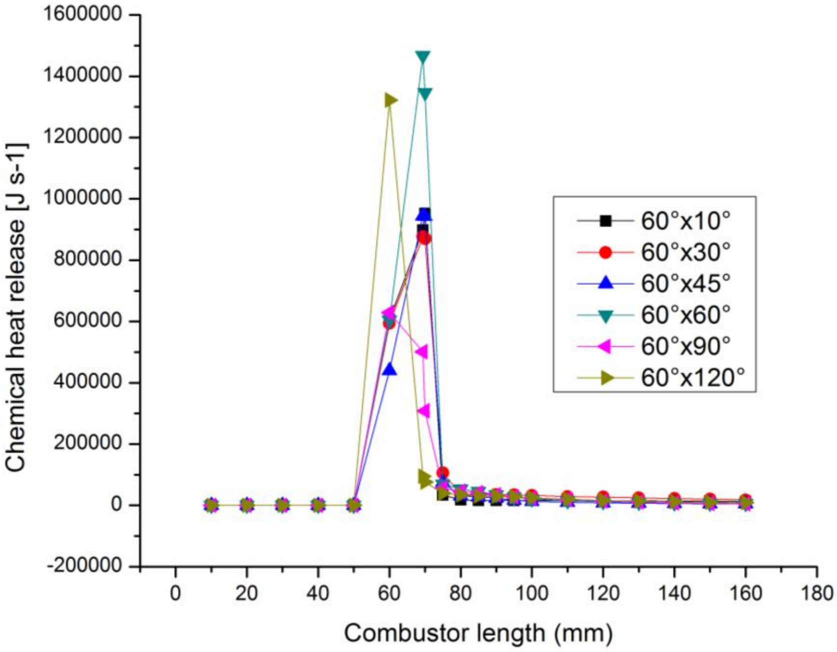

Figure 41 Chemical heat release for constant 60° upstream angles at fuel-lean conditions

The combustion takes place along the walls of the combustor, however, when angles on the downstream side are larger than 60°, due to the vortex breakdown in the recirculation area, first smaller vortices formed which increased heat loss for 60°x90° and later for 60°x120°, due to the up flow injection, the vortices arranged in a symmetrical way in the wake of the injector which increased the local equivalence ratio.

In Figure 21, the total heat loss in the combustor is plotted for variable downstream angles with a fixed upstream angle of 60°, shown by the [blue] triangles. As the angles increase on the downstream, the flame fronts near the walls reach higher temperatures which generate more chemical heat, part of which is lost at the walls. Due to the vortex breakdown suffered by the large angles, mixing is inhibited. This inhibited mixing lowers the heat loss suffered at the walls for large angles downstream i.e. 120°. The total heat loss is seen to increases as the angles increase on the downstream side until 60° on the downstream. After this value, fuel is injected direct at the walls and is reflected in the chamber which although locally generate higher heat loss, in total the heat loss is lowered.

Figure 42 presents the combustion efficiency for constant upstream angles of 60° and combustor length on the right side using the enthalpy approach (-a), the left side presents the chemical heat release approach (–b). The combustion efficiency follows the same trend as in the previous configuration.

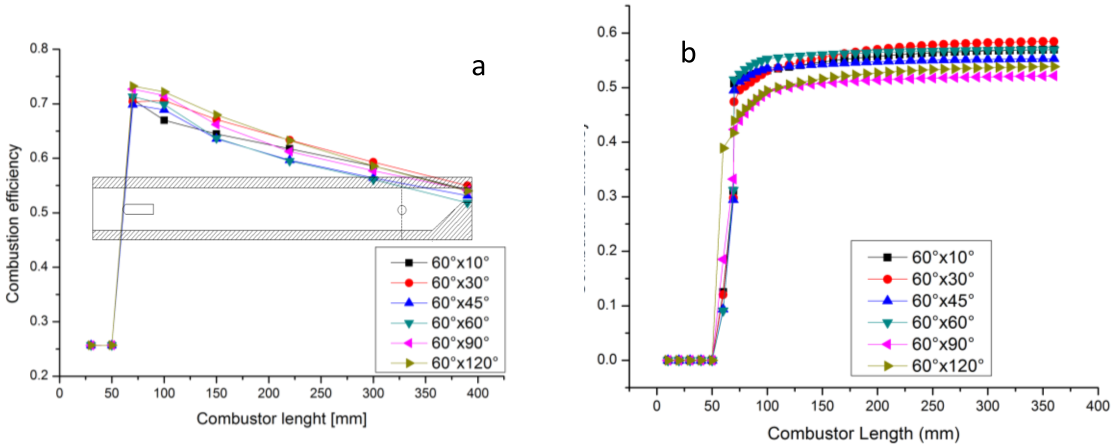

Figure 42 Combustion efficiency for constant upstream 60° angles at fuel-lean conditions; a- enthalpy difference approach, b- heat release approach

However, in comparison with the previous configuration, we observed that at larger angles downstream, hotter flame fronts exist and later are deflected from the walls decreases mixing and are responsible for vortex breakdown in the wake of the injector. As a result, the combustion efficiency recorded near the nozzle area varies only 5 % with the angle configuration.

In Figure 43 the overall combustion efficiency near the nozzle is plotted for variable downstream angles. The nozzle modification is small; the temperature and heat loss effect on the nozzle is small. However, as angles increase on the downstream pair, the combustion efficiency decreased.

Figure 44 presents the NO and NO2 mass fraction plotted in the length of the combustor for variable downstream angles at a fixed upstream angles of 60°. When the angles increase downstream, as the flame fronts are longer and concentrated along the walls, the NO is increasing in the chamber, as the residence time of the mixture along the walls is longer, and pockets of oxygen are found. The NO peaks around the middle of the combustor and as the reaction proceeds downstream, the NO decreased. The NO2 follows a similar trend although in a much smaller degree. When the angles downstream are increased past this value to 90° and 120°, due to vortex breakdowns that occurs in the wake of the injector, smaller vortices create and consume the available NO and NO2, which overall in the chamber, contributes to the dissociation of NO and NO2. As in the previous configuration, the presence of the ramp shaped nozzle at the exit side of the combustor is seen to have a very large effect on the creation of NOx. Through pockets of unburned oxygen coming together in a smaller area, NOx is enhanced.

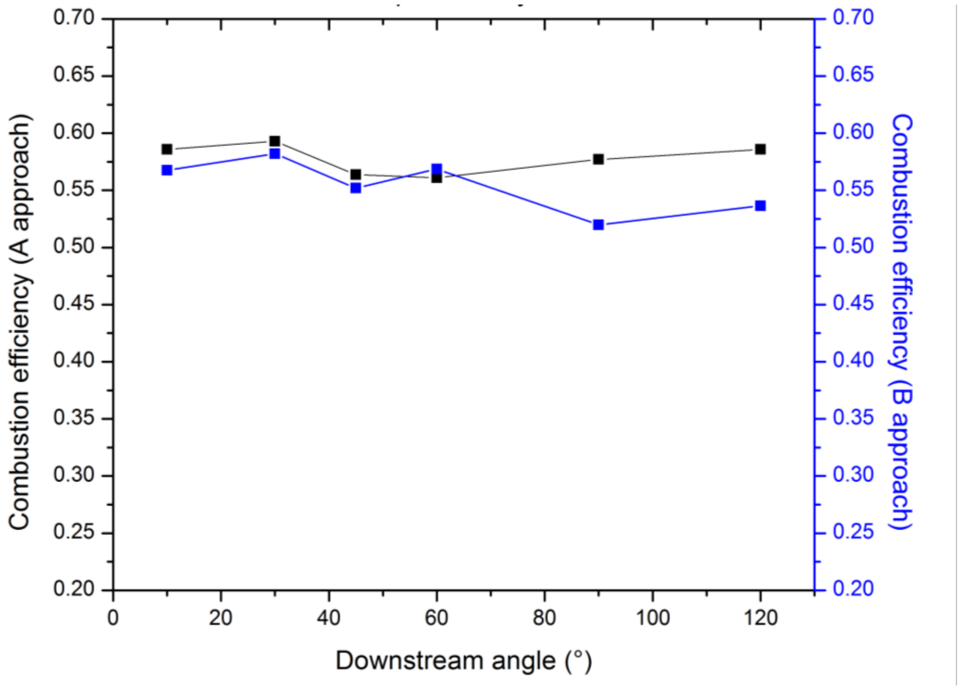

Figure 43 Overall combustion efficiency using the two approaches, enthalpy difference (black line) and chemical heat release (blue line) for constant upstream angles of 60°

When the EINOx is plotted, for variable downstream angles in Figure 26, shown by the [blue] triangles, the EINOx increased with 30°, and evened out for the range of increasing downstream angles, later decreasing for a 120° on the downstream. The EINOx increased in the first part due to an expansion of the flame in the chamber, thus enhancing mixing and allowing for the mixture to react with oxygen found there. However, as the angles increased, which as a result, caused the flame fronts to be concentrated in thinner reaction zones, which form alongside the walls.

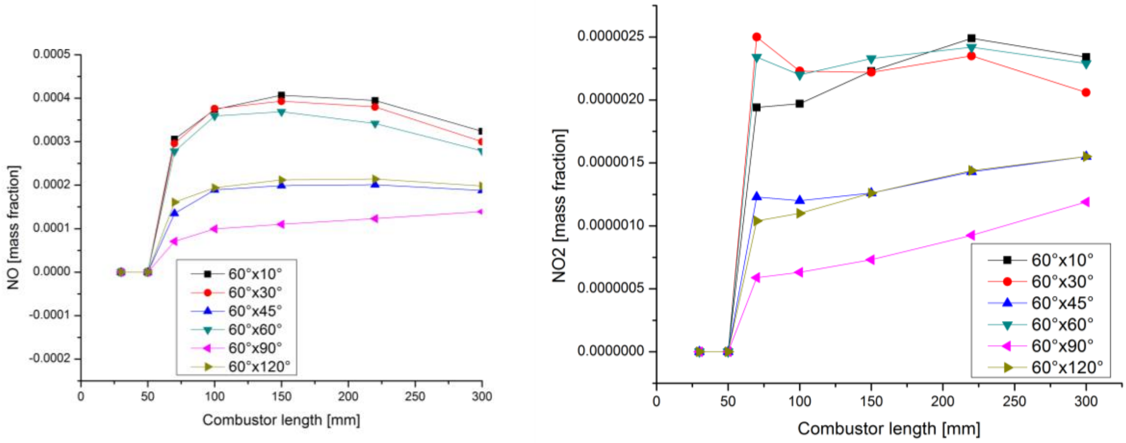

Figure 44 NO and NO2 mass fraction distribution in the combustor

This smaller reaction zone diluted the mixture which led to the creation of smaller amounts of NOx. However, when angles increased to 60° and 90°, the flame fronts on the upper side and lower side, although, still had the same shape, the temperature had higher values. This means that they were longer and the NOx amount increased. When the angles on the downstream side were set to 120°, due to breaking of the recirculation zone in the wake of the injector, the NOx was formed and diluted before reaching the nozzle, which as a result, lowered the overall NOx values recorded through the EINOx.

4.4.1.2. Constant downstream combustion

Figure 45 presents the temperature (on the top) and velocity distribution field (on the bottom) for constant downstream angles of 30°. In Figure 46 the enhanced views of temperature fields (on the left side) and velocity vector distribution (on the right side) for the constant downstream angle of 30° are presented. In Figure 45, from –a, to -f, the downstream angles increase from 10° (Figure 45-a) to 120° (Figure 45-f). For fixed downstream angles and variable upstream angles, the flame shape changed substantially. It starts as two small flame fronts seen in Figure 45 and Figure 46-a, that adhere to the sides of the injector due to (1) flow axial velocity and (2) large injection velocity of fuel coming from the upstream injection pair. As the angles increase, the flame still supports two flame fronts, but this time they are spread over larger reaction areas, generating wider flame fronts, and expand in the chamber, seen in Figure 45 and Figure 46-b. this trend continues for upstream angles from 30° to 60°, where the representing factor is that the flame fronts become thicker, and hotter, seen in Figure 45 and Figure 46-c and –d. When the angles are set to 90° on the upstream side, the perpendicular injection is clearly observed through the flame shape and the flame is separated into the 4 flame jets coming from the injection holes and later uniting on the upper side and lower side walls. Due to the recirculation zone forming in the wake of the injector due to the large angles on the upstream, the flame fronts expand in the chamber farther downstream, diluting the mixture and lowering the flame temperature, seen in Figure 45 and Figure 46-e. For upstream angles on 120°, seen in Figure 45 and Figure 46-f, due to the up-flow injection of the upstream angles, due to a recirculation zone, forming at the base of the upstream injection holes, the flame fronts do not connect, creating separate, short flame fronts, limiting the reaction zone to only around the injector area.

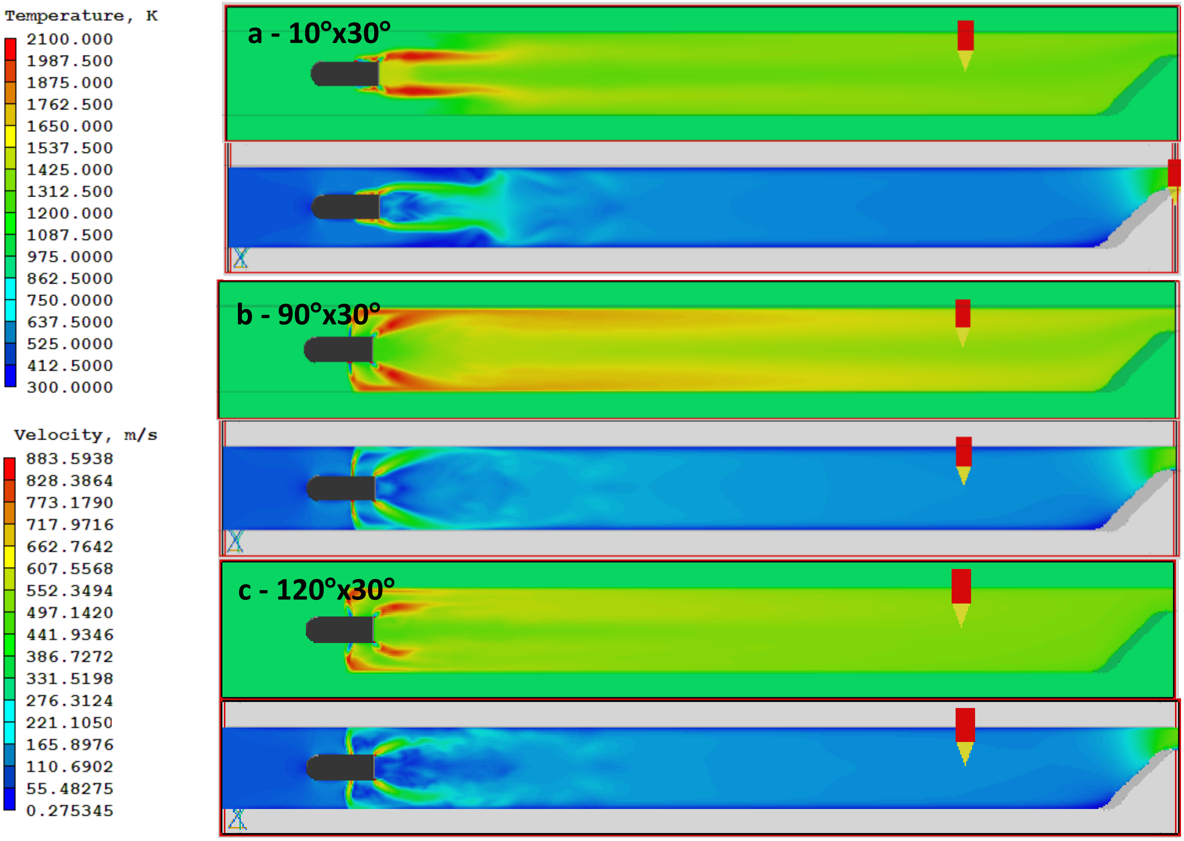

Figure 45 Temperature and velocity distribution field for constant downstream angle of 30° at fuel-lean conditions

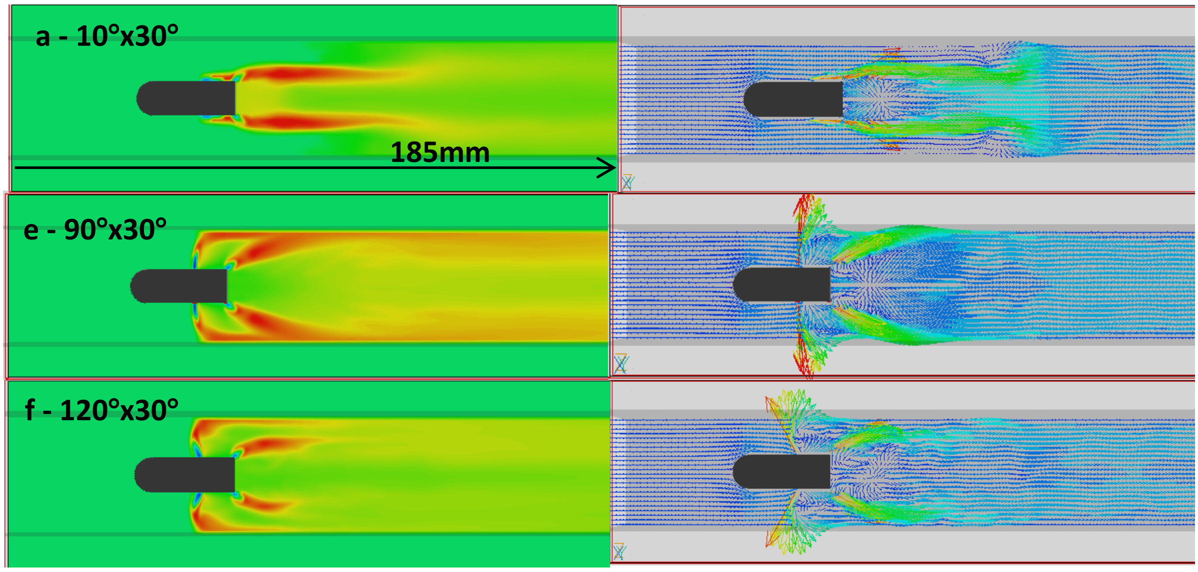

Figure 46 Enlarged temperature field distribution and velocity vector distribution near the injector for constant downstream angles 30°

For a 10°x30° configuration, seen in Figure 45 and Figure 46-a, the flame is concentrated near, and around the injector. Given the flow axial velocity and large injection velocity of fuel coming from the upstream injection pair, the flame is concentrated in the axial direction on the upper and lower sides of the injector. The average temperature and heat loss in the combustor for this configuration is plotted in Figure 47.

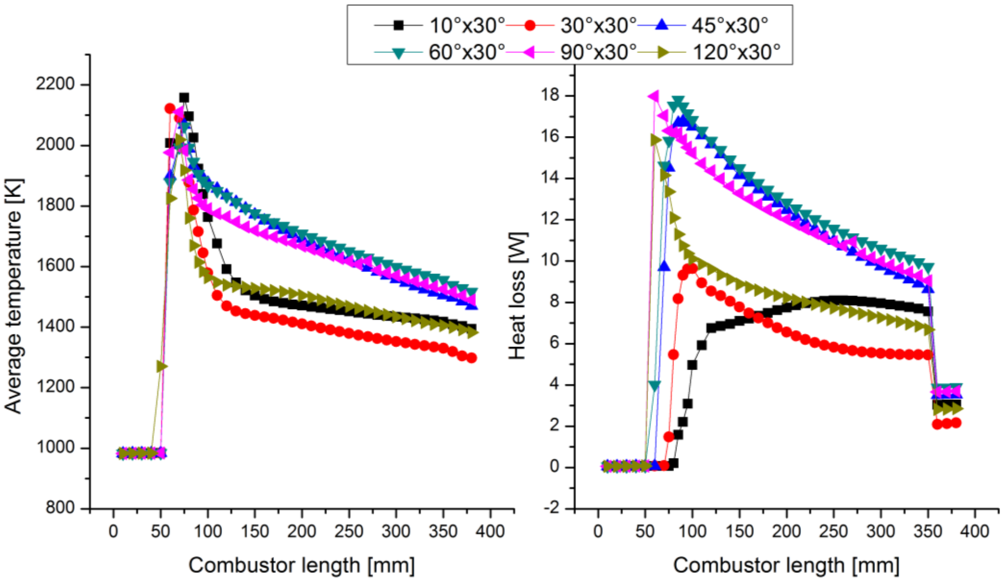

Figure 47 Average temperature (left side) and heat loss (right side) in the combustor for constant downstream 30° and variable upstream angles at fuel-lean conditions

Due to the low equivalence ratio, and small angles on the upstream side, fuel is carried in the axial direction, downstream, having little contact with the walls of the chamber. As a result the heat loss increases at the walls from the expanding heat in the chamber, increasing to a plateau near the nozzle. When the upstream angles increase to 30°, 45° and 60°, the effect is presented in the previous section 4.4.1.1.

When the angles are set to 90° upstream shown in Figure 45 and Figure 46-b, the perpendicular injection is clearly observed through the flame shape and the flame is separated into the 4 flame jets coming from the injection holes and later uniting on the upper side and lower side walls. For large angles on the upstream, and the presence of vortices on the lower side and upper side of the injector, small vortices start forming at the base of the injection holes, which create a cold region between the fuel injected from the upstream injection holes and the one coming through the downstream injection holes. These small vortices are shown in Figure 48, where velocity vector distribution is presented for comparison reasons for a 60°x30° and 90°x30°.

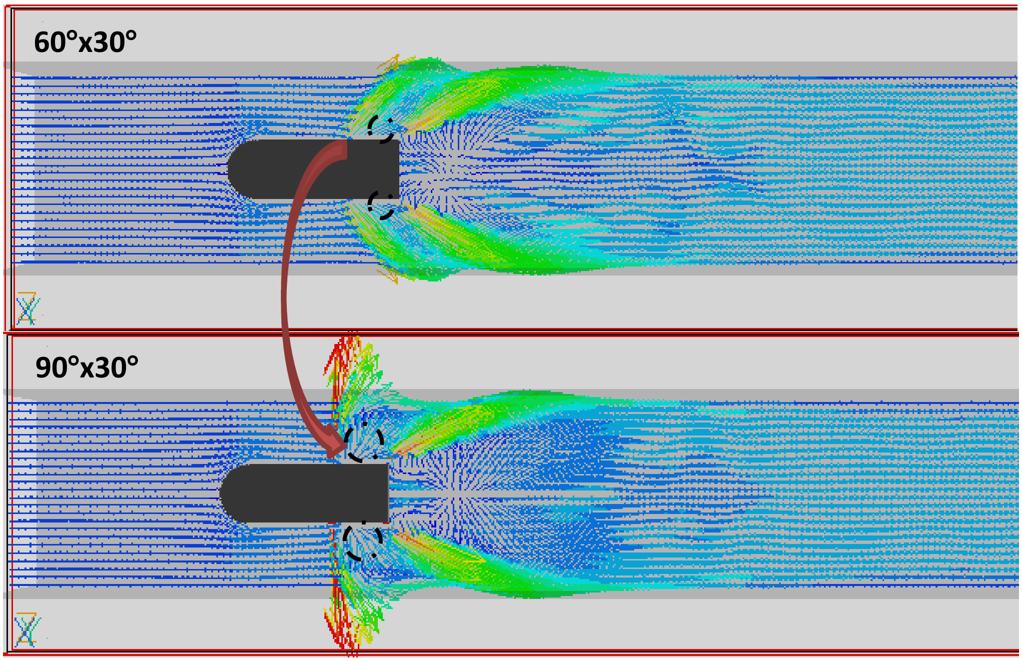

Figure 48 Eddy formations between injection holes for a 60°x30° and a 90°x30° configuration at fuel-lean conditions shown through velocity vector distribution

Due to the recirculation zone forming in the wake of the injector caused by large angles on the upstream, the flame fronts expand in the chamber farther downstream, diluting the mixture and lowering the flame temperature, seen in Figure 46 and Figure 47-b. The perpendicular injection increases the heat loss at the walls and as the mixture proceeds downstream, the heat loss decreases with the decrease of temperature of the flame, shown in Figure 53 through the average temperature and heat loss plot.

For upstream angles on 120°, seen in Figure 46 and Figure 47-c, the vortices that form in between the injection holes enlarge, and through their size, prevent from the flame fronts to combine, lowering the temperature and combustion efficiency. These small vortices start forming at the base of the injection holes for a 90°x30° configuration and later growing in size, move towards the upper and lower side walls of the combustor, creating a colder region of no combustion. The average temperature and heat loss in the combustor for 120°x30° configuration is presented in Figure 49. The combustion takes place in separate flame fronts, and after all the fuel is consumed locally, the temperature drops in the wake of the injector. The heat loss is highest, near the upstream injection holes, due to the large angle of injection, after which, it decreased. The average temperature in the chamber is plotted for the entire combustor at variable upstream angles and a fixed upstream angle of 30° in Figure 47. From the temperature plot, we see that the maximum temperature is almost similar for all configurations, however, the effect of the upstream angles is much more pronounced, especially for high upstream angles when the temperature drop is large. The temperature gap for a fixed upstream angle varied from 500 to 700 K.

In Figure 49, the chemical heat release is plotted for constant downstream angles of 30°. When the upstream angles were kept constant, the trend was an increase in heat release as the downstream angles became larger. It can be seen that most of the combustion took place near or around the injector and not towards the nozzle area. The heat release increases as the angles increase on the downstream. When the angles on the upstream side increase to larger values (>60°), the chemical heat release decreases as the flame spreads in the chamber, due to the flow configuration. As that happens, the local equivalence ratio decreases, shown in Figure 50 which decreases the heat release.

The heat release seems to have the highest value for a 10°x30° and 30°x30° configurations when, due to injection configuration, fuel is injected in the axial direction, maximizing the spread and enhancing the mixing. For the other configurations, it seems that although large angles affect the flame shape, most of the reaction takes place in the same place with similar chemical heat release.

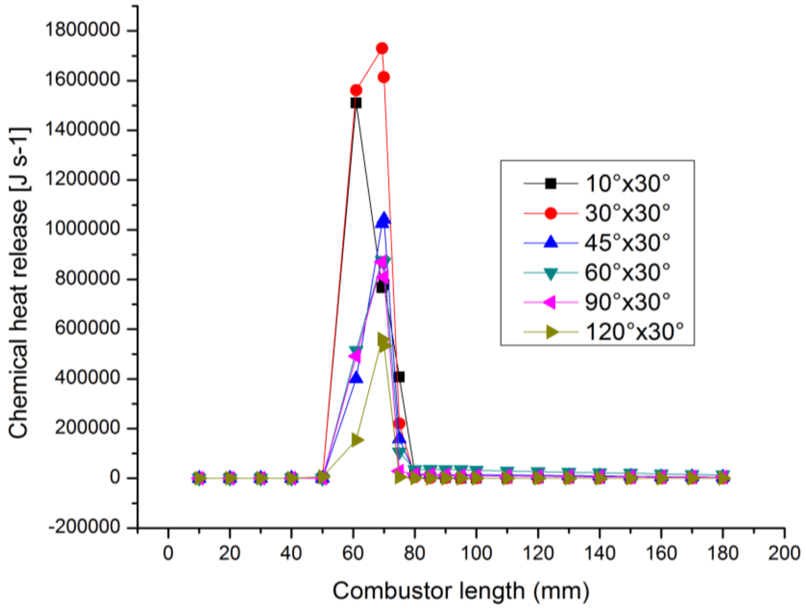

Figure 49 Chemical heat release for constant 30° downstream angles at fuel-lean conditions

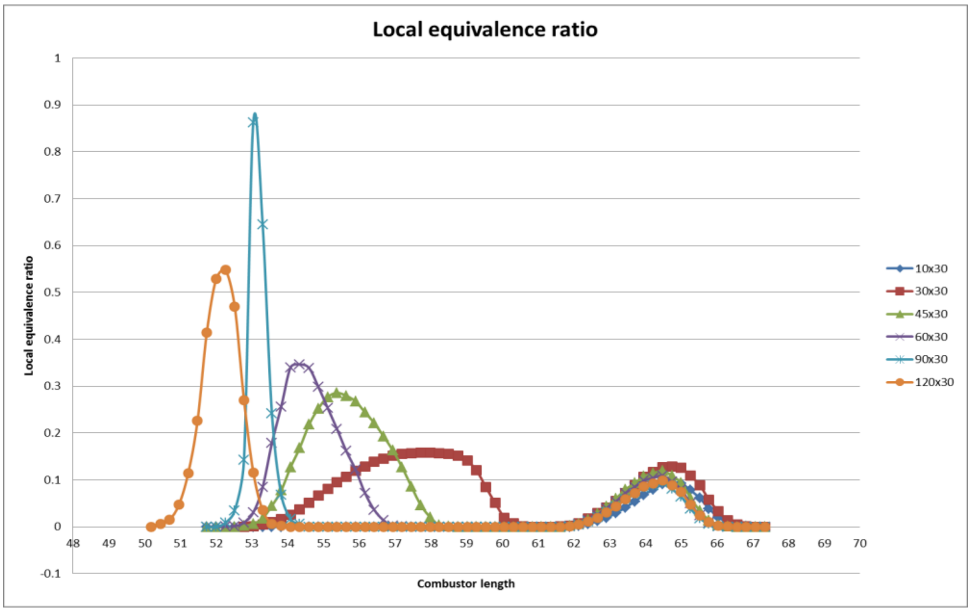

Figure 50 Local equivalence ratio of unburned products for a constant downstream angle of 30° and variable upstream angles at fuel-lean

Figure 51 presents the total heat loss plotted this time for the variable downstream angles. The total heat loss is seen to increases as the angles increase on the upstream side, similar with the previous configurations. For constant downstream of 30°, the increasing angles on the upstream side by pushing more fuel towards the walls, increase the mixture's contact with the walls of the combustor. The increase however is only seen for upstream angles higher than 45°, due to the shape of the flame. As the angles increase to a perpendicular injection, and as a result of the vortices forming between the injections holes, the heat loss decreased.

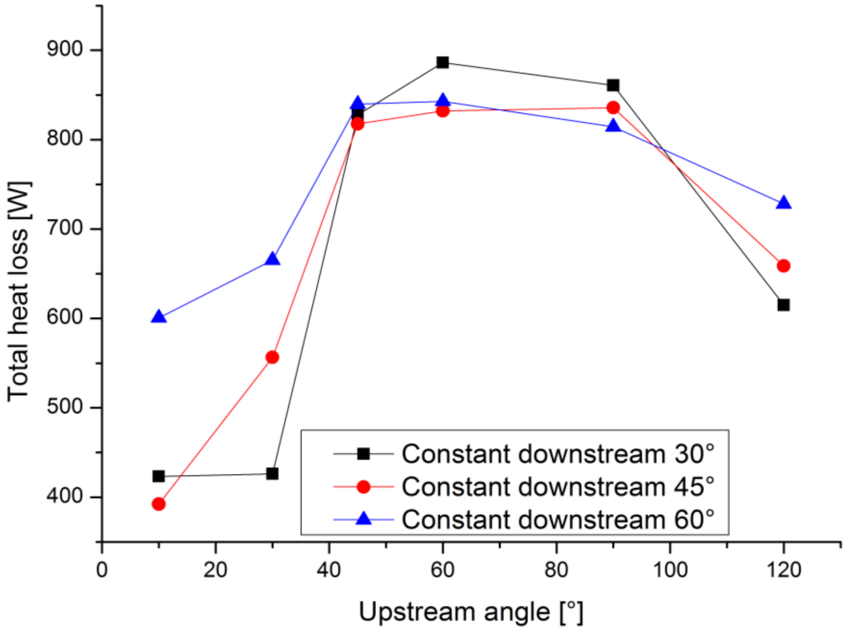

Figure 51 Total heat loss for constant downstream angles and variable upstream angles at fuel-lean conditions; [black] squares – upstream 30°,[red] circles – upstream 30°,[blue] triangles – upstream 30°

Figure 52 presents the combustion efficiency for constant downstream angles of 30° and combustor length on the right side using the enthalpy approach (-a), the left side presents the chemical heat release approach (–b).

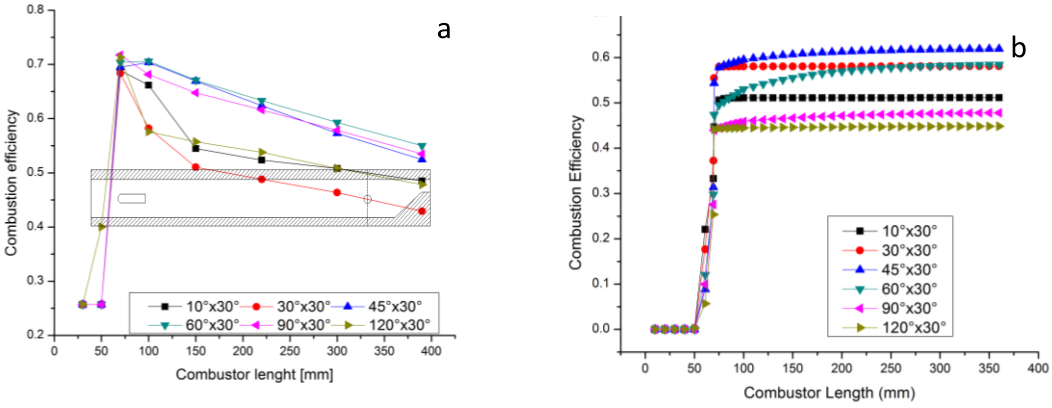

Figure 52 Combustion efficiency for constant downstream 30° angles at fuel-lean conditions; a- enthalpy difference approach, b- heat release approach

While the combustion efficiency set through the enthalpy approach, seen in Figure 52-a, small angles on the upstream create a concentrated flame near the injector. When angles increase on the upstream and the local equivalence ratio increased, the temperature of the flame is more uniform, with a higher combustion efficiency and higher heat loss. The configuration 30°x30°, however, shows a dip in combustion efficiency. From Figure 45 and Figure 46-a, and –b, the flame becomes thicker, with fuel being injected almost parallel. This decrease in temperature, and subsequent combustion efficiency, is related to the fact that when the flame fronts enlarge, the flame expands in the chamber, which in turn lowers the local equivalence ratio and the temperature drops relatively faster.

Figure 53 presents the overall combustion efficiency plotted for variable upstream angles when the downstream angles are constant to 30°.

When the upstream angles are increased, the combustion efficiency increases, however only to a point. A maximum value is seen when flame fronts are larger, observed in Figure 45 and Figure 46. Beyond this angle configuration, when upstream angles increase, the scale of the recirculation zones, induced by these larger angles, inhibits the mixing and lower the combustion efficiency.

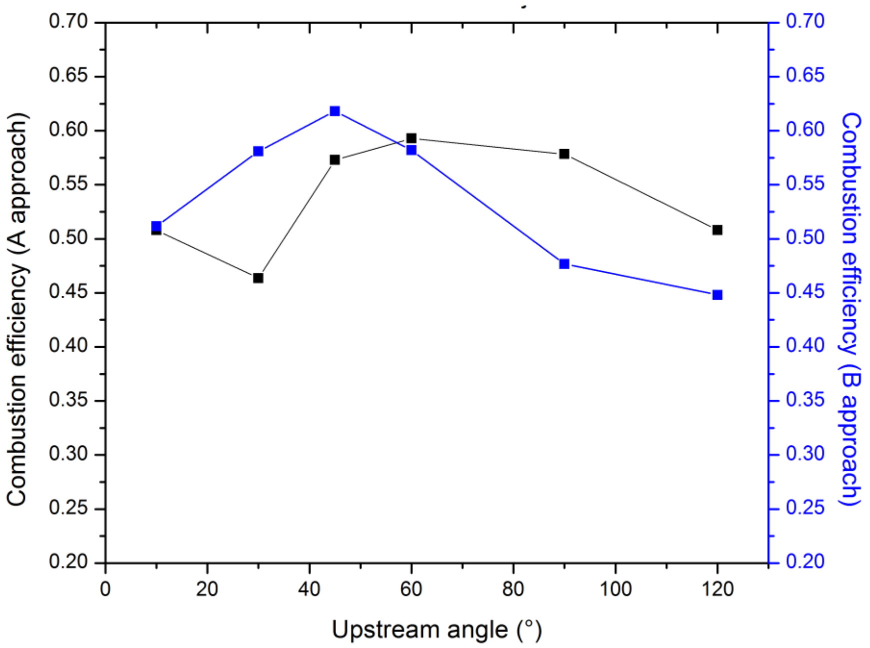

Figure 53 Overall combustion efficiency using the two approaches, enthalpy difference (black line) and chemical heat release (blue line) for constant downstream angles of 30°

Figure 54 presents the NO and NO2 mass fraction plotted in the length of the combustor for variable upstream angles at constant downstream angles of 30°. The NO forming from upstream angles seems to be independent from changing upstream angles, with a single exception. For a 60°x30° configuration has an increased production of NO and NO2 due to the flame shape. The angled configuration allows for an almost engulfing flame, that enhanced mixing, and through the recirculation zone in the wake of the injector, through the added local turbulence, enhances the production of NOx.

When the EINOx is plotted, for variable upstream angles, in Figure 55, the EINOx follows a similar trend to the evolution of the total heat loss and combustion efficiency presented in Figure 52 and Figure 53. Since the NO and NO2 created in the chamber have little changes with the upstream angles, the bulk of the NOx recorded at the nozzle are given by the influence of the ramp. When local velocity increased, more NOx created by the various configurations, has been multiplied. The effects are shown in the figure below.

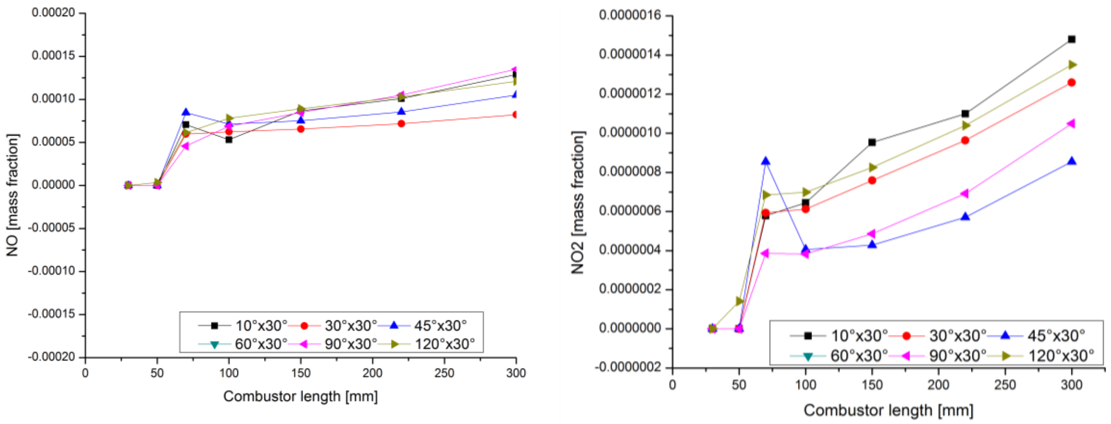

Figure 54 NO and NO2 mass fraction distribution in the combustor for constant downstream angles fixed at 30°

When angles are increased on the upstream, for the first configuration, the angles have little effect on the creation of NOx. However, when the fuel injected from both injection holes mixes and expands in the chamber, the local temperature is raised and the combustion efficiency increased. Having a hotter flame, that covered a larger part of the chamber, through available oxygen in the center of the flame, NOx were created, seen with an increase of the EINOx at the nozzle. When the angles increased to 90° and 120° on the upstream, due to the rarefication of the flame, and subsequent dilution, the NOx production was inhibited and the resulting EINOx decreased.

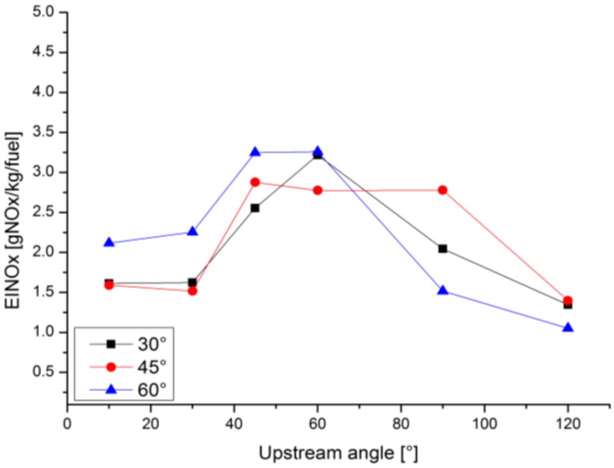

Figure 55 EINOx for constant downstream angles and variable upstream angles at fuel-lean conditions; [black] squares – upstream 30°,[red] circles – upstream 30°,[blue] triangles – upstream 30°

Through constant downstream angles, we have seen that the upstream angles have little influence on the production of NOx, where the bulk of the NOx was created as a result of the ramp shaped nozzle.

When the angles are increased on the downstream side to 45°, as observed in Figure 56 and Figure 57 through respective temperature (on the top and left side) and velocity vector distribution fields (on the bottom and the right side), the effect is similar to that of the above case only more pronounced. Fixed larger angles on the downstream with increasing angles on the upstream create a larger flame, that due to the large angles downstream, flow is reflected from the walls and flame temperature is affected farther downstream in the chamber.

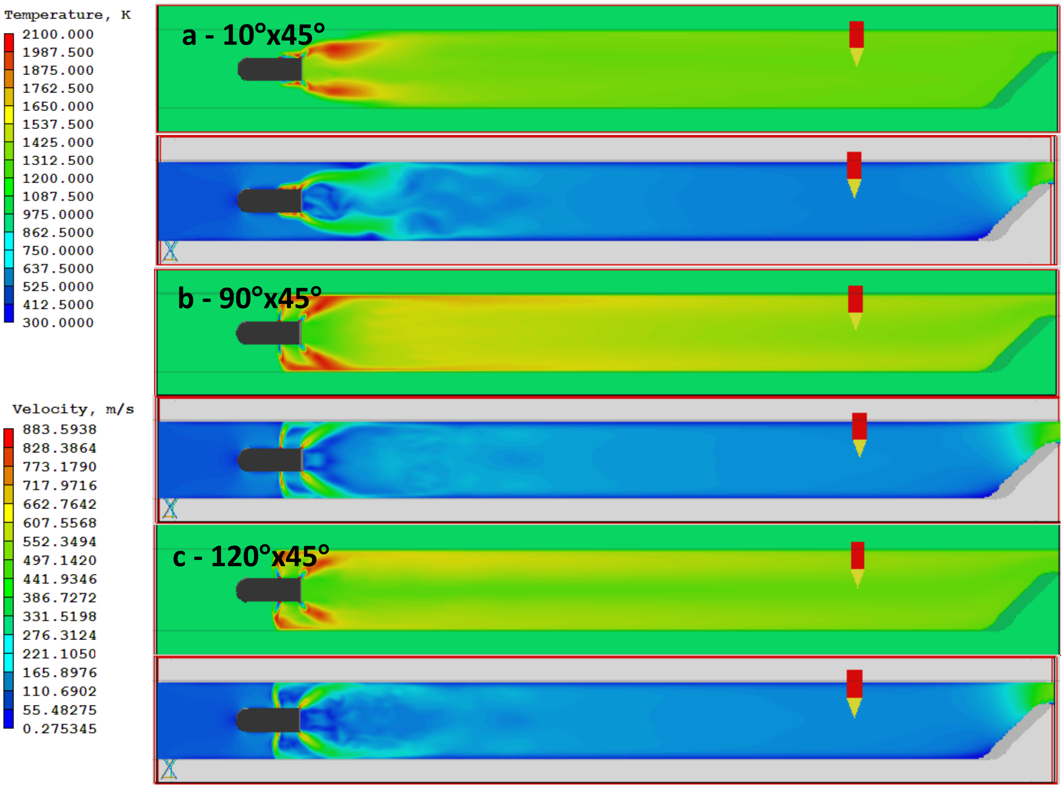

Figure 56 Temperature and velocity distribution field for constant downstream angle of 45° at fuel-lean conditions

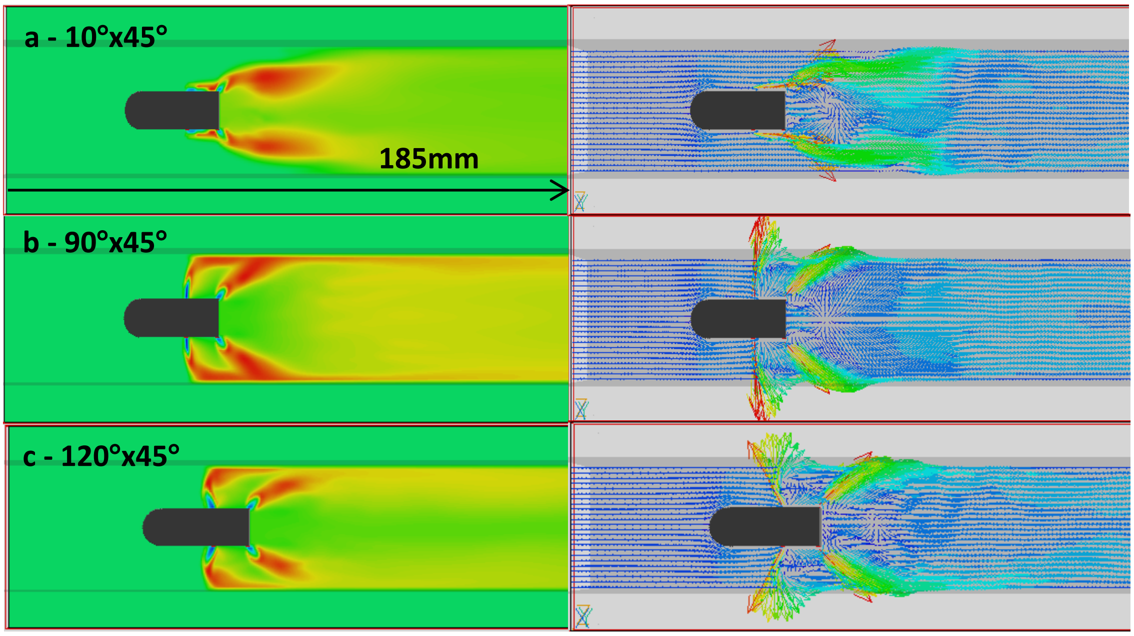

Figure 57 Enlarged temperature field distribution and velocity vector distribution near the injector for constant downstream angles 45°

For a 10°x45° configuration, seen in Figure 56 and Figure 57-a, the flame is concentrated near, and around the injector and shaped by the axial velocity of the flow, and large injection velocity of fuel coming from the upstream injection pair. The effect of larger angles downstream, compared with the previous configuration is seen as larger flame fronts that, are limited in flame width, shown in Figure 56, by the air axial velocity and upstream holes injection velocity.

As seen in Figure 60, the flame fronts on the upper side and lower side are more diffusive which yield a lower local temperature. The average temperature for these two configurations is shown plotted for the length of the combustor, in Figure 59.

The fuel mixes near the downstream side and is consumed farther on. As the flame proceeds in the chamber, the temperature drops to a plateau value. The heat loss increases at the walls from the expanding heat in the chamber, increasing to a plateau near the nozzle.

When the upstream angles increase to 30°, 45° and 60°, the effect is presented in the previous section 4.4.1.1.

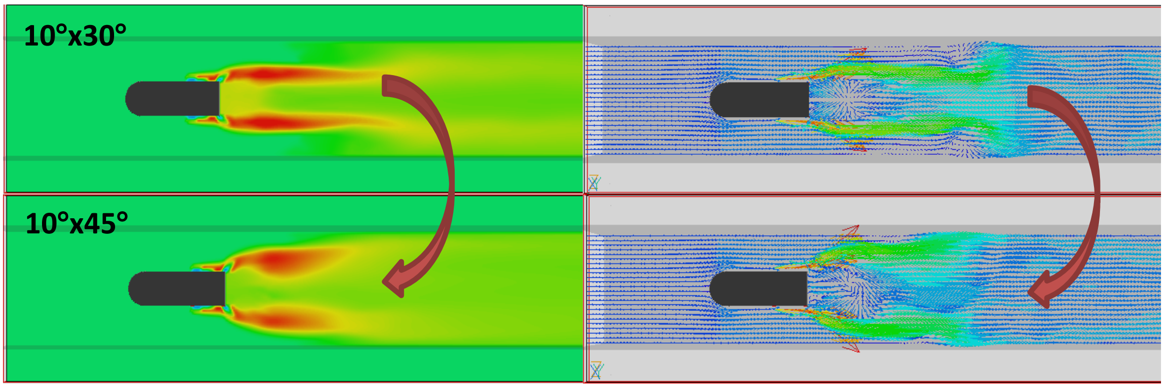

Figure 60 Enhanced temperature and velocity vector distribution fields for 10°x30° and 10°x45° at fuel-lean conditions

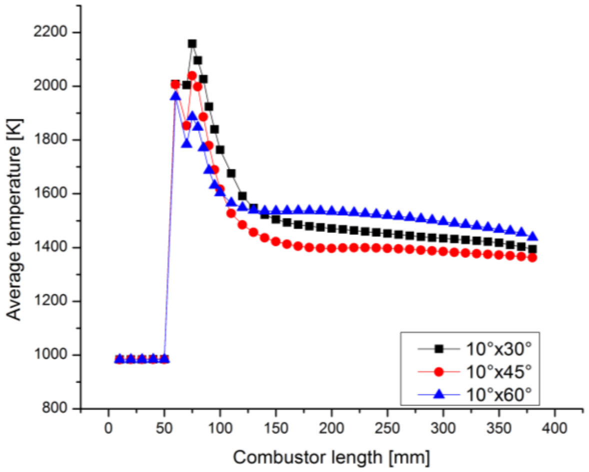

Figure 59 Average temperature in the combustor for 10°x30° (black points), 10°x45° (red points) and 10°x60° (blue points) at fuel-lean conditions

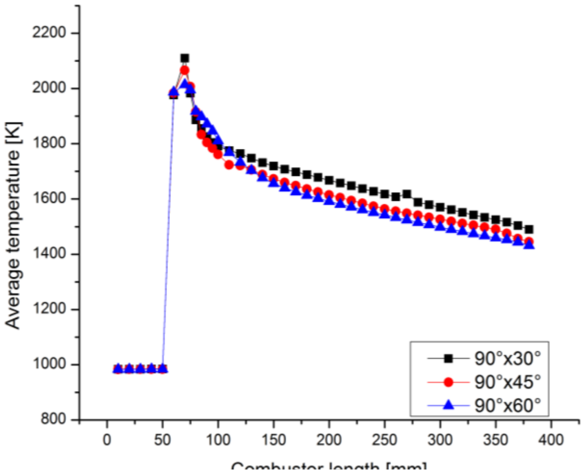

Figure 58 Average temperature in the combustor for 90°x30° (black points), 90°x45° (red points) and 90°x60° (blue points) at fuel-lean conditions

When the angles are set to 90° upstream shown in Figure 56 and Figure 57-b, the perpendicular injection is clearly observed through the flame shape and the flame is separated into the 4 flame jets as in the previous configuration, although this time the flame fronts seem to be wider, with a smaller low temperature region between them.

This actually decreases the temperature of the mixture, as the local equivalence ratio is expected to be lowered, shown in Figure 58 through average temperature in the combustor for constant 90° on the upstream and variable downstream angles.

The average temperature and associated heat loss in the combustor for this configuration is shown in Figure 61 alongside variable upstream angles. The perpendicular injection increases the heat loss at the walls and as the mixture proceeds downstream, the heat loss decreases with the decrease of temperature of the flame.

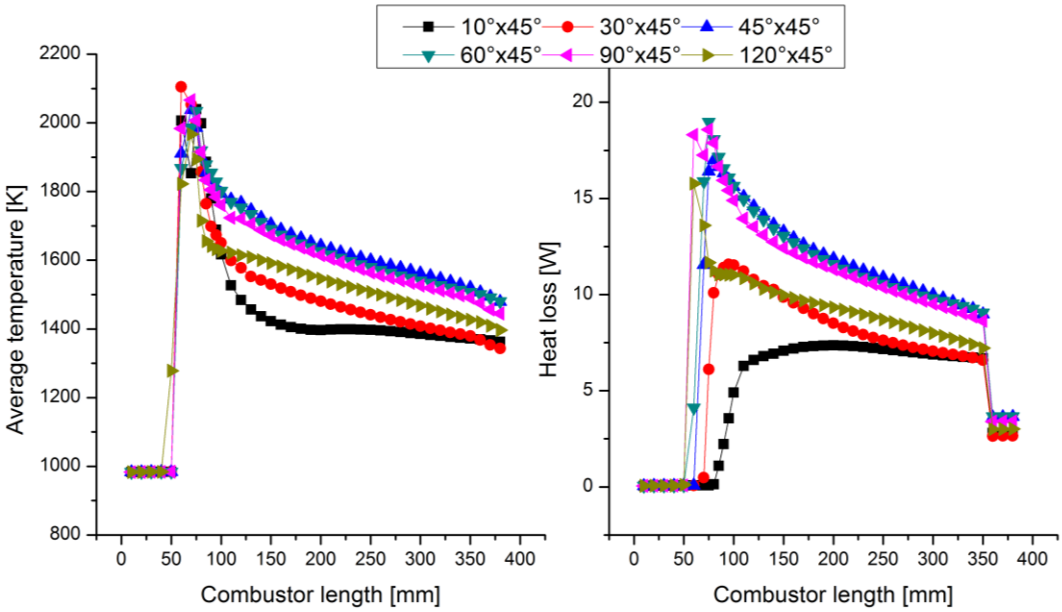

Figure 61 Average temperature (left side) and heat loss (right side) in the combustor for constant downstream 45° and variable upstream angles at fuel-lean conditions

The heat loss presents two peaks, given by the separate flame fronts that reach the upper and lower side walls of the combustor.

For upstream angles on 120°, seen in Figure 56 and Figure 57-c, the vortices that form in between the injection are not influenced by the increasing downstream angle, however, the recirculation zone in the wake of the injector becomes more pronounced, where the azimuthal velocity is assumed to have increased. The combustion takes place in the same separate flame fronts, however, due to larger angles on the downstream, the heat loss increases. The average temperature and heat loss in the combustor for 120°x30°, 120°x45° and 120°x60° configurations is presented in Figure 62. The average temperature is seen to increase with larger downstream angles, and thus the heat loss associated with hotter flames, increases as well.

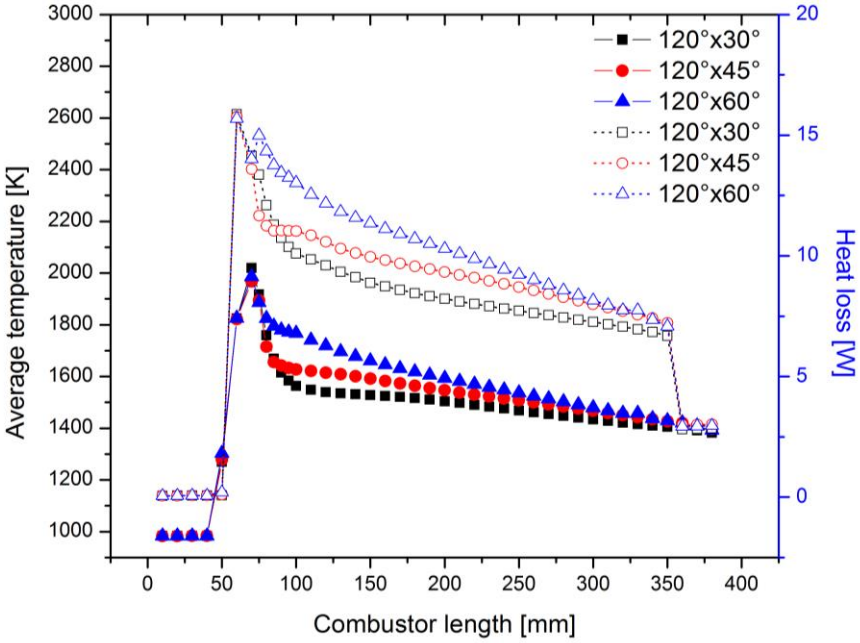

Figure 62 Average temperature (solid points) and heat loss (hallow points) in the combustor for 120°x30°(black), 120°x45°(red) and 120°x60°(blue) at fuel-lean conditions

The average temperature in the chamber is plotted for the entire combustor at variable upstream angles and a fixed downstream angle of 45° in Figure 61. The temperature in the chamber increases with larger upstream angles with a maximum found for 60°x45°, after which, due to the vortices that form between the injection holes, the temperature drops as the mixture is diluted. The temperature gap for a fixed upstream angle of 45° varied from 300 to 500 K.

In Figure 63, the chemical heat release is plotted for constant downstream angles of 45°. The heat release is highest when the downstream angles are small i.e. 10° and 30°. When the downstream angles increased, the heat release decreased. It can be seen that most of the combustion took place near or around the injector and not towards the nozzle area. The heat release increases as the angles increase on the downstream side until the two flame fronts are connected as a result of the “bridge” between the two flame fronts. As that happens, the local equivalence ratio decreases which decreases the heat release ratio.

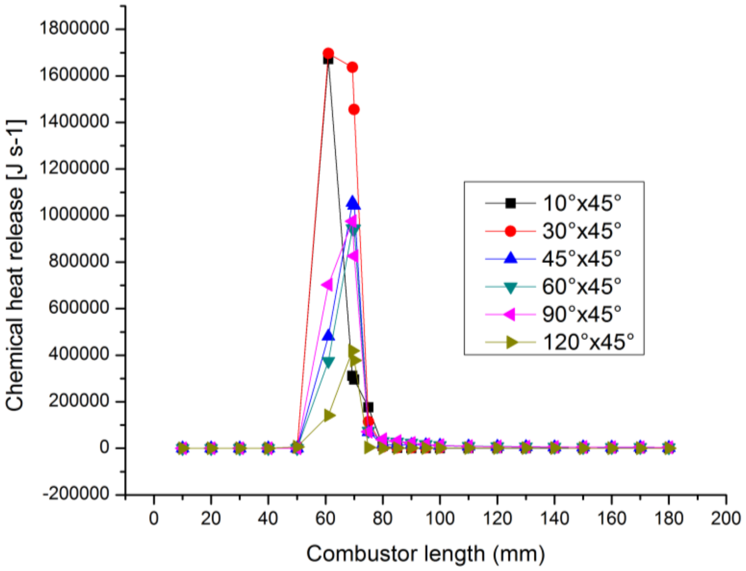

Figure 63 Heat release ratio for constant 45° downstream angles at fuel-lean conditions

Figure 51 presents the total heat loss plotted this time for the variable downstream angles. The total heat loss follows a similar trend as that of fixed downstream angles of 30°. The heat loss increases as angles increase on the upstream and the heat loss associated is higher as downstream angles increase.

Figure 64 presents the combustion efficiency for constant downstream angles of 45° and combustor length on the right side using the enthalpy approach (-a), the left side presents the chemical heat release approach (–b). When higher angles are set for the downstream pair, the combustion efficiency increases until it reaches a plateau, after which larger angles on the upstream lower the local equivalence ratio and temperature, which lead to decreasing combustion efficiencies.

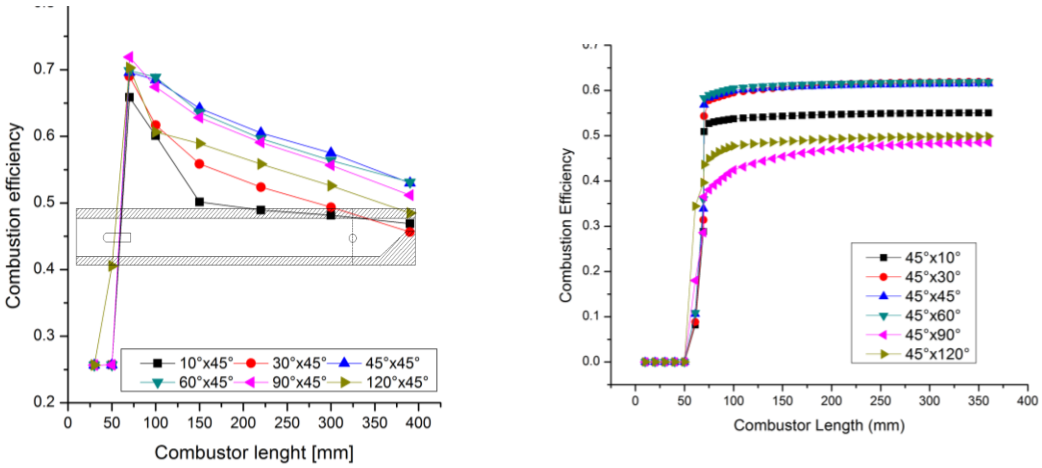

Figure 64 Combustion efficiency for constant downstream 30° angles at fuel-lean conditions; a- enthalpy difference approach, b- heat release approach

Highest angles on the upstream side decrease the combustion efficiency to larger values when the downstream angles are set to 45°. The overall combustion efficiency is presented in Figure 65 for the nozzle values of the combustion efficiencies. The combustion efficiency that is characteristic of the injection configuration is similar to the previous configuration when downstream angles were set to 30°. There is combustion efficiency peak when the recirculation zones in the wake of the injector are located into one coherent structure. As angles increase the size of the vortices that are induced by the angled flow, increases. This leads to lower local equivalence ratio and a decrease in local temperature. As a result, the combustion efficiency decreased.

Figure 66 presents the NO and NO2 mass fraction plotted in the length of the combustor for variable upstream angles at constant downstream angles of 45°. The NO concentration increases after the mixture combusts, and slowly decreases in the chamber. The NO2 follows a similar trend, only milder. However, high upstream angles i.e. 90° and

120°, actually generate more NOx, since the flame is separated in four independent flame fronts, instead of two. As a result, flame-formed NO and pre-flame NO2, increased as the separate flame fronts created their separate NOx, independent, which by not being in a single flame front, does not dissociate and recombine as easily.

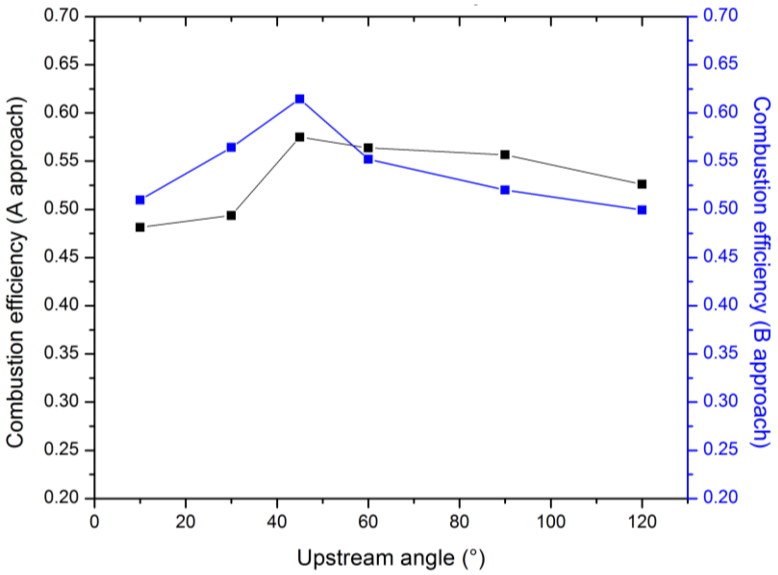

Figure 65 Overall combustion efficiency using the two approaches, enthalpy difference (black line) and chemical heat release (blue line) for constant downstream angles of 45°

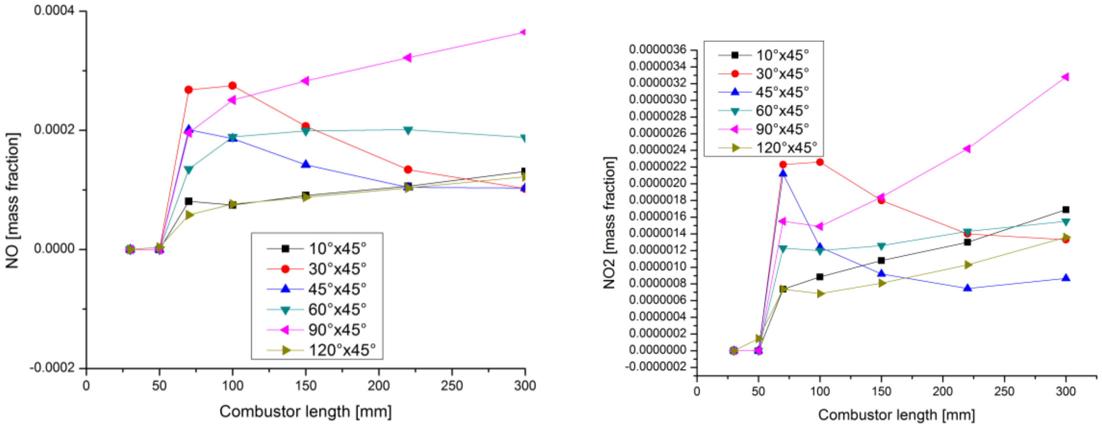

Figure 66 NO and NO2 mass fraction distribution in the combustor for constant downstream angles fixed at 30°

The EINOx, plotted in Figure 55, increases with larger upstream angles, albeit a 30° configuration on the upstream. As seen previously the bulk of the EINOx is given by the ramps shaped nozzle. When the angles increased to 120° on the upstream, due to the rarefication of the flame, and subsequent dilution, the NOx production was inhibited and the resulting EINOx decreased. Small downstream angles have little influence on the creation of NOx; however, larger angles on the downstream when the upstream angles increase, due to the flame shape and equivalence ratio, produce more NOx in the chamber.

Figure 67 and Figure 68 present the temperature (on the top) and velocity distribution fields (on the bottom) for variable downstream angles and constant upstream angles of 60°. The figures present enhanced temperature fields (on the left side) and velocity distribution fields (on the right side) from a, to c for 10° to 120° on the upstream. Larger angles on the downstream push a bigger amount of fuel towards the walls which either flows along the walls of the combustor, or are deflected and unite towards the middle of the combustor on the axial direction. More reflected flow yielded higher heat loss. For a 10°x60° configuration, shown in Figure 67 and Figure 68-a, the effect observed for the same configuration with 45° on the downstream, is enlarged here. The two flame fronts are more diffusive towards the middle of the combustor due to high velocity fuel coming from the upstream pair. From Figure 69, where the average temperature and heat loss in the combustor is plotted for 10° angles on the upstream and variable downstream angle shows the effect of this diffusiveness. The temperature decreased in the immediate wake of the injector, but due to the flow being injected towards the walls, it was higher farther downstream.

In Figure 69, the average temperature and heat loss, is plotted for constant upstream angles at 10° and variable downstream angles to show the effect of the diffusiveness of the flame fronts on the heat loss. When the downstream angles increase for fixed 10° injection, the average temperature, as observed in Figure 69, decreases in the nozzle area due to the lowering of the local equivalence ratio. The heat loss associated with larger angles downstream is largest when the downstream are highest, since the injection is at the walls of the combustor, and the flame fronts adhere to the walls of the combustor.

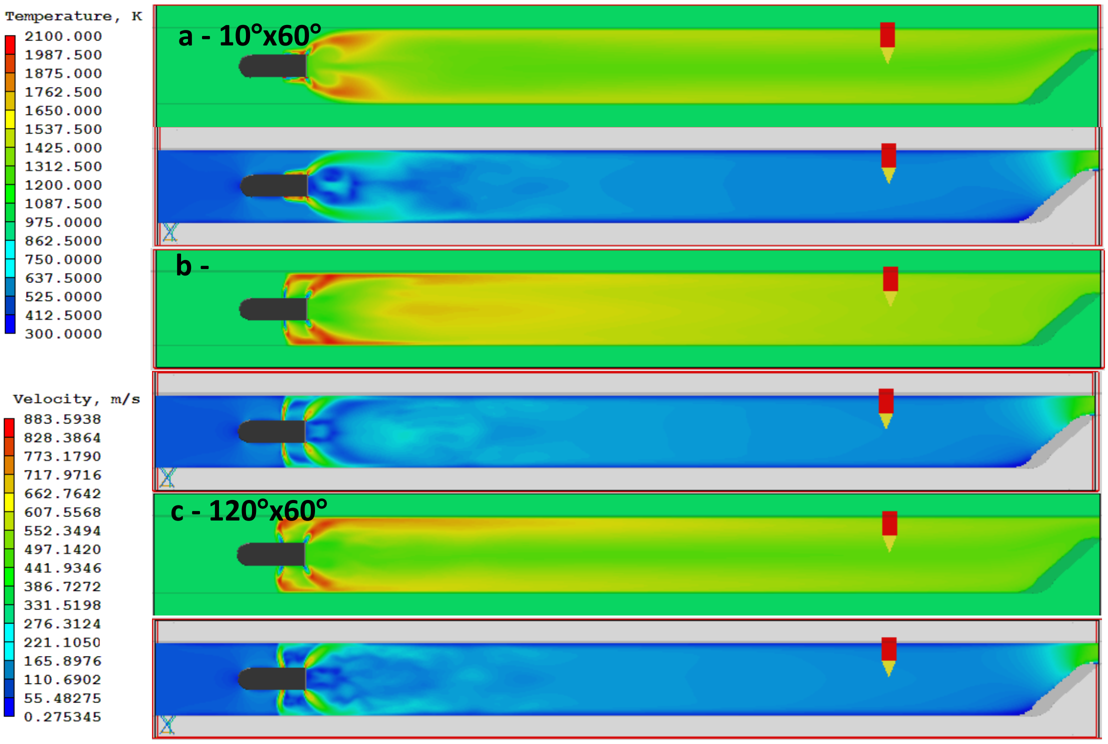

Figure 67 Temperature and velocity distribution field for constant downstream angle of 60° at fuel-lean conditions

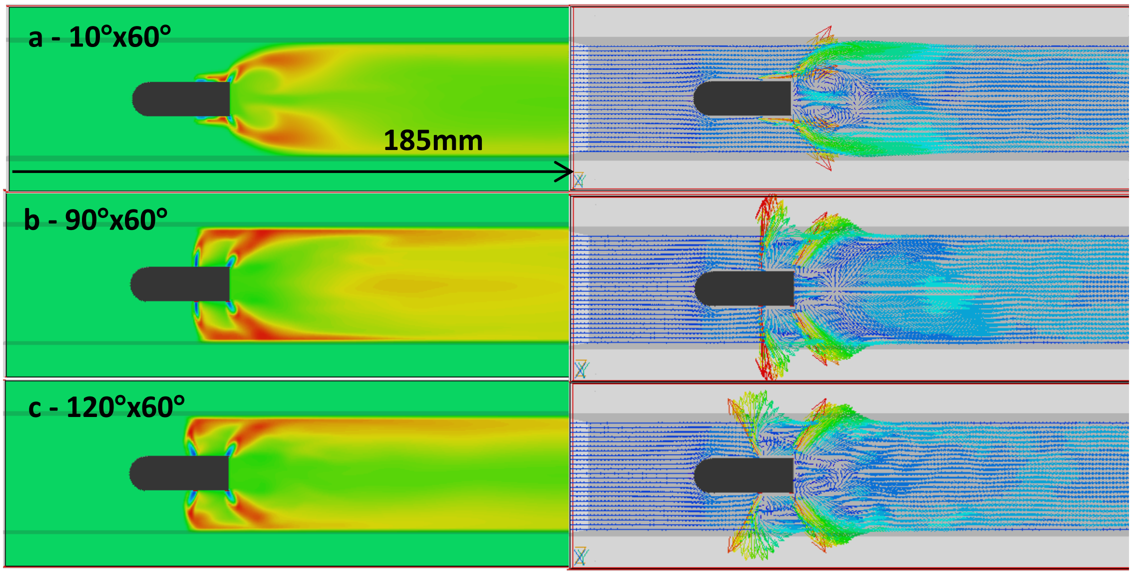

Figure 68 Enlarged temperature field distribution and velocity vector distribution near the injector for constant downstream angles 60°

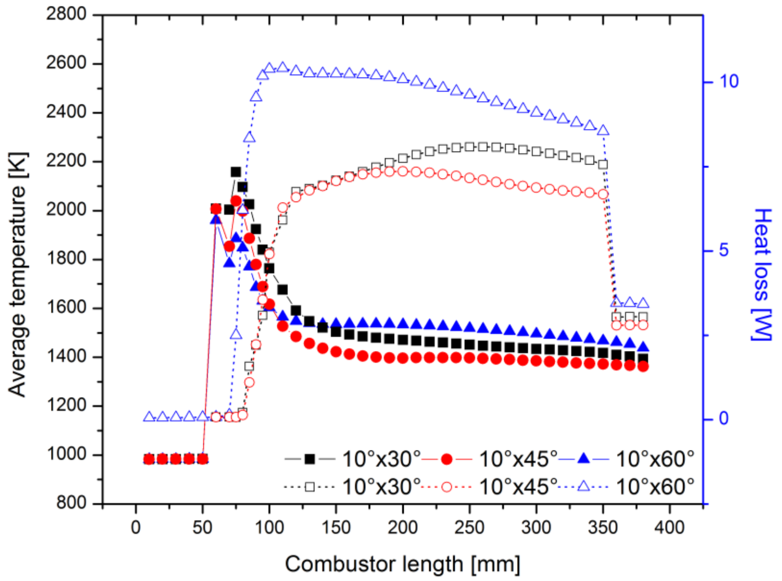

Figure 69 Average temperature (solid points) and heat loss (hallow points) in the combustor for 10°x30°(black), 10°x45°(red) and 10°x60°(blue) at fuel-lean conditions

When the upstream angles increase to 30°, 45° and 60°, the effect is presented in the previous section 4.4.1.1.

From Figure 67 and Figure 68-b, 90° upstream angles, are more pronounced than the previous configurations. Figure 58 showed that as larger angles are set for the upstream side, there is higher local temperature around the injector, however, farther in the chamber, the temperature decreases, due to the dilution, when the local equivalence ratio decreased. The perpendicular injection increases the heat loss at the walls and as the mixture proceeds downstream, the heat loss decreases with the decrease of temperature of the flame.

Heat loss is highest near the injector, and due to the large downstream angles, the mixture has contact with the wall for longer distances, which increases the heat loss. Later as the flame proceeds downstream, the heat decreases.

For upstream angles on 120°, seen in Figure 67 and Figure 68-c, the vortices that form in between the injection are not influenced by the increasing downstream angle, however, the recirculation zone in the wake of the injector becomes more pronounced, where the azimuthal velocity is assumed to have increased. The combustion takes place in the same separate flame fronts, however, due to larger angles on the downstream, the heat loss increases. The average temperature and heat loss in the combustor for 120°x30°, 120°x45° and 120°x60° configurations is presented in Figure 62. The average temperature is seen to increase with larger downstream angles, and thus the heat loss associated with hotter flames, increased as well.

The average temperature in the chamber is plotted for the entire combustor at variable upstream angles and a fixed upstream angle of 60° in Figure 70.

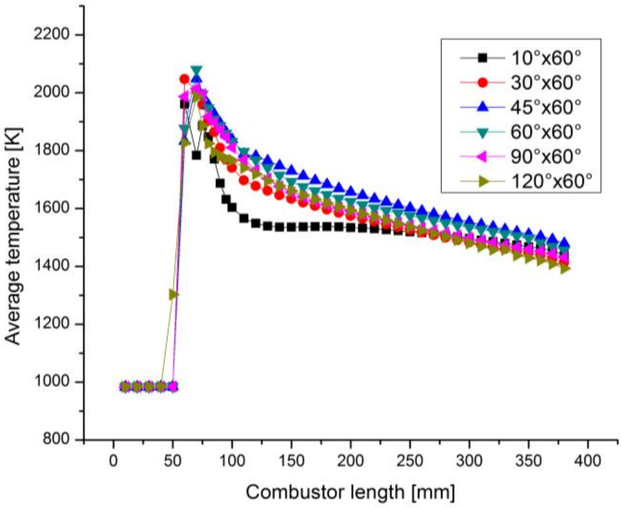

Figure 70 Average temperature in the combustor for fuel-lean configurations at constant downstream 60°

The temperature in the chamber increases with larger upstream angles with a maximum overall found for 45°x60°, after which, due to the vortices that form between the injection holes, the temperature drops as the mixture is diluted. The temperature gap for a fixed upstream angle of 60° varied from 400 to 600 K.

In Figure 71, the chemical heat release is plotted for constant downstream angles of 60°. The heat release ratio is highest when the downstream angles are small i.e. 10°**.** The same trend and observations were found as per the previous configuration i.e. the heat release decreased as the local equivalence ratio decreased. Larger angles induce the reaction zone to be closer to the injector, thus the maximum heat release peak can be found closer to the injector, and as a result the local equivalence ratio is smaller. This leads to a decrease in the chemical heat release.

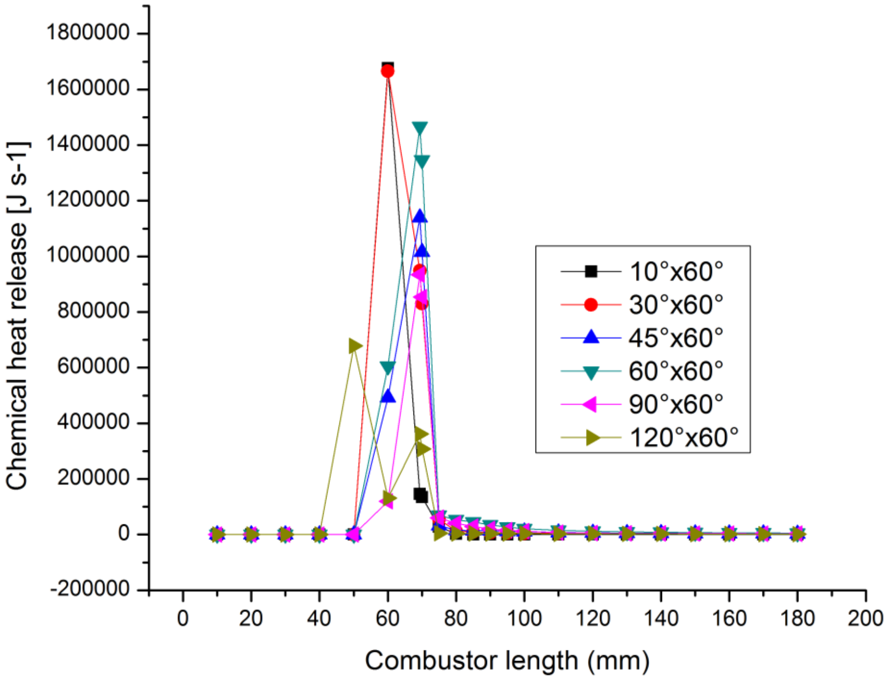

Figure 71 Chemical heat release for constant 60° downstream angles at fuel-lean conditions

The total heat loss increased as angles increase on the upstream and the heat loss associated is higher as downstream angles increase, shown in Figure 51. The total heat loss is higher for larger downstream and increases with upstream angles, reaching a maximum for the configuration with maximum temperature 45°x60°, after which, due to the separation of the flame fronts and subsequent dilution, the local temperature drops and so does the total heat loss associated.

Figure 72 presents the combustion efficiency for constant downstream angles of 60° and combustor length on the right side using the enthalpy approach (-a), the left side presents the chemical heat release approach (–b).

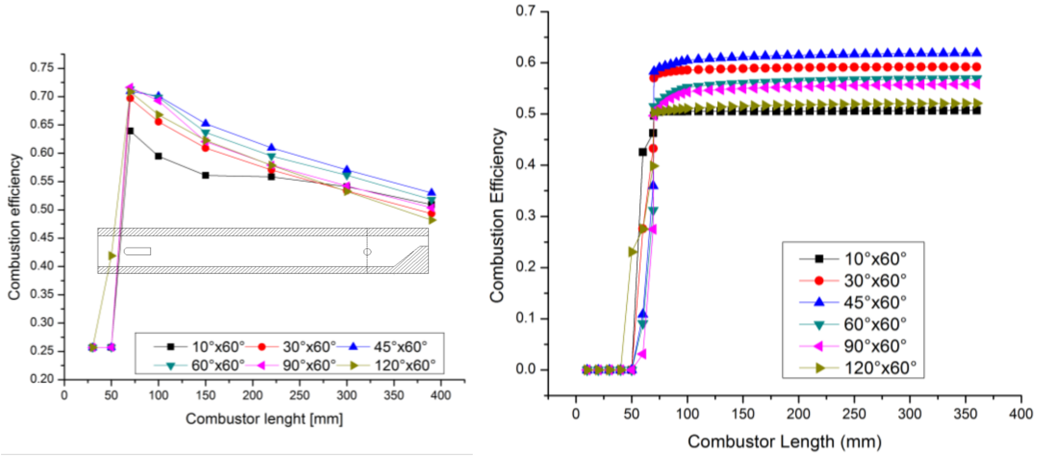

Figure 72 Combustion efficiency for constant downstream 30° angles at fuel-lean conditions; a- enthalpy difference approach, b- heat release approach

The combustion efficiency is smaller when angles are smaller on the upstream seen form Figure 72, due to low local equivalence ratio. When the angles are increased, the equivalence ratio increases and so does the combustion efficiency. A peak of the combustion efficiency is observed for a 45°x60° configuration, due to large temperature. Past this peak the combustion efficiency slowly decreased with increasing upstream angles due to a drop in temperature in the flame and local dilution.

Figure 73 presets the overall combustion efficiency near the nozzle. As in the previous configurations, there is a peak around the 45° injection angle. Larger angles on the upstream induce larger vortices in the wake of the injector, which lower the local equivalence ratio and decrease the combustion efficiency. Figure 74 presents the NO and NO2 mass fraction plotted in the length of the combustor for variable upstream angles at constant downstream angles of 60°. The NO concentration increases after the mixture combusts, and slowly decreases in the chamber.

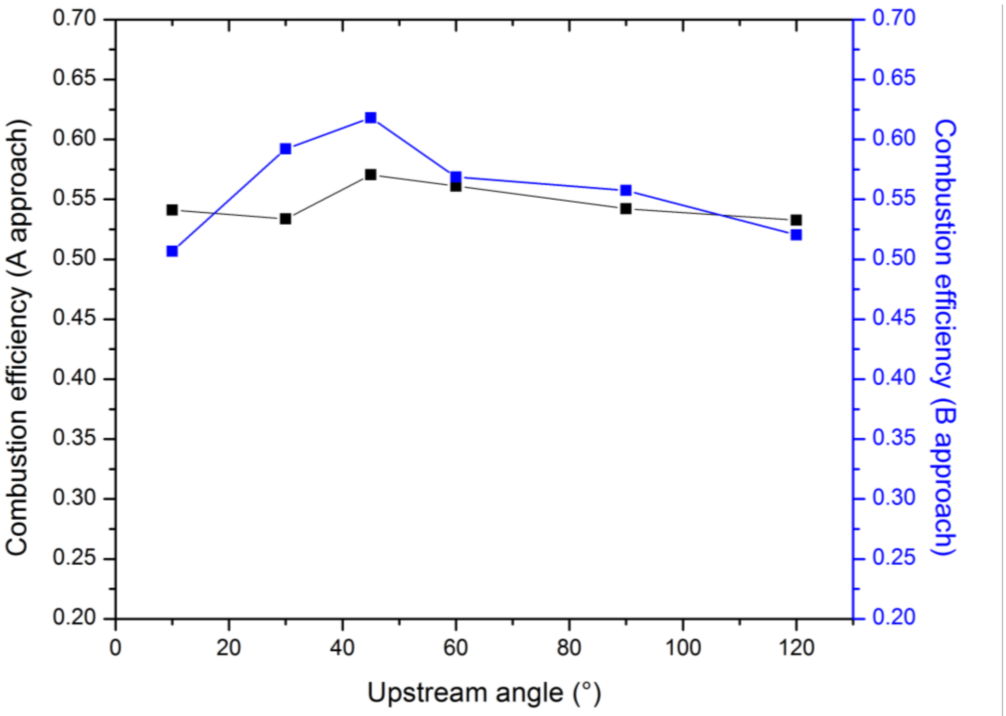

Figure 73 Overall combustion efficiency using the two approaches, enthalpy difference (black line) and chemical heat release (blue line) for constant downstream angles of 60°

The NO2 follows a similar trend, only milder. Large upstream angles coupled with large downstream angles do not generate larger amounts of NO as seen from Figure 74. The largest amount seems to be generated when the injection flow from the upstream and downstream injection holes is parallel. This parallel injection for configuration 60°x60° creates a large engulfing flame, with two pronounced flame fronts on the side walls and connected flame towards the middle of the combustor.

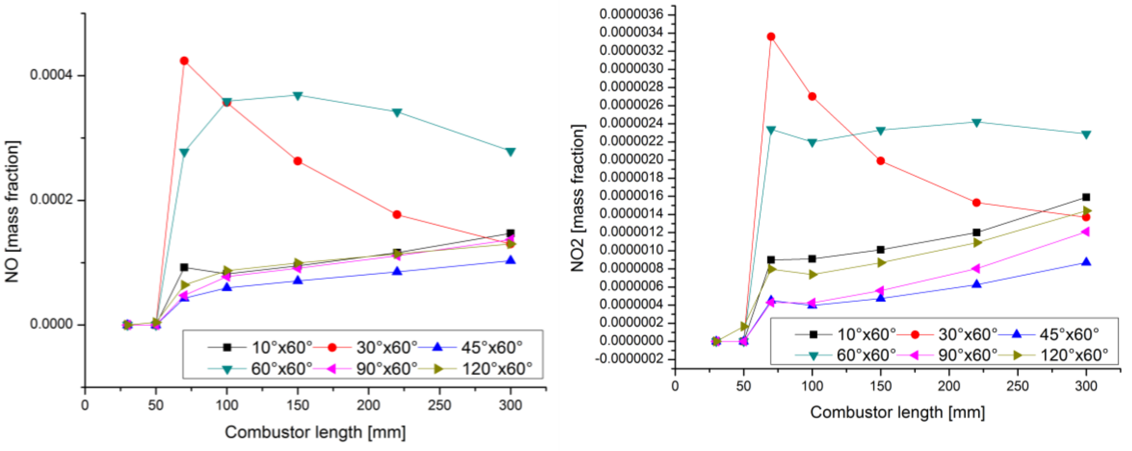

Figure 74 NO and NO2 mass fraction distribution in the combustor for constant downstream angles fixed at 60°

The EINOx, plotted in Figure 55, increases with larger upstream angles, albeit a 30° configuration on the upstream. As seen previously the bulk of the EINOx is given by the ramps shaped nozzle effect on the chamber production. The EINOx is highest when the chamber production of NO seen in Figure 74 is highest and decreases with increasing upstream angles, due to a dilution of the mixture induced by the vortices between the injection holes.

From Figure 75, the vortices that form around the injection holes are shown through the velocity vector distribution fields. The first configuration shown, 30°x60°, presents a large recirculation zone in the wake of the injector with high velocity fronts on the side, as fuel is injected in the chamber. When angles increase on the upstream side to 60°x60°, the high velocity fronts forming from the upstream pair are almost parallel to the downstream pair. This causes small vortices to form at the base of the upstream injection holes and in the same time creates another reaction zone, shown in Figure 76 through the local equivalence ratio near the injector. As these vortices form, the local equivalence ratio in the area increases, yielding two reaction zones. These two reaction zones generate more NOx, increasing the EINOx in the area. As vortices increase in size, with increasing upstream angles, a maximum equivalence ratio is achieved up flow of the upstream injection holes, however, the mixture in the area is then quickly diluted, which leads to lower temperatures in the area and lower EINOx.

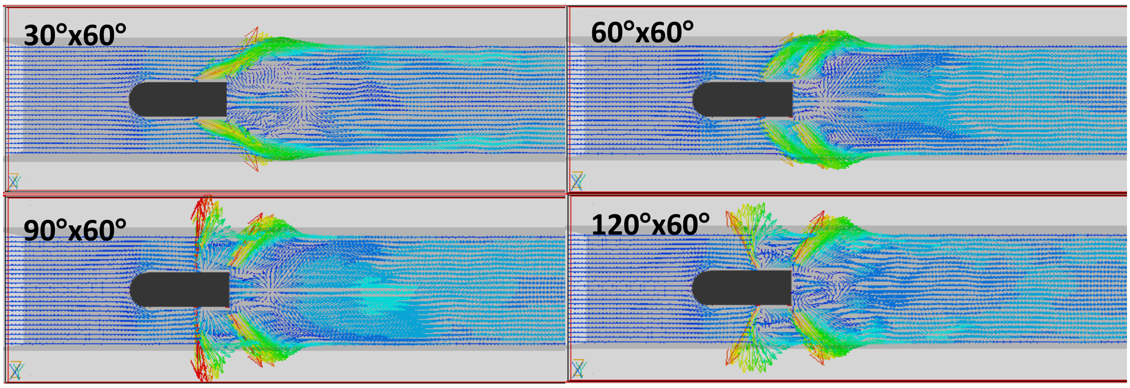

Figure 76 Velocity vector distribution for constant downstream angles of 60° and variable upstream angles at fuel-lean conditions

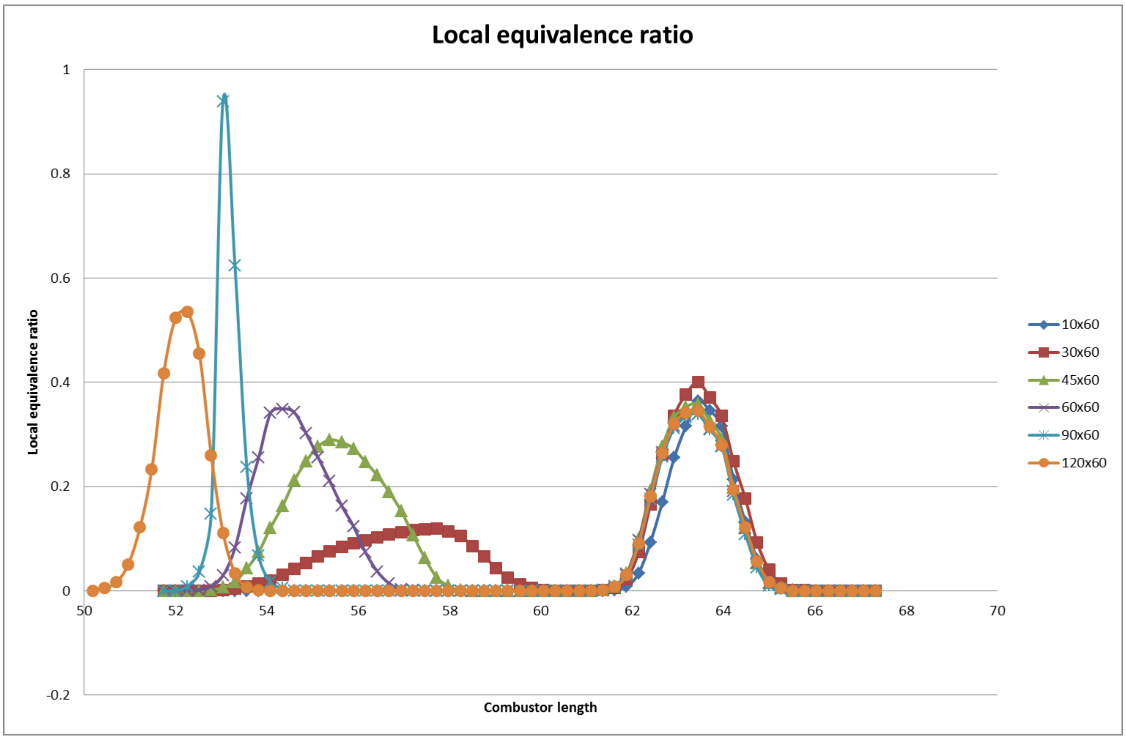

Figure 75 Local equivalence ratio around the injector for unburned radicals, at constant downstream angles of 60° and variable upstream angles, at fuel-lean conditions

Fuel-lean combustion has been performed for three pairs of fixed upstream angles 30°, 45° and 60° and variable downstream angles and repeated for variable upstream angles and fixed 30°, 45° and 60° downstream angles.

The following conclusions can be drawn from the study performed so far:

- The estimation of the combustion efficiency depends heavily on the location from which it is considered representative.
- Following experimental assumptions of combustion efficiency estimation, shorter combustion yields lower NOx and higher combustion efficiency for all configurations.
- Configurations with larger angles downstream generate more NOx.
- Upstream angles have little influence on the production of NOx for small downstream angles.
- Larger angles on the downstream coupled with large upstream angles produce more NOx in the chamber.

4.4.2. Rich combustion

In the simulations that have been performed to determine the effect of the injection configuration, the fuel-rich numerical equivalence ratio was fixed at 2.033. To investigate the effects, in the first phase we kept constant the upstream angles and varied the downstream angles from 10° to 120° for 6 different values - 10°, 30°, 45°, 60°, 90° and 120°. In the second phase, we repeated the simulations for 3 pairs of constant angles on the upstream: 30°, 45° and 60° respectively. Third and fourth phase have constant the downstream angles while the upstream angles are varied for the 3 pairs of constant angles on the downstream: 30°, 45° and 60° respectively.

4.4.2.1. Constant upstream combustion

When the equivalence ratio is on the rich side, the reaction is more powerful; the temperature is higher due to a larger equivalence ratio and so the reaction-induced velocity is higher. The flame comprises of one full shape with slightly apparent “shoulders” shown in Figure 77, around the injector, when the fuel is injected towards the walls and then reflected in the chamber.

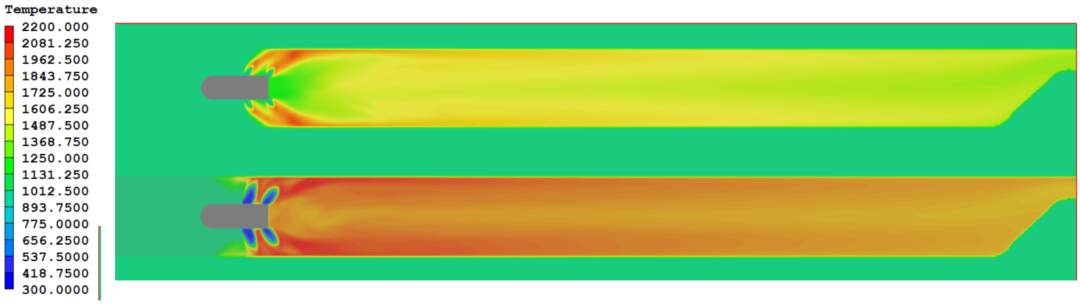

Figure 77 Flame shape for a 60°x45° configuration at fuel-lean $\phi = 0.35$ (top) and fuel-rich $\phi = 2.033$ (bottom) conditions

Compared to the fuel-lean case, the recirculation zones and afferent vortices and vortices have a bigger effect on the combustion performance. For a fuel-rich combustion there can be distinguished 4 major recirculation zones, shown in Figure 78, (1) a large one in the immediate wake of the injector. Farther downstream, as a result of high vortex breakdown, (2) a smaller recirculation zone is formed. This smaller zone is called hereafter downstream recirculation zone. The other two (3 and 4) are seen to form on the side of the injector before the upstream injection holes on the upper side and the lower side of the injector.

The influence of these recirculation zones on the flow becomes apparent and will be used to help explain the flame behavior, for different angle configurations. At high Reynolds numbers heat release has an effect on vorticity. Expansion of the fluid due to heat release reduces vorticity and destroys the local vortices.

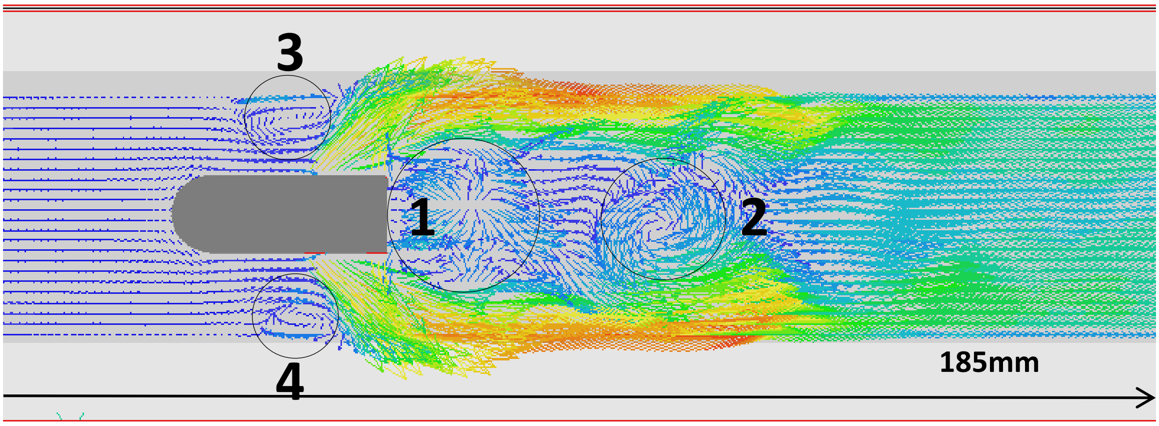

Figure 78 Recirculation zones for fuel-rich configurations

Figure 79 presents the temperature (on the top) and velocity distribution field (on the bottom) for constant upstream angles of 30°. Figure 80 presents an enlargement of the injector region for the temperature field (on the left side) and velocity vector distribution (on the right side) for the same configurations. In Figure 79 and Figure 80, from a, to d, the downstream angles increase from 10° (a) to 120° (f). When the upstream angles are fixed to 30° at low angles on the downstream seen in Figure 79-a, and Figure 80-a, the flame expanded fully in the chamber. For a 30°x10° configuration, the hottest regions of the flame seem to be the two flame fronts that form when the fuel, coming from the upstream and downstream injection holes, mixes. When the temperature is plotted for the length of the combustor vs. the heat loss in the chamber, observed in Figure 81, the mixture yields the highest temperature near the injector. The heat loss, due to small angles on the downstream is relatively small near this area, compared with the rest of the chamber. When the fuel injected by the upstream injection holes, is carried downstream and it encounters the fuel from the downstream injection holes, the mixture adheres to the walls on the upper side and lower side of the injector, creating an area of high heat loss, seen in Figure 81. As the flame evolves downstream, the average temperature decreases due to a dilution of the mixture by lower local equivalence ratio, shown in Figure 82. After which the average temperature reaches a plateau. The heat loss, following the same arguments, slowly decreases in the chamber as the temperature decreased near the injector, and continued to decrease even as the temperature remained constant due to a decrease of the local equivalence ratio.

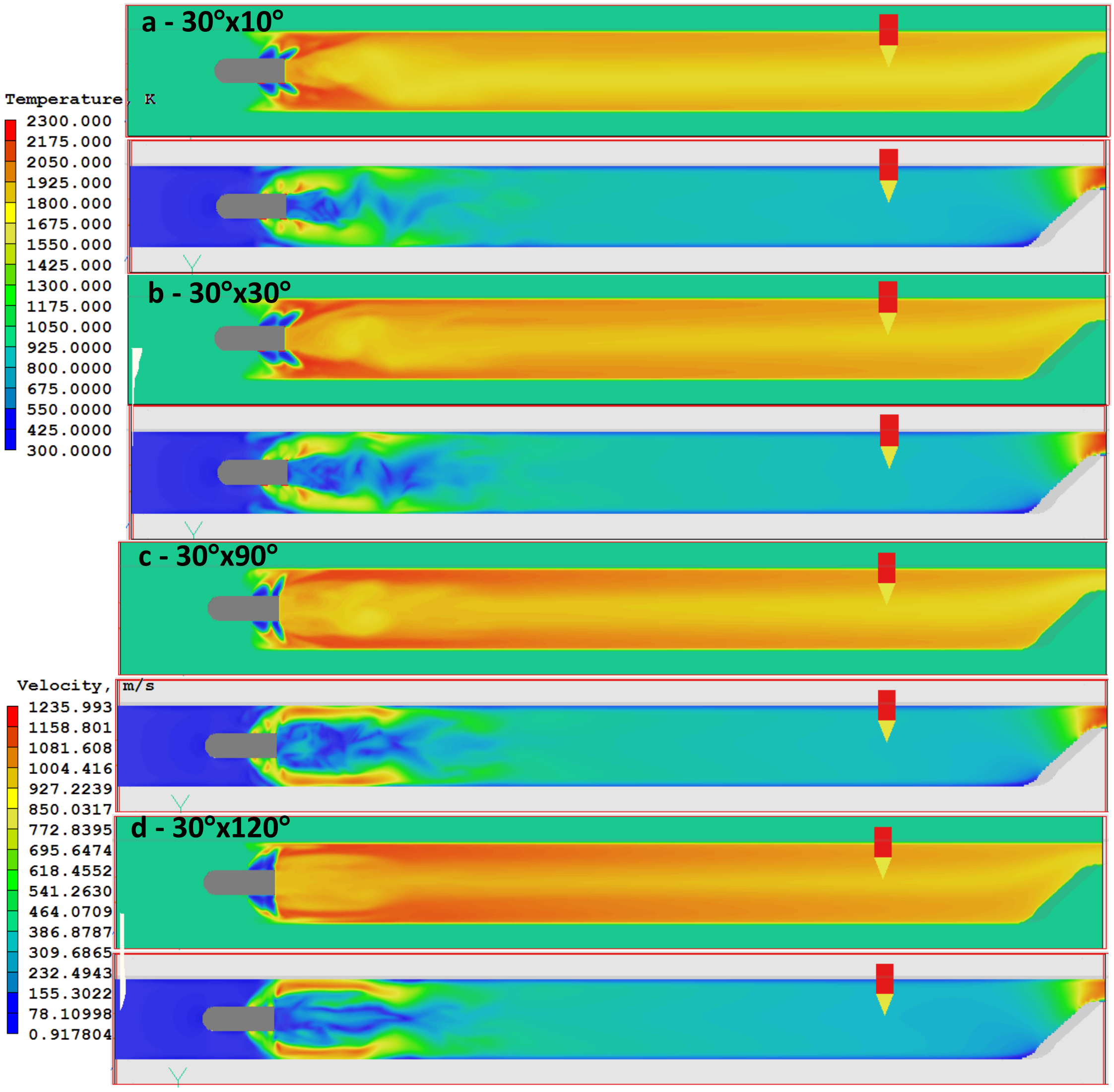

Figure 79 Temperature and velocity distribution field for constant upstream angle of 30° at fuel-rich conditions

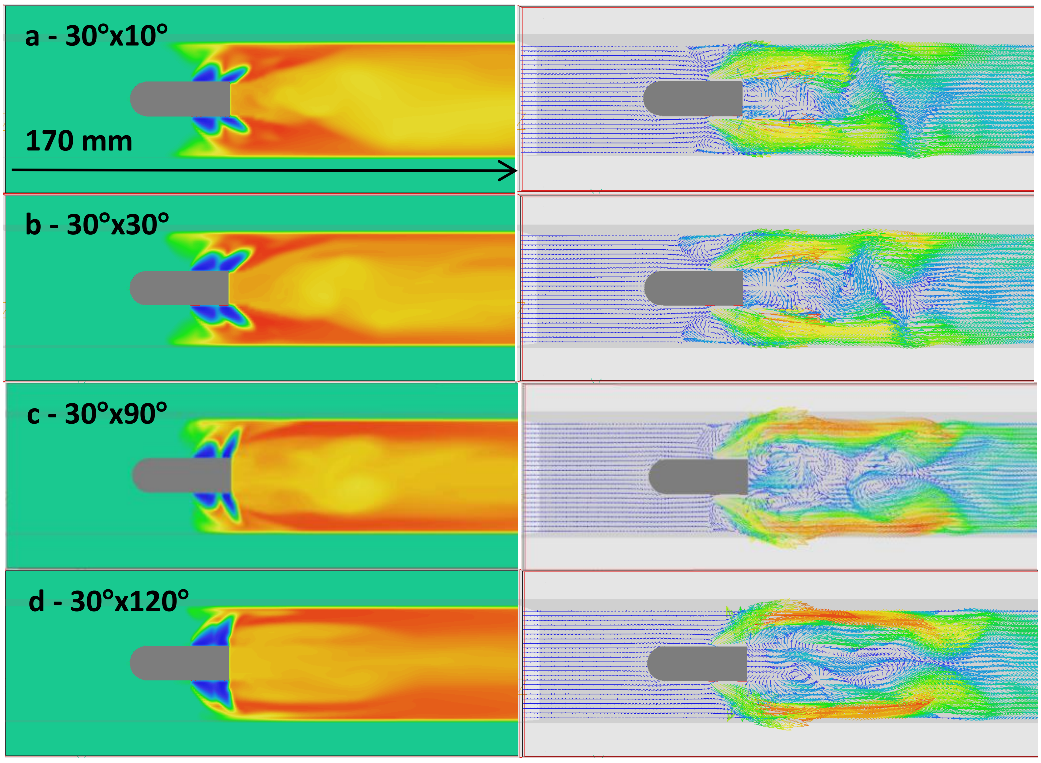

Figure 80 Enlarged temperature field distribution and velocity vector distribution near the injector for constant upstream angles 30° at fuel-rich conditions

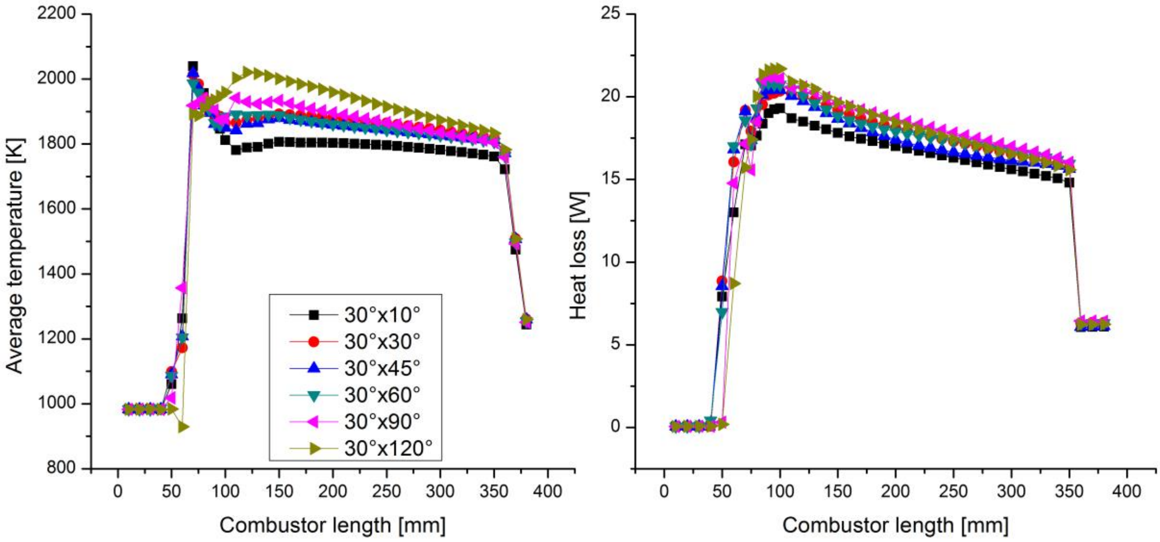

Figure 81 Average temperature (left side) and heat loss (right side) in the combustor for constant upstream 30° and variable downstream angles at fuel-rich conditions

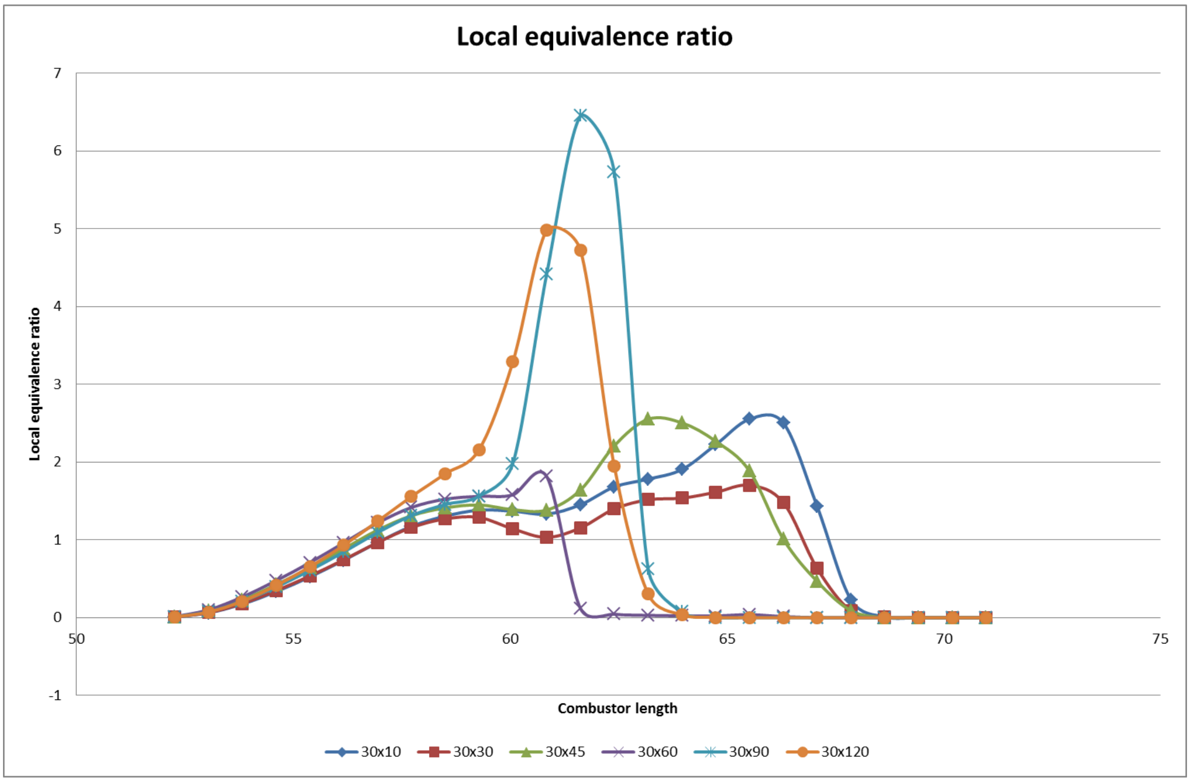

Figure 82 Local equivalence ratio of unburned radicals, in the wake of the injector for constant upstream angles of 30° with variable downstream angles at fuel-rich conditions

From Figure 80-a, through the velocity vector distribution, we observe that the 1st and 2nd recirculation zone very close to each other and due to the high fuel injection, the vortex breakdown in the wake of the injector, farther downstream is very pronounced. When the angles increase on the downstream, seen in Figure 79 and Figure 80-b, the injected fuel from the downstream pair, is carried closer to the walls of the combustor. This flow increases the contact of the mixture with the walls, increasing the heat loss, and also creates higher velocity areas close to the walls, due to reflected fuel. Another effect of larger angles downstream is that the 3rd and 4th vortex formations, forming at the upper and lower sides of the injector, enlarge. The average temperature and heat loss for a 30°x30° configuration is presented in Figure 81. With larger angles and on the downstream, the flame becomes more uniform, and we observe that although the temperature still decreased in the wake of the injector, due to a dilution of the mixture, shown in Figure 82, the decrease was smaller, the temperature, slightly higher, and reached a plateau faster.

For a configuration of 30°x45°, a similar trend to the previous configuration is observed. The increasing angles inject fuel closer to the walls and as a result the highest value of heat lost is closer to the injector. With larger angles, the downstream recirculation zone extends farther away from the 1st recirculation in the wake of the injector. This allows for a larger area in the center of the flame, where the temperature is lower. The recirculation zones can be observed from Figure 80. Another observation is that the effect of the ramp-shaped nozzle is observed more pronounced on the upper side of the injector through the 3rd recirculation zone. The average temperature and heat loss for this configuration is presented in Figure 81 with [red] circles. Due to larger angles on the downstream and prolonged contact of the mixture with the walls, the average temperature actually decreased. The heat loss is higher from the configurations near the injector, however due to the flow-induced, downstream recirculation zone, the heat loss decreased farther downstream.

With larger angles on the downstream, heat loss increased in the area, and due to the larger angles downstream, the first recirculation zone in the wake of the injector, is broken down into smaller vortices, shown in Figure 83, through the distribution of the turbulent kinetic energy in the wake of the injector, which create an area of low temperature and lower local equivalence ratio, shown in Figure 82. The average temperature and heat loss plot for a 30°x60° configuration is shown in Figure 81 through inverted [teal] triangles. The peak of the heat loss in the combustor is moved farther away from the injector, due to the large angles, which increased the overall values of the heat loss.

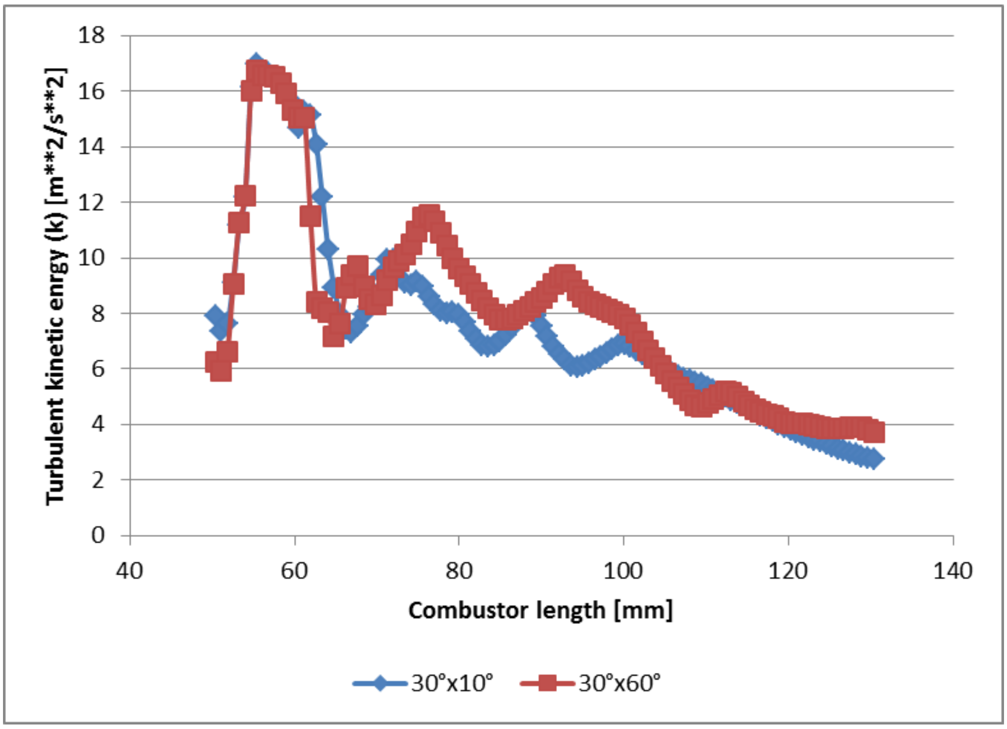

Figure 83 Turbulent kinetic energy in the wake of the injector for 30°x10° and 30°x60° at fuel-rich conditions

When the downstream angles are increased to 90°, a direct effect of this is larger heat loss associated, not only in the injection area, but overall, as more fuel is injected directly at the walls. This is a result of the recirculation zones that take shape in the wake of the injector. Due to large angles, the vortices grow in size, and actually impede mixing in the area. This effect is shown in Figure 82, through the local equivalence ratio plotted for variable downstream from the upstream injection holes to the wake of the injector.

The average temperature and heat loss in the combustor is shown in Figure 81. The heat loss is largest for this configuration as shown in Figure 81, right side. From Figure 81, the average temperature is higher for this configuration, shown from Figure 79 and Figure 80-c. Due to large angles on the downstream, and the presence of the large recirculation zones, the flame temperature is highest near the walls of the injector, which show in Figure 79 and Figure 80-c as redder flame fronts on the upper and lower side of the combustor. As a result, the average temperature reached a plateau in the chamber. The heat loss, as can be expected, due to larger temperature of the flame near the walls, is higher.

When the downstream angle is increased to 120°, seen in Figure 79-d and Figure 80-d, the large recirculation zones are constrained by the higher velocity boundary layers formed on the upper and lower side walls. Due to these two velocity fronts, mixture increased as seen in Figure 82. As a result, the effect observed in Figure 18 for a teardrop-shaped flame at fuel-lean conditions for this configuration, is the actual mixture that combusts in the wake of the injector. The rest of the flame has higher temperature and as a result higher heat loss.

The average temperature and heat loss plot, in the combustor for 30°x120° configuration is presented in Figure 81. Due to the large recirculation zone in the wake of the injector, the average temperature in the area is lower, and later it increases and the vortices fade away around 60 mm from the injector. The heat loss on the other hand is highest near the injector and decreases steadily in the chamber downstream.

The maximum temperature in the chamber, in Figure 81, left side, is achieved by large angles on the downstream i.e. 120°, however, due to their effect, this configuration also has the highest heat loss. When downstream angles increase, the average temperature increases in the chamber. Larger angles allow for larger recirculation zones in the wake of the injector, where pockets of unburned oxygen mix with fresh gases and allow for an increase in local equivalence ratios.

Figure 84 presents the chemical heat release plotted for constant upstream angles of 30°. When the upstream angles were kept constant, the trend was a decrease in heat release as the downstream angles became larger. When angles increased, the local equivalence ratio decreased, lowering the heat release.

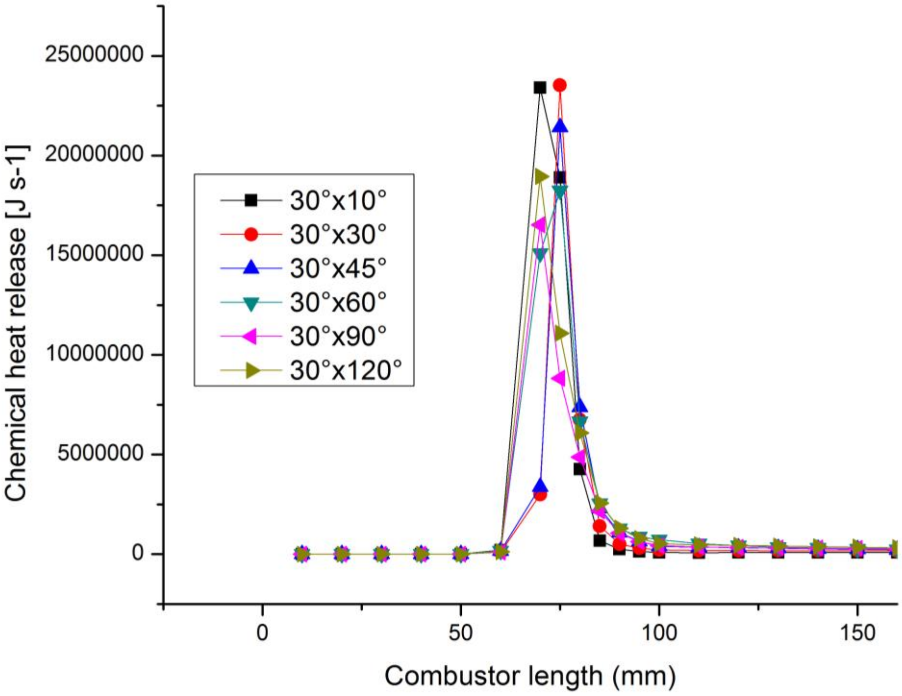

Figure 84 Chemical heat release for constant 30° upstream angles at fuel-rich conditions

The OH radical variation with increasing downstream angles for constant 30° on the upstream at fuel-rich conditions is presented in Figure 85-a. The formation and subsequent dissociation of the OH radical is influenced by the equivalence ratio. In Figure 85-b, -c and -d, the concentration of H2, O2 and N2 is plotted for different downstream angles, when the upstream angle is fixed at 30°. From the H2, O2 and N2 concentration we see that the mixture is consumed mostly around the downstream injection holes for small downstream angles, and later, for large downstream injection angles, it is consumed earlier, near the upstream injection holes.

This is easily understood since higher downstream angles push fuel closer to the walls and thus mixing and combustion take place in a shorter distance. What this means is that as the combustion “moves” closer to the injector, N2 reacts faster than O2, which in turn inhibits the formation of OH, which lowers the heat release in the area.

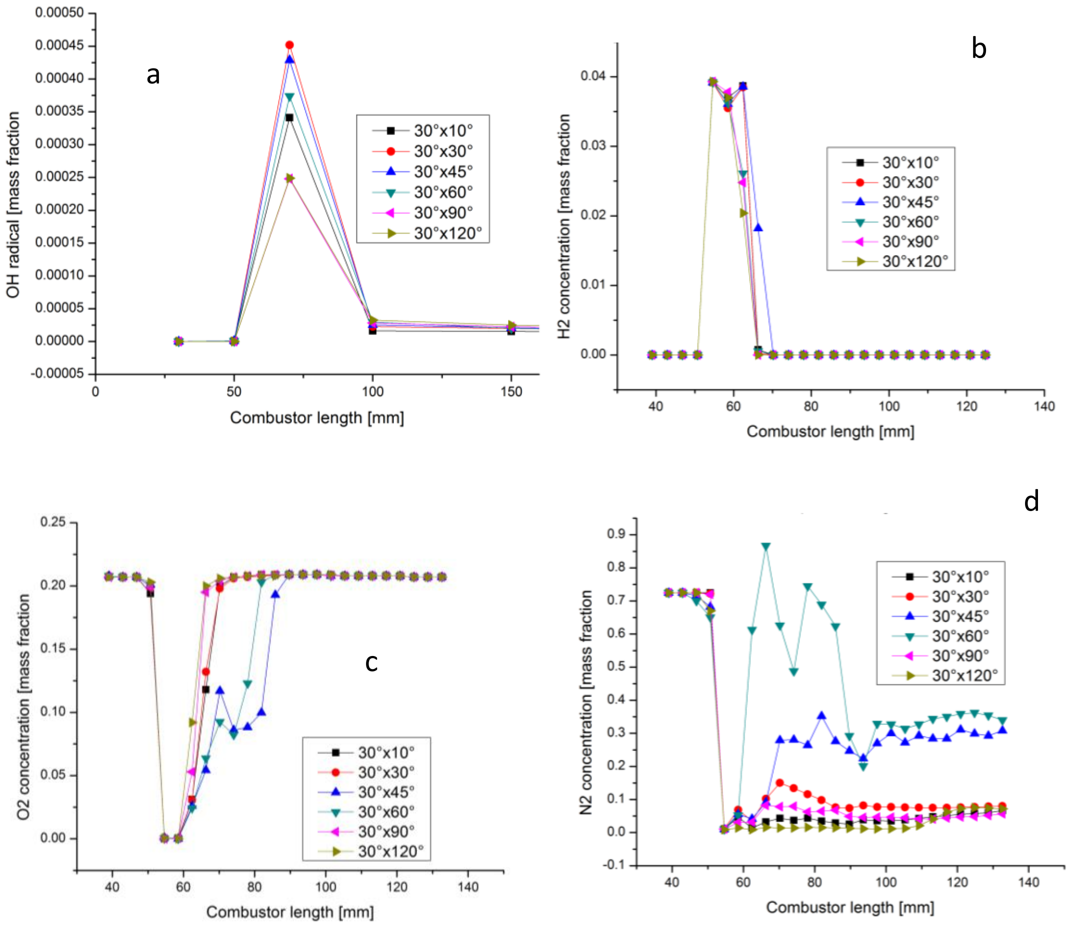

Figure 85 OH-a, H2-b, O2-c and N2-d average radical concentration [mass fraction] for 30° constant upstream angles at fuel-rich conditions

Figure 86 presents the total heat loss plotted for variable downstream angles. The total heat loss is seen to increases as the angles increase on the downstream side. For constant upstream of 30°, the increasing angles on the downstream side push more fuel towards the walls increasing the heat loss. There is a small gap for a 30°x45° configuration, where due to the separation of the recirculation zones, into two smaller, separate vortices, the flame is elongated towards the nozzle, removing some of the mixture from the walls. However, as angles increase, the vortices in the wake of the injector increase and the mixture is again pushed on the side walls, increasing the heat loss. This increase, at larger angles downstream, is smaller however. Due to the vortices in the wake of the injector and a lowering of the local equivalence ratio, the temperature of the flame decreased, lowering the degree of heat loss.

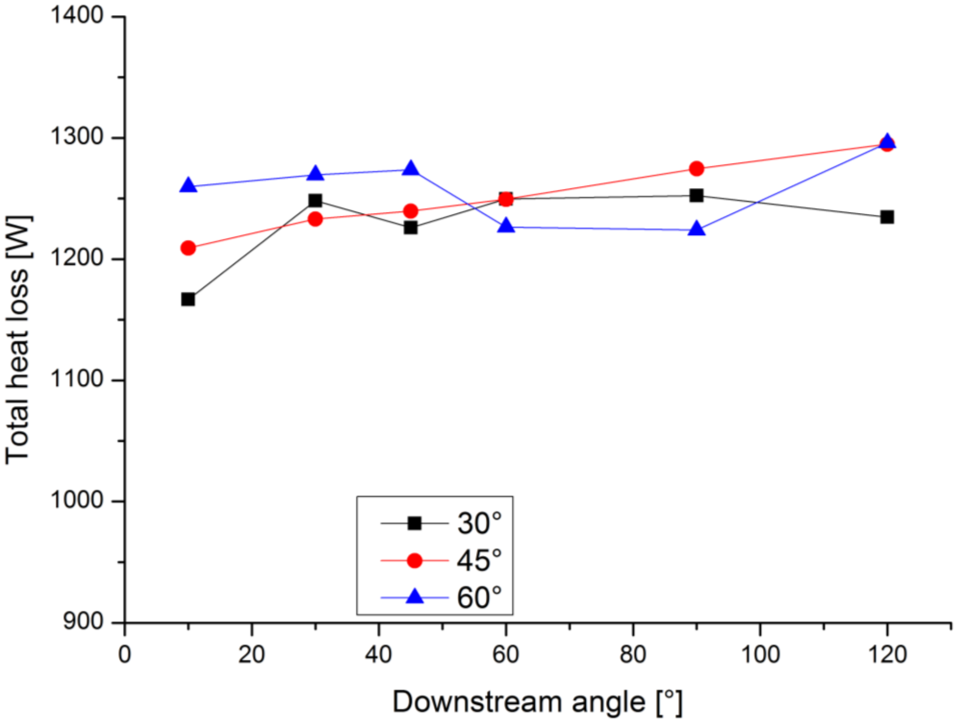

Figure 86 Total heat loss for constant upstream angles and variable downstream angles at fuel-rich conditions

Figure 87 presents the combustion efficiency for constant upstream angles of 30° and combustor length on the right side using the enthalpy approach (-a), the left side presents the chemical heat release approach (–b). The combustion efficiency is close to zero near the air inlet and increased after the injector. The peak of the combustion efficiency in the combustor is found between 100-150 mm from the inlet, which means maximum efficiency is achieved in the middle of the combustor. As the reaction has taken its course, with decreasing local equivalence ratio and temperature, the combustion efficiency slowly decreases downstream. In Figure 87-b, the heat release approach to the combustion efficiency is plotted for variable downstream angles. The graph presents a cumulative approach to the heat release in the wake of the injector. The trend of the heat release approach is however, indirect proportional to the enthalpy approach. The heat release in the chamber decreases as downstream angles increase, as the flow influences the mixing behavior of the flow, and subsequent heat loss at the walls increases.

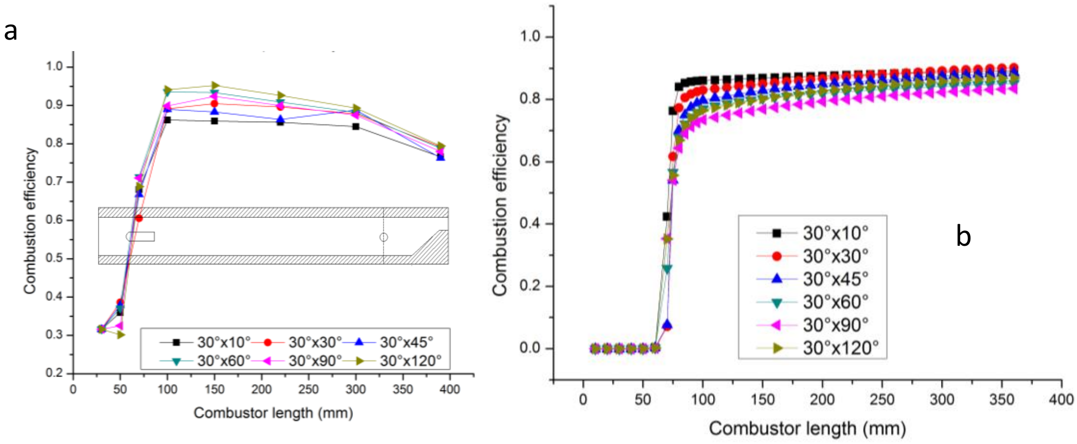

Figure 87 Combustion efficiency for constant upstream 30° angles at fuel-rich conditions; a- enthalpy difference approach, b- heat release approach

Figure 88 presents the overall combustion efficiency, using the two approaches, in the area of the nozzle of the combustor. The black lines present the A approach, the enthalpy difference, while the blue lines present the heat release approach at the spatial coordinate of 300 mm from the inlet. The combustion efficiency increases as the angles increase on the downstream angles, however, due to increasing heat loss at the walls, an independent approach to the combustion efficiency shows that as the angles increase, due to an enlargement of the recirculation zones in the wake of the injector, the combustion efficiency decreases.

Figure 89 presents the NO and NO2 distribution fields in the combustor for constant 30° upstream injection and variable downstream angles at fuel-rich conditions for 2 downstream angles. The configurations shown vary to show lowest and highest values of flame temperature. The distribution fields are enlarged to show the NO production in the combustor. Most of the NO and NO2 is formed in the wake of the injector and in the recirculation zones.

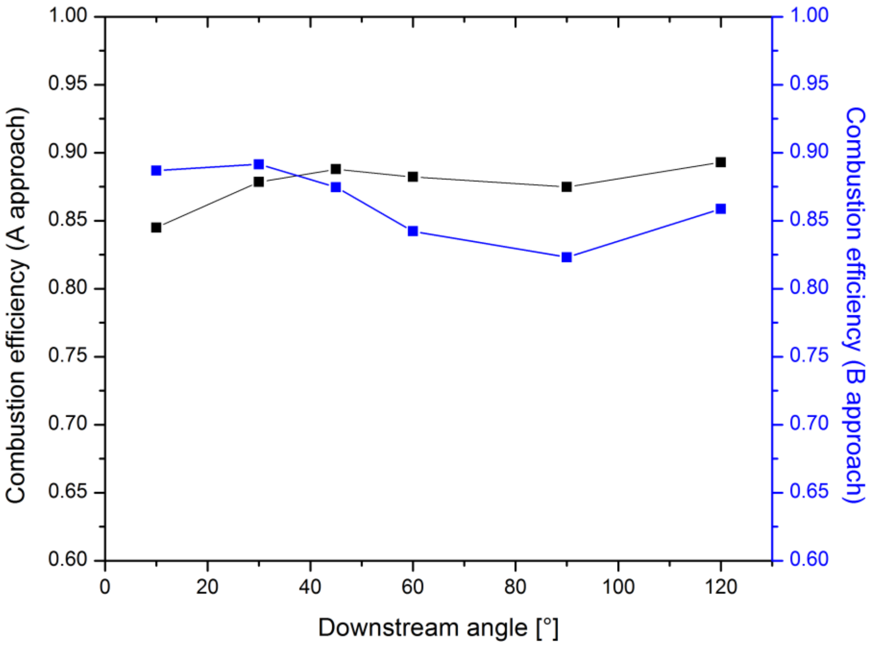

Figure 88 Overall combustion efficiency using the two approaches, enthalpy difference (black line) and chemical heat release (blue line) for constant upstream angles of 30°

The bulk of NO, seen in Figure 89 –a, and -c, was created in the center of the flame fronts, in what is called the post-flame region and in the center of the recirculation zones. It is created in the center of the flame fronts through thermal mechanisms that require high temperatures, and closer to the visible flame zone as the amount of oxygen in the area was sufficient to generate NO. The vortices entrap unburned gases and oxygen, thus the lower local equivalence ratio. Having pockets of unburned oxygen, NO creation is thus favored. The NO2 on the other hand, can be seen forming earlier than the NO, in the pre-flame region, continuing to increase in concentration farther downstream. The NO2, observed in Figure 89-b, and -d, is formed closer to the edges of the flame as the oxygen concentration is higher.

The concentration of NO2 decreased significantly in the wake of the injector, in the post-flame region, and was coincident with a corresponding formation of NO.

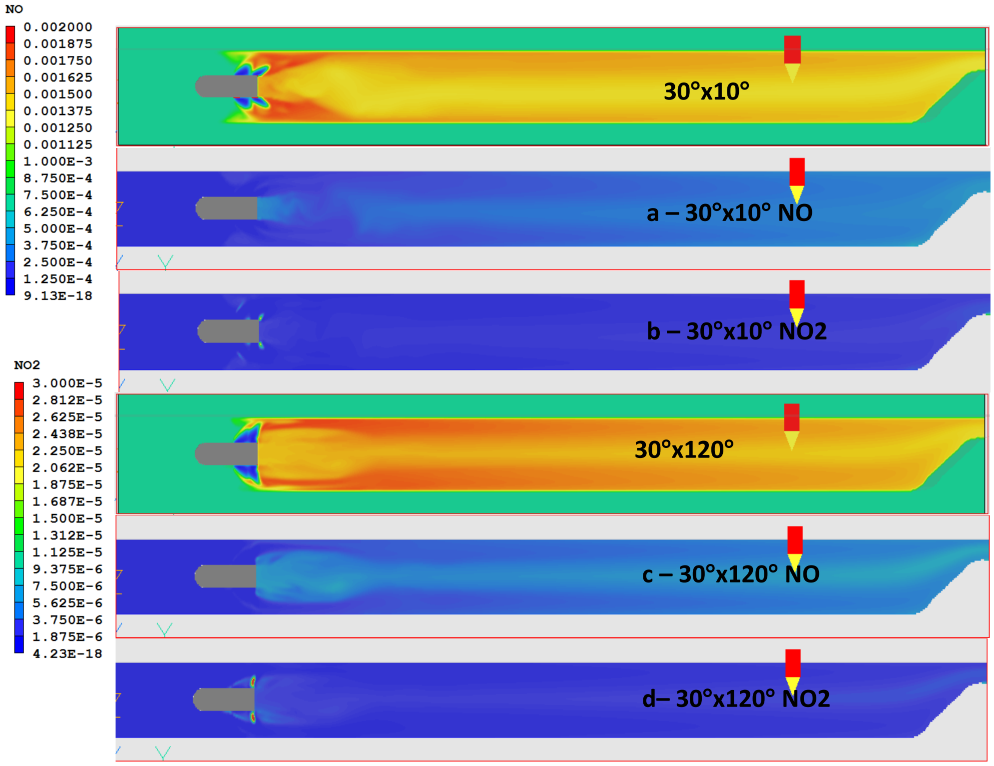

Figure 89 NO and NO2 mass fraction distribution fields in the combustor for a 30°x10° (a and b) and 30°x120° (c and d) configurations at fuel-rich conditions

Figure 90 presents the NO and NO2 mass fraction plotted in the length of the combustor for variable downstream angles at constant upstream angles of 30°. NO is created near the hot region of the flames and as seen in the previous figure, in the recirculation zones. The bulk is created near the injector, after which, due to a decrease in local equivalence ratio, the radicals are dissociated due to high temperatures and are recombined into NO and NO products. The NO2, on the other hand, as seen from Figure 90, is produced earlier in the combustor but follows the same trend as the NO production, for the same reasons. The results support previous conclusions found for fuel-lean configurations, that NO2 is not present in the main reaction zones at high temperatures and that it appears at the base of the flame and along the flame fronts, where temperatures are lower.

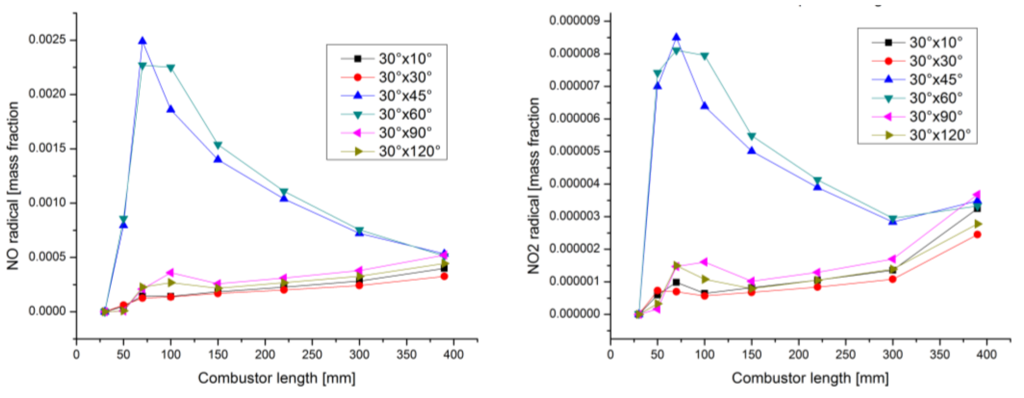

Figure 90 NO and NO2 mass fraction distribution in the combustor for constant 30° upstream injection at fuel-rich conditions

If for fuel-lean conditions, the shorter the combustor, the larger the amount of NO, for fuel-rich conditions the shorter the combustor the smaller the amounts of NOx produced, invariable of the injection angles.

When the EINOx is plotted, for variable downstream angles, in Figure 91, alongside the other configurations, the EINOx is seen to be directly proportional to the evolution of the combustion efficiency presented in Figure 88 and Figure 89. As the combustion efficiency increases, raised by the temperature near the nozzle, increased by the local equivalence ratio, the NOx index increases. While temperature alone is not the only cause of the NOx increase, various reactions taking place in the consumption and creation of NOx are of importance. A detail explanation of all reaction mechanism will be presented in section 4.5. As the recirculation zones expand and the average temperature decreases, so does the EINOx with larger downstream angles.

Figure 92 present the temperature field distributions on the top side and velocity fields for upstream angles of 45°, on the bottom. Figure 93 presents an enlargement of the injector region for the temperature field on the left side, and velocity vector distribution, on the right side, for the same configurations. In Figure 92 and Figure 93, from a, to f, the downstream angles increase from 10° (a) to 120° (f). As fuel is pushed with a larger angle towards the walls seen in Figure 92-a, and Figure 93-a, it is carried by the incoming airflow, mixing and producing higher heat loss at the walls.

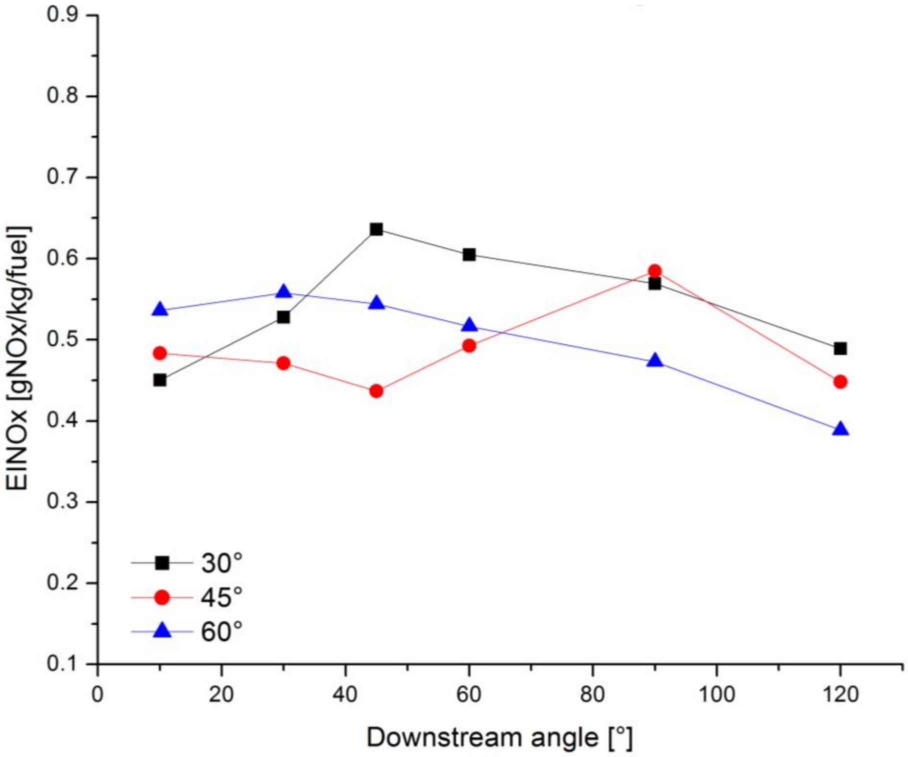

Figure 91 EINOx for constant upstream angles and variable downstream angles at at fuel-rich conditions

Through Figure 92 and Figure 93-b,-c and -d, the recirculation zone is clearly seen as getting smaller in size and stronger i.e. assumed faster azimuthal velocity. This increase in strength can be observed in Figure 93-d, where, although the airflow carries the fresh unburned gases downstream, the high-temperature mixture is pushed to the sides, by the strong vortices in the recirculation zone. It also can be observed that as the zone becomes stronger; its size shrinks, when the vortices break down into smaller structures. In Figure 92 and Figure 93-e and -f, the recirculation zone in the wake of the injector breaks down, as fuel is injected perpendicularly. As this happens, an increase in combustion efficiency is expected.

With increasing angles on the upstream, the flame height seemed more compact. For a 45°x10° configuration, the size and shape of the recirculation zones is compared with a 30°x10° configuration in Figure 94, through velocity vector distribution. These recirculation zones are the result of increased velocity on the upper and lower side flame fronts. By increasing the velocity in the area, so does the temperature and implicit heat loss at the walls.

When the temperature is plotted for the length of the combustor vs. the heat loss in the chamber, observed in Figure 95, the mixture yields the highest temperature near the injector. The heat loss, due to small angles on the downstream is relatively small near this area, compared with the rest of the chamber. In the figure, configurations with fixed downstream angles of 10° have been added for comparison.

From Figure 95, it can be seen that higher upstream angles with a fixed 10° angle on the downstream, not only raise the temperature in the chamber, due to an increase in the local equivalence ratio shown in Figure 96, but also raise the heat loss at the walls for the same reasons. As the flame evolves downstream, the average temperature decreases due to a dilution of the mixture by lower local equivalence ratio, after which the average temperature reaches a plateau faster for larger angles on the upstream, partly due to smaller recirculation zones. The heat loss, following the same arguments, slowly decreases in the chamber as the temperature decreased near the injector, and continued to decrease even as the temperature remained constant due to a decrease of the local equivalence ratio.

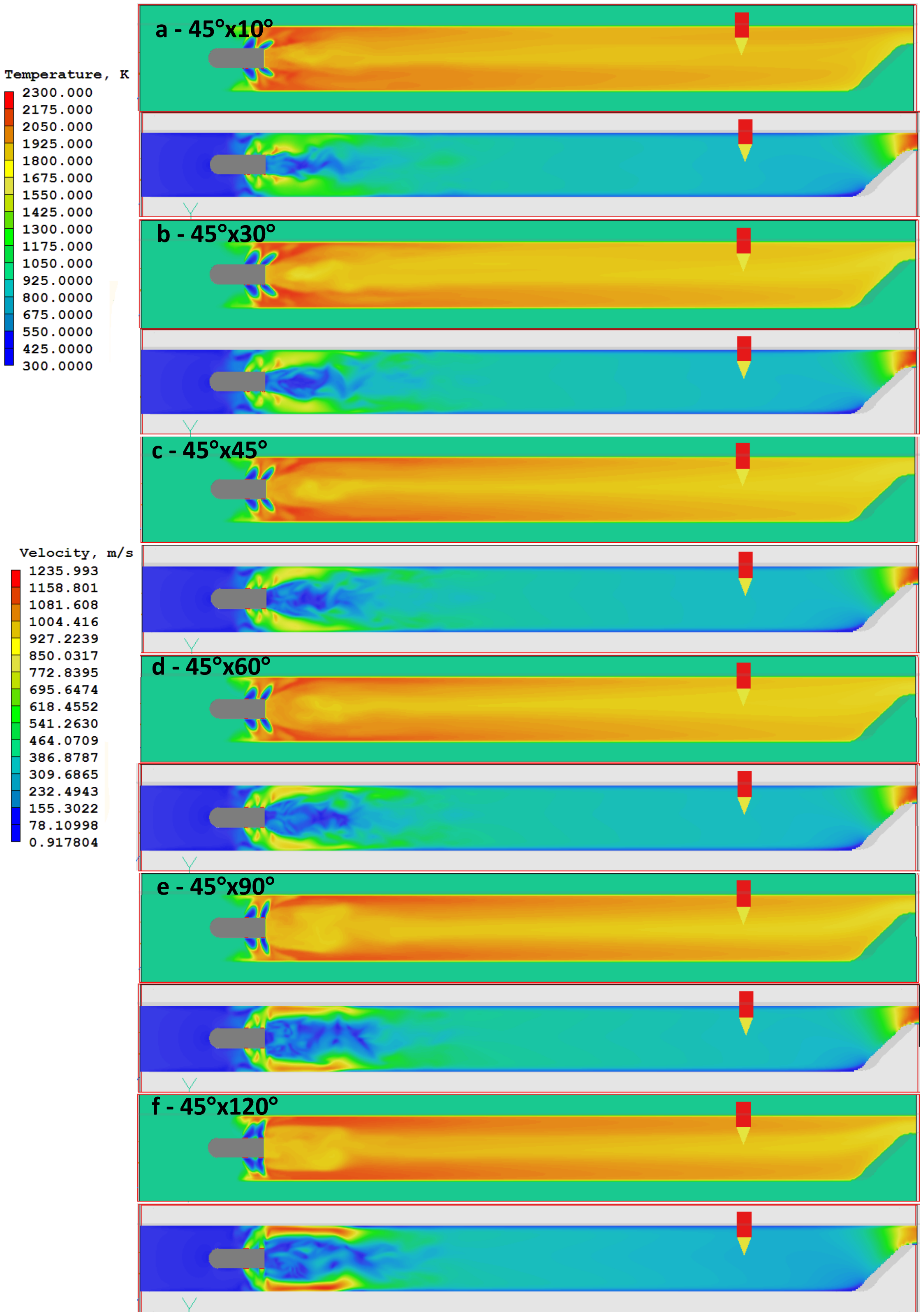

Figure 92 Temperature and velocity distribution field for constant upstream angle of 45° at fuel-rich conditions

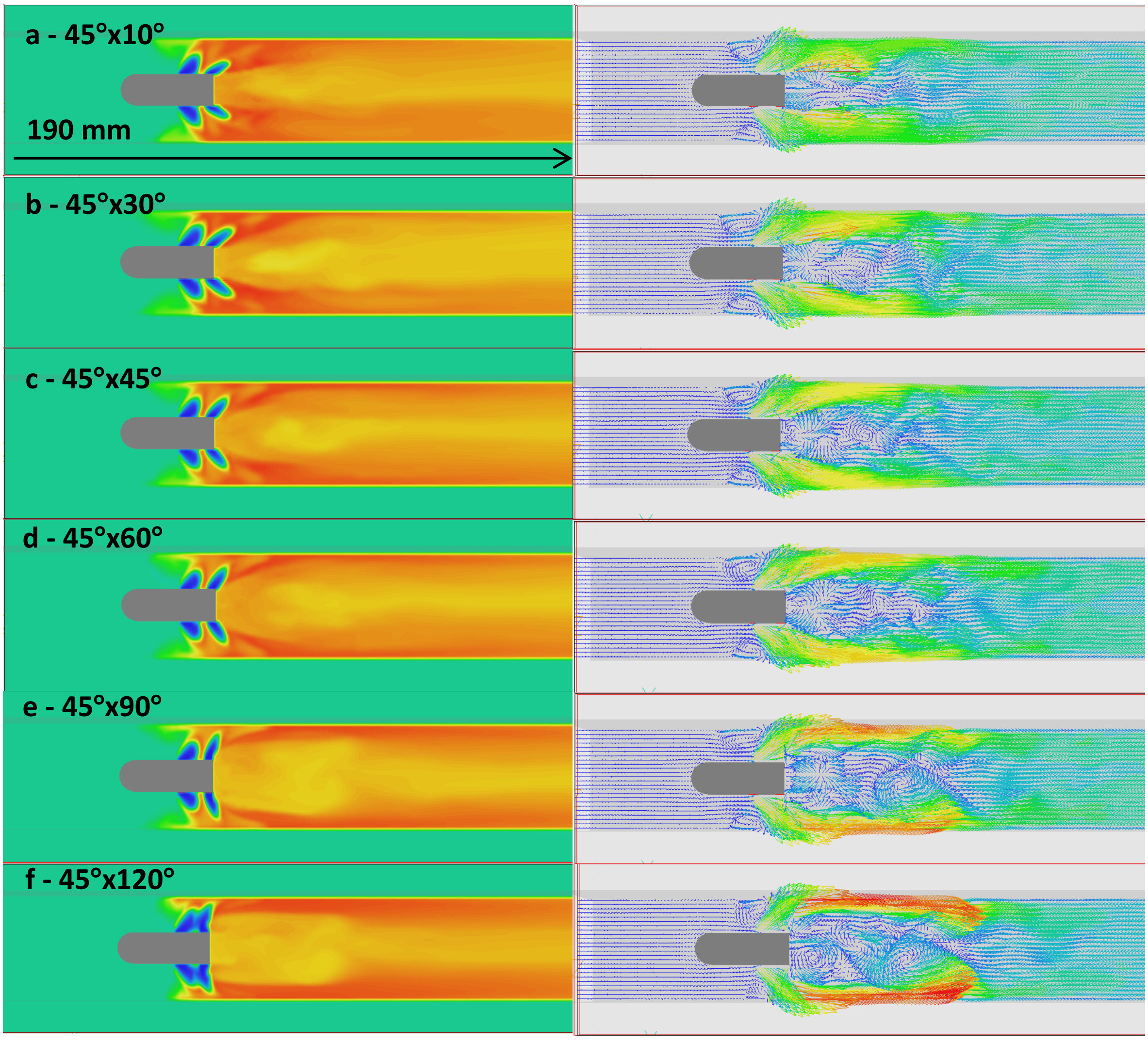

Figure 93 Enlarged temperature field distribution and velocity vector distribution near the injector for constant upstream angles 45° at fuel-rich conditions

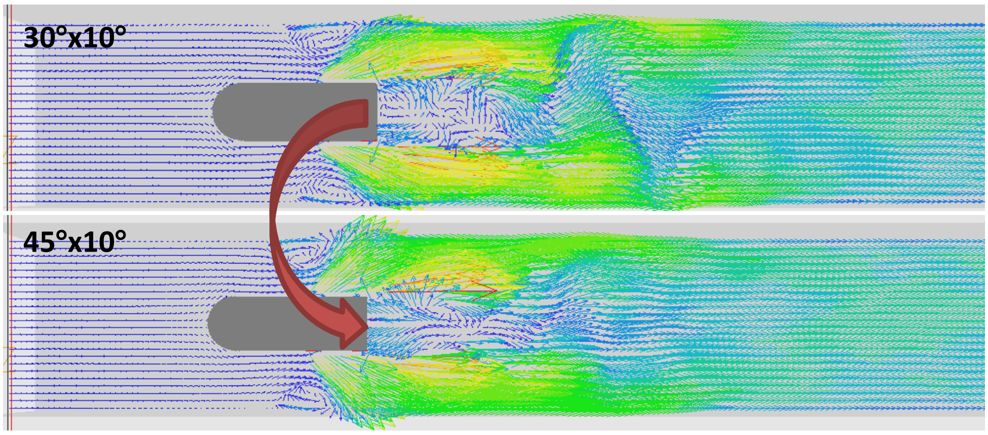

Figure 94 Enhanced recirculation zones in the wake of the injector for a 30°x10° (top) and 45°x10° (bottom) configurations at fuel-rich conditions

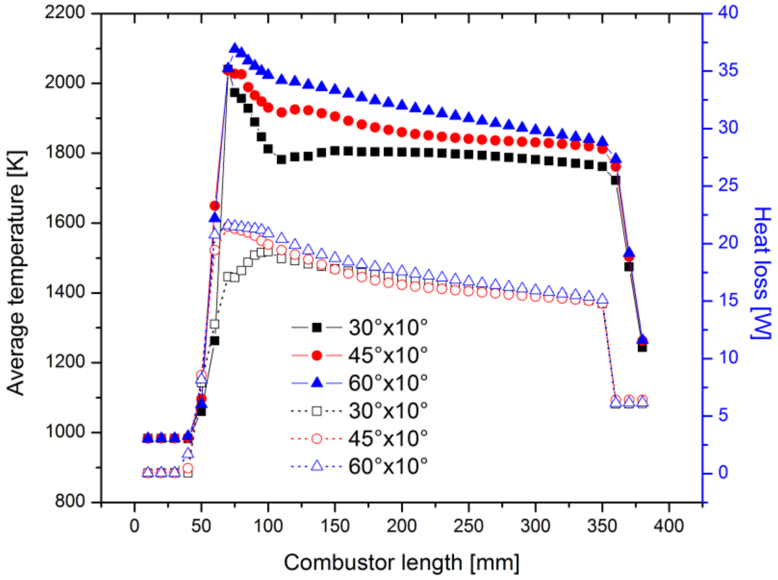

Figure 95 Average temperature (full points) and heat loss (hallow points) in the combustor for 30°x10° (black), 45°x10° (red) and 60°x10° (blue) at fuel-rich conditions

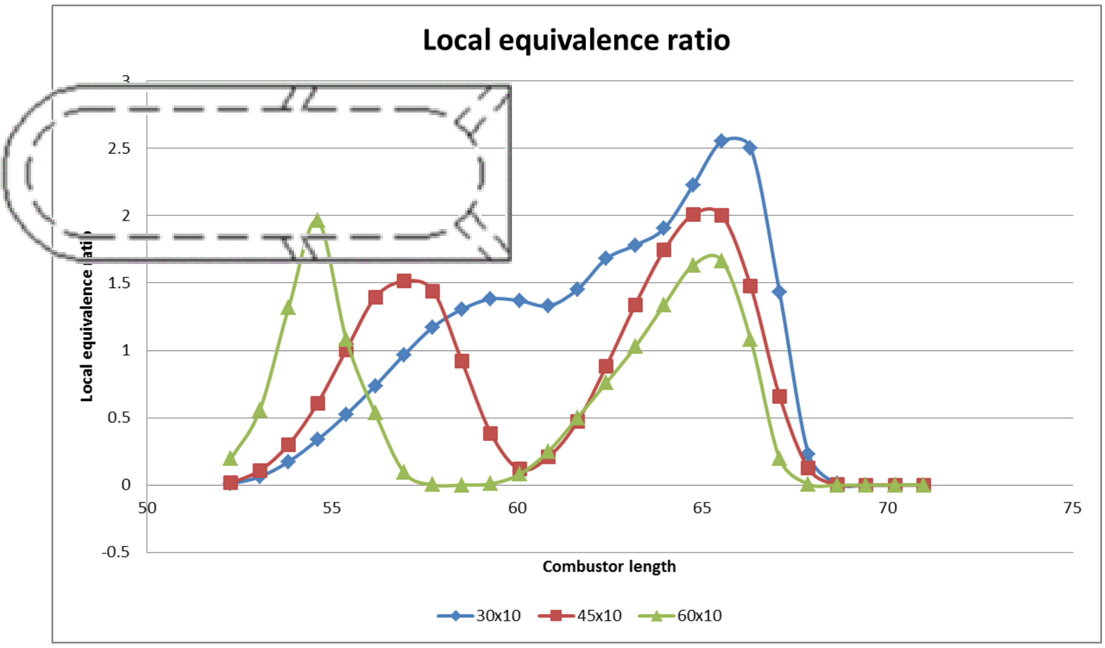

Figure 96 Local equivalence ratio in the wake of the injector for unburned products, for 30°x10° (blue), 45°x10° (red) and 60°x10° (green) at fuel-rich conditions

The local equivalence is highest for larger angles on the upstream injection pair, near the upstream and downstream injection holes but quickly drops in the wake of the injector due to recirculation zones that trapped amounts of unburned oxygen.

When the angles increase on the downstream, seen in Figure 92 and Figure 93-b, the injected fuel from the downstream pair, is carried closer to the walls of the combustor. This flow increases the contact of the mixture with the walls, increasing the heat loss, and also creates higher velocity areas close to the walls, due to reflected fuel. Another effect of larger angles downstream is that the major recirculation zone in the wake of the injector has its epicenter farther from the injector, which yields a lower temperature zone in the area seen in Figure 92 and Figure 93-b for the temperature distribution fields. The average temperature and heat loss for a 45°x30° configuration is presented in Figure 97. With larger angles and on the downstream, the flame temperature is higher on the walls sides, with slightly asymmetric behavior due to the ramp-shaped nozzle, and lower temperature near the axisymmetric axis, shown in Figure 93-b. The lower temperature regions are due to the presence of the recirculation zones, by a decrease of local equivalence ratio, and vortex breakdowns suffered downstream.

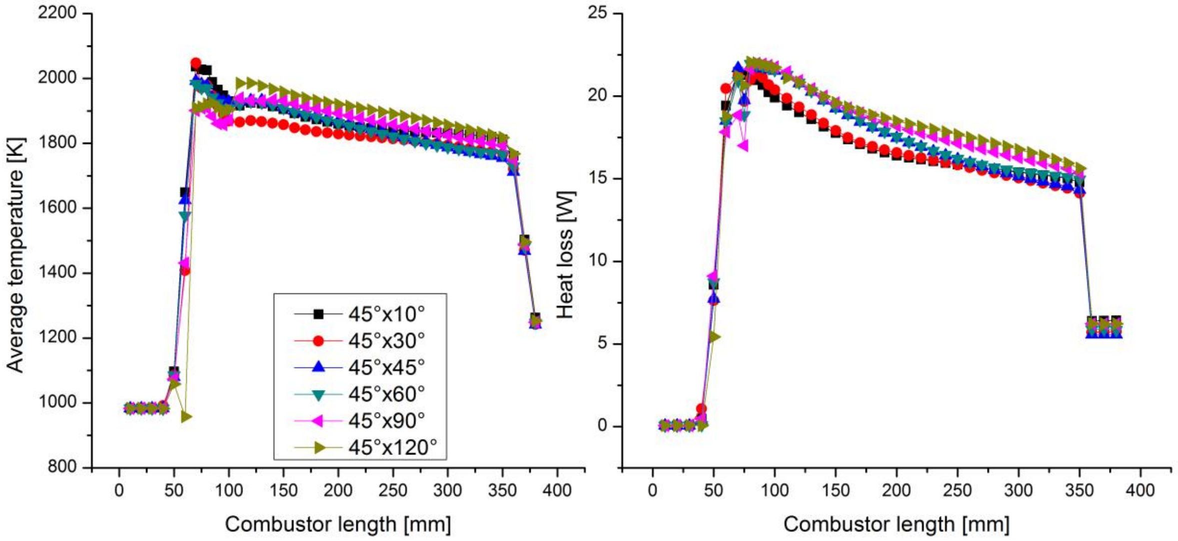

Figure 97 Average temperature (left side) and heat loss (right side) in the combustor for constant upstream 45° and variable downstream angles at fuel-rich conditions

For a configuration of 45°x45°, shown in Figure 92 and Figure 93-c, a similar trend to the previous configuration is observed. The increasing angles inject fuel closer to the walls and as a result the highest value of heat lost is closer to the injector. With larger angles, the downstream 1st recirculation zone actually becomes more compact as its epicenter moves closer to the injector, observed in Figure 92 and Figure 93-b, and -c. This allows for a smaller area in the center of the flame, where the temperature is lower and larger areas on the sides, in contact with the walls. Due to this effect, the local equivalence ratio increase (Figure 96), and so does the average temperature in the chamber seen in Figure 97, left side. The average temperature and heat loss for this configuration is presented in Figure 97 through the [blue] triangles.

Due to larger angles on the downstream and prolonged contact of the mixture with the walls, the average temperature actually decreased. The heat loss is higher near the injector, however due to the flow-induced, downstream recirculation zone, the heat loss decreased farther downstream.

When angles are increased to 60° on the downstream injection holes, shown in Figure 92 and Figure 93-d, heat loss increased in the area, shown in Figure 97, right side, and due to the larger angles downstream, the first recirculation zones in the wake of the injector, grow slightly in size. The average temperature and heat loss plot for a 45°x60° configuration is shown in Figure 97, through the inverted [teal] triangles. The peak of the heat loss in the combustor is moved farther away from the injector, due to the large angles, which increased the overall values of the heat loss.

When the downstream angles are increased to 90°, a direct effect of this is larger heat loss associated, not only in the injection area, but overall, as more fuel is injected directly at the walls. The second visible effect is that the flame temperature is higher farther downstream of the injector, than near the injection holes. This is a result of the 2nd recirculation zone that enlarges, shown in Figure 98. Due to this enlargement, larger amounts of mixed gases are trapped and the local temperature decreases, shown in Figure 97, impeding mixing in the area, shown in Figure 96. The average temperature and heat loss in the combustor is shown in Figure 97, left side. The heat loss is largest for this configuration as shown in Figure 97, right side.

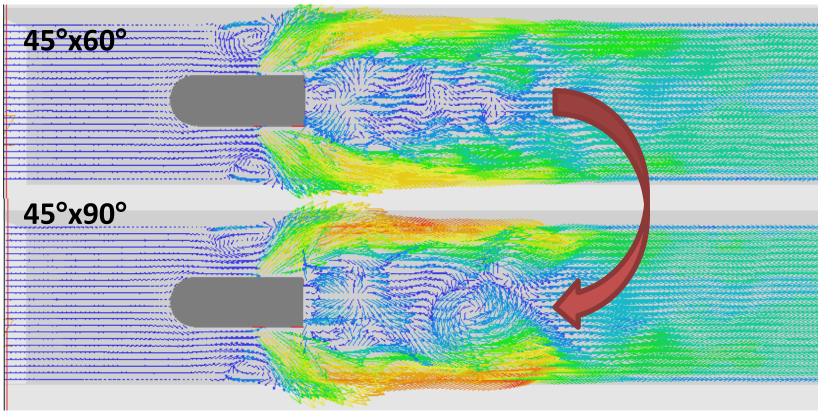

Figure 98 Enhanced recirculation zones in the wake of the injector for a 45°x60° (top) and 45°x90° (bottom) configurations at fuel-rich conditions

When the downstream angle is increased to 120°, seen in Figure 92-f and Figure 93-f, the large recirculation zones are broken down into smaller vortex structures. Due to these vortex structures, the high temperature part of the flame is on the sides of the combustor walls, where mixture increased, as seen in Figure 96. The average temperature and heat loss plot, in the combustor for 45°x120° configuration is presented in Figure 97. Due to the large recirculation zones in the wake of the injector, the average temperature near the injector is lower, and later it increased. The vortices finally break down away from the injector. The heat loss on the other hand is highest near the injector and decreases steadily in the chamber downstream.

The average temperature and heat loss for constant upstream angles of 45°, shown in Figure 97 follow the same trend as the previous configuration, where large angles on the downstream i.e. 120°, generate higher temperature and, due to their effect, higher heat loss. When downstream angles increase, the average temperature increases in the chamber. Larger angles on the downstream side coupled with larger angles on the upstream side, allow for larger recirculation zones farther away from the injector. As the angles increased on the upstream side, the recirculation zones in the wake of the injector were broken down for larger angles on the downstream i.e. 60° on the downstream, for constant 30° on the upstream, and 120° on the downstream for constant upstream 45°.

Figure 99 presents the chemical heat release plotted for constant upstream angles of 45°. When the upstream angles were kept constant, the heat release in the chamber increased, when a 45°x30° configuration was achieved, due to smaller recirculation zones in the wake of the injector which when the local equivalence ratio was higher. However, as angles increased on the downstream side, the local equivalence decreased due to an enlargement of the recirculation zones in the wake of the injector. In the figure, the maximum heat release is shown for a 45°x120° configuration. In the injector wake however, as can be seen from the OH concentration in the flame, in Figure 100-a, the 45°x30° configuration has the largest amount for the reasons explained above.

In Figure 100-b, -c and -d, the concentration of H2, O2 and N2 is plotted for different downstream angles, when the upstream angle is fixed at 45°. From the H2, O2 and N2 concentration we see that a large part of the radicals are consumed near the higher upstream angles, and the rest around the downstream injection holes. When the angles increase on the downstream side, the large bulk of the radicals are consumed near the downstream injection holes. There is a large variation of N2 farther downstream as an effect of vortex breakdown seen in Figure 92 and Figure 93-d.

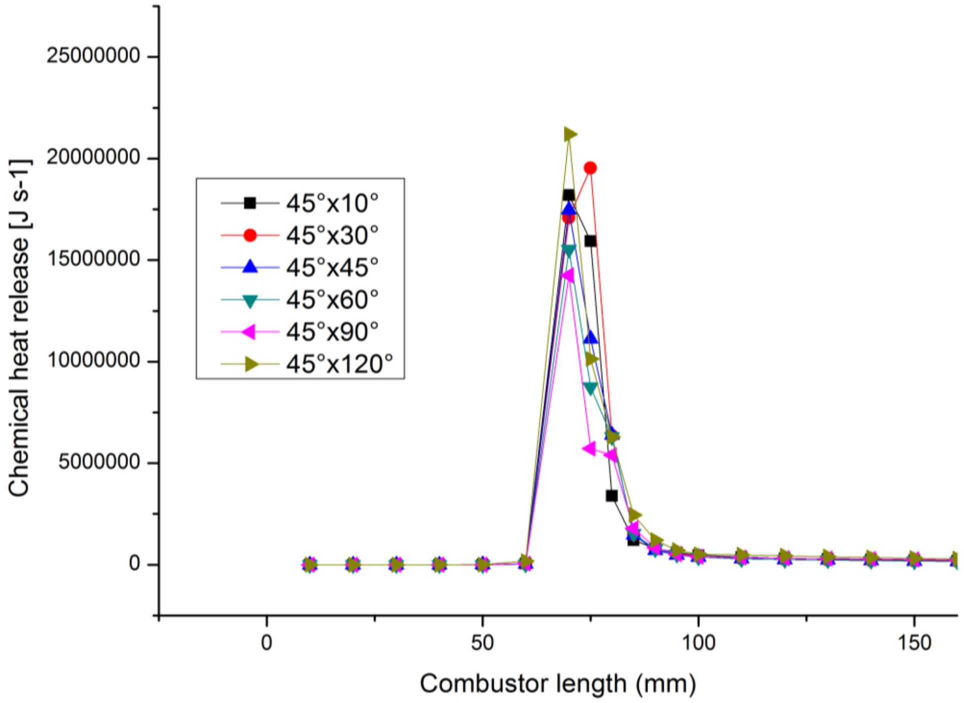

Figure 99 Chemical heat release for constant 45° upstream angles at fuel-rich conditions

Figure 86 presents the total heat loss plotted for variable downstream angles with fixed 45° upstream injection, through the [red] circles. The total heat loss is seen to increases uniformly, as the angles increase on the downstream side. Larger angles on the downstream as seen from Figure 97, right side, create recirculation zones that expand farther in the combustor, which “force” the high temperature part of the flame to be in longer contact with the walls of the combustor which add up to larger heat loss in the chamber.

Figure 101 presents the combustion efficiency for constant upstream angles of 45° and combustor length on the right side using the enthalpy approach (-a), the left side presents the chemical heat release approach (–b). The peak of the combustion efficiency in the combustor, for higher angles on the upstream is found closer to the injector around 100 mm from the inlet, which led to a larger temperature difference of about 70-150 K, compared with the previous configuration where it was around 10-100 K. In Figure 101-b, the values of combustion efficiency using the heat release approach, are plotted for variable downstream angles. While it is difficult to see the difference between the angles clearly, one observation can be made that higher downstream angles decrease the combustion efficiency.

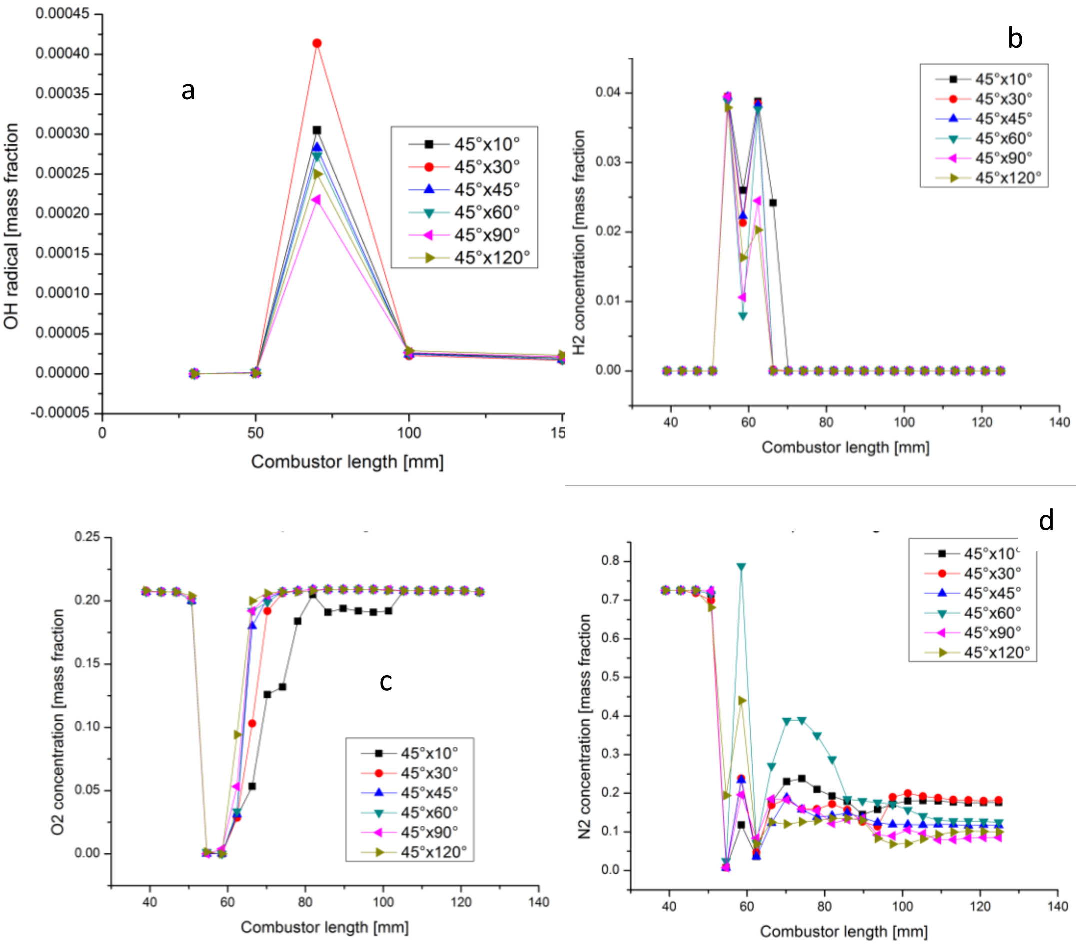

Figure 100 OH-a, H2-b, O2-c and N2-d average radical concentration [mass fraction] for 45° constant upstream angles at fuel-rich conditions

Figure 102 presents the overall combustion efficiency, using the two approaches, in the area of the nozzle of the combustor. The black lines present the A approach, the enthalpy difference, while the blue lines present the heat release approach at the spatial coordinate of 300 mm from the inlet. The combustion efficiency, evaluated using the enthalpy approach, for constant upstream angles of 45°, due to the presence of the recirculation zones, and the small difference in temperature caused by these vortices, reach similar values near the nozzle. The effect of the angles is situated closer to the injector, thus having little influence on the nozzle temperature. When the heat release approach is implemented, the combustion efficiency decreased with increasing angles on the downstream side. There is an increase for a configuration of 45°x120°, as explained in Figure 100, due to larger heat release in the chamber, as the equivalence ratio increased.

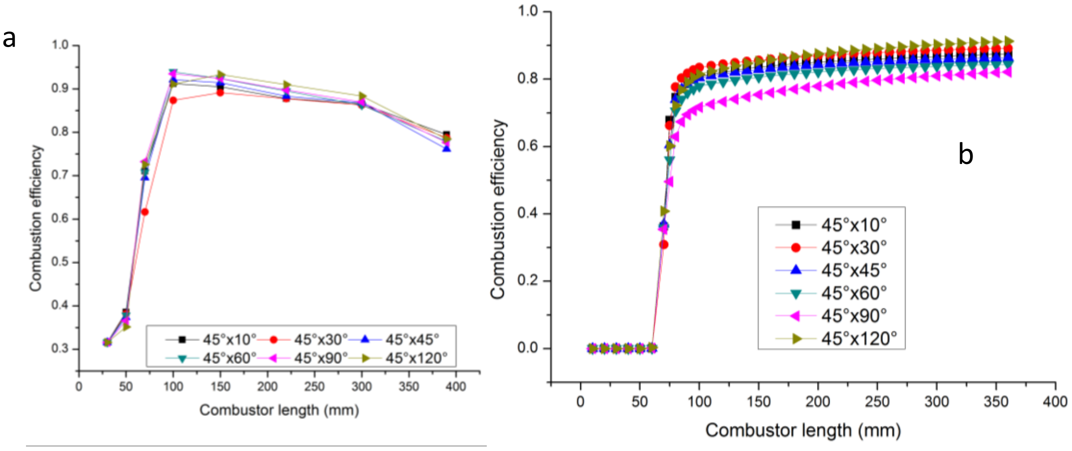

Figure 101 Combustion efficiency in the combustor for variable downstream angles at constant upstream 45° angles at fuel-rich conditions; a- enthalpy difference approach, b- heat release approach

Figure 103 presents the NO and NO2 mass fraction plotted in the length of the combustor for variable downstream angles at constant upstream angles of 45°. Large amounts of NO and NO2 are created in larger recirculation zones which are characteristic of 45°x10° configuration. When the two recirculation zones in the wake of the injector separate for angles on the downstream higher than 45°, the NO and NO2 production is lowered, only increasing when the vortices are broken down into smaller structures for a 45°x120° configuration.

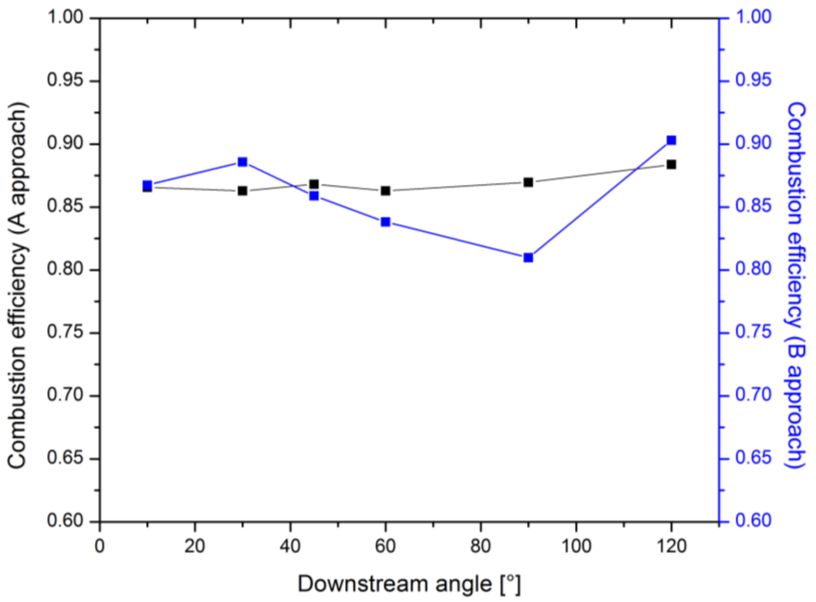

Figure 102 Overall combustion efficiency using the two approaches, enthalpy difference (black line) and chemical heat release (blue line) for constant upstream angles of 45°

The configurations that generate asymmetry are shown in Figure 103, and due to this exact effect, generate the largest amount of NO near the injector, after which the NOx production decreases downstream. The results support previous conclusions found for fuel-lean configurations, that NO2 is not present in the main reaction zones at high temperatures and that it appears at the base of the flame and along the flame fronts, where temperatures are lower.

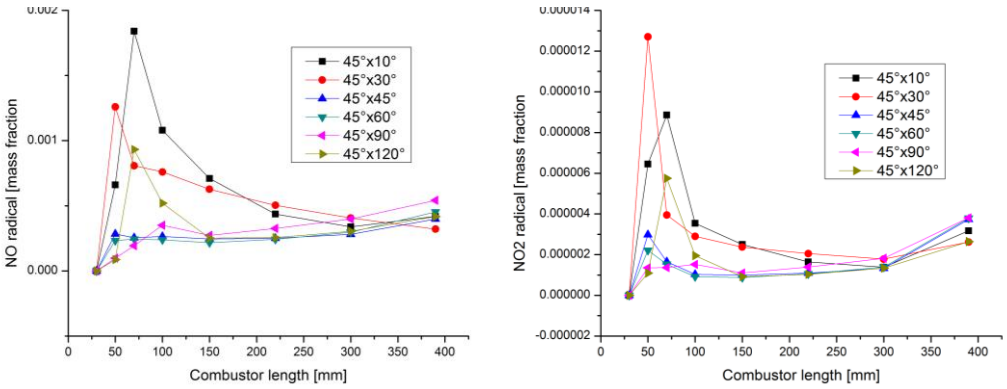

Figure 103 NO and NO2 mass fraction distribution in the combustor for constant 45° upstream injection at fuel-rich conditions

When the EINOx is plotted, for variable downstream angles, in Figure 91, the EINOx decreases due to the asymmetry effect on the NO and NO2, where the bulk is created in large amounts near the injector and as it is carried downstream it actually dissociates and the resulting EINOx is lower. For large angles on the downstream however, due to an extended recirculation zone, the NO has longer residence time in the flame thus, larger values measured near the nozzle, with the largest value for perpendicular injection at 45°x90°. As the vortices in the wake of the injector breakdown, the NOx values enlarged in the wake of the injector due to the turbulence effect, and lowered near the nozzle.

Preliminary conclusions for this configuration include:

- Flame asymmetry caused by larger angles on the upstream coupled with large angles on the downstream create more NOx in the area, and is consumed faster downstream, generating lower NOx overall.
- The angles have little influence on the combustion efficiency near the nozzle, when the maximum values move closer to the injector.
- Heat loss increases with larger downstream angles.

Figure 105 present the temperature field distributions, on the top, and velocity fields, on the bottom, for upstream angles of 60°. Figure 106 presents an enlargement of the injector region for the temperature field, on the left, and velocity vector distribution, on the right side for the same configurations. In Figure 105 and Figure 106, from a, to f, the downstream angles increase from 10° (a) to 120° (f). As fuel is pushed with a larger angle towards the walls seen in Figure 105-a, and Figure 106-a, it is carried by the incoming airflow, mixing and producing higher heat loss at the walls. When the angle are increased on the downstream side, the recirculation zones in the wake of the injector are smaller, forced by the overlapping injection fronts (fuel injected by the upstream and downstream injection holes)on the upper side and lower side of the combustor. By increasing the velocity in the area, so does the temperature and implicit heat loss at the walls.

When the temperature is plotted for the length of the combustor vs. the heat loss in the chamber, observed in Figure 95, the mixture yields the highest temperature near the injector. The heat loss, due to small angles on the downstream is relatively small near this area, compared with the rest of the chamber. In the figure, configurations with fixed downstream angles of 10° have been added for comparison. Higher angles on the upstream enhance mixing, seen in Figure 96, on the upper and lower sides of the combustor and as a result the local temperature increased. With this rise, an increase in the heat loss is observed as well. As the flame evolves downstream, the average temperature decreases due to a dilution of the mixture by lower local equivalence ratio, after which the average temperature reaches a plateau faster for larger angles on the upstream, partly due to smaller recirculation zones. The heat loss, following the same arguments, slowly decreases in the chamber as the temperature decreased near the injector, and continued to decrease even as the temperature remained constant due to a decrease of the local equivalence ratio.

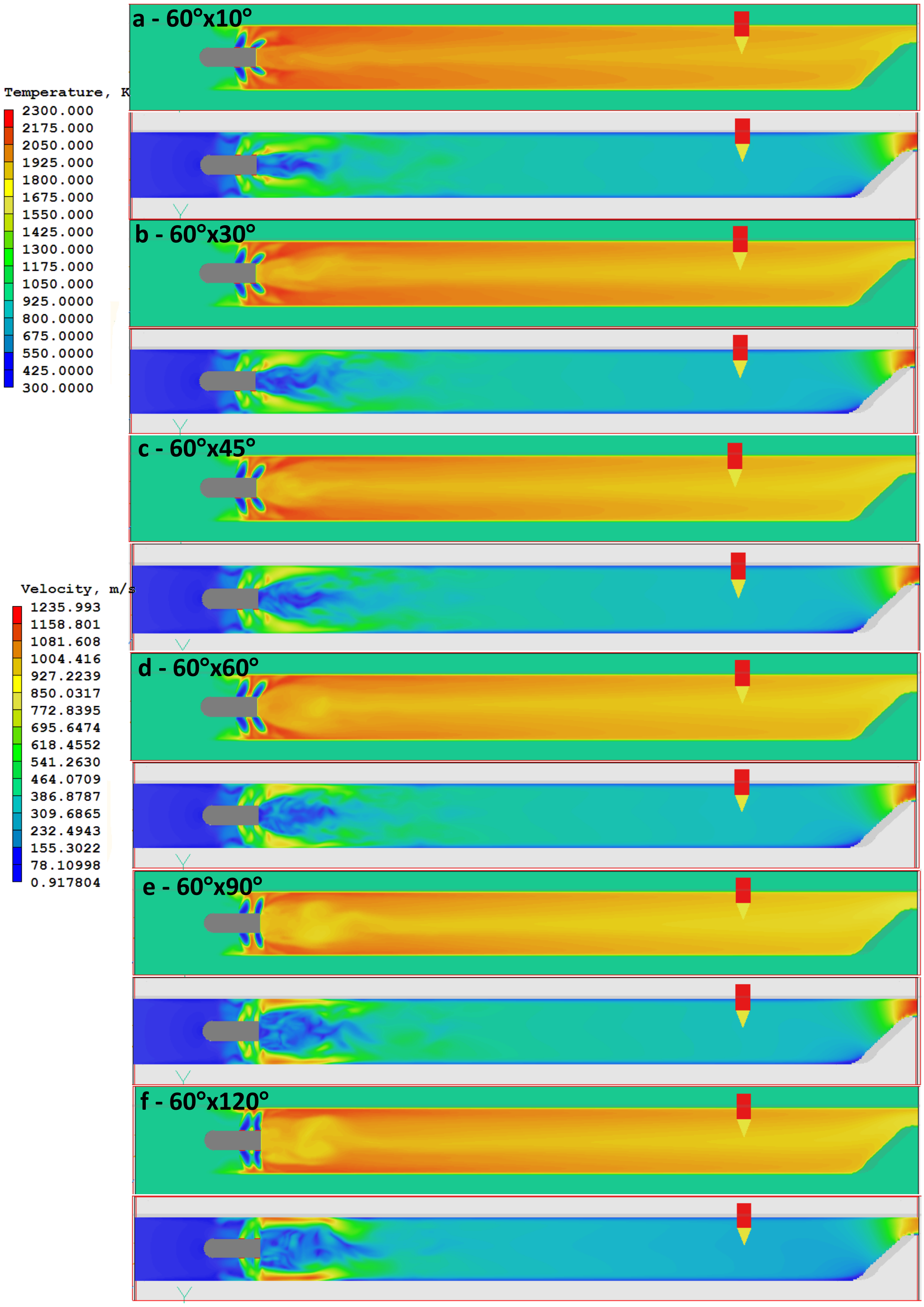

Figure 104 Temperature and velocity distribution field for constant upstream angle of 60° at fuel-rich conditions

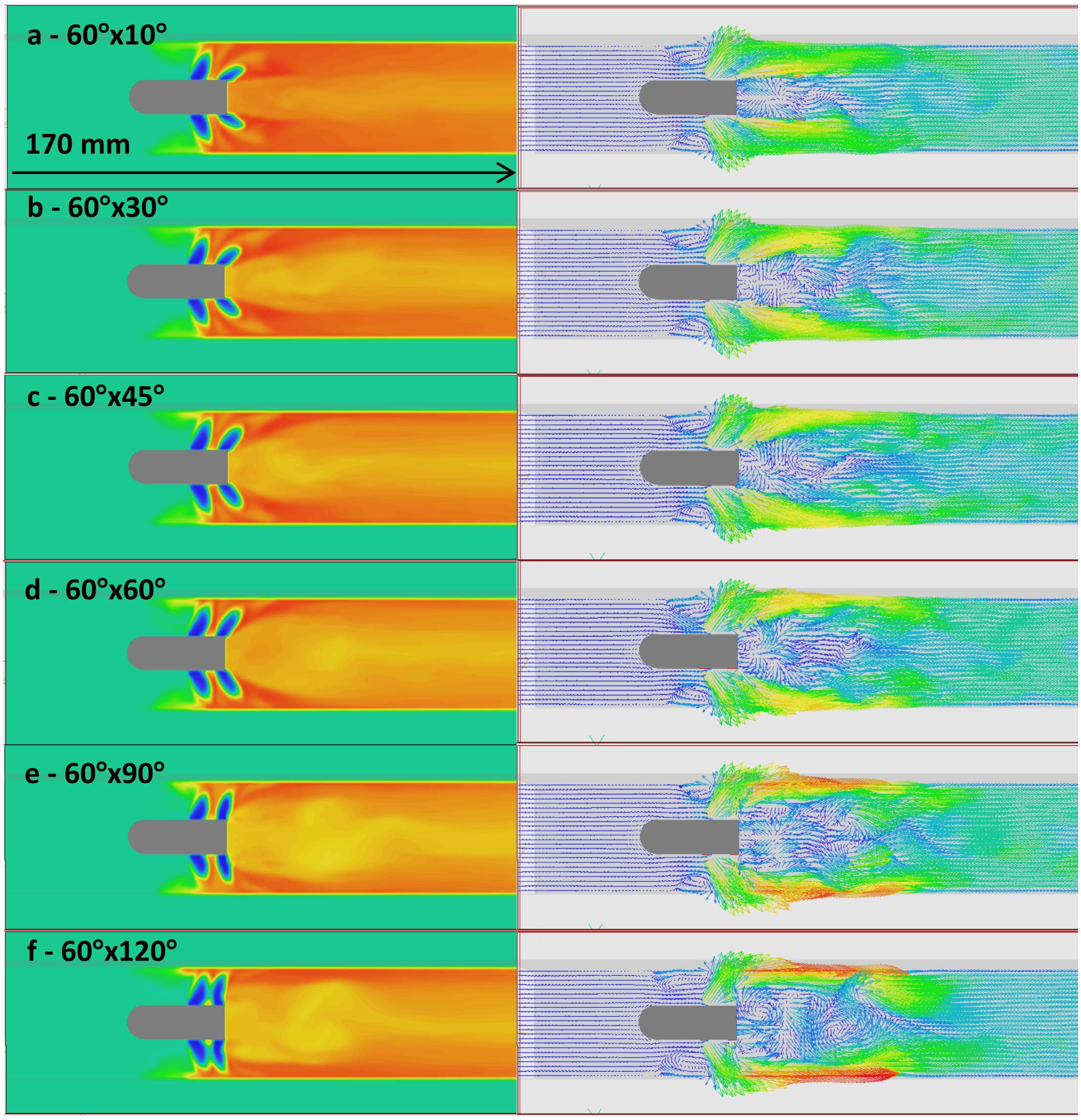

Figure 105 Enlarged temperature field distribution and velocity vector distribution near the injector for constant upstream angles 60° at fuel-rich conditions

When the angles increase on the downstream, seen in Figure 105 and Figure 106-b, the injected fuel from the downstream pair, is carried closer to the walls of the combustor increasing the heat loss and due to the effect of a single recirculation zone, decreases the local temperature in the area, lowering the average temperature. Another effect of larger angles downstream is that the major recirculation zone in the wake of the injector has its epicenter, this time closer to the injector. The average temperature and heat loss for a 60°x30° configuration is presented in **Error! Reference source not found.**, alongside the ther configurations with constant upstream angles. With larger angles and on the downstream, similar behavior is observed as for the previous configurations, higher temperature on the side walls and lower temperature near the middle of the chamber. The lower temperature regions are due to the presence of the recirculation zones, and as they increase with increasing downstream angles.

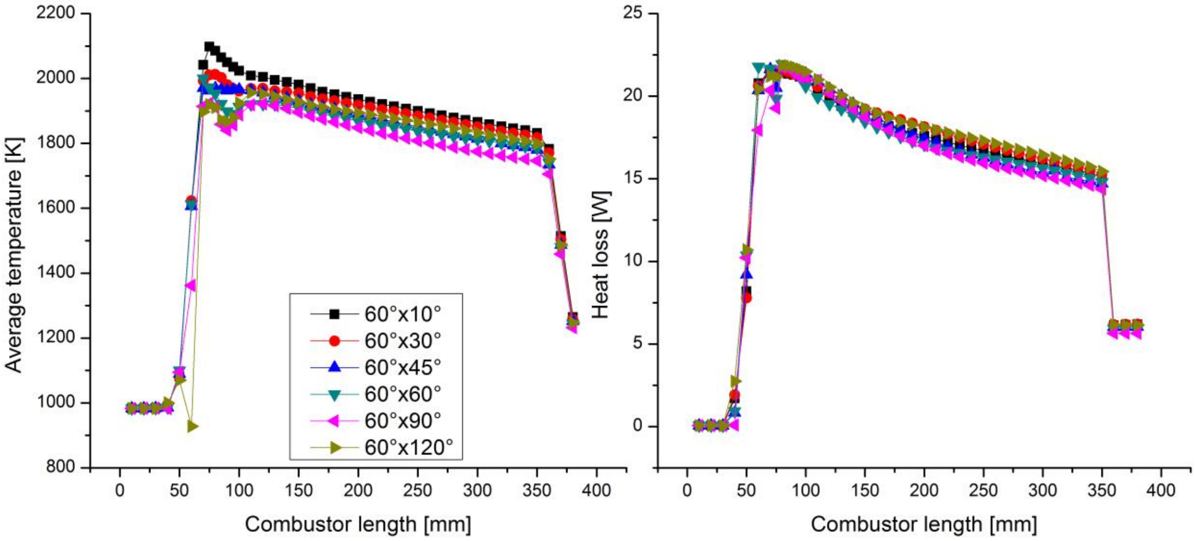

Figure 106 Average temperature (left side) and heat loss (right side) in the combustor for constant upstream 60° and variable downstream angles at fuel-rich conditions

For a configuration of 60°x45°, shown in Figure 105 and Figure 106-c, a similar trend to the previous configuration is observed. With larger angles, the downstream 1^{st} recirculation zone actually becomes larger as its epicenter moves farther from the injector, observed in Figure 105 and Figure 106-b, and -c. This allows for a larger area in the center of the flame, where the temperature is lower and smaller areas on the sides, in contact with the walls. Due to this effect, the local equivalence ratio decreases, and so does the average temperature in the chamber seen in **Error! Reference source not found.**, on the left side. he average temperature and heat loss for this configuration is presented in **Error! Reference source not found.**.

Due to larger angles on the downstream and an increasing recirculation zone in the wake of the injector, the average temperature actually decreased. The heat loss is higher near the injector, however due to the flow-induced, downstream recirculation zone, the heat loss decreased farther downstream.

When angles are increased to 60° on the downstream injection holes, shown in Figure 105 and Figure 106-d, heat loss increased in the area, but only slightly, shown in **Error! Reference source not found.**, right side, and due to the larger angles downstream, the first recirculation zones in the wake of the injector becomes more coherent, with its epicenter closer to the injector. The average temperature and heat loss plot for a 60°x60° configuration is shown in **Error! Reference source not found.**, as inverted [teal] triangles.

When the downstream angles are increased to 90°, a direct effect of this is larger heat loss associated, not only in the injection area, but overall, as more fuel is injected directly at the walls. The second visible effect is that the flame temperature is higher, farther downstream of the injector, than near the injection holes. This is a result of the 2nd recirculation zone that breaks apart from the 1st one and moves farther downstream, shown in Figure 106-e. Due to this enlargement, larger amounts of unburned gases are trapped and the local temperature decreases, shown in Figure 106, left side. The average temperature and heat loss in the combustor is shown in Figure 106.

When the downstream angle is increased to 120°, seen in Figure 105-f and Figure 106-f, the large recirculation zone, (1st – near the injector) broke down into smaller, symmetrical vortex structures. Due to these vortex structures, the high temperature part of the flame is on the sides of the combustor walls. The average temperature and heat loss plot, in the combustor for 60°x120° configuration is presented in Figure 106. Due to the large recirculation zones in the wake of the injector, the average temperature near the injector is lower, and later it increased.

The average temperature for constant upstream angles of 60° decreased as angles increased on the downstream side, with an enlargement of the vortices in the wake of the injector that caused a decrease in the local equivalence ratio. The heat loss, on the other hand increased slightly with larger downstream angles, due to direct injection at the walls, with only small differences induced by the downstream angles at such a high upstream angle.

Figure 107 presents the chemical heat release plotted for constant upstream angles of 60°. When the downstream angles were varied, the heat release in the chamber decreased as a result of a decrease in the local equivalence ratio. The OH concentration in the flame, in Figure 108-a, is higher for a 60°x10°, when the heat release is maximum and the local equivalence ratio is highest. In Figure 108-b, -c and -d, the concentration of H2, O2 and N2 is plotted for different downstream angles, when the upstream angle is fixed at 60°.

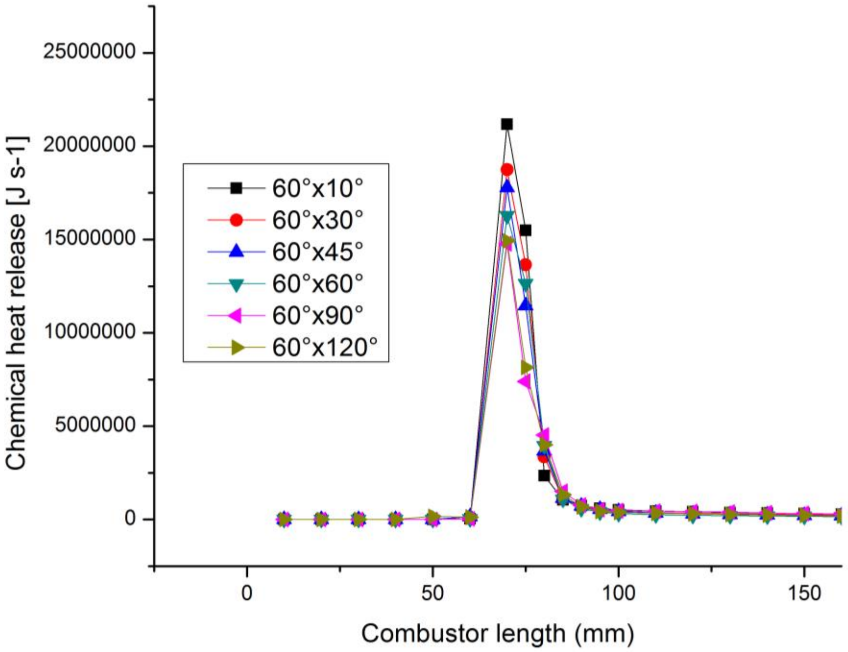

Figure 107 Chemical heat release for constant 60° upstream angles at fuel-rich conditions

From the H2, O2 and N2 concentration we see that a large part of the radicals are consumed near the higher upstream angles, and the rest around the downstream injection holes. When the angles increase on the downstream side, the large bulk of the radicals are consumed near the downstream injection holes. There is a large variation of N2 farther downstream as an effect of vortex breakdown seen in Figure 105 and Figure 106-d.

Figure 86 presents the total heat loss plotted for variable downstream angles with fixed 60° upstream injection. The total heat loss is seen to increases, as the angles increase on the downstream side. Larger angles on the downstream as seen from Figure 106-b, create recirculation zones that enlarge and later expand farther in the combustor, which “force” the high temperature part of the flame to be in longer contact with the walls of the combustor which add up to larger heat loss in the chamber. Although there are small differences for 60°x60° and 60°x90° configurations, these are mainly related to the vortices in the wake of the injector, as one is due to a coherent central vortex in the wake of the injector, and the latter, due to a division of this recirculation zone into smaller vortex structures.

Figure 109 presents the combustion efficiency for constant upstream angles of 60° and combustor length on the right side using the enthalpy approach (-a), the left side presents the chemical heat release approach (–b). For higher angles on the upstream, the peak of the combustion efficiency is found closer to the injector around 80 mm from the inlet, which led to a larger temperature difference of about 100-170 K.

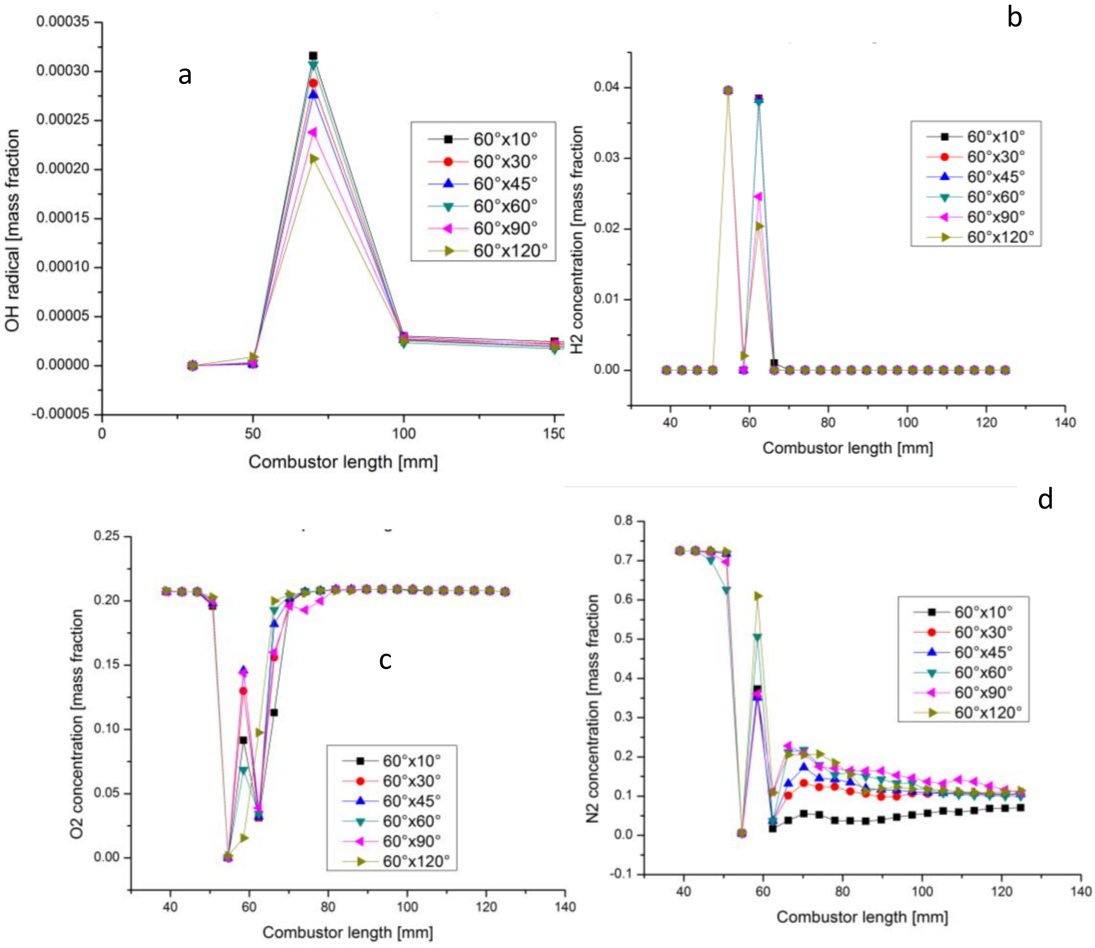

Figure 108 OH-a, H2-b, O2-c and N2-d average radical concentration [mass fraction] for 60° constant upstream angles at fuel-rich conditions

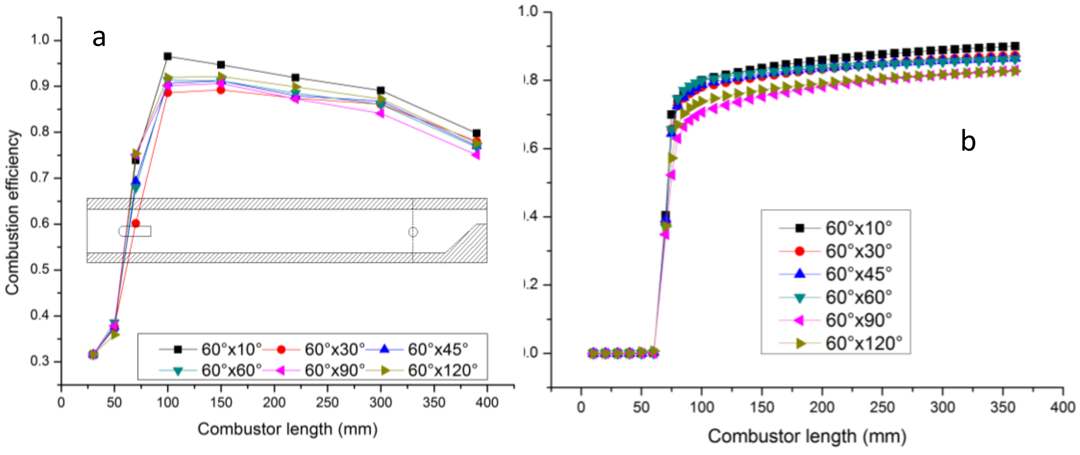

Figure 109 Combustion efficiency in the combustor for variable downstream angles at constant upstream 60° angles at fuel-rich conditions; a- enthalpy difference approach, b- heat release approach

In Figure 110, the values of combustion efficiency near the nozzle (as done in experiments) are plotted for variable downstream angles. The combustion efficiency for constant upstream angles of 60°, due to the presence of the recirculation zones, and the small difference in temperature caused by these vortices, reaches similar values near the nozzle. The effect of the angles is situated closer to the injector, thus having little influence on the nozzle temperature. However, when the heat release is considered, higher angles on the downstream side, decrease the combustion efficiency with almost 10%, providing an independent solution.

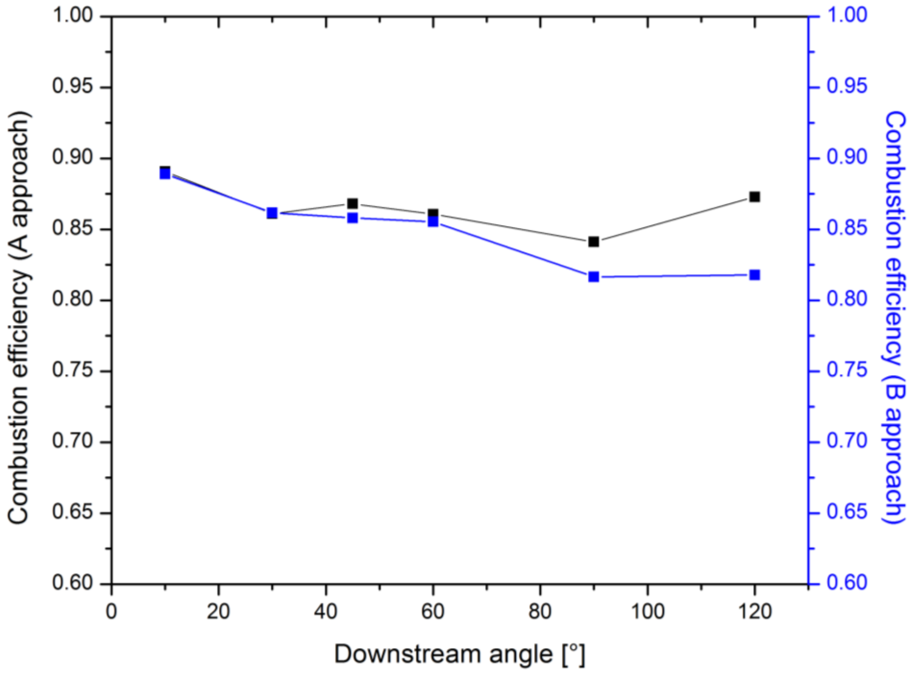

Figure 110 Overall combustion efficiency using the two approaches, enthalpy difference (black line) and chemical heat release (blue line) for constant upstream angles of 60°

Figure 111 presents the NO and NO2 mass fraction plotted in the length of the combustor for variable downstream angles at constant upstream angles of 60°. The configuration that creates the largest amount of NO and NO2 is found for the configuration with the lowest combustion efficiency, i.e. 60°x90°. As in the previous configuration, when angles increase on the downstream, larger vortices form in the wake of the injector, leading to larger amounts of NOx produced in the chamber.

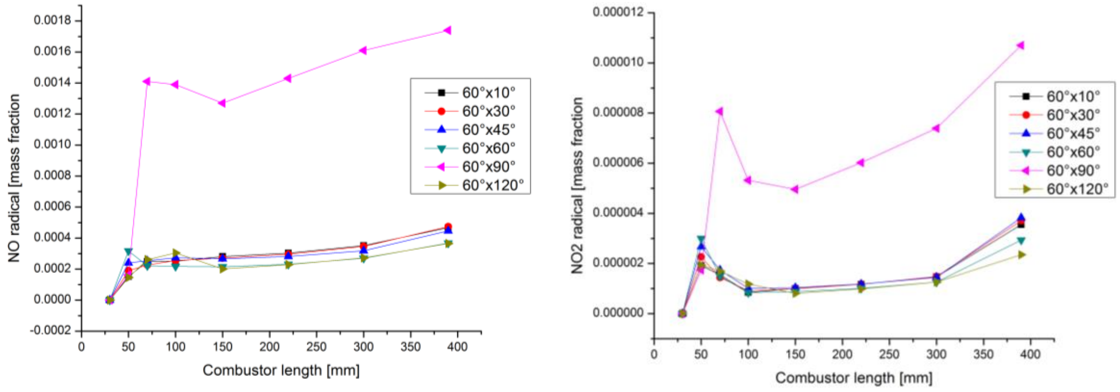

Figure 111 NO and NO2 mass fraction distribution in the combustor for constant 60° upstream injection at fuel-rich conditions

When the EINOx is plotted for variable downstream angles, shown in Figure 123, the EINOx decreases, as the overall temperature in the chamber, decreased with lower local equivalence ratios. The bulk is created in large amounts near the injector, and as it is carried downstream, it actually dissociates and the resulting EINOx is lower.

Preliminary conclusions for this configuration include:

- Flame asymmetry caused by larger angles on the upstream coupled with large angles on the downstream create more NOx on the lower side of the chamber.
- Higher downstream angles decrease the flame temperature and combustion efficiency.
- Heat loss increases with larger downstream angles.
- NO is created in the post-flame region and increases downstream in the combustor.

- The concentration of NO2 decreased significantly in the wake of the injector, in the post-flame region, and was coincident with a corresponding formation of NO.

4.4.2.2. Constant downstream combustion

Figure 112 presents the temperature on top, and velocity distribution field, on the bottom, for constant downstream angles of 30°. In Figure 113 the enhanced views of temperature fields on the left side, and velocity vector distribution, on the right side, for the constant downstream angle of 30° are presented. In Figure 112 and Figure 113, from –a, to -c, the downstream angles increase from 10° (Figure 112-a) to 120° (Figure 113-c). When the downstream angles are kept constant, the flame shape changes from a cone shaped flame for small angles seen in Figure 112 and Figure 113-a, and a rectangular shape for large angles seen in Figure 112 and Figure 113-c. The main factors that have a large influence on the flow behavior are the vortices that form on the upper side and lower side of the injector, near the upstream injection holes. The vortices that form near the upstream injection holes are shown in Figure 112-a, -b and -c for 10°x30°, 90°x30° and 120°x30° configurations. As the angles increase the vortices increase in size, and when the injection is perpendicular, due to the size of the angles on the upstream side, small vortices start forming at the base of the injection hole and increase with increasing angles on the upstream side. These, not only lower the local equivalence ratio by trapping unburned oxygen that have a lower temperature, but also help increase the NOx formation.

For a 10°x30° configuration, seen in Figure 112 and Figure 113-a, the flame is concentrated in the axial direction in the wake of the injector. Given the axial flow velocity and large injection velocity of fuel coming from the upstream injection pair, the flame is concentrated in the axial direction on the upper and lower sides of the injector. The average temperature and heat loss in the combustor for this configuration is plotted in Figure 114. The temperature reaches a maximum point farther away from the injector, when the flow has cleared the recirculation zones that formed in the wake of the injector. Due to these recirculation zones, heat loss rises, and later as the mixture proceeds downstream, the heat loss decreases with a decrease in average temperature.

When the upstream angles increase to 30°, 45° and 60°, the effect is presented in the previous section 4.4.2.1.

When the angles are set to 90° upstream shown in Figure 112 and Figure 113-b, the perpendicular injection is clearly observed through the flame shape and the flame is assumes a rectangular shape.

For large angles on the upstream, and the presence of the lower side and upper side of the injector vortices, small vortices start forming at the base of the injection holes, which create a cold region between the fuel injected from the upstream injection holes and the one coming through the downstream injection holes. These small vortices are shown in Figure 115, where velocity vector distribution is presented for comparison for a 60°x30° and 90°x30° configuration. Due to the recirculation zone forming in the wake of the injector caused by large angles on the upstream, the flame fronts expand in the chamber farther downstream, diluting the mixture and lowering the flame temperature, shown in Figure 116-a. The perpendicular injection increases the heat loss at the walls and as the mixture proceeds downstream, the heat loss decreases with the decrease of temperature of the flame, shown in Figure 114 through the average temperature and heat loss plot.

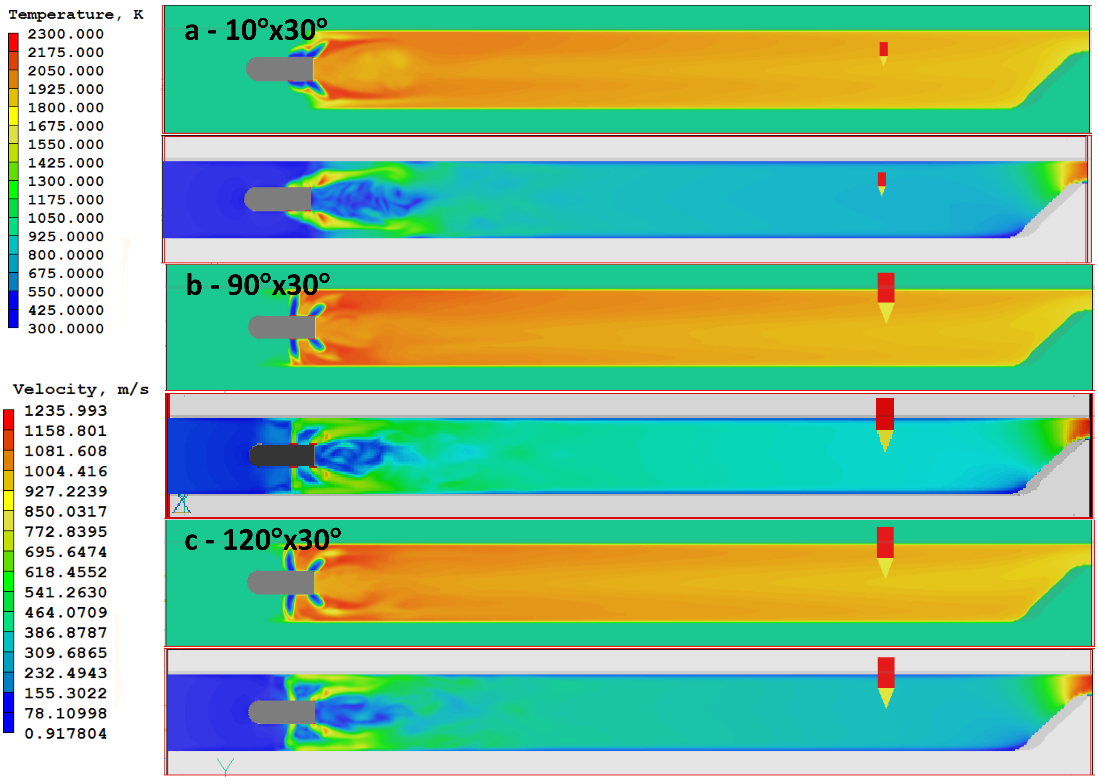

Figure 112 Temperature and velocity distribution field for constant downstream angle of 30° at fuel-rich conditions

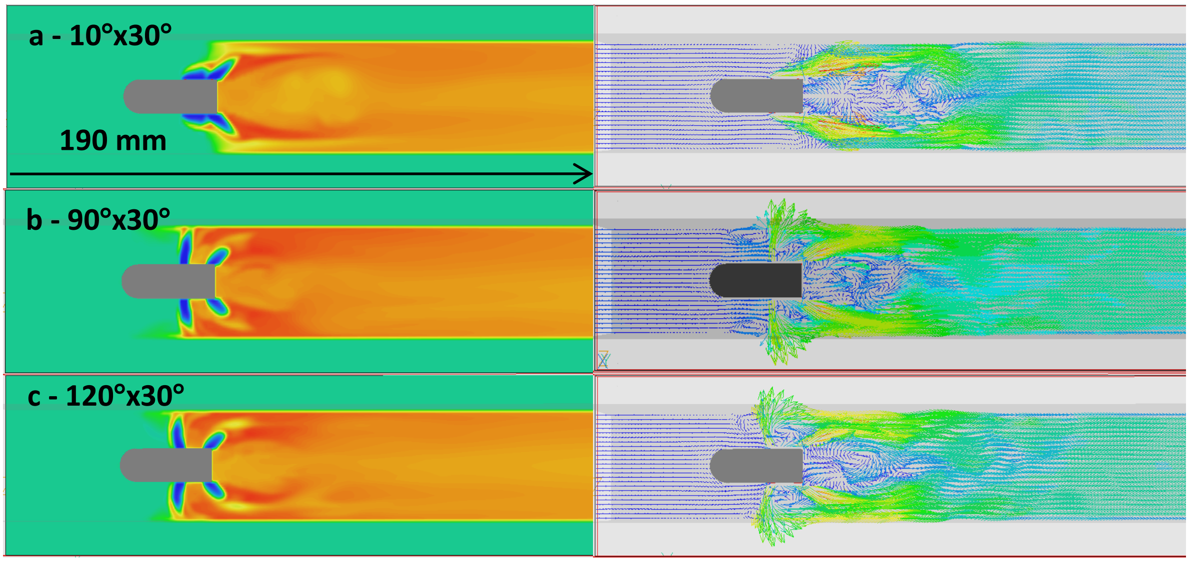

Figure 113 Enlarged temperature field distribution and velocity vector distribution near the injector for constant downstream angles 30° at fuel-rich conditions

For upstream angles on 120°, seen in Figure 112 and Figure 113-c, the vortices that form in between the injection holes enlarge, and through their size, lower the local equivalence ratio, shown in Figure 116. The local equivalence is highest when fuel from the upstream injection holes and downstream injection combine for a 10°x30° configuration. As angles increase on the upstream side, the local equivalence ratio decreases reaching minimum values for high upstream angles, i.e. 90° and 120°, when the vortices between the injection holes dilute the mixture.

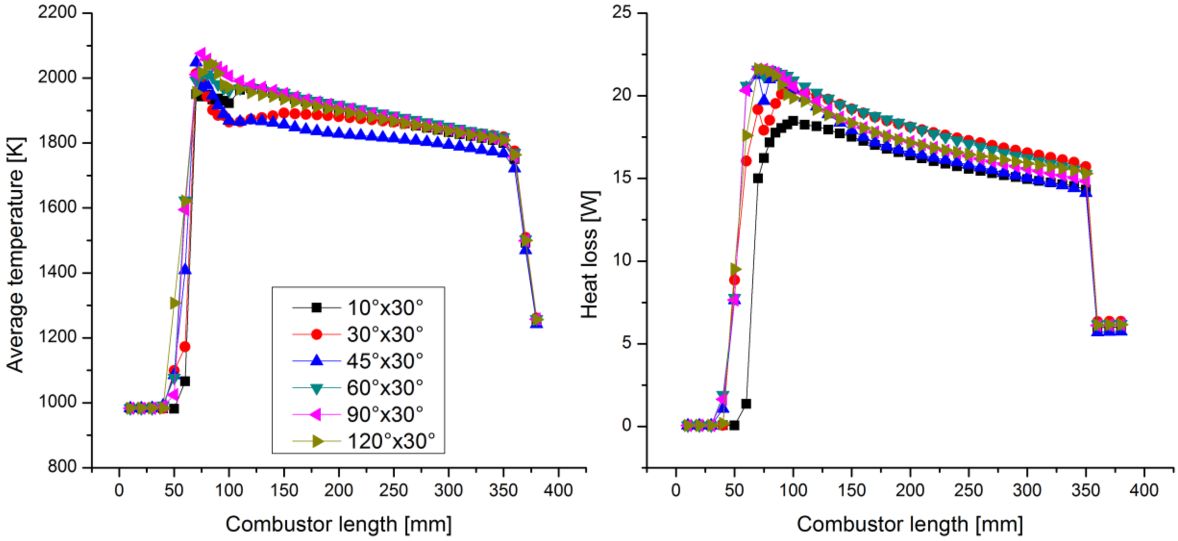

Figure 114 Average temperature (left side) and heat loss (right side) in the combustor for constant downstream 30° and variable upstream angles at fuel-rich conditions

These small vortices forming from deflected flow from the walls, caused by high upstream angles, grow in size with increasing angles on the upstream until they reach a maximum tolerant shape for angles of 45° on the upstream. Beyond this value, they seem to decrease in shape, because small vortices start forming at the base of the injection holes. As angles increase on the upstream the deflected flow vortices shrink and the vortices between the injection holes increase in size. The average temperature and heat loss in the combustor for 120°x30° configuration is presented in Figure 114.

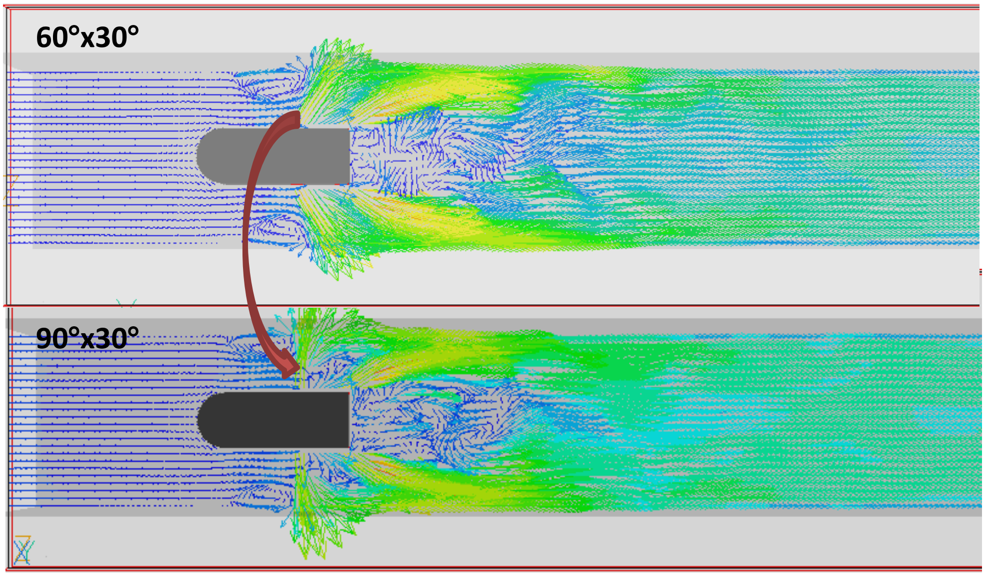

Figure 115 Vortex formations between injection holes for a 60°x30° and a 90°x30° configuration at fuel-rich conditions shown through velocity vector distribution

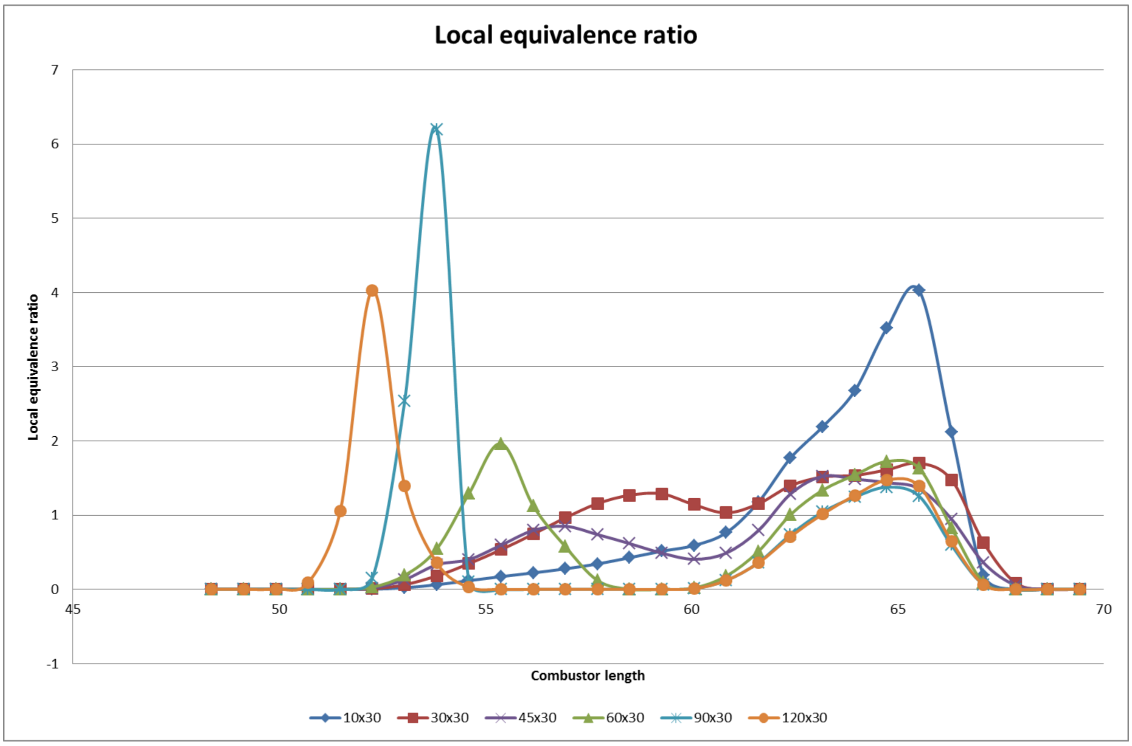

Figure 116 Local equivalence ratio for unburned products, for constant downstream angles and variable upstream angles in the wake of the injector

The flame temperature is highest around the injector, when locally the equivalence ratio is increased, shown in Figure 116, and later as the equivalence ratio drops, so does the temperature of the flame. The heat loss is highest, near the upstream injection holes, due to the large angle of injection, after which, it decreased.

The average temperature in the chamber is plotted for the entire combustor at variable upstream angles and a fixed upstream angle of 30° in Figure 114. Smaller angles on the upstream side create recirculation zones in the wake of the injector, which reduce the temperature in the area. However, later downstream as the vortices breakdown, flame temperature increases. For high upstream angles, on the other hand, the temperature has a maximum value around the injector, after which is gradually decreased in the chamber. From the temperature plot, we see that the maximum temperature is almost similar for all configurations, however, the effect of the upstream angles is much more pronounced, especially for low upstream angles when the temperature drop is large. The temperature gap for a fixed upstream angle varied from 30 to 150 K.

In Figure 117, the chemical heat release is plotted for constant downstream angles of 30°. When the downstream angles were kept constant, the heat release decreased as the upstream angles became larger. Due to an enlargement of recirculation zones near the upstream injection holes, the local equivalence ratio decreases.

The heat release seems to have the highest value for a 10°x30° and 30°x30° configurations when, due to an almost parallel injection (not exactly parallel, due to the effect of the axial velocity and interference of the injection pairs), fuel is injected in the axial direction, maximizing the spread and enhancing the mixing. For the other configurations, the large vortices trap unburned air which lowers the local equivalence ratio.

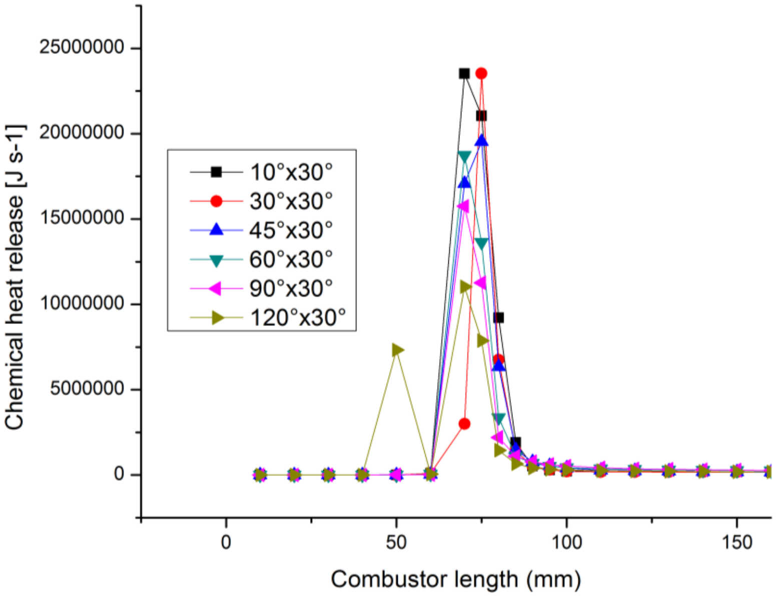

Figure 117 Chemical heat release for constant 30° downstream angles at fuel-rich conditions

The OH radical variation with increasing upstream angles for constant downstream angles 30° at fuel-rich conditions is presented in Figure 118-a. In Figure 118-b, -c and -d, the concentration of H2, O2 and N2 is plotted for different downstream angles, when the downstream angle is fixed at 30°.

The heat release is maximum when the OH radical production is highest, seen in Figure 118-a. As the angles increase on the upstream, most of the combustion takes place near the upstream injection seen through the consumption of O2 and N2 radicals in Figure 118-c and –d. The hydrogen consumption is highest near the upstream injection holes, which is being supplied by high upstream angles.

Figure 119 presents the total heat loss plotted this time for the variable downstream angles. The total heat loss is seen to increases as the angles increase on the upstream side, similar with the previous configurations. For constant downstream of 30°, the increasing angles on the upstream side by pushing more fuel towards the walls, increase the mixture’s contact with the walls of the combustor and as this happens the vortices near the upstream injection holes increase in size, reaching a maximum size, before moving in between the injection holes at 90° on the upstream. As they move there, the heat loss decreases a little as the temperature of the flame decreases.

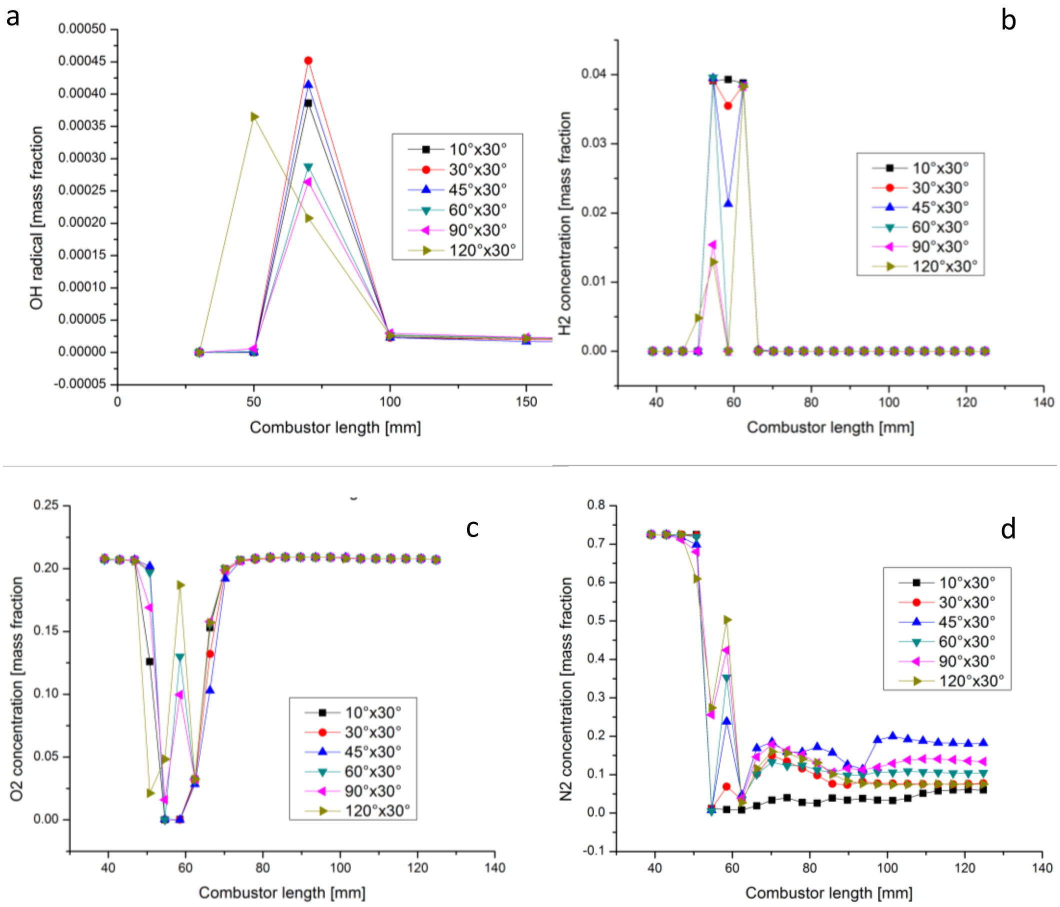

Figure 118 OH-a, H2-b, O2-c and N2-d average radical concentration [mass fraction] for constant 30° downstream angles at fuel-rich conditions

Figure 120 presents the combustion efficiency for constant downstream angles of 30° and combustor length on the right side using the enthalpy approach (-a), the left side presents the chemical heat release approach (–b). When angles increase on the upstream side, the combustion efficiency, evaluated as the enthalpy difference, is seen to increase, as the fuel injected from both pairs, interacts and mixing is enhanced. The configuration 45°x30°, however, shows a dip in combustion efficiency. From Figure 112 and Figure 113-a, and –b, the flame becomes thicker, with fuel being injected almost parallel.

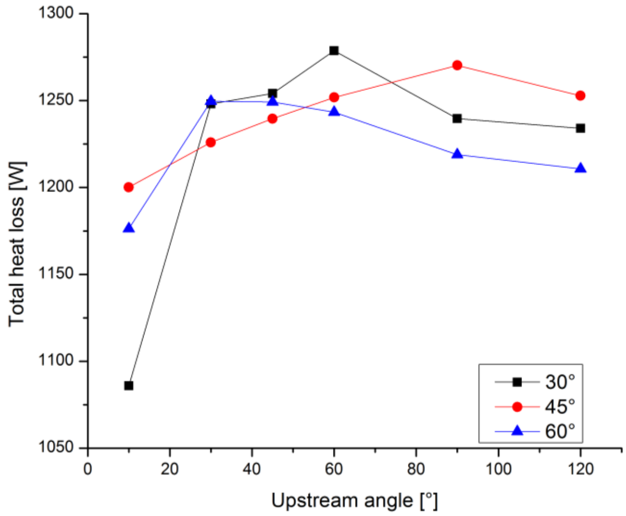

Figure 119 Total heat loss for constant downstream angles and variable upstream angles at fuel-rich conditions

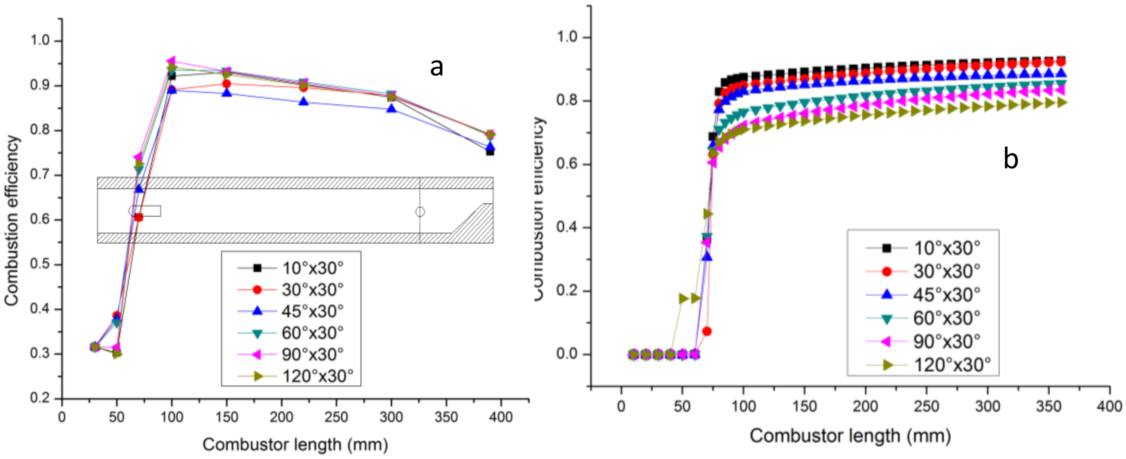

Figure 120 Combustion efficiency for constant downstream 30° angles at fuel-rich conditions

This decrease in temperature, and subsequent combustion efficiency, is related to the fact that when the flame fronts enlarge, the flame expands in the chamber, which in turn lowers the local equivalence ratio and the temperature drops relatively faster. The combustion efficiency increases slightly as angles increase on the upstream side, however, from Figure 121; we see that the variation is almost negligible. Using this evaluation, we observe that combustion efficiency does not depend on the upstream angles. On the other hand, when the heat release evaluation is used, there is a clear decrease in combustion efficiency as the angles increase on the upstream side. As explained in the previous sections, when angles increase, recirculation zones increase in size, the local equivalence ratio decreases, resulting in lower heat release and lower flame temperature.

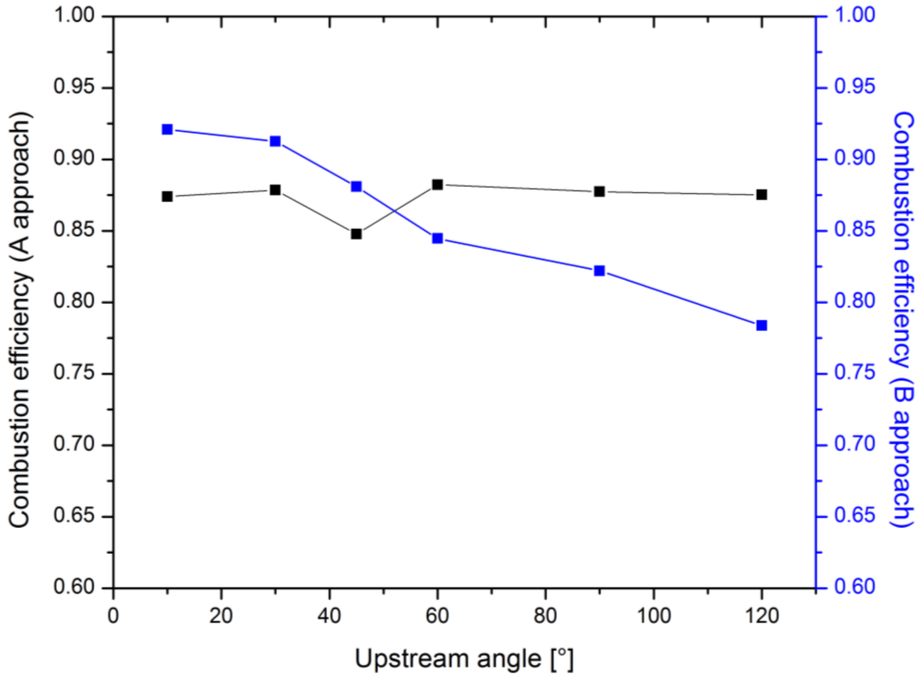

Figure 121 Overall combustion efficiency using the two approaches, enthalpy difference (black line) and chemical heat release (blue line) for constant downstream angles of 30°

Figure 122 presents the NO and NO2 mass fraction plotted in the length of the combustor for variable upstream angles at constant downstream angles of 30°. The NO forming from upstream angles seem to increase slightly due to an enlargement of the recirculation zones, where more oxygen is trapped allowing for more NOx formation. There is a single exception, for a 45°x30° configuration has an increased production of NO and NO2 due to the flame shape. This angled configuration allows for an asymmetric flame on the upper side, that enhanced mixing, and through the recirculation zone in the wake of the injector, through the added local turbulence, enhances the production of NOx.

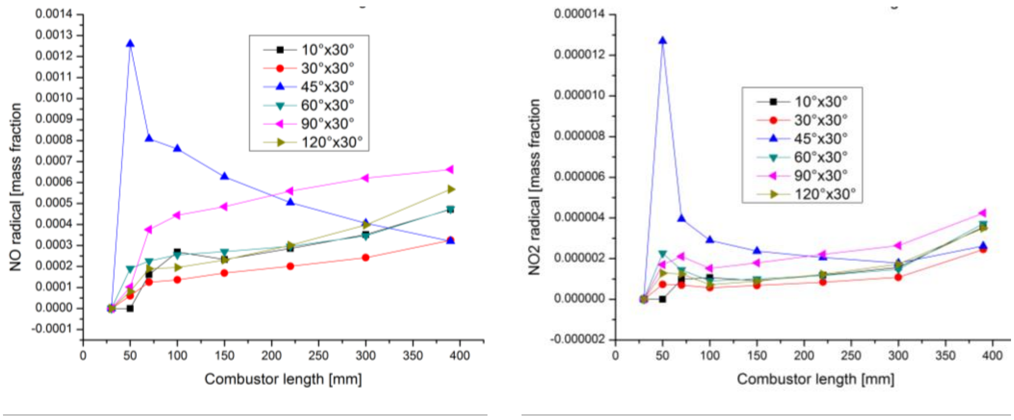

Figure 122 NO and NO2 mass fraction distribution in the combustor for constant downstream angles fixed at 30°

For this configuration the bulk of NO and NO2 is formed on the wake of the injector, after which it dissociates in the chamber. The other configurations, have a gradual increase in NO and NO2 concentration in the chamber as the mixture encounters new pockets of unburned oxygen, or through relative chemical dissociation and recombination.

When the EINOx is plotted, for variable upstream angles, in Figure 123, it varies quite a lot, and we can see that it is very dependent on the size of the vortices and flow behavior induced by the injection angles. For constant downstream angles of 30°, the NOx production decreases as angles increase, when the recirculation zones on the upper and lower side on the injector increase, observed in Figure 113. Due to a direct influence of the axial velocity, and a lower temperature in the area, the NOx are not produced. As the recirculation zones “move” in between the injection holes, observed in Figure 113, and enlarge, oxygen is trapped in the center of the vortex. The vortex being in between the injection holes helps the reaction create large amounts of NOx. Another effect that increases the EINOx for larger upstream angles, is the strong asymmetry effect induced in the flow.

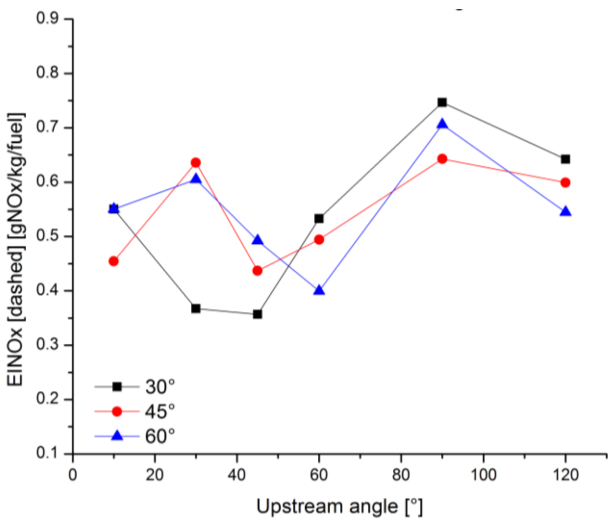

Figure 123 EINOx for constant downstream angles at fuel-rich conditions

When the angles are increased on the downstream side to 45°, as observed in Figure 125 and Figure 124 through respective temperature and velocity vector distribution fields, the effect is similar to that of the above case only more pronounced. Fixed larger angles on the downstream with increasing angles on the upstream create a larger flame, that due to the large angles downstream, flow is reflected from the walls and flame temperature is affected farther downstream in the chamber.

For a 10°x45° configuration, shown in Figure 125 and Figure 124-a, the effect of larger angles downstream, compared with the previous configuration is larger vortices that form in the wake of the injector. The average temperature for this configuration is presented in Figure 126, compared with the previous configurations. When the angles are increased on the downstream for similar low angles on the upstream 10°, due to an enlargement of recirculation zones in the wake of the injector, after they broke down, the local equivalence ratio actually increased on the area, and as a result the average temperature increased in the area. The heat loss for these configurations are presented in Figure 127, and as the previous figure, about temperature, the heat loss varies significantly with increasing downstream angles, due to an increase in injection angles.

The fuel mixes near the downstream side and is consumed farther on. As the flame proceeds in the chamber, the temperature drops to a plateau value. The heat loss increases at the walls from the expanding heat in the chamber, increasing to a plateau near the nozzle.

When the upstream angles increase to 30°, 45° and 60°, the effect is presented in the previous section 4.4.2.1.

When the angles are set to 90° upstream shown in Figure 125 and Figure 124-b, the perpendicular injection is clearly observed through the flame shape due to large recirculation zones in the wake of the injector, and on the upper and lower side of the injector. This actually decreases the temperature of the mixture, as the local equivalence ratio is expected to be diluted, shown in Figure 128 through average temperature in the combustor for constant 90° on the upstream and variable downstream angles.

The associated heat loss in the combustor for this configuration is shown in Figure 127. The perpendicular injection increases the heat loss at the walls and as the mixture proceeds downstream, the heat loss decreases with the decrease of temperature of the flame. For the 90° injection angle on the upstream, when injection is on the upstream, the heat loss is highest.

For upstream angles on 120°, seen in Figure 129-a, and –b shows the average temperature and heat loss in the combustor, in comparison with the previous configurations. The recirculation zone in between the injection holes, become more pronounced, where the azimuthal velocity is assumed to have increased. The average temperature and heat loss in the combustor for 120°x30°, 120°x45° and 120°x60° configurations is presented in Figure 129. The average temperature is seen to decrease with larger downstream angles, and thus the heat loss associated with hotter flames is actually lower.

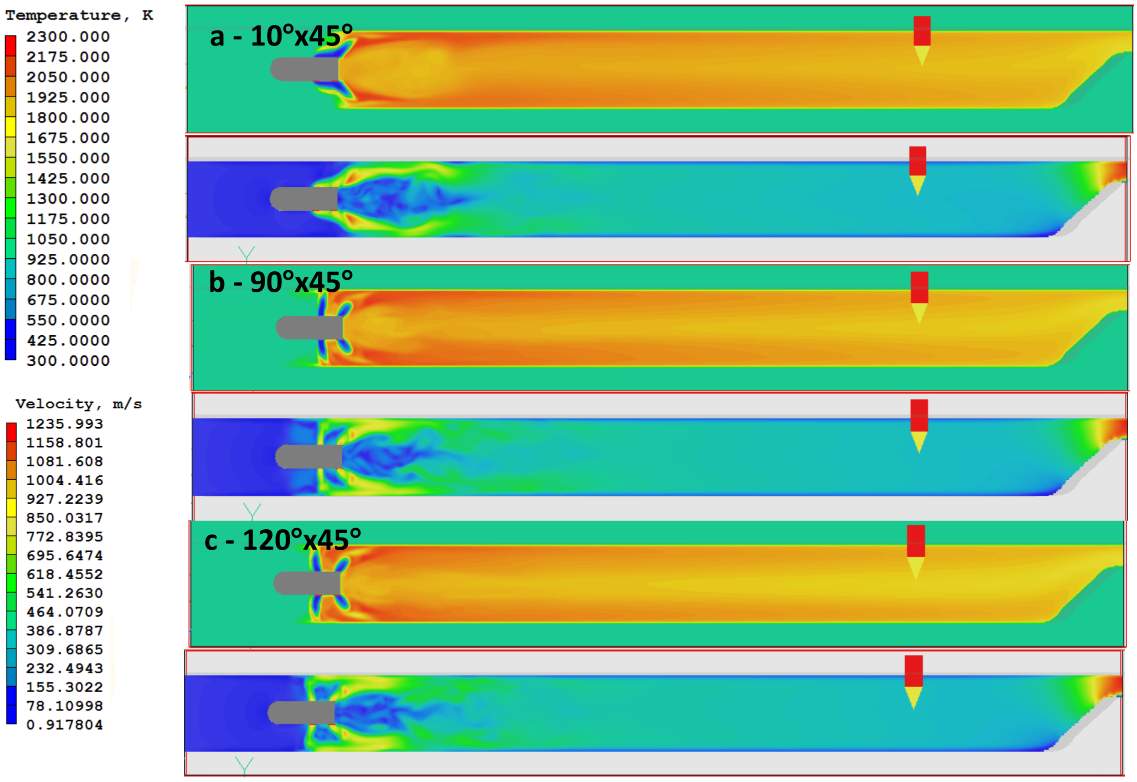

Figure 125 Temperature and velocity distribution field for constant downstream angle of 45° at fuel-rich conditions

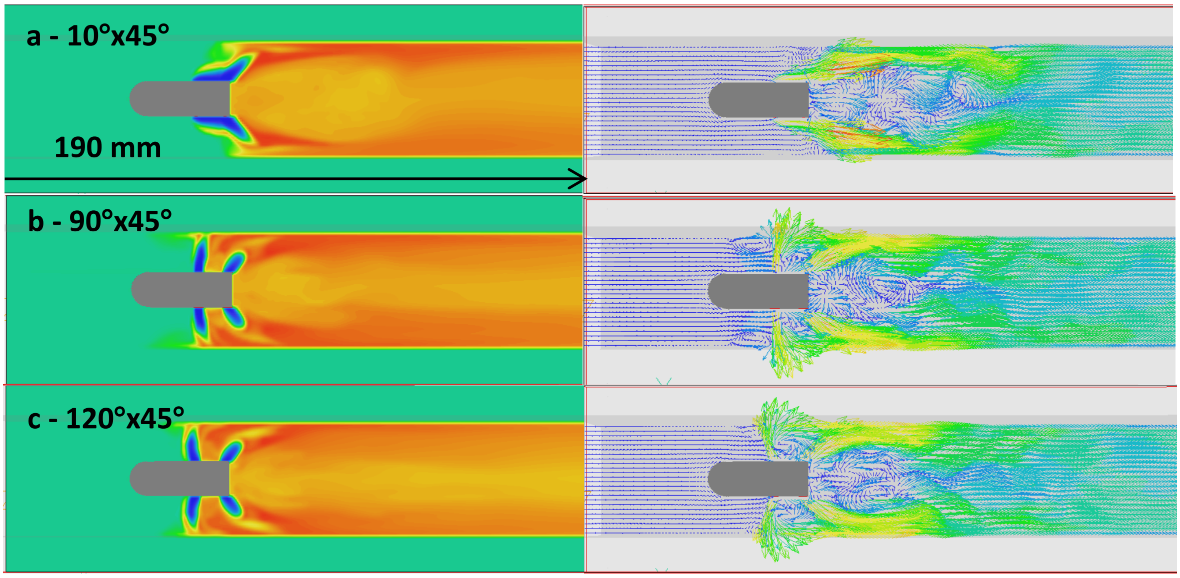

Figure 124 Enlarged temperature field distribution and velocity vector distribution near the injector for constant downstream angles 45°

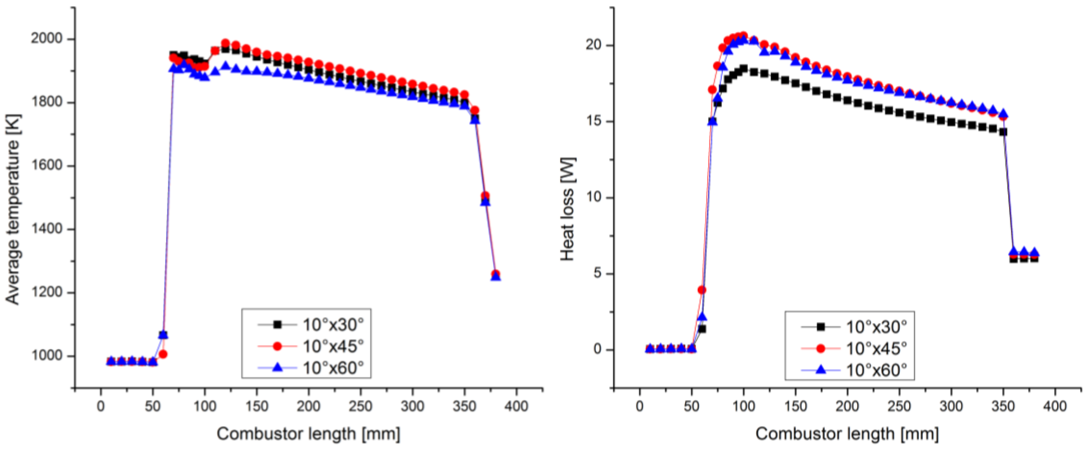

Figure 126 Average temperature and heat loss in the combustor for 10°x30° (black points), 10°x45° (red points) and 10°x60° (blue points) at fuel-rich conditions

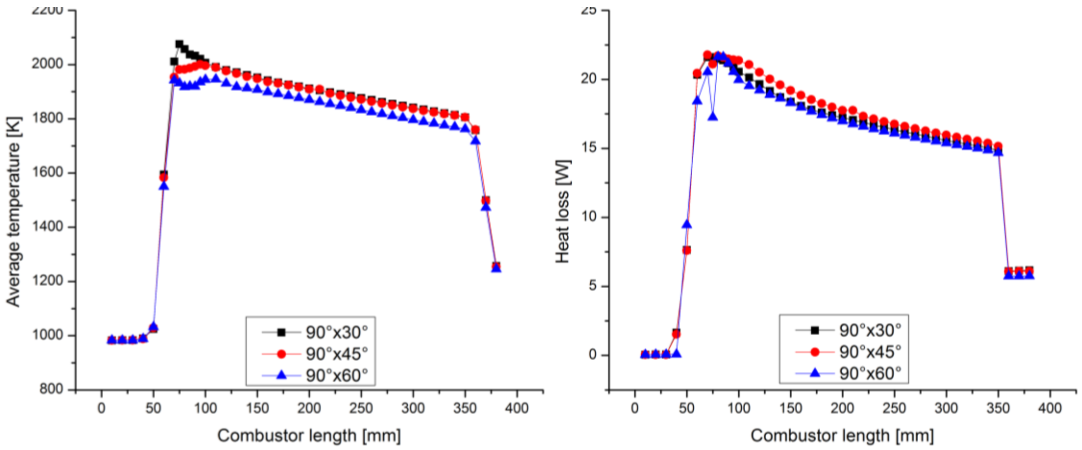

Figure 127 Average temperature in the combustor for 90°x30° (black points), 90°x45° (red points) and 90°x60° (blue points) at fuel-rich conditions

The average temperature for constant downstream angles of 45° in the chamber is presented in Figure 130. The temperature actually increases with larger upstream angles after in the injector area, but decreases due to larger vortices that form on in the wake of the injector, later downstream. The temperature gap for a fixed upstream angle of 45° varied from 30 to 150 K with smaller differences for larger upstream angles.

In Figure 131, the chemical heat release is plotted for constant downstream angles of 45°. The heat release is highest when the downstream angles are small i.e. 10°. When the upstream angles increased, the heat release decreased as the local equivalence ratio decreased, shown in Figure 131.

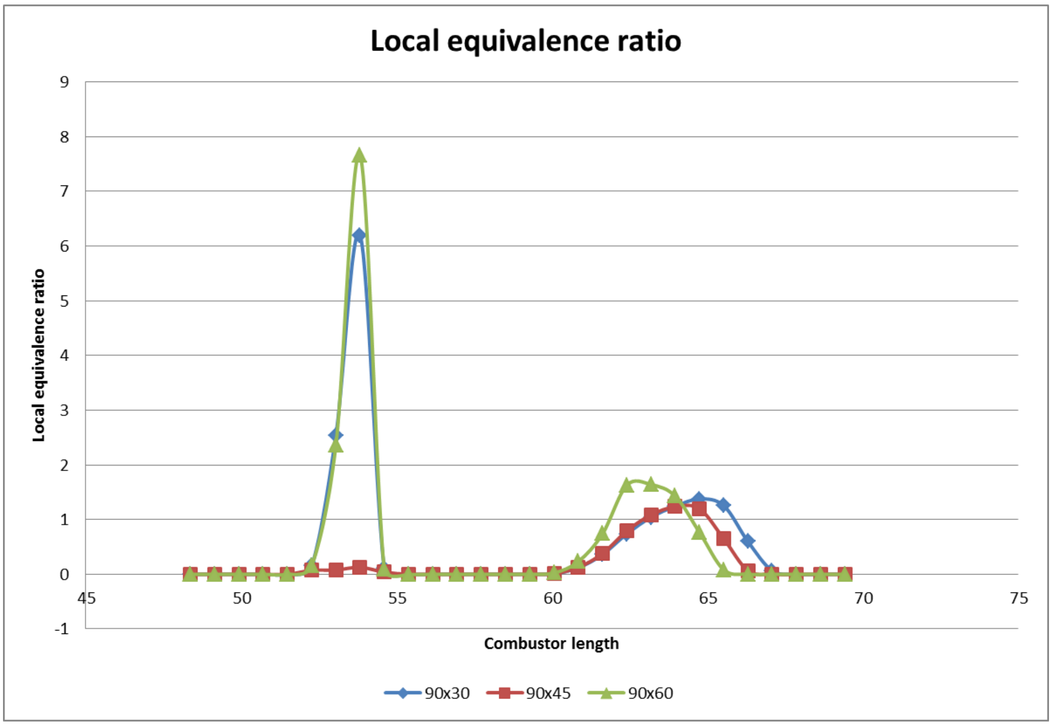

Figure 128 Local equivalence ratio for unburned products, in the wake of the injector for variable downstream angles at fuel-rich conditions

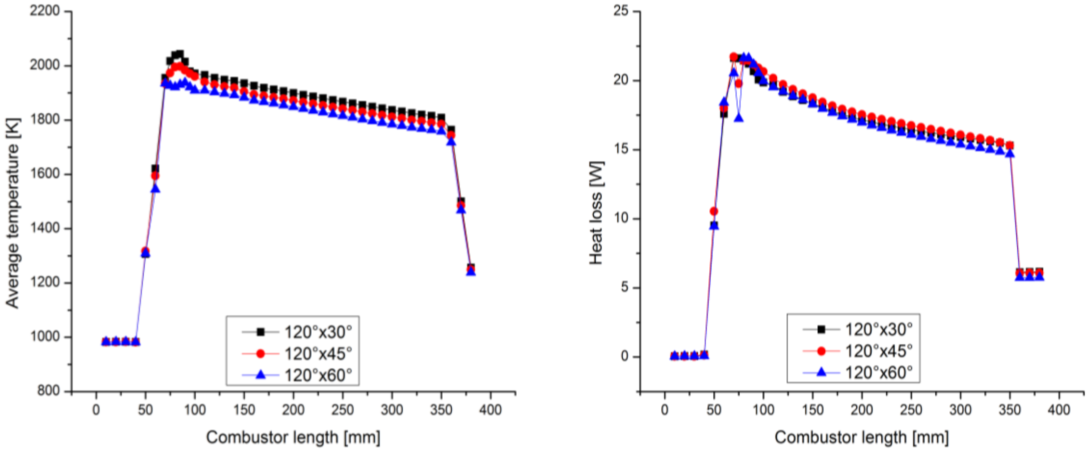

Figure 129 Average temperature and heat loss in the combustor for 120°x30° (black), 120°x45° (red) and 120°x60° (blue) at fuel-rich conditions

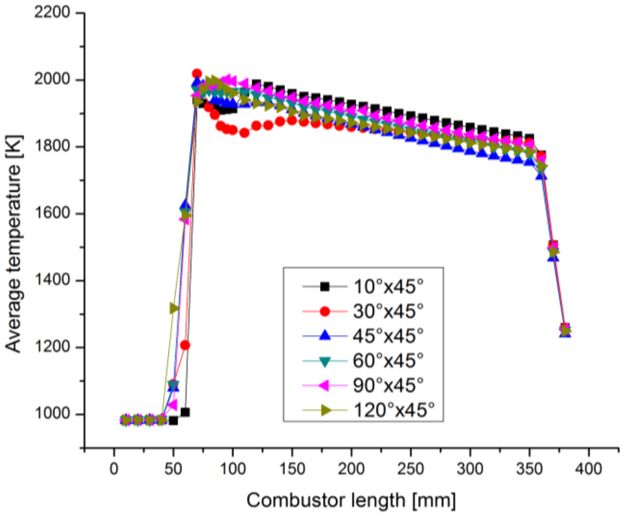

Figure 130 Average temperature in the combustor for fuel-rich at constant downstream 45°

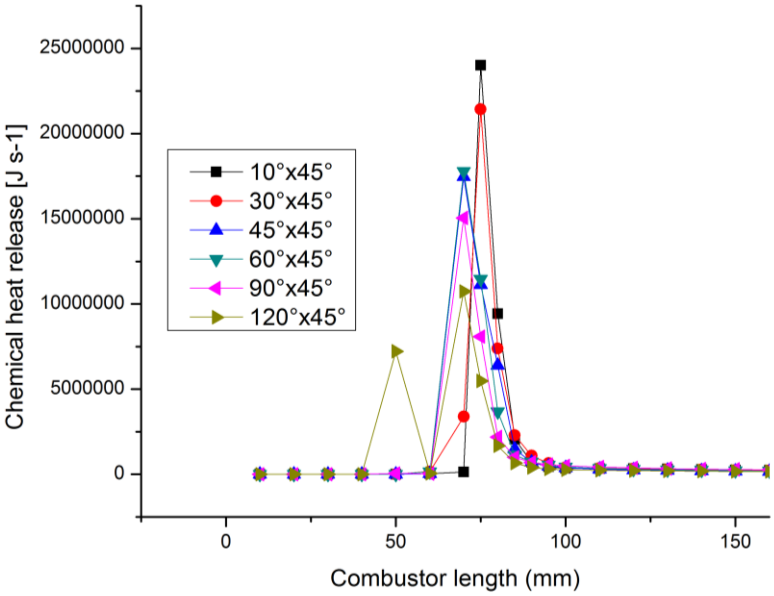

Figure 131 Chemical heat release for constant 45° downstream angles at fuel-rich conditions

The local equivalence ratio around the upstream injection holes and downstream injection holes is shown in Figure 128.

Figure 119 presented the total heat loss plotted this time for the variable downstream angles. The total heat loss follows a similar trend as that of fixed downstream angles of 30°, shown in the same figure. The heat loss increases as angles increase on the upstream and the heat loss associated is higher as downstream angles increase, shown in Figure 129.

Figure 132 presents the combustion efficiency for constant downstream angles of 45° and combustor length on the right side using the enthalpy approach (-a), the left side presents the chemical heat release approach (–b). When higher angles are set for the downstream pair, the combustion efficiency, using the enthalpy approach, increases until it reaches a plateau, after which larger angles on the upstream lower the local equivalence ratio and temperature, which lead to decreasing combustion efficiencies. From the nozzle combustion efficiency, the efficiency varies only about 3%, where due to the recirculation zones and asymmetry in the flame, the efficiency varies little. The heat release approach shows a decreasing trend as angles increase on the upstream side.

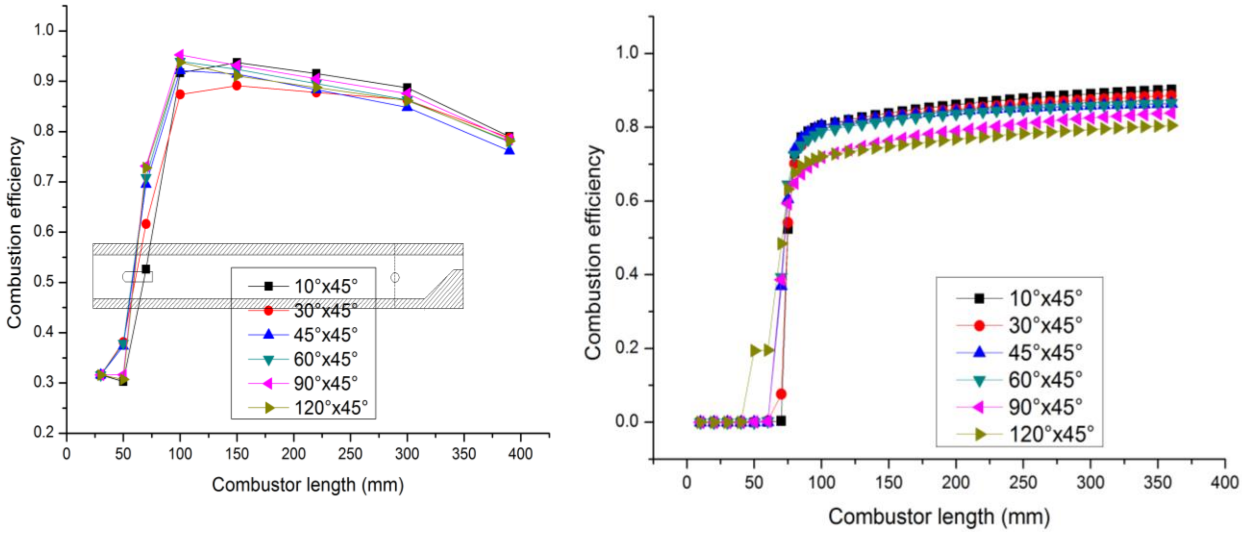

Figure 132 Combustion efficiency for constant downstream 45° angles at fuel-rich conditions

Figure 133 presents the overall combustion efficiency near the nozzle, evaluated using the two approaches. As in the previous configuration, as angles on the upstream increase, the efficiency decreases with almost 10%.

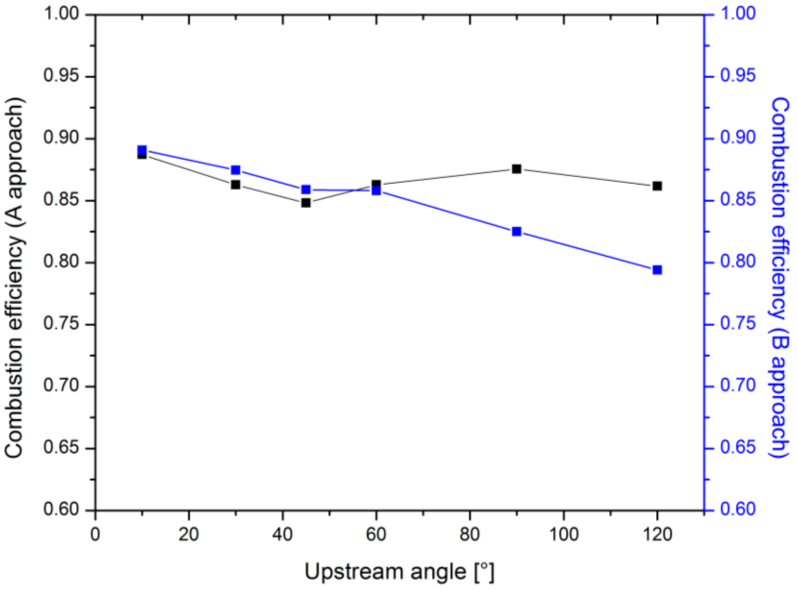

Figure 133 Overall combustion efficiency using the two approaches, enthalpy difference (black line) and chemical heat release (blue line) for constant downstream angles of 45°

Figure 134 presents the NO and NO2 mass fraction plotted in the length of the combustor for variable upstream angles at constant downstream angles of 45°. For the 30°x45° configuration, due to the presence of the ramp-shaped nozzle, asymmetry in the flame is observed through the recirculation zones. This asymmetry favored the upper side where larger vortices occur. These larger structures trap larger amounts of O2, leading to larger amounts of NO and NO2 in the area. As a result, flame-formed NO and pre-flame NO2,

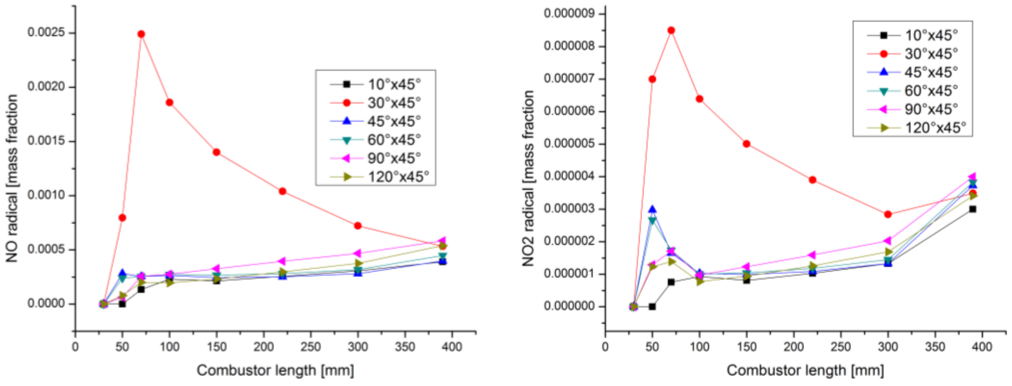

Figure 134 NO and NO2 mass fraction distribution in the combustor for constant downstream angles fixed at 45°

increased as the separate flame fronts created their separate NOx, independent, which by not being in a single flame front, does not dissociate and recombine as easily.

The EINOx, plotted in Figure 123, increases with larger upstream angles, albeit a 30° configuration on the upstream. As seen previously the bulk of the EINOx is given by the recirculation zones. When the angles increased to 120° on the upstream, due to the rarefication of the flame, and subsequent dilution, the NOx production was inhibited and the resulting EINOx decreased. Small downstream angles have little influence on the creation of NOx; however, larger angles on the downstream when the upstream angles increase, due to the flame shape and equivalence ratio, produce more NOx in the chamber.

Figure 135 and Figure 136 present the temperature, on the top and velocity distribution fields, on the bottom, variable upstream angles, and enhanced temperature fields, on the left side, and velocity distribution fields, on the right side, from a to c for 10° to 120° on the upstream. Larger angles on the downstream push a bigger amount of fuel towards the walls which either flows along the walls of the combustor, or are deflected and unite towards the middle of the combustor on the axial direction. More reflected flow yielded higher heat loss. As seen in previous configurations, when angles increase on the upstream and downstream, the recirculation zones compress in the wake of the injector, which increases heat loss increased near the injector, and decreased later downstream. The average temperature decreased due to an increase in the dilution-induced effect of the recirculation zones, seen in Figure 137. The average temperature and heat loss is presented in comparison with previous configurations with the same angles on the upstream angles, shown in Figure 127. The average temperature and heat loss in the combustor is plotted for 10° angles on the upstream and variable downstream angle shows the effect of this diffusiveness. The temperature decreased in the immediate wake of the injector, but due to the flow being injected towards the walls, it was higher farther downstream. The heat loss is high in the area, however, due to large recirculation zones, is it slightly lower than for lower angles on the downstream. When the upstream angles increase to 30°, 45° and 60°, the effect is presented in the previous section 4.4.2.1.

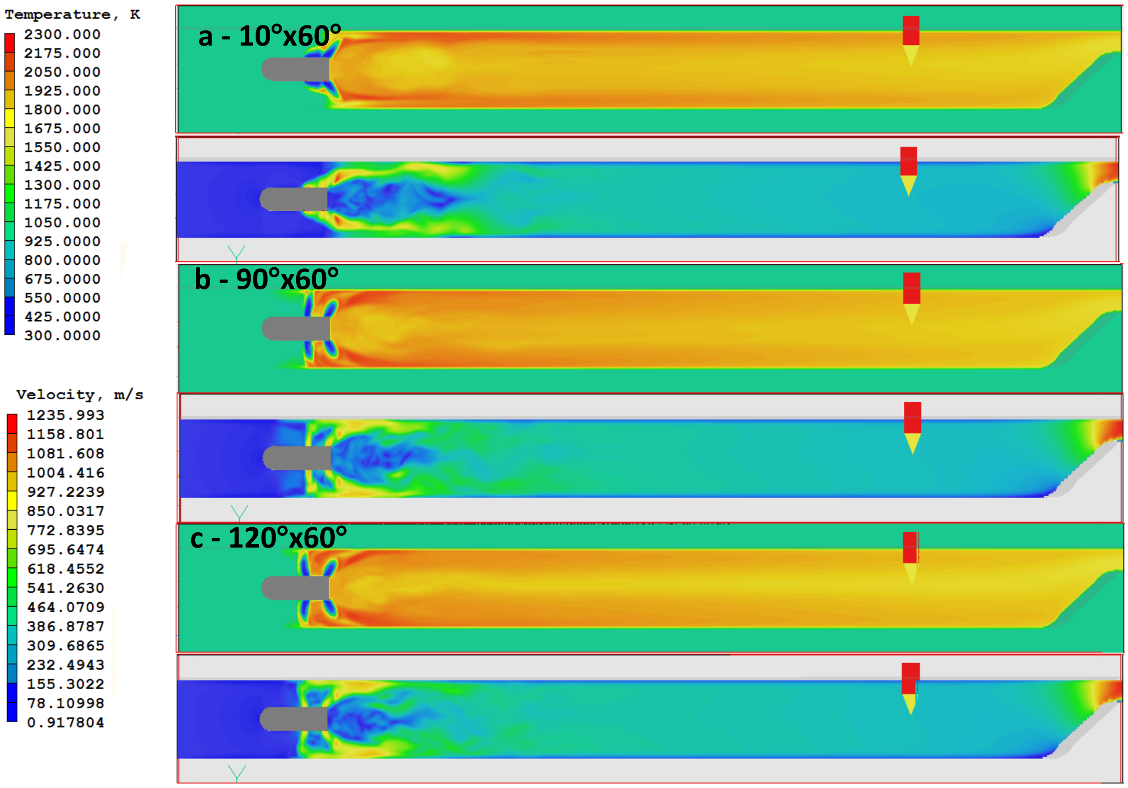

Figure 135 Temperature and velocity distribution field for constant downstream angle of 60° at fuel-rich conditions

From Figure 135 and Figure 136-b, 90° upstream angles, are more pronounced than the previous configurations due to larger vortices in between the injection holes on the upstream and downstream. The average temperature and associated heat loss in the combustor for this configuration is shown in Figure 127. Due to lower equivalence ratio, the average temperature decreased, thus having a small heat loss in the chamber.

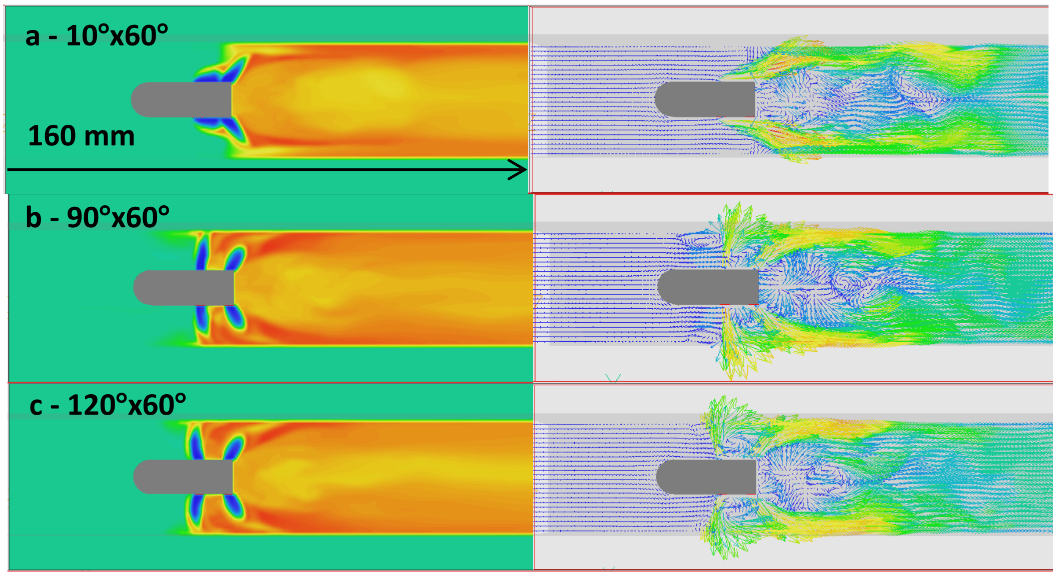

Figure 136 Enlarged temperature field distribution and velocity vector distribution near the injector for constant downstream angles 60°

For upstream angles on 120°, seen in Figure 135 and Figure 136-c, the vortices that form in between the injection are not influenced by the increasing downstream angle, however, the recirculation zone in the wake of the injector becomes more pronounced, where the azimuthal velocity is assumed to have increased. The combustion takes place in the same separate flame fronts, however, due to larger angles on the downstream, the heat loss increases in the area. The average temperature and heat loss in the combustor for 120°x30°, 120°x45° and 120°x60° configurations is presented in Figure 129. The average temperature is seen to decrease by the effect of these recirculation zones, with larger downstream angles, and thus the heat loss associated with the flames, decreased as well.

The average temperature in the chamber is plotted for the entire combustor at variable upstream angles and a fixed upstream angle of 60° in Figure 137.

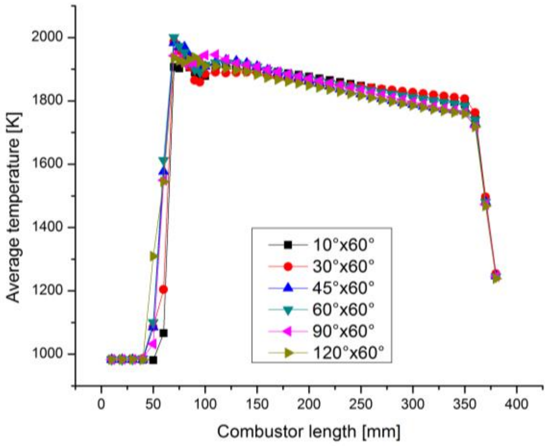

Figure 137 Average temperature in the combustor for fuel-rich at constant downstream 60°

The temperature in the chamber increases with larger upstream angles with a maximum overall found for 45°x60° near the injector, and later for a 120°x60°, due to vortex breakdown downstream of the injector, the local equivalence ratio increased. The temperature gap for a fixed upstream angle of 60° varied from 80 to 140 K.

Figure 138 presents the chemical heat release for variable upstream angles with fixed downstream angles of 60°. As the angles increase, due to the flow changes induced by the angles, the decrease of local equivalence ratio and flame temperature, the heat release decreases.

Figure 119 presented the total heat loss plotted this time for the variable downstream angles. The heat loss increases as angles increase on the upstream for a 60°x30° configuration, however, as angles increased, the recirculation zones in the wake of the injector enlarged. Due to a lower equivalence ratio overall, the total heat loss decreased with larger angles upstream for constant downstream angles of 60°.

Figure 139 presents the combustion efficiency for constant downstream angles of 60° and combustor length on the right side using the enthalpy approach (-a), the left side presents the chemical heat release approach (–b).

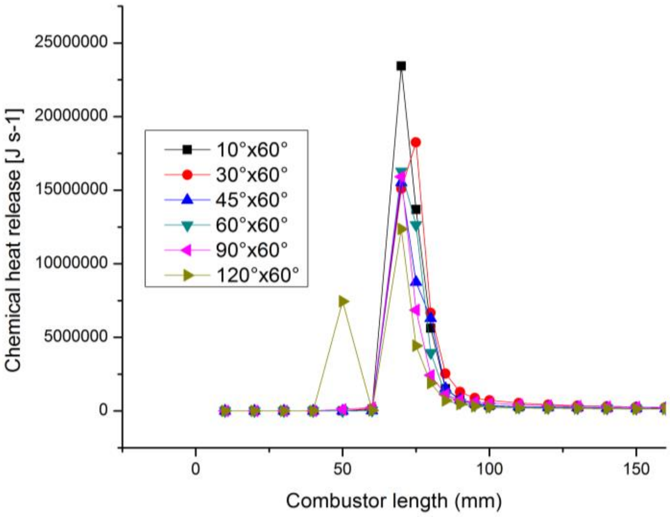

Figure 138 Chemical heat release for constant 60° downstream angles at fuel-rich conditions

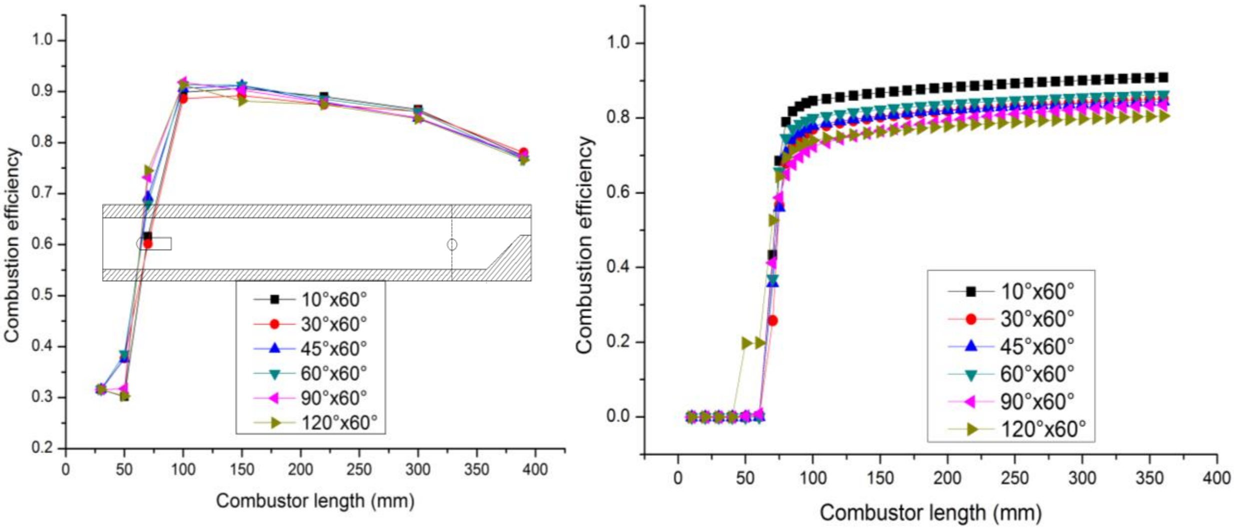

Figure 139 Combustion efficiency for constant downstream 60° angles at fuel-rich conditions

When higher angles are set for the downstream pair and the upstream angles increase, the using the enthalpy approach, the combustion efficiency increases until it reaches a plateau, after which larger angles on the upstream lower the local equivalence ratio and temperature, which lead to decreasing combustion efficiencies. From the nozzle combustion efficiency, observed in Figure 140, the efficiency varies only about 3%, where due to the recirculation zones and asymmetry in the flame, the efficiency varies little. As the angles increase on the downstream, the combustion efficiency decreases in the chamber. The variation is larger when the combustion efficiency is estimated using the chemical heat release approach i.e. 10%.

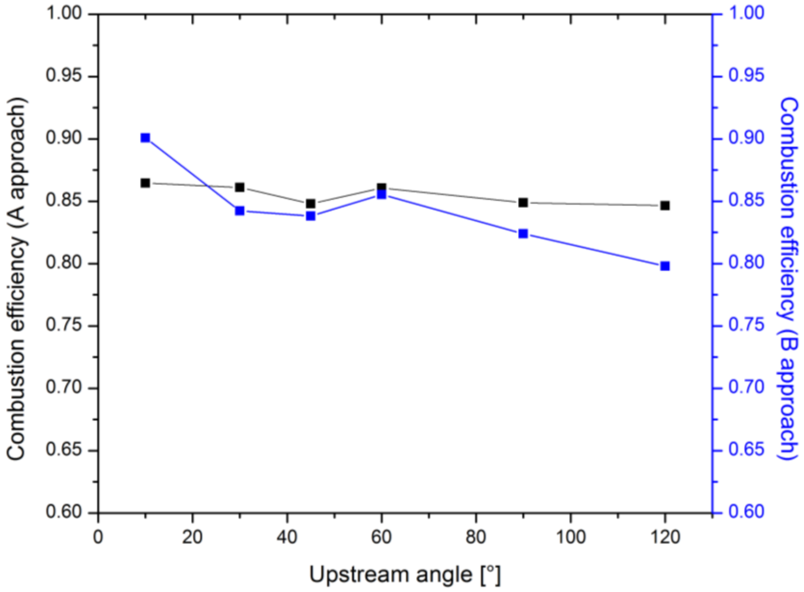

Figure 140 Overall combustion efficiency using the two approaches, enthalpy difference (black line) and chemical heat release (blue line) for constant downstream angles of 60°

Figure 141 presents the NO and NO2 mass fraction plotted in the length of the combustor for variable upstream angles at constant downstream angles of 60°. For the 30°x60° configuration, due to the presence of the ramp-shaped nozzle, asymmetry in the flame is observed through the recirculation zones. The two configurations that generate the higher asymmetry in the flame, due to this exact effect, generate the largest amount of NO near the injector, after which the NOx production decreases downstream. The NO2, on the other hand, as seen from Figure 141, is produced earlier in the combustor but follows the same trend as the NO production, for the same reasons. This asymmetry favored the upper side where larger vortices occur. These larger structures trap larger amounts of O2, leading to larger amounts of NO and NO2 in the area. As a result, flame-formed NO and pre-flame NO2, increased as the separate flame fronts created their separate NOx, independent, which by not being in a single flame front, does not dissociate and recombine as easily.

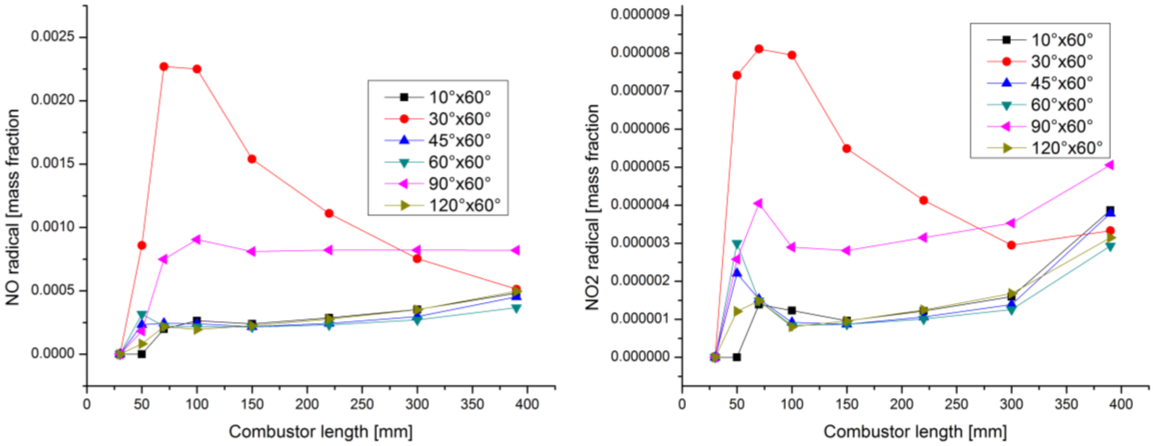

Figure 141 NO and NO2 mass fraction distribution in the combustor for constant downstream angles fixed at 60°

The EINOx, plotted in Figure 123, increases with larger upstream angles, albeit a 30° configuration on the upstream. As seen previously the bulk of the EINOx is given by the recirculation zones. When the angles increased to 120° on the upstream, due to the rarefication of the flame, and subsequent dilution, the NOx production was inhibited and the resulting EINOx decreased. Increasing the upstream angles at large downstream angles, decrease with the decrease of temperature. However, larger angles on the downstream when the upstream angles increase, due to the flame shape and equivalence ratio, produce more NOx in the chamber.

The following conclusions can be drawn from the study performed so far:

- Configurations with larger angles downstream generate more NOx.
- Upstream angles have little influence on the production of NOx for small downstream angles.
- As angles increase on the downstream, large eddy formations that precede the upstream injection holes, lower the combustion efficiency.
- As angles increase on the downstream, large vortices formations that precede the upstream injection holes, lower the combustion efficiency.
- Combustion efficiency has a peak when the vortices that precede the upstream injection holes as well as vortices between the injection holes are small.
- As the angles increase on the downstream, the combustion efficiency decreases in the chamber.

4.5. NOx sensitivity analysis

In the previous sections, the combustion characteristics of various angled configuration have been investigated in terms of heat loss, combustion efficiency and NOx production. Based on the results we have obtained we start now to consider the most important configurations. Once a single configuration has been determined a sensitivity study will be made to determine the NOx formation steps and routes that are important in the combustion process.

A sensitivity analysis is performed in order to determine the rate-limiting reactions and mechanisms in the formation of NOx. Since NOx are becoming increasingly regulated [31], an understanding of the formation mechanisms that take part is necessary. Bowman et al. [84] introduced a discussion on the current (at the time) and future control technologies of NOx.

In Figure 142 and Figure 143 the EINO, EINO2 and EINOx are presented for constant upstream angles and constant downstream angles, respectively, in relation to the variable angles on the downstream and upstream respectively.

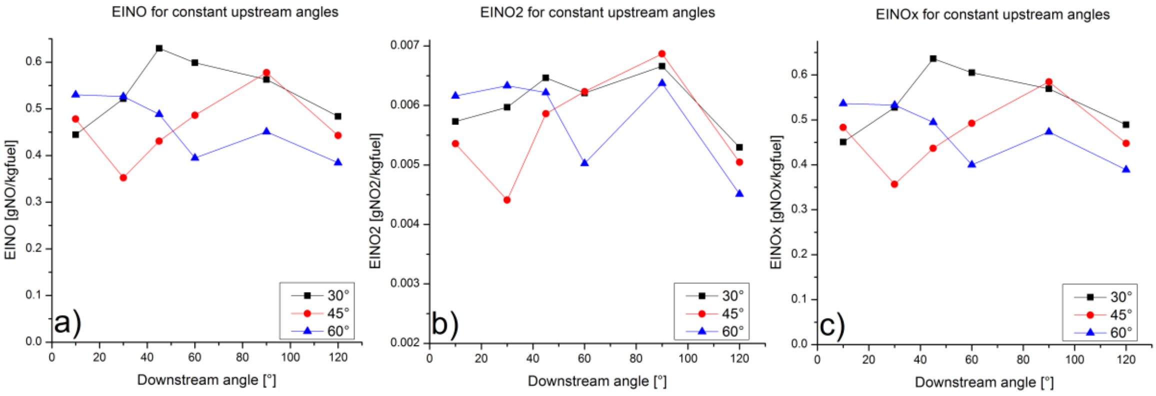

Figure 142 EINO a), EINO2 b), and EINOx c), plotted for variable downstream angles when the upstream angles are kept constant

From Figure 142, the configurations with the lowest amount of NOx exhausted in the burned gas are 45°x30°, 45°x45°, 60°x45°, 60°x60°, and 60°x120°, that have the lowest NOx content per kilogram of fuel injected at fuel rich conditions. When compared with the combustion efficiency for each configuration arranged in Figure 143, the combustion efficiency is highest for angles smaller than 60°. As a result, 60°x120° is neglected. Using the combustion efficiency approaches, we observe that higher values are found for 60°x10°, β°x30° and β°x45°. Comparing these results with the previous data, three configurations stand out: 45°x30°, 45°x45°, and 60°x45°.

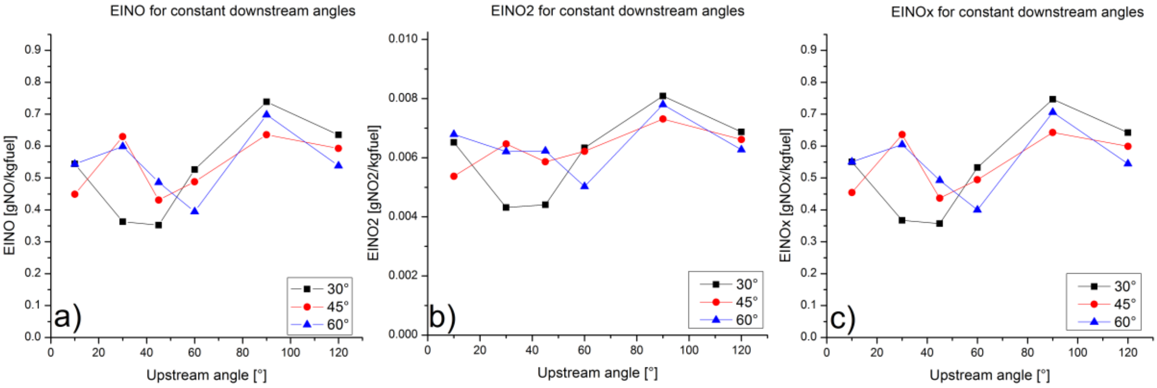

Figure 143 EINO a), EINO2 b), and EINOx c), plotted for variable upstream angles when the downstream angles are kept constant

From Figure 143, for constant upstream angles, lower EINOx configurations are 30°x30°, 30°x45°, 45°x30°, 60°x45° and 60°x60°. Comparing these configurations with the combustion efficiency, the largest values near the nozzle are given by 10°xθ°, 30°x30°, 30°x45°, 45°x30°, 45°x45°, 45°x60° and 60°x45° configurations. However, as stated in the introduction, the optimal configuration has to yield low heat loss, high combustion efficiency and low NOx in the exhaust gas. As a result, 30°x30°, 30°x45°, 45°x30° and 60°x45° remain viable solutions. When the solutions from both cases are compared, two are found in both situations: 45°x30° and 60°x45°. The configurations 45°x30° generate high asymmetry in the chamber that creates high NOx near the injection zones, which affect the flame shape. As a result, one configuration is found to satisfy all the conditions i.e. low NOx, high combustion efficiency, low heat loss - 60°x45°.

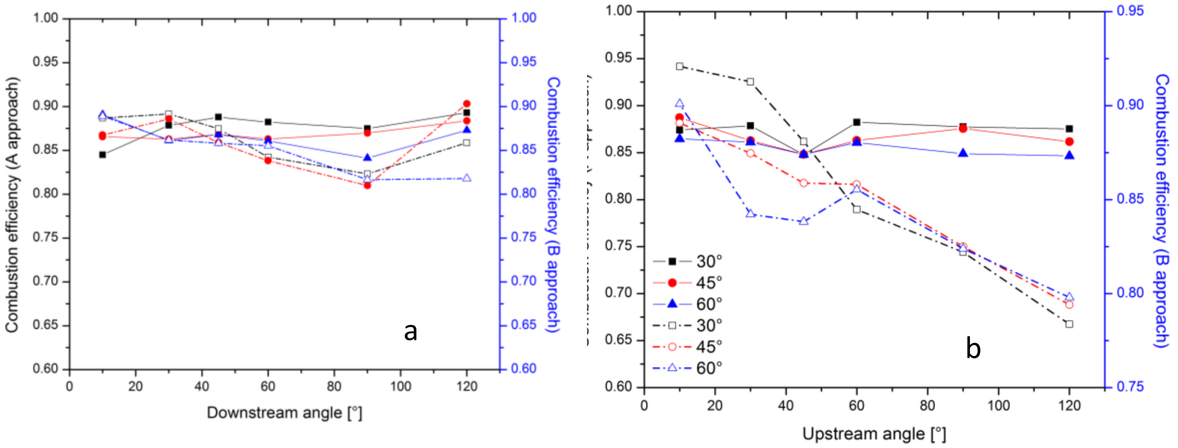

Figure 144 Combustion efficiency for a) constant downstream angles and variable upstream angles and b) constant upstream angles and variable downstream angles using two evaluation approaches; black lines 30°, red lines 45°, blue lines 60°; solid lines enthalpy approach, dashed lines heat release approach

Experiments performed so far[61] have determined that the 60°x45° is preferred in so far as it more stable than when downstream angles are increased. Following these arguments, a NOx sensitivity analysis is performed for the 60°x45° configuration to determine the sensitive reactions in the combustion process of the PCTJ.

Figure 145 presents the influence of enlarged reaction rate coefficients on the NOx production for a 60°x45° configuration at fuel-rich conditions. The simulations are performed using 188 elementary reactions accounting for 28 chemical species. In Figure 145, only the reaction that have at least a 20% effect on the NO and NO2 are presented. The horizontal axis presents the sensitivity index, while the vertical axis at Y=1, represents the standard mechanism. The normalized values of the reaction are presented on the left and right side, depending on the value of the resulting NO / NO2.

The NO sensitivity study presented here is a propulsion study and not a chemical reaction study. For more information on the behavior of hydrogen/air flames I would refer the reader to studies done by Dixon-Lewis et al.[85]. Detailed hydrogen combustion research has been conducted for rich hydrogen/air or hydrogen/oxygen flames by many authors in the past from works of Goyal el al.[86] or He et al.[87]. Numerous studies have investigated the sensitivity analysis of hydrogen/air flames [78, 44, 71] being just a few mentioned. In the present study, we shall show the important reactions that influence the production / consumption of NOx in the combustor for a fixed configuration.

A list of important reactions and the significance of their importance is presented in table 7

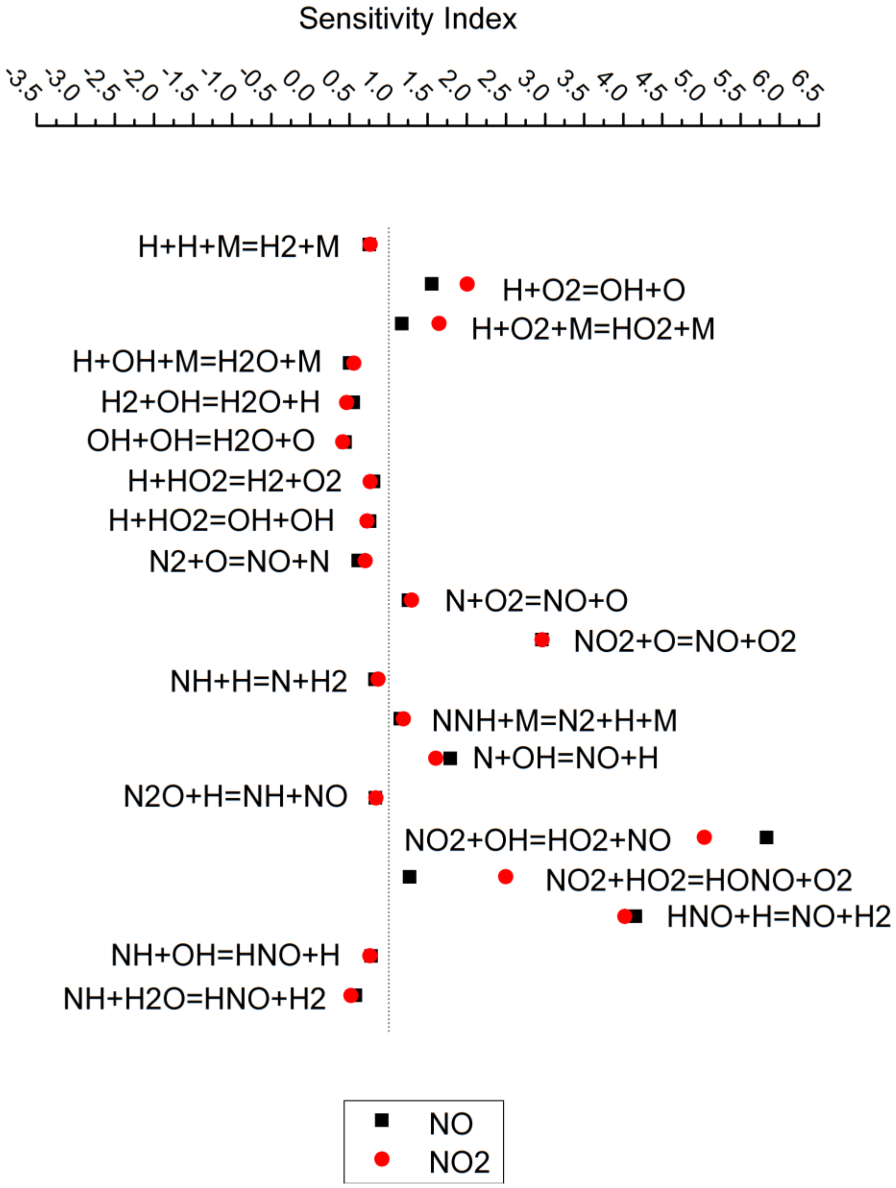

Figure 145 Influence of enlarged reaction rate coefficients on the NO/NO2 production in a 60°x45° configuration at fuel-rich conditions

Table 7 Important reactions as a result of 10x-enlarged reaction rates

Reaction number	Reaction	Reason for importance
1	H+H+M=H2+M	chain initiating / chain terminating
7	H+O2=OH+O	chain branching / precursor of NO through the Zel'dovich route
8	H+O2+M=HO2+M	formation of HO2, precursor of NO through the NO2 route
9	H+OH+M=H2O+M	chain terminating
10	H2+OH=H2O+H	chain branching / precursor of NO through the Zel'dovich route
11	OH+OH=H2O+O	chain branching
14	H+HO2=H2+O2	chain initiating / formation of HO2, precursor of the NO2 route
15	H+HO2=OH+OH	precursor of NO through NO2 route
25	N2+O=NO+N	main reaction in Zel'dovich route
26	N+O2=NO+O	main reaction in Zel'dovich route
35	NO2+O=NO+O2	main reaction in the NO2 route
52	NH+H=N+H2	dissociation of NH from NNH / precursor to NO via the NNH route
69	NNH+M=N2+H+M	redissociation of NNH / precursor to NO via the NNH route
100	N+OH=NO+H	main reaction in Zel'dovich route
102	N2O+H=NH+NO	N2O destruction, formation of NO via the N2O route
111	NO2+OH=HO2+NO	main NO2 reaction in NO2 route
112	NO2+HO2=HONO+O2	main NO2 reaction in NO2 route
122	HNO+H=NO+H2	deNOx reaction (NO – HNO – N2)
158	NH+OH=HNO+H	deNOx reaction (NO – HNO – N2)
163	NH+H2O=HNO+H2	deNOx reaction (NO – HNO – N2)

From the sensitivity study, and the reaction analysis, the reactions that stand out, as more sensitive to a reaction rate enlargement, are part of the known mechanisms that from

NO. The NO that form for this configuration are influenced by Zel'dovich mechanism that depends on the temperature of the flame and residence time of the radical at that temperature, and since the temperature varies little between the different configurations, NOx formed by this mechanism is assumed to be influenced by the injection configuration to a smaller degree. The other mechanism that seems to be of importance is the NO2 route. At high temperatures, NO2 conversion into NO is usually rapid, due to high concentrations of intermediate radicals.[84] We have seen that due to different angles of injection on the upstream and downstream side, vortices form and break down, either in the wake of the injector (constant upstream angles), or in between the injection holes (constant downstream angles). Also, since NO2 is seen to form in the center of these vortices, as shown in the previous chapters, we can conclude that the injection angles influence the formation of NOx through the flow-induced vortices that form. As a result, the NO2 conversion is found to be very sensitive to the injection angles.

The other mechanism that is observed is part of the deNOx process, which enhances when the respective reaction rates are enlarged. Since usually the deNOx process does not contribute to the addition of larger NOx to the process, it is not considered as a NOx producing mechanism. Small contributions to the NOx are given through the N2O destruction and NNH path.

5. Conclusions and general considerations

A study to determine the combustion characteristics on hydrogen angled injection has been performed in the simulated afterburner chamber of the PCTJ. Fuel-lean and fuel-rich experiments and simulations have been performed at different injection configurations to determine the heat loss, heat release ration, combustion efficiency and EINOx. A sensitivity study has also been performed to determine the important reactions that create NOx in the current combustor in order to better understand and correct NOx emissions. The following conclusions have been drawn:

- Equivalence ratio
    - At fuel-lean conditions, for constant upstream angles, when downstream angles increase, the average temperature increases in the chamber.
    - At fuel-lean conditions, constant upstream angles with variable downstream, the combustion efficiency increases.
    - Large upstream angles have little influence on the combustion efficiency near the nozzle, when the combustion efficiency peak moves closer to the injector.
    - At fuel rich conditions the angled injection modifies the combustion efficiency to almost 10%.
- Heat loss
    - As angles increase on the downstream, the total heat loss increased by the mixture’s prolonged contact with the walls.

    - As angles increase on the upstream, they had minor influences on the total heat loss.
- Flow behavior
    - Vortices in the recirculation zone break down when fuel is injected with large angles on the downstream.
    - High upstream angles create vortices up-flow of the upstream injection holes and in-between the injection holes
- NOx
    - NO is produced in the post-flame region of the flame.
    - NO2 is produced in the pre-flame region of the flame.
    - For fuel-rich combustion, NOx is produces, in larger degree by the NO2 conversion, and thermal NOx, with small contribution given by the N2O destruction and NNH path.
- Combustion efficiency
    - The position where the combustion efficiency is estimated is quite important in considering the enthalpy difference. For hydrogen-fueled combustion at fuel-rich conditions, a shorter combustor would yield higher combustion efficiency.

- Combustion efficiency using the heat release in the chamber is independent of temperature and heat loss and properly determines the effect of angled injection in the combustor.
- Higher upstream angles with constant downstream always decrease the combustion efficiency.
- Combustion efficiency reaches a peak when vortices in the wake of the injector are superimposed into one structure
- Combustion efficiency is influenced by angle-induced vortices that form in the wake of the injector and later break down (for constant upstream angles) and in between the injection holes (for constant downstream angles).

The study was performed as part of a joint project between the university of Tokyo and JAXA, in order to understand the behavior of angled injection in the combustor. Several experiments have shown flow instabilities and different combustion phenomena in the combustor, so a series of experiments have begun to search for an optimal injector shape, while in parallel; an optimal injection angle was studies. The present simulations help provide an understanding of the flow induced behavior of different injection angles, as well as low NOx and high combustion efficiency configurations. These results will help the experimental combustor with choosing a set of configurations that can work to provide optimal conditions. The experimental results, themselves, are helping a larger experimental of a small sized engine performed at JAXA which in the end can and will facilitate better design, configurations and understanding of the engine’s functionality. As such, some general considerations are presented below:

Flow behavior

- Perpendicular and up-flow injection decreases the combustion efficiency.
- Upstream angles when the downstream angles are constant have little influence on the combustion efficiency.

NOx

- Fuel-rich combustion allows for less variation, with angles, and lower NOx emissions in the combustor then fuel-lean combustion.

Combustion efficiency

- The position where the combustion efficiency is estimated is quite important in considering the enthalpy difference. For hydrogen-fueled combustion at fuel-rich conditions, and the same design with one injector, a shorter combustor would yield higher combustion efficiency.
- Combustion efficiency using the heat release in the chamber is independent of temperature and heat loss and properly determines the effect of angled injection in the combustor.

Configurations

- Low-NOx and high combustion efficiency configurations have injection angles between 30° to 60° on downstream and upstream injection holes.

Acknowledgements

First and foremost I want to thank my advisor Tsue Mitsuhiro. It has been an honor to be his Ph.D. student. He has taught me, above all else, the value of practical research. I appreciate all his advice, contribution, effort, and ideas as well as his valued support throughout my Ph.D. study. Associate Professor Nakaya Shinji has contributed immensely to my professional development during my study at the University of Tokyo. His invaluable advice and constant monitoring has brought this work to fruition. I would also like to thank professor Shimada, professor Teramoto and professor Dobashi for providing much needed comments that led to the completion of this study. Thank you.

The various members of the laboratory, and friends that have helped me in everyday life, adapting to a foreign society, whether it was personal affairs or professional advice, they have been a stepping stone that is at the base of this thesis. Without their enthusiasm, cheerfulness and camaraderie, my experience and work would have been lacking.

Relating to the thesis, I wish to thank Masafumi Utsumi and Takeo Okunuki for their assistance at the Kashiwa Hypersonic Wind Tunnel experiments and Dr. Yamashita for his invaluable support with the PHOENICS code. Thanks need to be given to my friends that have helped me with suggestions and overall moral support Theerapol “Zun” Thurakitseree and Jae-Ho Lee.

I gratefully acknowledge the funding sources that made my Ph.D. work possible. I was funded by the MEXT: Ministry of Education, Culture, Sports, Science and Technology through the 5 years it took to complete my Master’s program and my Doctorate program.

Lastly, I would like to thank my mother and my sister for all their love and encouragement. I would like to mention the continuous advice and support throughout the years from Mr. Moldoveanu Ioan. Without his support I know I would have been lost along the way. He has been my mentor and my inspiration.

And most of all I would like to thank my loving, supportive, encouraging and patient future wife, Marina, whose constant quiet support during the long hours, desperation and elation moments, of this Ph.D. has brought it to the finish. Thank you.

Ianus George

The University of Tokyo

October 2013

References

1 Kuo, K., *Principles of combustion*, Wiley-Interscience, 2005.

2 Barber, T., Maicke, B., and Majdalani, J., "Current State of High Speed Propulsion: Gaps, Obstacles, and Technological Challenges in Hypersonic Applications," *Proceedings of the 45th AIAA/ASME/SAE/ASEE Joint Propulsion Conference & Exhibit*, Denver, Colorado: AIAA, 2009, pp. 1–28.

3 Rolls Royce, *The Jet Engine*, Rolls Royce Technical Publication (1996), 2005.

4 Fry, R. S., "A century of ramjet propulsion technology evolution," *Journal of propulsion and power*, vol. 20, 2004, pp. 27–58.

5 Murthy, S. N. B., *High-Speed Flight Propulsion Systems (Progress in Astronautics and Aeronautics)*, AIAA, 1991.

6 Tsujikawa, Y., Tsukamoto, Y., Fuji, S., and Fujii, S., "Performance analysis of scramjet engine with quasi-one-dimensional flow model," *International journal of hydrogen energy*, vol. 16, 1991, pp. 135–142.

7 Taguchi, H., and Futamura, H., "Analytical study of pre-cooled turbojet engine for TSTO spaceplane," *Proceedings of the 10th International Space Hypersonic Systems and Conference*, Kyoto: AIAA, 2001.

8 Taguchi, H., Kobayashi, H., Kojima, T., Ueno, A., Imamura, S., Hongoh, M., and Harada, K., "Research on hypersonic aircraft using pre-cooled turbojet engines," *Acta Astronautica*, vol. 73, Apr. 2011, pp. 164–172.

9 JAXA Report, *JAXA Long Term Vision*, 2005.

10 Tanatusgu, N., Sato, T., Naruo, Y., Kashiwagi, T., Tanatsugu, N., and Omi, J., "Development study on ATREX engine," *Acta astronautica*, vol. 40, 1997, pp. 165–170.

11 WANG, Q., WANG, Z., LEI, J., and WEN, C., "Review of Research on Air Turbo Rocket," *Proceedings of Asian Joint Conference on Propulsion and Power*, 2012.

12 Spalding, D., "Combustion and mass transfer: a textbook with multiple-choice exercises for engineering students," *Pergamon Press Ltd.*, 1979.

13 Taguchi, H., Kobayashi, H., Kojima, T., Hongoh, M., Masaki, D., Sawai, S., Maru, Y., Sato, T., and Agency, E., "Qualification Test of a Hypersonic Turbojet Engine for a Flight Experiment," *Proceedings of the Asian Joint Conference on Propulsion and Power*, 2010, pp. 77–84.

14 Papamoschou, D., and Roshko, A., "Observations of supersonic free shear layers," *Sadhana*, vol. 12, 1986, pp. 1–14.

[15] Edwards, T., “Liquid fuels and propellants for aerospace propulsion,” *Journal of Propulsion and Power*, vol. 19, 2003.

[16] Suzuki, Y., “On hydrogen as fuel gas,” *International Journal of Hydrogen Energy*, vol. 7, 1982, pp. 227–230.

[17] Cecere, D., Ingenito, a., Giacomazzi, E., Romagnosi, L., and Bruno, C., “Hydrogen/air supersonic combustion for future hypersonic vehicles,” *International Journal of Hydrogen Energy*, vol. 36, Sep. 2011, pp. 11969–11984.

[18] Ramanathan, V., and Inamdar, A., *The radiative forcing due to clouds and water vapor*, 2006.

[19] Goody, R., and Yung, Y., *Atmospheric radiation: theoretical basis*, Oxford University Press, 1995.

[20] Sherwood, S., and Roca, R., “Tropospheric water vapor, convection, and climate,” *Reviews of Geophysics*, 2010.

[21] Tsujikawa, Y., and Northam, G., “Effects of hydrogen active cooling on scramjet engine performance,” *International journal of hydrogen energy*, vol. C, 1996.

[22] Larsson, J., Vicquelin, R., and Bermejo-Moreno, I., “Large eddy simulations of the HyShot II scramjet,” *ctr.stanford.edu*, 2012, pp. 63–74.

[23] Fox, J., and Gaston, M., “Comparison Of Hypermixing Injectors Using A Mixture-Fraction-Sensitive Imaging Techinique,” *13th Australasian Fluid Mechanics Conference*, Melbourne: 1998.

[24] Gerlinger, P., Stoll, P., Kindler, M., Schneider, F., and Aigner, M., “Numerical investigation of mixing and combustion enhancement in supersonic combustors by strut induced streamwise vorticity,” *Aerospace Science and Technology*, vol. 12, Mar. 2008, pp. 159–168.

[25] Schetz, J. a., Maddalena, L., Throckmorton, R., and Neel, R., “Complex Wall Injector Array for High-Speed Combustors,” *Journal of Propulsion and Power*, vol. 24, Jul. 2008, pp. 673–680.

[26] Marzouk, Y. M., and Ghoniem, A. F., “Mechanism of streamwise vorticity formation in a transverse jet,” *Proceedings of the 40th AIAA Aerospace Sciences Meeting and Exhibit*, Reno, NV: AIAA, 2002.

[27] Hönig, R., Theisen, D., and Fink, R., “Experimental investigation of a SCRAMJET model combustor with injection through a swept ramp using laser-induced fluorescence with tunable excimer lasers,” *Twenty-Sixth Symposium (International) on Combustion*, 1996, pp. 2949–2956.

[28] Fernando, E., and Menon, S., “Mixing enhancement in compressible mixing layers: an experimental study,” *AIAA journal*, May. 1993.

[29] Kim, J., Yoon, Y., Jeung, I., Huh, H., and Choi, J., “Numerical study of mixing enhancement by shock waves in model scramjet engine,” *AIAA journal*, vol. 41, 2003.

[30] Araki, S., Sakaue, S., Arai, T., and Taguchi, H., “Wake Flow Control on the Afterburner behind Fuel Injection and Flame Holding Strut for Hypersonic Vehicle,” *18th AIAA/3AF International Space Planes and Hypersonic Systems and Technologies Conference*, Reston, Virigina: American Institute of Aeronautics and Astronautics, 2012, pp. 1–10.

[31] Cummins Emission Solutions, “Worldwide Emissions Regulations” Available: http://cumminsemissionsolutions.com/ces/navigationAction.do?url=SiteContent+en+HTML+EmissionsTechnology+Worldwide_Emissions_Regualtions.

[32] Warnatz, J., Maas, U., and Dibble, R. W., *Combustion: physical and chemical fundamentals, modeling and simulation, experiments, pollutant formation*, Springer, 2006.

[33] U.S. Environmental Protection Agency, Act, C. S., Agency, T., and Web, C. S., *Overview of the Human Health and Environmental Effects of Power Generation : Focus on Sulfur Dioxide (SO 2), Nitrogen Oxides (NO X) and Mercury (Hg)*, 2003.

[34] Lee, D. S., Fahey, D. W., Forster, P. M., Newton, P. J., Wit, R. C. N., Lim, L. L., Owen, B., and Sausen, R., “Aviation and global climate change in the 21st century,” *Atmospheric Environment*, vol. 43, Jul. 2009, pp. 3520–3537.

[35] Driscoll, J. F., Chen, R.-H., and Yoon, Y., “Nitric oxide levels of turbulent jet diffusion flames: Effects of residence time and damkohler number,” *Combustion and Flame*, vol. 88, Jan. 1992, pp. 37–49.

[36] Bozzelli, J. W., and Dean, A. M., “O + NNH: A Possible New Route for NOx Formation in Flames,” *International Journal of Chemical Kinetics*, vol. 27, 1995, pp. 1097–1109.

[37] Nishida, S., Ianus, G., Taneda, H., Kita, S., Taguchi, H., Utsumi, M., Okunuki, T., Araki, M., Takahashi, S., Imamura, O., and Tsue, M., “Measurements of Combustion and NOx Emission Characteristics in Afterburner of Pre-Cooled Turbo Jet,” *Proceedings of the 28th ISTS*, 2011.

[38] Nishida, S., Taneda, H., Taguchi, H., Kojima, T., Hongoh, M., Imamura, O., Ianus, G., Utsumi, M., Okunuki, T., Araki, M., Tsue, M., and Combustion, R., “Combustion Characteristics of Pre-Cooled Turbo Jet Afterburner,” *Proceedings of the Asian Joint Conference on Propulsion and Power*, Okinawa, Japan: 2010.

[39] Kojima, T., Kobayashi, H., Taguchi, H., Goto, K., and Sato, T., “Design and Fabrication of Variable Nozzle for Precooled Turbojet Engine,” *Proceedings of the 16th AIAA/DLR/DGLR International Space Planes and Hypersonic Systems and Technologies Conference*, American Institute of Aeronautics and Astronautics, 2009.

[40] Fujita, K., Sawai, S., Kobayashi, H., Tsuboi, N., Taguchi, H., Kojima, T., Okai, K., Sato, T., and Miyaji, K., "Precooled turbojet engine flight experiment using balloon-based operation vehicle," *Acta Astronautica*, vol. 59, Jul. 2006, pp. 263–270.

[41] Sato, T., Taguchi, H., Kobayashi, H., Kojima, T., Okai, K., Fujita, K., Masaki, D., Hongo, M., and Ohta, T., "Development study of precooled-cycle hypersonic turbojet engine for flight demonstration," *Acta Astronautica*, vol. 61, Apr. 2007, pp. 367–375.

[42] Kee, R., Rupley, F., Meeks, E., and Miller, J., *CHEMKIN-III: A FORTRAN chemical kinetics package for the analysis of gas-phase chemical and plasma kinetics*, 1996.

[43] Kee, R., *Transport: a software package for the evaluation of gas-phase, multicomponent transport properties*, 1999.

[44] Konnov, A. A., Colson, G., and Ruyck, J. De, "NO formation rates for hydrogen combustion in stirred reactors," *Fuel*, vol. 80, Jan. 2001, pp. 49–65.

[45] Marinov, N. M. M. N., Westbrook, C. K. K., and Pitz, W. J. J., "Ddetailed and global chemical kinetics model for Hydrogen," *Proceedings of the 8th International Symposium on Transport Properties*, San Francisco, CA: 1995, pp. 118–129.

[46] Mueller, M., and Kim, T., "Flow reactor studies and kinetic modeling of the H2/O2 reaction," *International Journal of Chemical Kinetics*, vol. 2, 1999, pp. 113–125.

[47] Poinsot, T., and Veynante, D., *Theoretical and numerical combustion*, 2005.

[48] Métais, O., and Ferziger, J., "New tools in turbulence modelling," *… Springer-Verlag Berlin Heidelberg New …*, 1997.

[49] Veynante, D., and Vervisch, L., "Turbulent combustion modeling," *Progress in Energy and Combustion Science*, vol. 28, Mar. 2002, pp. 193–266.

[50] Tu, J., Yeoh, G., and Liu, C., *Computational fluid dynamics: a practical approach*, Butterworth-Heinemann, 2007.

[51] Pitsch, H., "Large-Eddy Simulation of Turbulent Combustion," *Annual Review of Fluid Mechanics*, vol. 38, Jan. 2006, pp. 453–482.

[52] Chen, Y. S., and Kim, S. W., "Computation of turbulent flows using an extended k-epsilon turbulence closure model," *NASA STI/Recon Technical Report N*, 1987.

[53] Monson, D., Seegmiller, H., and McConnaughey, P., "Comparison of experiment with calculations using curvature-corrected zero and two equation turbulence models for a two-dimensional U-duct," *Proceedings of the 21st Fluid Dynamics, Plasma Dynamics and Lasers Conference*, 1990.

[54] Hedberg, P. K., Rosten, H. I., and Spalding, D. B., "The PHOENICS equations," *CHAM Report TR/99, CHAM UK*, 1986.

55 Waterson, N. P., and Deconinck, H., “Design principles for bounded higher-order convection schemes – a unified approach,” *Journal of Computational Physics*, vol. 224, May. 2007, pp. 182–207.

56 Sweby, P., “High resolution schemes using flux limiters for hyperbolic conservation laws,” *SIAM journal on numerical analysis*, vol. 21, 1984, pp. 995–1011.

57 Bagabir, a., and Drikakis, D., “Numerical experiments using high-resolution schemes for unsteady, inviscid, compressible flows,” *Computer Methods in Applied Mechanics and Engineering*, vol. 193, Oct. 2004, pp. 4675–4705.

58 Patankar, S., and Spalding, D., “A calculation procedure for heat, mass and momentum transfer in three-dimensional parabolic flows,” *Journal of Heat and Mass Transfer*, vol. I, 1972, pp. 1787–1806.

59 Zeng, M., and Tao, W. Q., “A comparison study of the convergence characteristics and robustness for four variants of SIMPLE-family at fine grids,” *Engineering Computations*, vol. 20, 2003, pp. 320–340.

60 Nakaya, S., Hatori, K., Tsue, M., Kono, M., Segawa, D., and Kadota, T., “Numerical Analysis on Flame Kernel in Spark Ignition Methane/Air Mixtures,” *Journal of Propulsion and Power*, vol. 27, Mar. 2011, pp. 363–370.

61 Nishida, S., “The study of hydrogen combustion in afterburner of a Precooled Turbojet engine [予冷ターボジェットエンジンのアフターバー ナにおける水素燃焼に関する研究],” Ph.D. Thesis / The University of Tokyo, 2012.

62 Gordon, S., and McBride, B. J., “Computer program for calculation of complex chemical equilibrium compositions rocket performance incident and reflected shocks, and Chapman-Jouguet detonations,” *Computer program for calculation of complex chemical equilibrium compositions rocket performance incident and reflected shocks and ChapmanJouguet detonations*, 1971, p. 250.

63 Zehe, M. J., Gordon, S., and Mcbride, B. J., *CAP : A Computer Code for Generating Tabular Thermodynamic Functions from NASA Lewis Coefficients*, 2002.

64 “Biennial Report on Hydrogen Safety (Version 1.2)” Available: http://www.hysafe.org/brhs.

65 Bossel, U., and Eliasson, B., “Energy and the hydrogen economy,” *Methanol Institute, Arlington, VA*, 2003.

66 Cox, L., and Blaszczak, R., *Nitrogen oxides (NOx) why and how they are controlled*, 1999.

67 Gottschaldt, K., Voigt, C., Jöckel, P., Righi, M., Deckert, R., and Dietmüller, S., “Global sensitivity of aviation NO_x effects to the HNO_3-forming channel of the HO_2 + NO reaction,” *Atmospheric Chemistry and Physics*, vol. 13, Mar. 2013, pp. 3003–3025.

68 Zeldovich, Y., “The oxidation of nitrogen in combustion and explosions,” *Acta Physicochimica URSS*, 1946.

69 Fenimore, C. P., “Formation of nitric oxide in premixed hydrocarbon flames,” *Symposium (International) on Combustion*, vol. 13, Jan. 1971, pp. 373–380.

70 MALTE, P. C., and PRATT, D. T., “The Role of Energy-Releasing Kinetics in NO x Formation: Fuel-Lean, Jet-Stirred CO-Air Combustion,” *Combustion Science and Technology*, vol. 9, Jan. 1974, pp. 221–231.

71 Skottene, M., and Rian, K. E., “A study of NOx formation in hydrogen flames,” *International Journal of Hydrogen Energy*, vol. 32, Oct. 2007, pp. 3572–3585.

72 Miller, J., Branch, M., and Kee, R., “A chemical kinetic model for the selective reduction of nitric oxide by ammonia,” *Combustion and Flame*, vol. 43, 1981, pp. 81–98.

73 Konnov, A., and Ruyck, J. De, “Temperature-dependent rate constant for the reaction NNH+ O --> NH+ NO,” *Combustion and flame*, vol. 1264, 2001, pp. 1258–1264.

74 Konnov, A. A., Colson, G., and Ruyck, J. D. E., “The new route forming NO via NNH,” *Combustion and flame*, vol. 550, 2000, pp. 548–550.

75 Ouimette, P., and Seers, P., “NOx emission characteristics of partially premixed laminar flames of H2/CO/CO2 mixtures,” *International Journal of Hydrogen Energy*, vol. 34, Dec. 2009, pp. 9603–9610.

76 Miller, D. R., Evers, R. L., and Skinner, G. B., “Effects of various inhibitors on hydrogen-air flame speeds,” *Combustion and Flame*, 1963.

77 Bowman, C., Bartok, W., and Sarofim, A., *Fossil Fuel Combustion-A source Book*, Wiley-Interscience, 1991.

78 Miller, J., and Bowman, C., “Mechanism and modeling of nitrogen chemistry in combustion,” *Progress in Energy and Combustion Science*, vol. 15, 1989, pp. 287–338.

79 Taguchi, H., Murakami, A., Sato, T., and Tsuchiya, T., “Conceptual study on hypersonic airplanes using pre-cooled turbojet,” *Proceedings of the 15th AIAA International Space Planes and Hypersonic Systems and Technologies Conference*, Ohio: AIAA, 2008, pp. 1–12.

80 Kobayashi, H., Taguchi, H., Kojima, T., Maru, Y., and Sawai, S., “Windmilling start of the precooled turbojet engine during supersonic flight,” *Proceedings of the Asian Joint Conference on Propulsion and Power 2010*, 2010, pp. 85–90.

81 Saito, R., Araki, S., Sakaue, S., Arai, T., Taguchi, H., Kojima, T., and Kobayashi, Hi., “Mixing Enhancement on the Afterburner with Fuel Injection Struts for Hypersonic Vehicle,” *17th AIAA International Space Planes and Hypersonic Systems and*

Technologies Conference, AIAA, ed., Reston, Virigina: American Institute of Aeronautics and Astronautics, 2011, pp. 1–12.

[82] Hill, S. ., and Douglas Smoot, L., “Modeling of nitrogen oxides formation and destruction in combustion systems,” *Progress in Energy and Combustion Science*, vol. 26, Aug. 2000, pp. 417–458.

[83] Cernansky, N. P., and Sawyer, R. F., “NO and NO2 formation in a turbulent hydrocarbon/air diffusion flame,” *Symposium (International) on Combustion*, vol. 15, Jan. 1975, pp. 1039–1050.

[84] Bowman, C., “Control of combustion-generated nitrogen oxide emissions: technology driven by regulation,” *Symposium (International) on Combustion*, 1992, pp. 859–878.

[85] Dixon-Lewis, G., and Williams, A., “Stability of rich hydrogen-oxygen-nitrogen flames on a flat flame burner,” *Combustion and Flame*, vol. 4, Jan. 1960, pp. 382–384.

[86] Goyal, G., Maas, U., and Warnatz, J., “Simulation of the behavior of rich hydrogen-air flames near the flammability limit,” *Combustion science and technology*, vol. 105, Apr. 1995, pp. 183–193.

[87] He, L., and Clavin, P., “Premixed hydrogen-oxygen flames. Part II: Quasi-isobaric ignition near the flammability limits,” *Combustion and Flame*, vol. 93, Jun. 1993, pp. 408–420.

[88] Clyne, M. A. A. A., and McDermid, I. S. S., “B**3(0+) states of IF, ICl and IBr. Part 2 - Observation and analysis of the excitation spectra of IF and ICl,” *Journal of the Chemical Society, Faraday Transactions 2*, vol. 72, Jan. 1976, p. 2252.

Appendix 1

Table 8 H/N/O kinetic mechanism

Units are cm^3-mole-s-cal-K, $k = A \cdot T^n\ exp(-E_a/RT)$

No.	Reaction	A	n	E_a	Third body coefficients
1	H+H+M=H2+M	6.50E+17	-1	0	a
2	H+H+H2=H2+H2	1.00E+17	-0.6	0	
3	O+O+M=O2+M	1.00E+17	-1	0	b
4	O+H+M=OH+M	6.20E+16	-0.6	0	c
5	H2+O2=OH+OH	1.70E+13	0	48150	
6	O+H2=OH+H	5.06E+04	2.67	6285	
7	H+O2=OH+O	1.00E+14	0	14843	
8	H+O2+M=HO2+M	1.40E+18	-0.8	0	d
9	H+OH+M=H2O+M	2.20E+22	-2	0	e
10	H2+OH=H2O+H	1.00E+08	1.6	3300	
11	OH+OH=H2O+O	1.50E+09	1.14	100	
12	HO2+OH=H2O+O2	1.90E+16	-1	0	
13	HO2+O=OH+O2	3.25E+13	0	0	
14	H+HO2=H2+O2	4.22E+13	0	1411	
15	H+HO2=OH+OH	1.70E+14	0	875	
16	H+HO2=H2O+O	3.00E+13	0	1700	
17	HO2+HO2=H2O2+O2	4.20E+14	0	12000	f
18	HO2+HO2=H2O2+O2	1.30E+11	0	-1640	g, h
19	OH+OH(+M)=H2O2(+M)	7.20E+13	-0.37	0	g
20	OH+OH(+H2O)=H2O2(+H2O)	7.20E+13	-0.37	0	
21	H2O2+OH=HO2+H2O	7.80E+12	0	1320	

22	H2O2+H=HO2+H2	1.70E+12	0	3750	
23	H2O2+H=H2O+OH	1.00E+13	0	3575	
24	H2O2+O=HO2+OH	6.60E+11	0	4000	
25	N2+O=NO+N	1.80E+14	0	76100	
26	N+O2=NO+O	9.00E+09	1	6500	i
27	NO+M=N+O+M	9.64E+14	0	148300	
28	NO+NO=N2+O2	3.00E+11	0	65000	g, j
29	N2O(+M)=N2+O(+M)	1.26E+12	0	62620	
30	N2O+O=N2+O2	1.00E+14	0	28200	
31	N2O+O=NO+NO	6.92E+13	0	26630	
32	N2O+N=N2+NO	1.00E+13	0	20000	
33	N2O+NO=N2+NO2	2.75E+14	0	50000	g, k
34	NO+O(+M)=NO2(+M)	1.30E+15	-0.74	0	
35	NO2+O=NO+O2	3.91E+12	0	-238	l
36	NO2+N=NO+NO	1.00E+12	0	0	
37	NO2+N=N2O+O	8.40E+11	0	0	
38	NO2+NO=N2O+O2	1.00E+12	0	60000	
39	NO2+NO2=NO+NO+O2	3.95E+12	0	27590	
40	NO2+NO2=NO3+NO	1.13E+04	2.58	22720	g, m
41	NO2+O(+M)=NO3(+M)	1.33E+13	0	0	
42	NO3=NO+O2	2.50E+06	0	12120	
43	NO3+O=NO2+O2	1.02E+13	0	0	
44	NO3+NO2=NO+NO2+O2	1.20E+11	0	3200	
45	NO3+NO3=NO2+NO2+O2	5.12E+11	0	4870	g, n
46	N2O4(+M)=NO2+NO2(+M)	4.05E+18	-1.1	12840	

47	N2O4+O=N2O3+O2	1.21E+12	0	0	
48	NO2+NO(+M)=N2O3(+M)	1.60E+09	1.4	0	
49	N2O3+O=NO2+NO2	2.71E+11	0	0	o
50	N2+M=N+N+M	1.00E+28	-3.33	225000	
51	NH+M=N+H+M	2.65E+14	0	75500	
52	NH+H=N+H2	3.20E+13	0	325	
53	NH+N=N2+H	9.00E+11	0.5	0	
54	NH+NH=NNH+H	5.10E+13	0	0	
55	NH+NH=NH2+N	5.95E+02	2.89	-2000	
56	NH+NH=N2+H2	1.00E+08	1	0	
57	NH2+M=NH+H+M	3.16E+23	-2	91400	
58	NH+H2=NH2+H	1.00E+14	0	20070	
59	NH2+N=N2+H+H	6.90E+13	0	0	
60	NH2+NH=N2H2+H	1.50E+15	-0.5	0	
61	NH2+NH=NH3+N	1.00E+13	0	2000	
62	NH3+NH=NH2+NH2	3.16E+14	0	26800	
63	NH2+NH2=N2H2+H2	7.80E+11	0	0	
64	NH3+M=NH2+H+M	2.20E+16	0	93470	
65	NH3+M=NH+H2+M	6.30E+14	0	93390	
66	NH3+H=NH2+H2	5.42E+05	2.4	9920	
67	NH3+NH2=N2H3+H2	1.00E+11	0.5	21600	f
68	NNH=N2+H	3.00E+08	0	0	
69	NNH+M=N2+H+M	1.00E+13	0.5	3060	
70	NNH+H=N2+H2	1.00E+14	0	0	
71	NNH+N=NH+N2	3.00E+13	0	2000	

72	NNH+NH=N2+NH2	2.00E+11	0.5	2000	
73	NNH+NH2=N2+NH3	1.00E+13	0	0	estimate p
74	NNH+NNH=N2H2+N2	1.00E+13	0	4000	estimate p
75	N2H2+M=NNH+H+M	5.00E+16	0	45000	
76	N2H2+M=NH+NH+M	5.00E+16	0	103000	
77	N2H2+H=NNH+H2	8.50E+04	2.63	-230	
78	N2H2+N=NNH+NH	1.00E+06	2	0	
79	N2H2+NH=NNH+NH2	1.00E+13	0	6000	
80	N2H2+NH2=NH3+NNH	8.80E-02	4.05	-1610	
81	N2H3+M=NH2+NH+M	5.00E+17	0	50000	
82	N2H3+M=N2H2+H+M	1.00E+17	0	29000	
83	N2H3+H=N2H2+H2	1.00E+13	0	0	
84	N2H3+H=NH2+NH2	5.00E+13	0	2000	
85	N2H3+H=NH+NH3	1.00E+11	0	0	
86	N2H3+N=N2H2+NH	1.00E+06	2	0	
87	N2H3+NH=N2H2+NH2	2.00E+13	0	0	
88	N2H3+NH2=N2H2+NH3	1.00E+11	0.5	0	
89	N2H3+NNH=N2H2+N2H2	1.00E+13	0	4000	
90	N2H3+N2H2=N2H4+NNH	1.00E+13	0	6000	g, u
91	N2H3+N2H3=NH3+NH3+N2	3.00E+12	0	0	estimate u
92	N2H4(+M)=NH2+NH2(+M)	5.00E+14	0	60000	
93	N2H4+M=N2H3+H+M	1.00E+15	0	60000	
94	N2H4+H=N2H3+H2	7.00E+12	0	2500	
95	N2H4+H=NH2+NH3	2.40E+09	0	3100	
96	N2H4+N=N2H3+NH	1.00E+10	1	2000	

97	N2H4+NH=NH2+N2H3	1.00E+09	1.5	2000	
98	N2H4+NH2=N2H3+NH3	1.80E+06	1.71	-1380	
99	N2H3+N2H3=N2H4+N2H2	1.20E+13	0	0	
100	N+OH=NO+H	2.80E+13	0	0	
101	N2O+H=N2+OH	2.20E+14	0	16750	
102	N2O+H=NH+NO	6.70E+22	-2.16	37155	
103	N2O+H=HNNO	8.00E+24	-4.39	10530	
104	HNNO+H=H2+N2O	1.00E+13	0	0	
105	HNNO+H=NH2+NO	1.00E+12	0	0	
106	HNNO+OH=H2O+N2O	1.00E+13	0	0	
107	N2O+H=NNH+O	5.50E+18	-1.06	47290	
108	N2O+OH=N2+HO2	1.00E+14	0	30000	
109	HNO+NO=N2O+OH	8.50E+12	0	29580	
110	NO2+H=NO+OH	1.32E+14	0	362	
111	NO2+OH=HO2+NO	1.81E+13	0	6676	
112	NO2+HO2=HONO+O2	4.64E+11	0	-479	
113	NO2+H2=HONO+H	3.21E+12	0	28810	
114	NO2+NH=N2O+OH	1.00E+13	0	0	
115	NO3+H=NO2+OH	6.62E+13	0	0	
116	NO3+OH=NO2+HO2	1.39E+13	0	0	
117	NO3+HO2=HNO3+O2	5.55E+11	0	0	
118	NO3+HO2=NO2+OH+O2	1.51E+12	0	0	
119	N2O4+H2O=HONO+HNO3	2.52E+14	0	11590	g, q
120	N2O3+H2O=HONO+HONO	3.79E+13	0	8880	
121	NO+H(+M)=HNO(+M)	1.52E+15	-0.41	0	

122	HNO+H=NO+H2	4.46E+11	0.72	655	
123	HNO+OH=NO+H2O	1.30E+07	1.88	-956	
124	HNO+O=OH+NO	5.00E+11	0.5	2000	
125	HNO+O=NO2+H	5.00E+10	0	2000	
126	HNO+O2=NO+HO2	2.20E+10	0	9140	
127	HNO+N=NO+NH	1.00E+11	0.5	2000	
128	HNO+N=H+N2O	5.00E+10	0.5	3000	
129	HNO+NH=NH2+NO	5.00E+11	0.5	0	
130	HNO+NH2=NH3+NO	2.00E+13	0	1000	
131	HNO+HNO=N2O+H2O	8.50E+08	0	3080	g, q
132	HNO+NO2=HONO+NO	6.02E+11	0	2000	
133	NO+OH(+M)=HONO(+M)	2.00E+12	-0.05	-721	
134	NO2+H+M=HONO+M	1.40E+18	-1.5	900	
135	HONO+O=OH+NO2	1.20E+13	0	5960	
136	HONO+OH=H2O+NO2	1.26E+10	1	135	
137	HONO+HONO=H2O+NO2+NO	2.30E+12	0	8400	g, q
138	HONO+NH2=NO2+NH3	5.00E+12	0	0	
139	NO2+OH(+M)=HNO3(+M)	2.41E+13	0	0	
140	NO+HO2+M=HNO3+M	1.50E+24	-3.5	2200	
141	HNO3+OH=NO3+H2O	1.03E+10	0	-1240	
142	NH3+O=NH2+OH	1.10E+06	2.1	5210	
143	NH3+OH=NH2+H2O	5.00E+07	1.6	950	
144	NH3+HO2=NH2+H2O2	3.00E+11	0	22000	
145	NH2+O=H2+NO	5.00E+12	0	0	
146	NH2+O=HNO+H	4.50E+13	0	0	

147	NH2+O=NH+OH	7.00E+12	0	0	
148	NH2+OH=NH+H2O	9.00E+07	1.5	-460	
149	NH2+HO2=HNO+H2O	3.00E+13	0	0	
150	NH2+HO2=NH3+O2	4.50E+13	0	0	r
151	NH2+O2=HNO+OH	4.50E+12	0	25000	
152	NH2+NO=NNH+OH	9.30E+11	0	0	estimate (s)
153	NH2+NO=N2+H2O	2.00E+20	-2.6	920	
154	NH2+NO=H2+N2O	1.00E+13	0	33700	t
155	NH2+NO2=N2O+H2O	1.10E+18	-2	0	t
156	NH+O=NO+H	4.50E+13	0	0	
157	NH+O=N+OH	4.50E+13	0	0	
158	NH+OH=HNO+H	2.00E+13	0	0	
159	NH+OH=N+H2O	5.00E+11	0.5	2000	
160	NH+HO2=HNO+OH	1.00E+13	0	2000	
161	NH+O2=HNO+O	4.00E+13	0	18000	
162	NH+O2=NO+OH	7.80E+10	0	1530	
163	NH+H2O=HNO+H2	2.00E+13	0	13850	
164	NH+N2O=N2+HNO	2.00E+12	0	6000	
165	NH+NO=NNH+O	5.60E+12	0.21	10870	
166	NH+NO=N2+OH	6.10E+13	-0.5	120	
167	NH+NO2=NO+HNO	1.00E+11	0.5	4000	
168	N2H4+O=N2H2+H2O	8.50E+13	0	1200	
169	N2H4+O=N2H3+OH	2.50E+12	0	1200	
170	N2H4+OH=N2H3+H2O	3.00E+10	0.68	1290	
171	N2H4+HO2=N2H3+H2O2	4.00E+13	0	2000	

172	N2H3+O=N2H2+OH	2.00E+13	0	1000
173	N2H3+O=NNH+H2O	3.16E+11	0.5	0
174	N2H3+OH=N2H2+H2O	3.00E+10	0.7	1290
175	N2H3+O2=N2H2+HO2	3.00E+12	0	0
176	N2H3+HO2=N2H2+H2O2	1.00E+13	0	2000
177	N2H3+HO2=N2H4+O2	8.00E+12	0	0
178	N2H2+O=NH2+NO	1.00E+13	0	0
179	N2H2+O=NNH+OH	2.00E+13	0	1000
180	N2H2+OH=NNH+H2O	1.00E+13	0	1000
181	N2H2+HO2=NNH+H2O2	1.00E+13	0	2000
182	N2H2+NO=N2O+NH2	3.00E+10	0	0
183	NNH+O=N2+OH	1.70E+16	-1.23	500
184	NNH+OH=N2+H2O	2.40E+22	-2.88	2444
185	NNH+O2=N2+HO2	1.20E+12	-0.34	150
186	NNH+O2=N2O+OH	2.90E+11	-0.34	150
187	NNH+HO2=N2+H2O2	1.00E+13	0	2000
188	NNH+NO=N2+HNO	5.00E+13	0	0

a) Enhanced third-body efficiencies (relative to Ar): H_2 = 0.0, H_2O=6.2

b) Enhanced third-body efficiencies (relative to Ar): H_2 = 2.5, H_2O=6.2, O_2=20, NO=5, N_2=5, N=5

c) Enhanced third-body efficiencies (relative to N_2): H_2 = 2.5, H_2O=6.2, Ar=0.88

d) Enhanced third-body efficiencies (relative to N_2): H_2 = 1.5, H_2O=1.1, Ar=0.44

e) Enhanced third-body efficiencies (relative to N_2): H_2 = 2.5, H_2O=6.4, Ar=0.38

f) Rate constant is the sum of two expressions

g) Pressure-dependent reaction. k_0 and k_∞ refer to the low- and high-pressure limits, respectively. Reaction with specified F_{cent} parameters use the Troe form, all others use the Lindemann expression

h) Enhanced third-body efficiencies: H_2O=0.0

i) Enhanced third-body efficiencies (relative to Ar): NO=3, N_2=1.5

j) Enhanced third-body efficiencies (relative to Ar): O_2=1.4, N_2=1.7, N_2O=3.5, NO=3, H_2O=12

k) Enhanced third-body efficiencies (relative to N_2): N_2O = 4.4, O_2=0.8, Ar=0.6, NO=1.8, NO_2=6.2

l) Rate constant has been measured by Clyne and McDermid [88]

m) Enhanced third-body efficiencies (relative to Ar): O_2=0.8, H_2=2, H_2O=10

n) Enhanced third-body efficiencies (relative to N_2): N_2O_4=2, Ar=0.8, NO_2=2

o) Enhanced third-body efficiencies (relative to Ar): N=5, O=2.2

p) Enhanced third-body efficiencies (relative to Ar): N_2=2.0, H_2=2, O_2=2, H_2O=15

q) Enhanced third-body efficiencies (relative to N_2): H_2O=10, O_2=2.0, Ar=0.75, H_2=2.0

r) The rate constant is attributed to the reaction $NH_2 + NO = N_2 + H + OH$

s) Estimation based on the calculated activation energy

t) ½ of the total rate constant recommended for the reaction NH + O = Products

u) Enhanced third-body efficiencies : N_2=2.4, NH_3=3.0, He=0.6, N_2H_4=4.0